Exploring the Physics behind Dynamic Fragmentation through Parallel Simulations

THÈSE N^O 4898 (2010)

PAR

Sarah LEVY

Abstract

The physical mechanisms underlying the dynamic fragmentation of heterogeneous brittle materials are explored through numerical simulations. The use of computational facilities, rather than experimental or fundamental sciences, ensures the accurate tracking of rapidly evolving fields (such as stress field, energies and damage). The numerical framework is based on Galerkin approximations coupled to the Cohesive Zone model, which addresses the failure response. Depending on the number of degrees of freedom, serial or parallel simulations are performed. The finite element method with dynamic insertion of cohesive elements constitutes the basis of the serial calculations. However, it is replaced by the scalable discontinuous Galerkin formulation for parallel computing. Both frameworks recover accurately the physical mechanisms behind dynamic fragmentation.

The thesis is organized to handle gradually increasing complexity. First, the fragmentation of a quasi one-dimensional expanding ring, constituted of a heterogeneous material, is simulated. It involves two major mechanisms: crack initiation and crack interaction. Fragment sizes are highly dependent upon strain rate, material properties, and microstructural heterogeneity. Scaling laws of the average fragment size, as well as of the distribution of fragment masses, are proposed and lead to predictable laws.

Then, crack propagation mechanisms are investigated through parallel simulations of the quasi three-dimensional breakage of a thin plate. By analyzing the energetic response, two regimes are defined: the strength controlled and the toughness controlled. At low strain rates, defects play a key role and govern energy levels. They correspond to the strength controlled regime and induce disordered responses. At high strain rates, fragmentation is more organized, fragment masses follow Weibull distributions, and crack interactions become secondary. This is the toughness controlled regime, governed by energetic arguments. The transition between the two regimes is derived as a function of material parameters.

Finally, the transition between two- and three-dimensional fragmentation is analyzed. Massively parallel simulations of the fragmentation of a hollow sphere with variable thickness are conducted. The effect of dimensionality upon fragment shape and fragment mass distributions is analyzed.

Interestingly, although these three tests involve distinct mechanisms due to the specimen geometry, they share common behaviors. Quasi-static loadings lead to

highly dynamic fragmentation processes, involving extensive stress wave interactions. Defect distributions play a key role. By contrast, dynamic loadings are associated to smoother and more deterministic responses. They are primarily controlled by energy arguments. As suggested by Grady's energy balance theory, this results in a predictable dependence of the average fragment size and strain rate, characterized by a power law of exponent -2/3. However, we recover more fragments than Grady because of our ability to reproduce explicitly and accurately time-dependent mechanisms (dynamics of stress waves and energy transfers).

Therefore, the interpretation of these numerical results sheds light on the complexity of the physics underlying fragmentation. The dynamics of stress waves, energetic arguments, the loading conditions, the dimensionality of the geometry, and the material itself (bulk and defects) must be all evoked to draw a global picture of the phenomenon. Reproducing such processes requires a high level of accuracy that novel parallel numerical frameworks are able to provide.

Résumé

La fragmentation dynamique de matériaux fragiles et hétérogènes s'accompagne
de mécanismes complexes. La simulation numérique d'un tel phénomène offre la
possibilité d'examiner des grandeurs physiques dont l'évolution rapide est difficile-
ment prévisible analytiquement et observable expérimentalement. Dans cette thèse,
le schéma numérique est basé sur le couplage des méthodes de Galerkin, qui four-
nissent une approximation de la réponse structurelle sans endommagement, et de
l'approche cohésive pour modéliser la rupture. Lorsque le nombre de degrés de
liberté n'est pas excessif, la méthode de Galerkin continue (i.e. la méthode des élé-
ments finis) est utilisée sur un processeur. Cependant, lorsque le maillage s'affine, le
calcul parallèle devient nécessaire et la méthode de Galerkin discontinue adéquate.
En effet, aisément parallélisable, scalable et intégrant naturellement des disconti-
nuités telles que les chemins de ruptures, cette dernière rend possible la simulation
parallèle de la fragmentation de structures tridimensionnelles à des hautes vitesses
de déformation.

Cette thèse est construite de manière à accroître graduellement la complexité
des études. Dans un premier temps, la fragmentation d'un anneau constitué d'un
matériau hétérogène est étudiée. Cette géométrie engage deux mécanismes : l'ini-
tiation et l'interaction des fissures. Bien que la taille des morceaux soit fortement
dépendente du chargement et du type de matériau, une normalisation adaptée per-
met de prédire le nombre de morceaux générés ainsi que la distribution de leur
taille.

Ensuite, les mécanismes de propagation de fissures sont analysés. La fragmenta-
tion d'une plaque composée d'un matériau fragile est simulée en parallèle. L'étude
de l'évolution des énergies débouche sur la définition de deux régimes. En quasi-
statique, les défauts jouent un rôle prépondérant ; leurs contraintes à la rupture
contrôlent ce régime désordonné. En dynamique, des critères énergétiques justifient
une réponse ordonnée et prévisible. Les distributions des masses de fragments suiv-
ent alors une loi de Weibull et l'effet des interactions de fissures devient négligeable.
La limite entre les deux régimes est fonction des propriétés matériaux.

Enfin, la transition entre fragmentation en deux et trois dimensions est examinée.
Une sphère creuse d'épaisseur variable est sollicitée en tension. Le nombre de degrés
de liberté peut accroître considérablement, ce qui nécessite des moyens de calcul
conséquents. L'attention est portée sur la forme des fragments et la distribution de
leurs masses qui affichent une forte dépendence à la dimensionalité du problème.

Par ailleurs, bien que la géométrie de ces trois tests diffère et génère des mécanismes physiques distincts, un point commun se dégage. Dans toutes les simulations, le régime dynamique est contrôlé par des critères énergétiques, alors que le régime quasi-statique est dominé par l'effet des ondes dynamiques ainsi que par les contraintes à la rupture des défauts. Le modèle énergétique de Grady, qui prédit que la taille caractéristique des morceaux suit une loi puissance dont l'exposant associé à la vitesse de chargement est -2/3, est vérifié en dynamique. Cependant, la présence des ondes de relaxation dans notre modèle numérique est à l'origine de fragments de taille moindre. Cette constatation souligne le rôle déterminant des ondes dans le processus de fragmentation, à la fois en quasi-statique et en dynamique, et pour tout type de géometrie et de matériau.

Ainsi, l'interprétation de ces résultats numériques atteste de la complexité du phénomene de fragmentation. Les interactions non linéaires des ondes mécaniques, l'évolution rapide des énergies, l'initiation et la propagation des fissures, l'influence des conditions aux limites, de la dimensionalité et des propriétés du matériau doivent être confrontées.

Mots Clés: fragmentation dynamique, matériaux fragiles et hétérogènes, simulation numérique parallèle, distribution de taille de morceaux, conversion des énergies, ondes mécaniques de décharge.

Acknowledgments

It was a great pleasure to work in EPFL over the past three years, and to contribute to the evolution of the LSMS. Since my arrival, the LSMS laboratory has evolved amazingly. The research team has expanded and diversified. This continuous enrichment has undoubtedly motivated me and has inspired my research. Therefore, I would like to acknowledge everybody who contributed to the successful realization of this thesis, professors and colleagues, friends and family.

My deepest gratitude goes to my advisor, Prof. Jean-François Molinari, for his valuable guidance. His great enthusiasm and his perpetual energy created a positive team-work atmosphere, enhancing his advisees' creativity. His involvement and original ideas have triggered and nourished my intellectual maturity that I will benefit from, for a long time to come.

I was delighted to work with Prof. Raul Radovitzky during his sabbatical year at LSMS. He was an irreplaceable colleague with outstanding advices. He was always available, willing to help and debate. His crucial contribution was a backbone of this research and thesis.

I owe special acknowledgments to Prof. Lyesse Laloui, Prof. Jian Zhao, Prof. Alain Combescure, and Prof. Raul Radovitzky, as my thesis committee members.

I am indebted to my colleagues for their support, the stimulating scientific discussions, and even more important, their overall good company. In particular, I would like to thank those who were patient when technical difficulties arose (I have to admit that, I did kill nodes of the cluster!).

Words cannot express my appreciation to you, Jean-Baptiste. Your love and persistent confidence in me, have taken the load off my shoulders. Despite the geographical distance, you have accompanied me, every single day of these three years.

Finally, my friends and my dear family, I would not have been able to write this manuscript without you. Thanks for your precious support and enthusiasm.

Contents

Introduction

Writing a thesis requires profound faith in its usefulness for the scientific community, the industrial world, and the society as a whole. As an introduction, this chapter sheds light on the major motivations governing this study. It also describes the strategy used to answer the two main questions that are the focus of this work:

*What are the physical mechanisms governing the
dynamic fragmentation of heterogeneous materials?
Can numerical simulations predict accurately such a
complex phenomenon?*

1.1 At any scale and in diverse contexts

Fragmentation is the breakage of a contiguous body into several pieces. Dynamic fragmentation focuses on mechanical loadings with a strong dependence on time. It occurs in very distinct contexts and at any scale. For instance, at astronomic scales, a supernova results from the fragmentation of a giant star; objects throughout the asteroid belt and other regions of the solar system, as well as spatial debris orbiting the Earth's atmosphere are subjected to regular collisions. Observing the Earth from space also reveals that its surface is covered with various fragments of rocks. Similarly, at the small scales, DNA fragmentation controls cell replication [Gudwska-Nowak 2009], nuclear and elementary particle collisions constantly occur in daily life [Holian 1988].

Numerous human-scale applications have also been used by engineers. In structural engineering, major technical developments concern mitigating collisions on thin structures, such as the impact of flying objects on a plane, in car crashes, in glass breakage. Moreover, in nuclear power plants, since protective shells are expected to survive the impact loading of an incoming missile, concrete structures are designed to resist extreme loadings. In the military domain, intensive research is carried out to strengthen tanks and bullet-proofing for army personnel. Fragmentation also concerns the medical industry: a technique to help with the elimination of kidney stones without surgical intervention involves sending pressure pulses onto the stone to break it into smaller pieces, which may then be eliminated naturally. Again, in mining and crushing processes, rocks are fragmented to the required size. Finally, objects in daily life are frequently subjected to dynamic fragmentation: a kitchen plate or a glass dropping onto the ground will naturally break into many fragments.

Fragmentation is thus a physical process which occurs at various scales and in multiple contexts. It is a key issue in the rock industry, military protection, medical surgery, transport safety, and in many other spheres. Its understanding may thus contribute to the improvement of industrial capabilities, the design of novel materials, and the development of innovative medical applications. At the most fundamental level, it may also help to recount the history of our galaxy and the Earth.

(a) *A meteorite collapse*
astrosurf.com
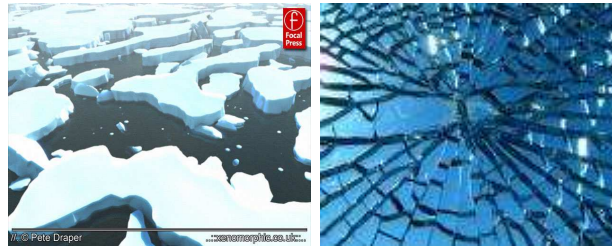
(b) *Fragmentation of a glacier*
xenomorphic.co.uk

(c) *Shattering of a security glass*
frozen-reality.de

(d) *Car crash*
koolyaar.wordpress.com

Figure 1.1: Fragmentation of different materials at different scales and for different loadings

1.2   Some major contributions of the 20th century

This vast range of applications emphasizes the relevance of the past and current research on fragmentation. Understanding the physics and controlling fragmentation were of special interest during the previous century. Because of the violence of the process, scientists began by studying the results of fragmentation, e.g. the number of fragments and the distribution of fragment sizes. In the thirties, Rosin and Rammler [Rosin 1933] who worked in the coal and ore crushing industry, proposed the first empirical description of fragment sizes. They noticed that all the fragmentation processes they had encountered generated Weibull distribution. Interested in this empirical result, Lienau [Lienau 1936] published in 1936, a statistical derivation of the exponential form for one-dimensional bars, governed by the Poisson point process. In the forties, Schuhmann [Schuhmann 1941] modeled fragmentation as a fractal process, and thus, the distribution of fragment sizes as a power law.

During the same period, Weibull [Weibull 1939] conducted quasi-static experiments and explained that failure originates at some special locations, where the material is weakened by the presence of defects. Weibull's main contribution was to conclude that every material is inherently heterogeneous and that structural defects are the origin of failure. Since specimens have different microstructures, their failure strengths are not properly identical. Weibull introduced the concept of probability of failure in quasi static, and derived the Weibull distribution, which is only based on material parameters and specimen size.

During World War II, the Nobel laureate N.F.Mott achieved seminal investigations on fragmentation resulting from the explosive rupture of cylindrical bombs. In association with Linfoot [Mott 1943b], he generalized the Lienau distribution to two-dimensional structures. His deep understanding of the physical process led him to devise the wave theory of fragmentation [Mott 1947]. The key idea lies in stress relaxation of the body: when a crack opens, it releases stress waves that protect the encompassed areas from incurring further damage. For the first time, the notion of time was included. Fragmentation is a non-instantaneous process in which dynamic effects prevail. His extensive output has had a profound impact on subsequent studies. Mott's theories were the first derivations based both on physics and statistics.

Later, in the sixties, Gilvarry [Gilvarry 1961a] came back to Lienau's conclusions and noted some inconsistencies. He published an elaborate physics-based statistical development of fragment size distributions. Following Weibull's ideas, he postulated the existence of flaws distributed independently within the volume, the surfaces and the edges of the body. He assigned a Poisson process to each type of flaw. However, all these substantial developments are based on statistics and none properly includes the physics underlying fragmentation.

In the eighties another major contribution was made. Instead of considering fragmentation through its dynamics effects, Grady carefully investigated the evolution of the local energy of an expanding body [Grady 2007]. He formulated an expression of the characteristic fragment size, based on loading rate and relevant material properties. His simple law predicts the number of fragments resulting from the fragmentation of a one-,two-, or three-dimensional structure. He also considered separately brittle and ductile processes, which until then had been mismatched.

However, although physical and statistical theories help conceptualize complex processes, they cannot fully account for all the details. In the case of fragmentation, experiments and numerical simulations strengthen the knowledge associated with this probabilistic and irreversible phenomenon. Shockey et al. empirically described the nature of the physical processes occurring during rock fragmentation [Shockey 1974]. They also implemented a wave propagation code to trace the stress history in the specimen volume. Following the same tendency, current research is now using the latest experimental and numerical techniques to obtain an in-depth insight of the physics underlying fragmentation. New resources are constantly required to model accurately the real process in order to understand it better.

Our work here is in line with these computational and physically-based considerations. The main objective of the present thesis is the understanding of the mechanisms of dynamic fragmentation. We restrict the study to brittle materials, such as many types of rocks, ceramics, polymers, and hard metals, which are characterized by low fracture energy and little tendency to deform before failure. Although this limitation significantly alleviates the problem, there remain many challenging issues.

1.3 Challenges in fragmentation modeling

Dynamic fragmentation undergone by brittle materials is based on complex processes which may be classified in three stages: crack nucleation, crack propagation, and fragment coalescence. They infer distinct physical mechanisms based on material defects, dynamics of stress waves, and energetic arguments.

The nucleation phase determines the number of initiated cracks. It depends both on the density and size of material defects, and on the rate and duration of the driving force. The rate of loading has a key effect in determining activated cracks because of unloading wave effects. Indeed, when a crack is activated, it opens until failure, which makes the stress decrease locally to zero. This stress drop alters the surrounding areas through stress waves that propagate from the activated defects in every direction. In a first stage, the encompassed zones are protected and no crack activation occurs. If the loading rate is very low, the stress waves have time to encompass most of the structure; only a few defects are nucleated. For high loading

rates, stress waves do not have time to propagate which leads to a higher rate of defect nucleation; a large amount of defects may be activated. The modeling of the microstructure and the accurate description of the highly non-linear network of stress waves constitute the main challenges of the nucleation phase.

The second step in dynamic fragmentation of brittle materials is crack propagation. Many issues then arise. How fast can a crack propagate? How far can it go? What orientation and what path does it follow? A crack grows until it reaches a free surface (that a boundary or another crack may constitute), or until the stress intensity factor at its tip falls below a critical threshold. Predicting crack path is rather complex due to the high non-linearity of the stress field, affected both by interacting stress waves and defects. Crack orientation is controlled by the direction of the maximum tensile stress and may deviate from the nominal path because of the presence of material heterogeneities. In addition, since the motion of a crack alters the stress field, crack orientation also depends on surrounding cracks. Moreover, bifurcation is commonly observed in brittle materials: an initial single crack may branch into two cracks, which in turn may also branch. Energy requirements have been cited to predict whether bifurcation occurs. Instability at crack tip has also been detected [Fineberg 1991]. Hence, the propagation and the branching of a crack depend on the microstructure and on the other crack states.

Finally, cracks coalesce, forming fragments of different sizes and shapes. Understanding crack coalescence is crucial in determining the distribution of fragment sizes. The obvious lack of understanding justifies the large number of empirical and statistical formulations, which scarcely include the physics underlying fragmentation. Nonetheless, the biggest challenge overall is the sheer number of fragments, which may become quickly untractable.

1.4 Objectives and strategy

The present thesis aims at contributing to the research dealing with fragmentation by providing some answers to the previously described issues. How many fragments do high rate loadings produce? Can the role of microstructure be quantified in crack nucleation and crack coalescence phases? What is the effect of stress unloading waves? What are the physical parameters controlling the process? Are quasi static and dynamic responses identical? In this manuscript, we attempt to shed light on the complexity of these matters and to propose some answers.

We choose to use numerical simulations to tackle these questions because of the inability of analytical derivations to fully account for the inherent complexity of the phenomenon. The network of stress wave interactions, favored by material defects, is highly non linear and hardly predictable. Its accurate description requires a level

of complexity that only computers can provide. As a result, numerical modeling is an appropriate tool to study fragmentation. Our simulations naturally incorporate dynamic and energetic aspects. Establishing a numerical framework is generally based on both modeling the phenomenon and writing efficient algorithms. Physical and numerical errors can arise. Therefore, a major question raised by numerical modeling is whether the computed solution is valid: how can one be sure that this approximate solution is representative of the actual behavior? Does a dependence on the mesh exist? Therefore, convergence is first verified before interpreting the results. We also emphasize the need for high performance computing. In the context of dynamic fragmentation, since numerous cracks may nucleate, significant computational power and adequate parallel codes are required to yield numerical convergence.

We focus on three different geometries (ring, plate, and hollow sphere) and load them in tension to reproduce explosion loadings. Materials are mostly brittle and are thus subjected to the three phases described above. Their response is sensitive to defects, which concentrate stresses, and since failure dissipates only a small amount of energy in brittle materials, many cracks nucleate simultaneously. In order to avoid artificial stress concentration that boundary conditions and geometry may generate, we load the body uniformly before failure onset by imposing adequate velocities and displacements. The elastic response is computed by use of general finite element procedures (continuous and discontinuous Galerkin frameworks), while failure is modeled with cohesive zone laws. This framework makes it possible to represent fragments explicitly, and to track the evolution of potential, kinetic and dissipated energies.

The global strategy of the thesis lies in its gradual increase in complexity. First, we conduct a simple test. It is quasi one-dimensional and only involves crack initiation. Issues related to crack interactions and material heterogeneity are addressed. Secondly, a quasi two-dimensional plate is fragmented. Crack propagation, bifurcation, and nucleation are included. Finally, the last tests simulate the response of a three-dimensional structure, a hollow sphere with variable thickness. Besides physical complexity, technical complexity is also added. Going from one to three dimensions naturally requires finer meshes and increased computational power. One-dimensional tests can be simulated using a single processor. However, parallel programming is necessary when moving to two and three dimensions. We benefit from the considerable computational capabilities (Pleiades2, Callisto, and BlueGene clusters) that EPFL provides to access fine meshes and multi-dimensionality. This step-by-step strategy allows us to convey some simple fundamental concepts and to test the accuracy of our results.

1.5 Main physical contributions of the thesis

The expanding ring problem was first defined by Mott when he studied stress wave healing effect. Because of the simplicity of the ring's geometry, it has been widely studied since then. However, in these prior studies, the role of defects has been insufficiently investigated. In this present research, we are interested in understanding how defects affect the dynamics of stress wave interactions. We benefit from the quasi one-dimensional geometry of the ring to focus solely on crack initiation. Crack propagation and coalescence are of no interest in Mott's test. This is clearly an advantage in achieving our objective of quantifying the role of defect distribution in the overall process. We define a new material parameter dependent upon the weakest defect, the left tail of the defect distribution as well as its mean value. It relates the defect distribution to the rate of failure initiation that is shown to significantly affect the material response. We also propose scaling laws that involve this new parameter, the average fragment size and the loading rate, and that predict the number of fragments. The main contributions of this study rely on understanding that defects do play a crucial role during the crack initiation phase, and on quantifying this role through scaling laws.

In addition, since all the fragments do not have the same size, we also investigate the properties of the distribution of fragment sizes and of the largest fragments through statistical analyzes. In the ring problem, we show that fragment size distributions exhibit a predictable shape, irrespective of the loading rate, the length of the ring and defect parameters. By contrast, an investigation of the largest fragment behavior highlights a strong dependence upon these quantities. The key information here is that one-dimensional geometries lead to fragment size distributions that are independent of material heterogeneity and loading. These only affect fragmentation response through the number of fragments and the largest fragments.

As already mentioned, the ring geometry only involves crack initiation. Crack propagation cannot be analyzed with such a simple geometry. We thus consider a thin plate submitted to biaxial tension. Naturally, since this geometry has a volume larger than the ring's geometry, the number of degrees of freedom may reach extensive values that a single processor cannot handle. Particular attention is thus paid to parallelization issues. The traditional finite element/cohesive elements framework can hardly be efficiently parallelized because of the substantial inter-processor communication. We thus use another technique, the discontinuous Galerkin method coupled to cohesive zone modeling, to reach numerical convergence at high strain rates for multi-dimensional geometries. Then, we provide insights into the physics of fragmentation through energy-based arguments. We show that quasi static and dynamic regimes are governed by separate mechanisms. In quasi static, fragmentation is controlled by defect failure strength and failure occurs very rapidly compared to the loading phase. Stress wave extensively interact leading to irregular frag-

mentation pattern. The average fragment size is highly dependent upon material microstructure. The quasi-static regime is thus chaotic (in physics, chaotic systems are highly sensitive to initial conditions, such as geometry, material, boundary conditions, etc). By contrast, in dynamics, fragmentation is controlled by energy arguments. Since they travel approximately at the same speed as material points, stress waves barely interact. Average fragment size and fragment size distributions follow more regular patterns. This dynamic regime is thus deterministic (in physics, determinism is the view that a behavior is governed by causality and may thus be described by physical laws). The limit between these two regimes is dependent upon material and defects parameters. The main contribution of this study lies in the understanding of the physics governing fragmentation. Crack propagation obviously renders it more complex, and recourse to energy arguments constitutes an efficient way to deal with it.

Nonetheless, the plate geometry remains quasi two-dimensional and cannot capture three-dimensional failure mechanisms. Therefore, we study the fragmentation of a hollow sphere through its energy consumption, the fragment masses, and the shape of the fragments. By varying its thickness, the transition between two to three dimensions is investigated. We show that the distribution of fragment masses, as well as the fragment shapes, are highly dependent upon the dimensionality of the geometry. Very thin sphere induces flat fragments, whereas when it is very thick, equally-sized fragments tend to be encountered. During the transition between both regimes, fragments are more elongated. To the best of our knowledge, this is the first time that the issue of fragment shapes resulting from three-dimensional fragmentation is tackled.

1.6 Outline of the following chapters

In the following chapters, we describe in depth these results. The thesis is divided into nine chapters:

- **Chapter two** is a collection of fragmentation models that have been proposed during the past century. Empirical, statistical, energy-based models of fragmentation are outlined. We emphasize that most of them consider homogeneous materials, and that the issue of heterogeneity is increasingly appealing to researchers. Some experimental devices, as well as numerical tools, are also reported.

- **Chapter three** is dedicated to our modeling and implementing. We detail the finite element and the discontinuous Galerkin methods, which handle the elastic response. The cohesive zone approach is used to address failure. We describe the cohesive methodology and ultimately focus on linear irreversible cohesive law. The question of code parallelization and efficiency is also addressed. Statistical defect modeling is tackled as well: based on both the

weakest link theory and statistical arguments, we emphasize that Weibull distributions are the most appropriate distributions to represent defects in brittle materials.

- **Chapter four** is a transitional chapter, which specifies the main physical mechanisms occurring during a fragmentation process. Dynamic effects related to stress wave interactions, as well as energy arguments are detailed.

- **Chapter five** reports the expanding ring results. We quantify the role of defects via a characteristic parameter, which is afterward used in scaling relationships. The normalized average fragment size, as a function of normalized strain rate, is shown to follow a unique law.

- **Chapter six** concentrates on fragment mass statistics in one dimension. We show that the shape of the distribution is fully predictable, whereas largest fragments' behavior is strongly dependent upon length of the ring, strain rate and defects.

- **Chapter seven** presents the results obtained for the plate under biaxial tension. An enrichment of Grady's energy-based theory is proposed and yields to two regimes. Quasi static and dynamic responses are shown to be based on distinct physical mechanisms.

- **Chapter eight** provides a glimpse of the mechanisms underlying three dimensional fragmentation by focusing on fragment masses and shapes.

- **Chapter nine** is a summary of the answers provided by this thesis and proposes directions for future work.

Each chapter can be read independently from the others, but a linear reading will naturally facilitate their understanding.

A collection of fragmentation models in dynamics

During the past century, fragmentation has appealed to researchers from diverse fields. Engineers in mechanics, civil engineering, computer science, as well as statisticians, and physicists have developed a large amount of models that analyze the breakage of a structure subjected to high loadings. In the thirties, the first empirical observations concerning fragmentation have emerged. In this chapter, we first introduce these pioneering empirical models, mainly concerned by fragment mass distributions. Then, we present in the second section, some analytical models based on statistical and geometrical arguments. The third section is devoted to physics-based models; it details how energetic and dynamic arguments lead to complex principles, and rather simple laws. However, these physics-based arguments do not include material heterogeneity. In section four, the role of defects in fragmentation is described. Finally, in the two last sections, experimental and numerical techniques are enumerated.

2.1 Early experimental theories

2.1.1 Rosin-Rammler's empirical distribution

In the thirties, Rosin and Rammler [Rosin 1933] conducted fragmentation experiments in the fields of coal and ore crushing. They determined empirical fragment size distributions by separating fragments within a given size range, using a collection of sieving screens. They noticed that Weibull-type distributions [Weibull 1939] fitted well their experimental observations. Denoting s the characteristic size of a fragment, the Rosin-Rammler's distribution can be written as the cumulative fraction greater than size s:

$$F(s) = 1 - e^{-(s/s_0)^\beta} \tag{2.1}$$

where s_0 is characteristic size and β is the shape parameter. Several attempts have been made to justify analytically the Rosin-Rammler's distribution, among which Lienau [Lienau 1936] and Bennett [Bennett 1936] (see section 2.2.1). They based their theory on Poisson statistics in one and multiple dimensions.

2.1.2   Schuhmann's law and the concept of criticality in fragmentation

Historically attributed to Schuhmann [Schuhmann 1941], the limiting form of Rosin and Rammler's distribution for small fragments is a power law:

$$F(s) = (s/s_0)^\beta \qquad (2.2)$$

Defined in the forties, Schuhmann's distribution has been reused since the seventies to highlight that fragmentation is a self-similar phenomenon. The concept of self-similarity in fragmentation has appealed to many engineers and physicists during the past decades [Bershadskii 2000, Bird 2009, Perfect 1997, Bennett 1936, Moukarzel 2007, Oddershede 1993, Andersen 1997, Johansen 2000]. Their theories stem from the observation of natural phenomena and of experimental results. As pointed out by Turcotte in [Turcotte 1986b], this power law is related to the fractal process:

$$N(s) \propto s^{-D} \text{ with } D > 0 \qquad (2.3)$$

where N is the number of objects whose size is greater than s, and D is the fractal dimension. If $M(s)$ is the mass of the fragments with size smaller than s, then $N \propto M/s^3$ in three dimensions, which directly gives $D = 3 - \beta$. Since $D > 0$, a necessary condition for the fragmentation to be fractal is $\beta < 3$. Examples of objects whose fragment size distribution is fractal were listed by Turcotte. For any of his 21 cases, Turcotte showed that $0.5 < \beta < 1.5$ [Turcotte 1986a, Turcotte 1986b].

2.1.3   Mott-Linfoot's distribution

During World War II, Mott and Linfoot [Mott 1943b] carried out experiments on fragmentation of bomb shells. They gathered the large amount of data on fragment masses and fitted their results with:

$$F(m) = 1 - e^{-\left(\frac{m}{m_0}\right)^{1/2}} \qquad (2.4)$$

where m is the fragment mass, and m_0 is a characteristic mass. They proposed a theoretical justification of this distribution based on Poisson statistics in two dimensions. Mott and Linfoot also wrote several reports, which have had a profound impact on future works. They still constitute the basis of current models and their distribution is still widely used to describe explosion of ductile materials.

2.2   Geometric distributions

2.2.1   Lienau's theoretical distribution

Lienau [Lienau 1936] considered an infinite line that is about to collapse into several fragments. Breakpoints are introduced with an equal probability at any point

on the line. Lienau aimed at describing statistically the length of the fragments, demarcated by randomly-placed breakpoints.

Let us thus consider a line in which breakpoints are introduced randomly. If the failure sequence follows a Poisson point process (events occur continuously and independently of one another), the probability of finding k breakpoints within a given length l is:

$$P(k, l) = \frac{\left(\frac{l}{l_0}\right)^k e^{-\frac{l}{l_0}}}{k!} \tag{2.5}$$

where l_0 is the average spacing between breaks. Therefore, the probability of occurrence of fragments of length l within a tolerance dl is:

$$f(l)dl = P(0, l)P(1, dl) = (1/l_0)\, e^{-l/l_0} dl \tag{2.6}$$

f is the probability density function associated to the process. By integrating f, we compute the cumulative fragment distribution:

$$F(l) = 1 - e^{-l/l_0} \tag{2.7}$$

Binomial distribution for finite-size lines: If the line has a finite size L, then the random placement of breakpoints does not follow Poisson statistics anymore but the binomial probability [Grady 1990]. The cumulative distribution is then:

$$F(l) = 1 - \left(1 - \frac{l}{L}\right)^{N_f - 1} \tag{2.8}$$

where N_f is the number of fragments. Naturally, it converges to Lienau's exponential distribution when N_f becomes large.
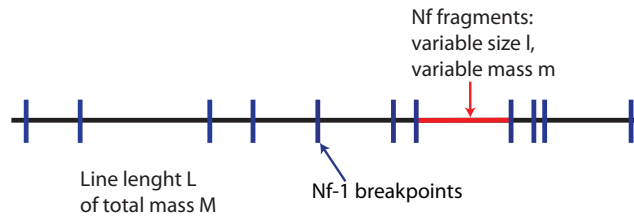
Figure 2.1: Finite line, broken at some random places, which results in distinct fragment lengths [Grady 1990].

Effect of grain sizes: An interesting constraint consists in taking into account the limiting grain size of a body, which determines the minimum spacing between two breakpoints [Grady 2007]. Setting this minimum size to δ, the number of breakpoints per unit length is $N = 1/\delta$. If N_f is the number of fractured sites, then the

probability of fracture at any breakpoint is $p = N_f/N = \delta * N_f$. The probability of finding a fragment of length $l = n.\delta$ is:

$$P(l) = (1 - p)^n p \tag{2.9}$$

This relation converges to the exponential distribution as δ becomes small.

2.2.2   Mott-Linfoot's random lines model

In an attempt to justify their distribution defined in section 2.1.3, Mott and Linfoot pursued geometric study of the two-dimensional fragmentation of a plate submitted to biaxial tension. Figure 2.2 illustrates the geometric algorithms that they studied. Grady described accurately their arguments [Grady 2007, Grady 2006b, Grady 1985]. Depending on the fragmentation pattern, Mott and Linfoot derived analytical or empirical models of fragment size distribution. They were, however, not able to deal with all the scenarios in figure 2.2. They simply concluded their study by observing that the distribution of fragment sizes is strongly dependent upon the geometric partitioning of the plate.
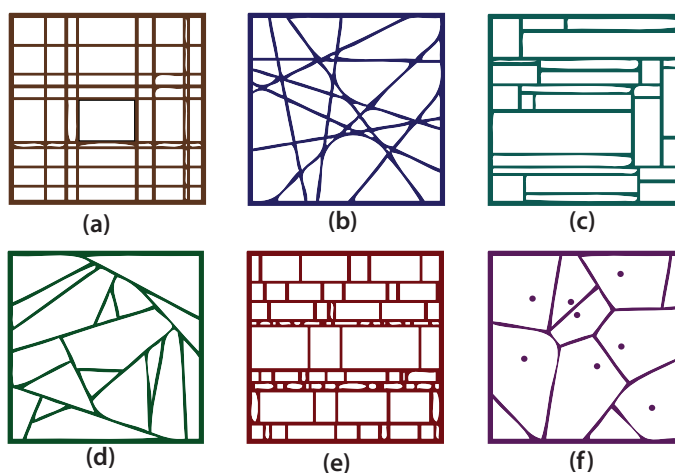
Figure 2.2: Various geometric fragmentation patterns explored by Mott and well detailed in [Grady 1985]. Picture is taken from [Grady 2006b]. (a) Random horizontal and vertical lines of equal length. (b) Randomly distributed and oriented lines. (c) Random horizontal and vertical segments. (d) Same algorithm as (c) with a deterministic condition on the fragment shortest dimension. (e) Randomly distributed and oriented segments. (f) Voronoi fragmentation.

2.2.3   Voronoi-Dirichlet's fragmentation

The Voronoi-Dirichlet construction (figure 2.2(f)) has received extensive attention in diverse fields such as natural sciences, mathematics, as well as computer sciences. For instance, Voronoi decomposition has been employed in shape analysis

of giraffe skin and honeycomb [Blum 1973], in cosmology [Coles 1991], in climate modeling [Ringler 2008], in crystallography [Aurenhammer 1991], in fracture mechanics [Bishop 2009]. The two-dimensional construction begins with a random distribution of points on the plate. Space is then partitioned by construction of perpendicular bisecting lines.

One dimensional distribution: In one dimension, the Voronoi-Dirichlet construction is the dual of the Lienau distribution (whereas Lienau's points represented breakpoints, they are the center of fragments in Voronoi-Dirichlet's construction). The probability of finding a length l is given by a Poisson point process:

$$f(l)dl = (1/l_0)\, e^{-l/l_0} dl \tag{2.10}$$

The probability of finding a length l_1 adjacent to a length l_2 is:

$$f(l_1)f(l_2)dl_1 dl_2 = \left(1/l_0^2\right) e^{-(l_1+l_2)/l_0} dl_1 dl_2 \tag{2.11}$$

Using the transformation $L = (l_1 + l_2)/2$ and $\psi = (l_1 - l_2)/2$ leads to the Voronoi-Dirichlet distribution on a line:

$$f(L) = \frac{2}{l_0}\frac{2L}{l_0}e^{-2L/l_0} \tag{2.12}$$

Multi-dimensional distribution: Equation 2.12 is the gamma function with shape parameter 2. Kiang [Kiang 1966] offered without proof that symmetrically higher order gamma functions would provide analytic fragment distributions for Voronoi-Dirichlet partitioning (of an area or a volume). The general expression of the fragment distribution, as a function of the fragment mass m is:

$$f(m) = \frac{1}{m_0}\frac{n}{\Gamma(n)}\left(\frac{nm}{m_0}\right)^{n-1} e^{-nm/m_0} \tag{2.13}$$

where m is the fragment mass, and n=2, 4, or 6 for a line, surface, or volume. More details can be found in [Grady 2006b].

2.2.4 Grady-Kipp's postulate

Grady and Kipp [Grady 1995] observed that Mott and Linfoot's distribution, which has been proved to be valid for exploding steel cylinders, is not necessarily the best fitting distribution in multiple dimensions. They suggested that, similarly as Lienau's assumption in one-dimension, fragmentation is a Poisson point process in two and three dimensions. It is determined by breakpoints distributed randomly over the scalar measure of mass. Contrary to Mott and Linfoot's distribution, Grady and Kipp's keeps the same linear exponential functional for both area and volume:

$$F(s) = 1 - e^{-(s/s_0)} \tag{2.14}$$

2.3   Physics-based fragmentation

2.3.1   Mott's description of the dynamics of fragmentation

2.3.1.1   Wave propagation and associated characteristic length

The dynamic analysis pursued by Mott was based on the expanding ring test, as illustrated in figure 2.3. Prior to fracture, the ring undergoes uniform expansion at a constant strain rate $\dot{\varepsilon}$. Mott considered the material to be perfectly plastic with yield strength Y. Failure occurs randomly in both time and space. Mott also assumes that failure is an instantaneous process, relieving stress from Y to 0, in a negligible amount of time, at the breakpoint location. This sudden drop causes a non-linearity in the stress field, which results in stress waves, propagating from the breakpoint to the surrounding areas (figure 2.4). Regions experiencing tensile stress lower than Y are rigid. The boundary between rigid and perfectly plastic zones is located at the position x relatively to the breakpoint:

$$x(t) = \sqrt{\frac{2Yt}{\rho\dot{\varepsilon}}} \tag{2.15}$$

where ρ is the volumetric mass. The interface velocity thus depends both on material (Y, ρ) and kinematic $(\dot{\varepsilon}, t)$ parameters. Within the regions encompassed by stress waves, further fracture will not occur, since the stress drops to a value lower than Y.
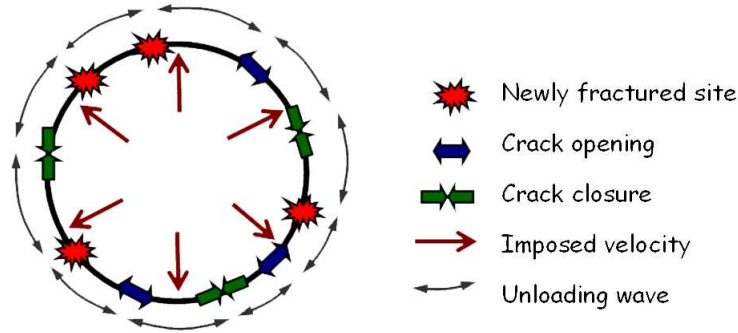
Figure 2.3: Mott's expanding ring.

However, Mott recognized that the rigid-plastic assumption could lead to inconsistencies. Years later, Lee [Lee 1967] considered the same problem with an elasto-plastic material. Waves are propagating at the elastic wave speed $c = \sqrt{E/\rho}$, where E is the Young's modulus. He showed that the shock discontinuity decays to zero at the distance h and time τ:

$$h = \frac{2Y}{\rho c\dot{\varepsilon}} \text{ and } \tau = \frac{h}{c} \tag{2.16}$$

Grady [Grady 2006b] showed that Mott's rigid-plastic solution and Lee's elasto-plastic solution are in good agreement. Although simple, Mott's theory offers a very good approximation to both the position of the interface, and to the stress and velocity fields behind the interface [Grady 2006b].
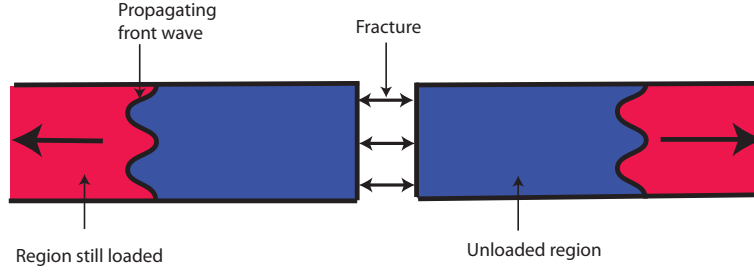
Figure 2.4: Mott's unloading waves, propagating from the breakpoint to surrounding areas. Loaded regions behave with a perfectly-plastic response, while unloaded regions are rigid. Unloaded regions cannot experience fracture anymore.

2.3.1.2 Statistical description of the occurrence of fracture and average fragment size

Mott proposed that the occurrence of fracture is governed by the fracture frequency $\lambda(\varepsilon)$, where ε is the strain. λ is also called the hazard function. He focused on three forms for λ [Mott 1943a] :

$$\lambda(\varepsilon) = \lambda_0 \tag{2.17}$$

$$\lambda(\varepsilon) = \frac{n}{\varepsilon_0}\left(\frac{\varepsilon}{\varepsilon_0}\right)^{n-1} \text{ with } n \geq 1 \tag{2.18}$$

$$\lambda(\varepsilon) = Ae^{\gamma\varepsilon} \tag{2.19}$$

Equation 2.17 leads to the exponential distribution; equation 2.18 refers to the Weibull distribution; equation 2.19 induces Gumbel distribution.

The probability that fracture occurs in a length dl at strain ε, within an interval $d\varepsilon$, is $\lambda(\varepsilon)d\varepsilon dl$. Let L be the length of the ring, which has not undergone fracture yet. At strain ε,

$$\frac{dL}{L} = -\lambda(\varepsilon)d\varepsilon \tag{2.20}$$

The expression of L is not trivial. Mott derived a complex geometrical analysis involving dynamic activation of breakpoints and subsequent stress release waves. He defined a function that accounts for stress wave releasing effects to model the interaction of multiple fractures. After complex developments detailed in length in [Grady 2006b], the length scale (or equivalently characteristic spacing between

breakpoints) emerging from the statistical fragmentation theory of Mott is:

$$\mu = \sqrt{\frac{2Y}{\rho\varepsilon^2\gamma}}$$

(2.21)

where γ is the scale parameter in the exponential hazard function 2.19.

2.3.1.3   Statistical description of the fragment masses

Along with deriving a characteristic length scale, Mott was interested in quantifying statistically the sizes of all the fragments. Here is a very brief overview of the derivation (more details can be found in [Grady 2006b]). Let us consider a body whose fragmentation has generated fragments of mass m. We define the function $h(m)$ such that $h(m)dm$ represents the chance to encounter one fragment of mass between m and $m+dm$. The chance to find a fragment of mass m within the interval dm is the product of finding no breaks within the interval 0 to m, and one break within the interval m to $m + dm$:

$$f(m)dm = e^{-\int_0^m h} \, h(m)dm$$

(2.22)

this leads to the cumulative fragment distribution:

$$F(m) = 1 - e^{-\int_0^m h}$$

(2.23)

The constant hazard function ($h(m) = h_0$) corresponds to the Poisson process, and results in the exponential distribution (equation 2.7). In two dimensions, the mass is proportional to the square root of 2, which directly leads to the Mott and Linfoot's distribution (equation 2.4). It is thus equivalent to consider Poisson point process in two dimensions and the power like hazard function with $n = 1/2$ (equation 2.18).

2.3.2   Grady's model of energy equilibrium

2.3.2.1   Average fragment size and local energy balance

In his key paper [Grady 1982], Grady derived a characteristic length scale based on the local balance of kinetic and fracture energy. Consider a body breaking into equally sized fragments. Uniform kinetic energy is introduced in each fragment that expands very rapidly. This energy is used into local expansion and rigid-body motion. The only part that contributes to failure is the local kinetic energy.

Let us consider a fragment undergoing rapid uniform expansion at the strain rate:

$$\dot{\varepsilon} = \frac{\dot{\rho}}{3\rho}$$

(2.24)
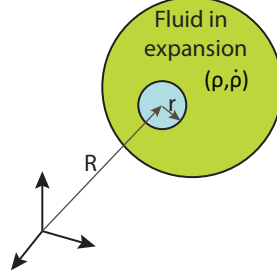
Figure 2.5: Grady's expanding fluid model. The large sphere represents the whole body. The small sphere of radius r limits a region of the fluid that will form a fragment.

ρ is the density, $\dot{\rho}$ is the derivative of ρ with time. Grady derived the expression of the local kinetic energy density for the expanding fluid problem:

$$T = \frac{27}{10}\frac{\rho\varepsilon^2}{A^2} \tag{2.25}$$

$$\text{where } A = \frac{4\pi r^2}{\frac{4}{3}\pi r^3} \tag{2.26}$$

If Γ is a surface energy, the fracture surface energy density is:

$$\rho e_s = \Gamma A \tag{2.27}$$

The energy driving fragmentation is thus:

$$U(A) = \frac{27}{10}\frac{\rho\varepsilon^2}{A^2} + \Gamma A \tag{2.28}$$

Minimizing this energy function leads to the characteristic fragment size:

$$d = \left(\frac{\sqrt{20}K_{IC}}{\rho c\dot{\varepsilon}^2}\right)^{1/3} \tag{2.29}$$

where K_{IC} is the fracture toughness. This relation exhibits very good qualitative agreement with dynamic experiments. It is now considered as a reference expression of the mean fragment size for dynamic loadings. However, it does not fit quasi-static experimental values. To correct this inconsistency, Glenn and Chudnovsky [Glenn 1986a, Glenn 1986b] proposed a model that fits well Grady's model in dynamics and that adds the effect of potential energy, which is dominating in quasi-statics. The energy balance:

$$\Delta E_{kinetic} = \Delta E_{potential} + \Delta E_{fracture} \tag{2.30}$$

leads to the length scale:

$$d = 2\sqrt{\alpha/3} \sinh{(\phi/3)} \tag{2.31}$$

$$\text{where } \phi = \sinh^{-1}\left(\beta\left(\frac{3}{\alpha}\right)^{3/2}\right) \tag{2.32}$$

where α and β depend on material properties and strain rate. Figure 2.12 compares Glenn and Chudnovsky's to Grady's models.

2.3.2.2 Comparison of explosive fragmentation to spall and turbulence fragmentation

Grady pursued other conceptual theories based on the comparison of explosive fragmentation to other physical phenomena, such as spall [Grady 1988] and turbulence [Grady 2008]. Grady showed that, in spall fragmentation, potential energy should not always be neglected. Since brittle and ductile fragmentation involve distinct mechanisms, he distinguished elastic and plastic responses. The expansion of an elastic body is governed by potential energy and involves few kinetic energy (about 15%), while expansion of a rigid-plastic body is driven by kinetic energy and potential energy contribution is small.

Interestingly, Grady also relates brittle fragmentation to hydrodynamic turbulence of fluids [Grady 2008]. He explains that turbulence emerges because large scale laminar flow is not sufficient to dissipate the energy through viscous friction. Similarly as brittle fragmentation, turbulence is a weakly dissipative process which occurs on successively smaller length scales. The initial stored energy requires energy dissipation at successively finer length scales, through a cascade of cracks (self-similar behavior, see section 2.1.2). To fulfill these physical requirements, Grady proposes the fragment size distribution to be:

$$F(s) = \frac{1}{1 + (s/s_0)^m} \tag{2.33}$$

This functional exhibits power-law dependencies in the two ranges $s \gg s_0$ and $s \ll s_0$.

2.3.3 Dynamic models

2.3.3.1 Enrichment of Mott's model

Dynamic models originated after Mott's theory of wave propagation. Mott assumed that the material is perfectly plastic and that fracture occurs instantaneously (which amounts to neglecting fracture resistance). To remedy these physical limitations, several authors enriched Mott's model by adding some failure duration. As displayed in figure 2.6(a), each element is surrounded by two damageable springs, whose gradual opening releases energy. When the spring is fully opened, it is broken

and has released the toughness G_c. The law governing spring opening is called the fracture law. Grady assumed a linear decreasing law [Grady 2006b], whereas Drugan [Drugan 2001] used an exponential one. Both laws (figures 2.6(b) and 2.6(c)) are related to the cohesive element approach, developed in length in chapter 3.
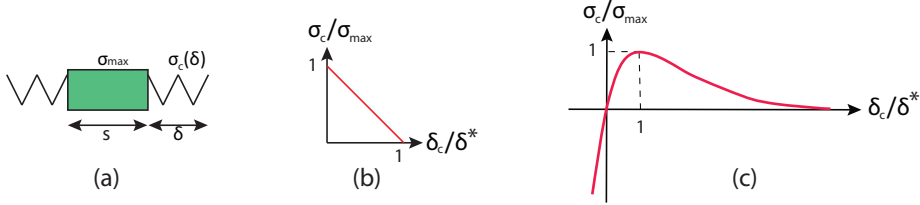
Figure 2.6: (a) Dynamic model representing a fragment of size s and two damageable springs. σ_c is the longitudinal stress in the spring, δ is its opening. (b) Linear fracture law. (c) Exponential fracture law.

Grady's approach: Grady [Grady 2006b] suggested that stress linearly decreases from σ_{max} to 0, while crack opens from 0 to a given length δ_c, releasing the fracture energy $G_c = \frac{\sigma_{max}\delta_c}{2}$. He derived the equation of motion and showed that the nominal spacing between two breakpoints is:

$$s = \left(\frac{24G_c}{\rho\dot{\varepsilon}^2}\right)^{1/3} \tag{2.34}$$

Note that this expression is very close to equation 2.29 that Grady derived from energy balance argument.

Drugan's approach: Drugan [Drugan 2001] derives the classical wave equation for a homogeneous, isotropic linear elastic solid. He also shows that the material parameter t_0 (which was first established by Camacho and Ortiz [Camacho 1996]) quantifies the duration of the spring opening.

$$t_0 = \frac{E\,G_c}{\sigma_c^2\,c} \tag{2.35}$$

where E is the Young's modulus, G_c is the toughness, σ_c is the failure strength, and c is the elastic wave speed. However, in all those models, wave interactions cannot be represented analytically. When there is one breakpoint, the solution is straightforward. When there are numerous breakpoints, the problem becomes more complex and cannot be solved exactly. Two possibilities arise: making more assumptions and/or using numerical tools. Examples of numerical simulations solving the wave equation when the bar is constituted of multiple defects are [Zhou 2006a, Shenoy 2003].

2.3.3.2 Continuous fragmentation

Some physicists describe theoretically fragmentation through its time evolution, using continuous models. The name 'continuous' stems from the time continuity of the description. Fragmentation occurs through breakup sequences, which may have of course very distinct characteristics. They are usually classified into three categories [Åström 2006]: uncorrelated breakup history, cascade fragmentation, and statistical rate equations.

Uncorrelated breakup history: In the uncorrelated breakup history, each time a fragment breaks, it is split into D+1 equal size pieces (where D is the dimension of the problem). If a fragment has undergone i breakups, where i has a Gaussian probability distribution, then it can be shown that the probability density function of the fragment size distribution is lognormal:

$$f(s) \propto exp^{-\left(\frac{ln(s)-\mu}{\sigma^2}\right)} \tag{2.36}$$

where μ and σ are two constant parameters. Since the original work of Kolmogorov [Kolmogorov 1941], the lognormal distribution has been applied to polymer fragments, soil particles, tectonic plates, etc. More details on the derivation can be found in [Delannay 1996].

Cascade fragmentation: A fragment of unit area is broken into a pieces of area $1/a$. Each fragment is further split with the probability p. For each fragment that is not broken, the process is terminated. For the broken ones, it continues. This pattern leads to the probability density function:

$$f(s) \propto s^{-\frac{D\,ln(p)}{ln(a)}-(D+1)} \tag{2.37}$$

where D is the space dimension. By construction, cascade fragmentation is scale-invariant [Turcotte 1986b, Botet 1996, Krapivsky 2000, Kadono 2002].

Rate equations for fragmentation: A rate equation generally combines differential and integral equations, which determines fragment sizes. A kernel $k(s,x)$ defines the probability to form a fragment of size s from a fragment of size x. The breakup rate for a fragment of size s in a time interval dt is $a(x,t)dt$. The most general form of the rate equation is:

$$\frac{\partial f(s,t)}{\partial t} = -a(s,t)f(s,t) + \int_s^\infty f(x,t)a(x,t)k(x,t)dx \tag{2.38}$$

where f is the probability density function of the fragment sizes. The first term on the right-hand size determines the breakup of fragments (loss term), while the second term represents the formation of fragments (gain term). Although this formulation is very general, it is rather difficult to obtain kernels describing experimental conditions [Ziff 1985].

2.3.4   Entropy models

An alternative derivation of fragment mass distribution is based on entropy methods [Grady 2007, Englman 1991] in which the entropy associated to a fragmentation event is maximized. Maximizing entropy leads Grady [Grady 2007] to derive an exponential probability density function. Englman et al. [Englman 1991] include further constraints and propose a more complex distribution, which behaves as a power law over a limited range of fragment sizes and accounts for structural finite size effects.

2.4   Fragmentation of heterogeneous materials

2.4.1   Defects influence failure properties

The idea that defects have a profound impact on failure properties of the material first arose with Leonardo Da Vinci during the sixteenth century, and later with Weibull [Weibull 1939]. Weibull's main contribution lies in relating quasi static failure strength to defects. As detailed in chapter 3, he suggests that a bar subjected to quasi static loading breaks at its weakest link, e.g. at the location of the larger defects. Though, this model only involves one crack and is thus limited to specific experiments. More complex evaluations in which multiple fractures initiate have later been developed [Alava 2006, Hassold 1989]. For instance, Andersons et al. [Andersons 2000] investigate the sequential cracking of uniaxial thin brittle coatings attached to substrates with adhesives, loaded in tension. They propose an analytical expression relating average fragment length to strain rate and distribution of the strengths of the coating. Daphalapurkar et al. [Daphalapurkar 2010] perform two-dimensional simulations of a specimen in biaxial tension with pre-existing microcracks. They quantitatively relate flaw distribution (size, shape, spatial distribution, and defect failure strength) and overall dynamic failure strength.

Besides analytical and numerical models, experiments have also been conducted. However, for practical reasons, most are carried out in confined compression rather than in pure multiaxial tension [Chen 1996, Huang 2003, Momber 2000]. For instance, Lankford [Lankford 1979, Lankford 1981, Lankford 1991] studies the compressive strength of SiC and Al2O3 over a wide range of loading rates and interprets material response in terms of tensile growth of axial microcracks. He defines two distinct mechanisms: at relatively low strain rates, thermally activated process operates at defect locations, while at higher loading rates, strain-rate sensitive inertial process controls failure. More recently, Paliwal et al. [Paliwal 2006] have conducted dynamic compressive failure tests in transparent brittle materials. They explain that, under dynamic loads, a part of the defects nucleate into cracks, while the other is intact. The macroscopic failure strength is the result of the competition between applied strain rate and kinetics of crack growth.

Both for tension and compression loadings, defects obviously influence failure. Although the mechanisms might differ, the issues that are at the core of fragmentation (e.g. crack initiation and stress field interactions) are identical. Both topics are thus reviewed.

2.4.2   Statistical models with no crack interactions

Among the two mechanisms associated to defects (defect nucleation and stress field interactions), most statistical theories only account for one: defects are placed randomly within the materials, but they do not influence each other. Lindborg approaches the outcome of coalescence of small cracks into larger cracks by statistical methods [Lindborg 1969] . He neglects stress concentration from existing cracks and assumes that nucleation of cracks is random and independent from other cracks. He considers a specimen with N rectangular grains and shows that, if complete fracture occurs when n cracks aggregate, then the fraction of cracked grains is given by:

$$p = 0.2 \left(\frac{2n}{N} \right)^{1/n} \tag{2.39}$$

In any case, at least 20% of the grains are cracked before complete fracture. He applies equation 2.39 to transgranular cleavage cracks, intercrystalline wedge cracks, and to small intercrystalline pores.

Similarly, Gilvarry enriches Griffith's investigations [Griffith 1943] and postulates the existence of uncorrelated edge, surface and volume flaws, where failure may initiate [Gilvarry 1961a]. He assumes that each type of flaws verifies Poisson statistics, which amounts to neglecting their interactions. It yields the probability to generate a new fragment with the edge length, face area and volume in the ranges l to $l + dl$, s to $s + ds$, and v to $v + dv$:

$$dp(l, s, v) = P(0|l, s, v) \ P(1|dl, ds, dv) = e^{-Q} dQ \tag{2.40}$$

where Q is the linear form in l, s and v:

$$Q = \gamma_l l + \gamma_s s + \gamma_v v \tag{2.41}$$

γ_l, γ_s, γ_v are respectively the line, area and volume densities of flaws.
The fragment size distribution is thus defined by its probability density function:

$$df(Q) = V_0 v^{-1} e^{-Q} dQ \tag{2.42}$$

where V_0 is the volume of the unbroken body. Integrating f leads to the Gilvarry distribution expressed as a function of fragment size x:

$$F(x) = 1 - e^{-\left(\frac{x}{\gamma_l} + \left(\frac{x}{\gamma_s} \right)^2 + \left(\frac{x}{\gamma_v} \right)^3 \right)} \tag{2.43}$$

This expression is very general since it includes the three possible types of defects. However, in order to fit Rosin-Rammler's and Schuhmann's distributions, Gilvarry notes that edge flaws dominate instantaneous fragmentation.

In other papers [Gilvarry 1961b, Gilvarry 1962a, Gilvarry 1962b, Gilvarry 1962c], Gilvarry and Bergstrom present experimental results of the compressive fragmentation of brittle spheres. By containing the fragments into a gelatin matrix (figure 2.7), they inhibit secondary fractures (resulting from the contact between two fragments) and only focus on single fracture. This enables the comparison with Gilvarry's theoretical development on single fracture. This experimental configuration leads to three large fragments, and a distribution of smaller fragments. Doing so, Gilvarry and Bergstrom encounter a good agreement between the Poisson theory and their experiments.
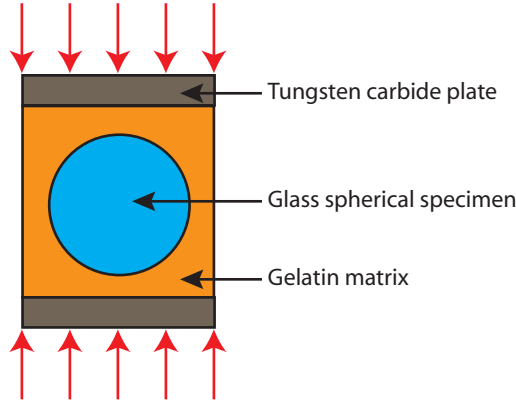
Figure 2.7: Gilvarry and Bergstrom's brittle spheres, loaded in compression.

2.4.3   Åström's model accounting for crack interactions

In [Åström 2004b, Åström 2006], Åström showed that Gilvarry's model of fragment size distribution accurately represents the behavior of the larger fragments, because cracks barely interact if they are far from each other. On the contrary, if they are close enough, their interaction cannot be neglected and Gilvarry's model is not valid anymore. Åström [Åström 2000, Åström 2004a] argues that in the small range, crack branching-merging processes prevail and induce scale-invariant size distribution. He proposes the distribution of fragment mass:

$$F(m) = a \, m^\alpha \, f(m) \tag{2.44}$$

where a and α are constant, and f is a function of the mass. In the small range, the power law dominates, whereas the large range is controlled by f. The function f represents the cut-off that the specimen finite size necessarily leads to. Following

Gilvarry's derivation and the Oddershede et al.'s [Oddershede 1993] experimental evidences, Åström recommends f to have an exponential form:

$$F(m) = a \, m^{\alpha} e^{-m/M_0} \tag{2.45}$$

M_0 is a system-dependent length. The value of α depends on the loading condition. In the case of impact loading, both Åström and Oddershede et al. fit $\alpha \simeq 0.5$.

2.4.4   Damage evolution laws

The continuous approach is based on the homogeneization of the cracked solid over a representative volume, and the deterioration of the Young's modulus [Allen 2001]. Grady and Kipp [Grady 1980] develop a model coupling fracture, fragmentation, and stress wave propagation. Activation and growth of an initial Weibull distribution of flaws describes rate-dependent fracture phenomena. The damage variable is updated, depending on the theoretical determination of the number of activated flaws. Ashby and Sammis [Ashby 1990] analyze crack initiation at pre-existing flaws, crack growth under uniaxial compression. They examine the conditions under which cracks interact. Homogeneization based on discrete damage models (cohesive zones) has also been developed [Espinosa 1998, Espinosa 2003a, Espinosa 2003b, Cazes 2009] .

Another interesting model of fragmentation has been proposed by Hild and coworkers [Denoual 2002]. They derive the expression of the damage variable, over a wide range of loadings (from quasi-static to dynamics). Micro-cracking results from crack nucleation, which they suppose to emanate at defect locations. The population of defects is characterized by Poisson statistics [Brajer 2003, Forquin 2003a, Forquin 2003b]. Following the idea of Mott, they note that when a defect is activated, it generates stress waves, which propagate away, from the location of the defect to the surrounding areas [Denoual 1997]. The regions encompassed by stress waves are released and are definitively protected. They cannot break anymore. Figure 2.8 displays the mechanisms of this obscuration phenomenon. Based on this obscuration zone concept, they deduce the density of broken defects and a damage variable, which they inject into a continuous model.

Hild et coworkers also emphasize that there exists a transition delimiting two mechanisms: for low loading rates, fragmentation is probabilistic, whereas for high loading rates, it becomes deterministic [Hild 2003].

2.4.5   Fragmentation in compression

Due to the difficulty of controlling brittle fragmentation in tension at high strain rates, many experiments have been conducted in compression with confinement. Numerical analyzes have also been performed for such problems. Nemat-Nasser
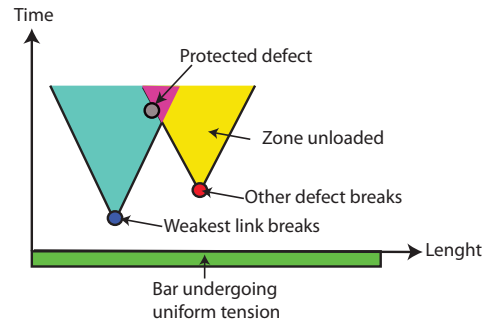
Figure 2.8: Hild's healing wave concept: when a zone is encompassed by Mott's wave, it is definitively protected from further damage.

and Deng [Nemat-Nasser 1994] model dynamically interacting wing cracks and simulate brittle failure under compression. They examine the coalescence of interacting tensile microcracks and focus on the relation between microstructure and rate dependency of the overall response. Following the same trend, Paliwal and Ramesh [Paliwal 2008] incorporate pre-existing flaws in an inelastic material, submitted to compression loading. Inelasticity is attributed to nucleation and growth of tensile wing micro-cracks and to defects frictional sliding. The authors underline the role of initial flaw distribution on crack growth dynamics: at low strain rates, the spread of the distribution is critical, while at high strain rates, density of flaws is prevailing. The use of numerical simulations allows an explicit representation of flaws. Kraft et al. [Kraft 2008a, Kraft 2008b] simulate the effects of grain boundaries (spatial distribution and strength distribution) on the response of a brittle ceramic in compression, through two-dimensional computations.

2.5   Experimental fragmentation

High rate and impact experiments have required substantial creativity to capture as precisely as possible the rapidly evolving physics of fragmentation. A review of the experimental set-ups can be found in [Grady 2006b, Ramesh 2008].

2.5.1   Expanding ring test by electromagnetic loading

Expanding ring experiments to test the dynamic failure at high strain rates, for both brittle and ductile materials, have been performed by number of authors. Figure 2.9 details the experimental set-up of Grady and Olsen [Grady 2003]. The specimen is a ring made of ductile material (U6Nb or uranium-6%-niobium) and undergoes radial expansion until failure. Strain rate can reach $10^4 s^{-1}$. A continuous current goes through the solenoid, which generates a controllable magnetic field. This field induces a current in the driver ring that supports the specimen. Applying electric pulses generates discontinuities that result in the radial expan-

sion of the driver ring, and a fortiori the sample ring. The arrestor fixture blocks the driver ring, and the wax cavity recover fragments. Although this experimental set-up evolves from one author to the other, most are based on electromagnetic accelerations [Hoggat 1969, Gourdin 1989, Grady 1983, Zhang 2006, Zhang 2007, Goto 2008].
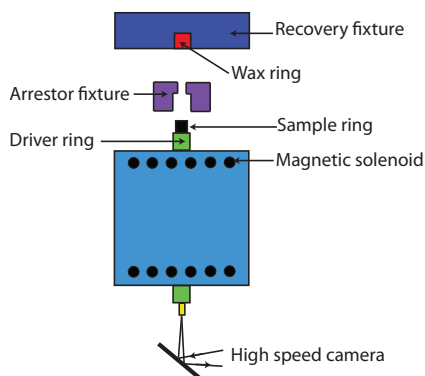
Figure 2.9: Schematic of the experimental set-up for expanding ring experiment based on electromagnetic loading [Grady 2003].

2.5.2   Cylinder fragmentation test using gas gun techniques

In order to explore multi-dimensional fragmentation, Winter [Winter 1979] defined a technique in which thin cylinders are loaded with gas guns. In figure 2.10(a), a projectile impacts the insert. The axial compression of the two elastic and highly deformable plastic objects results in radial expansion. A pressure is abruptly imposed in the inner surface of the specimen that expands symmetrically. Radial and axial stretchings are related to the velocity of the projectile. High speed photography provides deformation history and axial fractures. This test has been adapted by several authors [Butcher 1975, Mock Jr. 1983, Thornhill 2001]. Thornhill and coworkers added a soft catch to recover the fragments and analyze their features. Both Winter [Winter 1979] and Thornhill et al. [Thornhill 2001] both focused on ductile explosive fragmentation, but gas gun techniques have also been employed to investigate impact fragmentation [Shockey 1974] (figure 2.10(b)).

2.5.3   Hopkinson's bar

The Hopkinson pressure bar was first suggested by Bertram Hopkinson as a way to measure stress pulse propagation in a metal bar [Hopkinson 1914]. The original experimental set-ups were improved by Kolsky [Kolsky 1949] who added a second bar to Hopkinsons's apparatus, naming it the *split* Hopkinson bar. Instead of attaching a billet at the end of a bar, Kolsky sandwiched a specimen between two instrumented bars (figure 2.11). Strain gages mounted on the incident and transmitter bars enable stress waves measure. After a compression load, the specimen
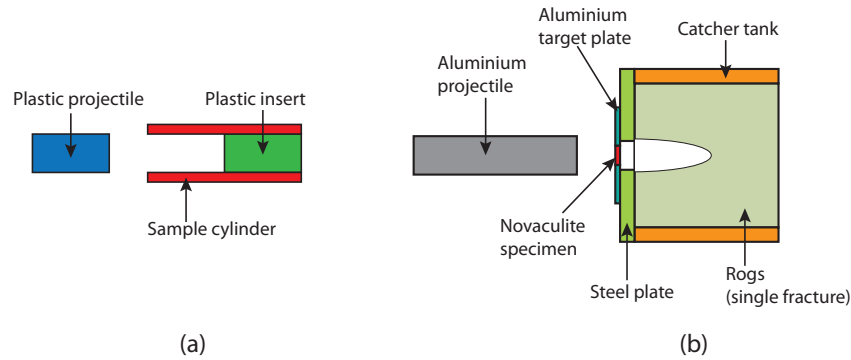
Figure 2.10: Schematic of experimental set-up based on gas gun technique: (a) for cylinder explosion [Winter 1979], (b) for plate impact [Shockey 1974].

experiences a tension load due to the reflection of stress waves [Lindholm 1964, Lindholm 1968]. Nowadays, this experimental device achieves very high strain rates reaching $10^4 s^{-1}$. It has been employed to measure metal strengths subjected to shear [Klopp 1985] and compression [Lennon 2000], to investigate glass dynamic response [Clifton 1997, Bouzid 2001], to study failure and fragmentation properties of brittle solids, such as natural rocks, minerals and concrete [Green 1968, Lundberg 1976, Grote 2001]. It has also been used for examining ultra-high strength ceramics [Chen 1996, Subhash 2000, Lankford 1979].
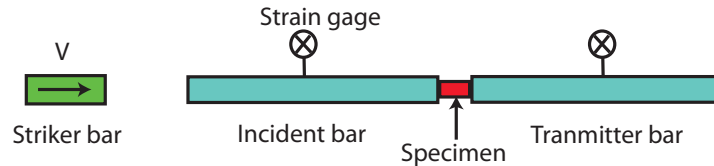
Figure 2.11: Split Hopkinson bar or Kolsky bar

2.5.4 Other experiments

To reach high loading rates (up to 10^5 s^{-1}), other experimental set-ups letting fragmentation evolve naturally, have been designed. Examples are multiple: observation of natural phenomena [Capaccioni 1986, Ryan 1998, Housen 1999, Kiang 1966], arena tests, exploding cylinders [Mott 1947, Taylor 1963, Gurney 1943, Grady 1992], shock on the edge techniques [Forquin 2003a], specimen drop on the ground [De Oliveira 2007, Ishi 1992], impact of balls [Ari 1993, Fujiwara 1980] and shells [Wittel 2005], among others. The large amount of data on distribution of fragment sizes have helped understanding the physics of fragmentation.

2.6   Numerical fragmentation

2.6.1   Overview of the numerical methods

The rapid increase in computational power has opened the door to novel possibilities. Researchers can now explore fragmentation through numerical simulations. General formulations used in the literature fall in one of the two categories: continuous and discontinuous formulations.

2.6.1.1   Continuous problems

Although material microstructure is discontinuous, lots of engineering problems do not need to account for it. Quantities of interest are defined at a large enough scale so that the microstructure can be averaged by continuous material properties. Governing equations are usually given as a set of partial differential equations (strong formulation) or integral equations (weak formulation). When coupled with external actions in the form of boundary and initial conditions, they constitute a boundary value problem. The solution of such problems is usually approximated by numerical solutions. Continuous methods include finite difference method [Zhang 1996, Zukas 2004], finite volume method [Eymard 2000], finite element method (see chapter 3). Depending on the referential used, they can be either Lagrangian (the computational grid follows the material), Eulerian (the computational grid is fixed and the material flows through it) [Belytschko 2000], or Lagrangian-Eulerian. The most often used is the finite element method (FEM). As detailed in chapter 3, it is based on discretization of the domain into finite subdomains or elements. Elements share nodes, edges, and surfaces. All together, they form a finite element mesh. The solution is expressed in terms of displacements at the nodes of the mesh.

Conventional finite element methods have been employed for decades to model impact, penetration, and fragmentation. Simulating failure requires a special treatment. Cracks can be represented explicitly (using the cohesive approach or the extended finite element method), or they can be embodied by an appropriate damage number (continuum methods). The cohesive approach is widely used in diverse contexts because of its simple implementation and its ability to handle efficiently multiple cracks simultaneously (see chapter 3). For instance, Repetto et al. [Repetto 2000] investigate fragmentation of glass, Mota et al. [Mota 2003] focus on cranium impact, Espinosa et al. [Espinosa 1998] and Blackman [Blackman 2003] are interested in fracture of composites. Fragmentation features may be addressed in postprocessing stage [Mota 2008]. Numerous other examples and technical developments can be found in [Xu 1994, Camacho 1996, Zhou 2005b, Ortiz 1999, Pandolfi 2002, Cirak 2005]. In practice, cohesive elements are inserted into the mesh between two edges; they are interface elements and allow two adjacent volumetric elements to separate. They concentrate failure features (crack opening and energy dissipation) while

the rest of the mesh behaves as if the structure was not undergoing fracture. The coupling between the cohesive approach and the finite element method is detailed in chapter 3, along with its historical origins. However, the main drawback of the cohesive approach is mesh dependency: cracks follow the element inter-boundaries and the failure pattern necessarily depends on the mesh.

In order to avoid this numerical restriction, the extended finite element method (XFEM), which is based on enriching shape functions [Moes 2002], calculates failure path irrespective to the mesh geometry. Its accuracy can be enhanced by remeshing [Prabel 2007]. Although this technique has the advantage of predicting exactly crack pattern [Grégoire 2007] and of being energy conservative [Réthoré 2005], it is computationally very expensive and does not handle easily crack branching and crack coalescence. In fragmentation problems, when multiple cracks are evolving simultaneously, using XFEM would be inadequate.

Another approach is based on damage variables [Lemaitre 1985, Chaboche 1988a, Chaboche 1988b, Ladevèze 2000, Peerlings 1996, Allix 1992, Combescure 1990]. Failure is represented by a continuous value, commonly called damage, considered as an internal value of the finite element problem. It can thus easily be implemented in a finite element code. However, crack path is not computed explicitly (since damage is a volumetric parameter and cracks open surfaces). The description of a fragmentation pattern with damage models is thus not obvious.

Nonetheless, in the case of fragmentation, some authors prefer to use discrete methods that have higher order continuous shape functions, and that naturally handle discontinuities such as cracks and contact. Indeed, in finite element simulations, even though frictional contact can be accurately modeled [Repetto 2000], the contact law is less natural than in discrete models. When multiple contacts occur with large deformations, discrete frameworks may be more adequate.

2.6.1.2 Discontinuous problems

By contrast to continuous description, discontinuous problems take inherent material discontinuities into account. For instance, at the smallest scale, elementary particles, atoms, molecules are represented (atomic simulations and molecular dynamics). Since failure occurs at a larger scale, the idea of averaging a representative amount of molecules into a particle has arisen. In discontinuous representations, the material is considered as a compact body of representative volumes called particles. Mathematical description includes the shape, size, and mass of each particle, as well as their interactions. Typical formulation involves balance principles and interaction laws. Analytical solutions are rarely available and approximate numerical solutions are sought.

Among them, the discrete element method (DEM) and the smooth particle hydrodynamics (SPH) have been designed to handle large deformations and contact between large numbers of irregular particles. In both methods, no fixed connectivity between particles exists and interaction laws link them. In DEM, particles are related by beams, which may have complex evolution law including friction, plasticity, etc. Interactions are thus of one-to-one type. In SPH, an interacting zone of arbitrary radius is drawn. All particles falling into this zone interact with the particle located in its center. This makes the result more accurate but is computationally more demanding. Developed in the seventies [Gingold 1977, Lucy 1977], DEM and SPH are now extensively used to simulate dynamic failure of solids and large distortions [Maurel 2008, Gingold 1977, Belytschko 1994, D'Addetta 2001, Kun 1996, Libersky 1991, Liu 1997, Magnier 1998, Swegle 1995, Hidalgo 2007, Herrmann 2006, Wittel 2003].

However, these formulations have major drawbacks. Since the meshfree shape functions do not satisfy the Kronecker property, we talk about approximation rather than interpolation. This entails certain difficulties in imposing essential boundary conditions. Alternatives have been proposed to apply correctly boundary conditions (such as the Element Free Galerkin method [Belytschko 1994]). Coupling with the finite element method has also been studied [Fahrenthold 2001, Johnson 2001, Johnson 2003, Munjiza 2004]. However, the major limitation of these methods lies in its computational cost. Simulations can rapidly be very expensive compared to the continuum techniques.

2.6.2 Illustration: The Mott's expanding ring (by Zhou et al.)

In the recent years, numerous analyzes of the expanding ring have been conducted for brittle failure [Shenoy 2003, Zhou 2006a, Elek 2005], and mostly for ductile failure [Guduru 2002, Rusinek 2007, Pandolfi 1999, Goto 2008, Meulbroek 2008, Gold 2008]. We present here the results from Zhou et al., who used the method of characteristics coupled to cohesive elements. This framework captures stress wave propagation and interactions. Zhou et al. considered the material to be homogeneous and studied the effect of material properties on the average fragment size [Zhou 2006c]. They proposed an empirical law to predict the evolution of the average fragment size with strain rate [Zhou 2006b]. Figure 2.12 compares their law with Grady's [Grady 1982] and Glenn and Chudnovsky's [Glenn 1986a] models. The axes are normalized by the characteristic size s_0 and strain rate $\dot{\varepsilon}_0$:

$$\bar{s} = \frac{s}{s_0} = \frac{s}{c.t_0} \tag{2.46}$$

$$\bar{\dot{\varepsilon}} = \frac{\dot{\varepsilon}}{\dot{\varepsilon}_0} \tag{2.47}$$

where t_0 is defined by equations 2.35, c is the elastic wave speed, and $\dot{\varepsilon}_0$ is a characteristic loading rate defined by:

$$\dot{\varepsilon}_0 = \frac{\sigma_c}{E\, t_0} \tag{2.48}$$

where σ_c is the failure strength, E is the Young's modulus.

Zhou et al.'s model behaves as:

$$\bar{s} = \frac{4.5}{1 + 4.5\, \bar{\dot{\varepsilon}}^{2/3}} \tag{2.49}$$

Zhou et al. explain the differences observed between the models with energetic arguments. In the quasi-static regime, although Glenn and Chudnovsky supposed that the totality of the potential energy is converted into fracture energy, Zhou et al. notice that only half of the potential energy is effectively converted into fracture energy, the other part accounts for wave propagation. In the high strain rate domain, they predict smaller average fragment size than energetic models in closer agreement to experimental data. The reason put forward is that the system extracts more kinetic energy from the ring's global motion to create new cracks.
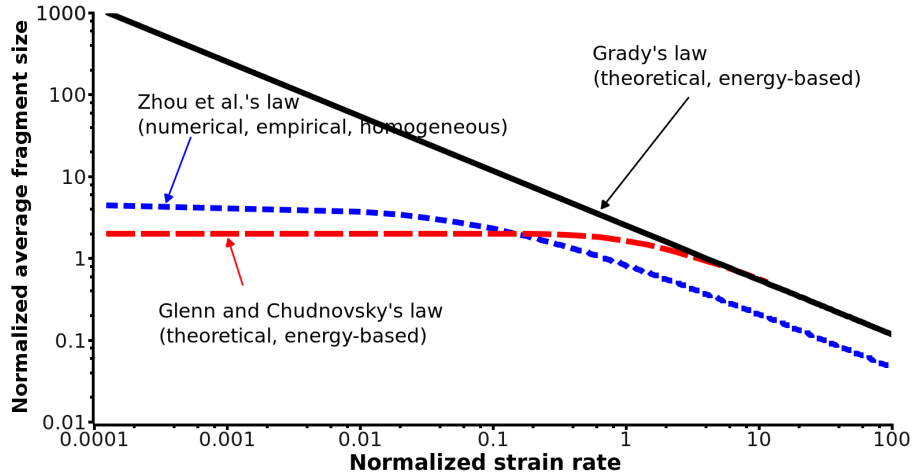
Figure 2.12: Normalized average fragment size in function of the normalized strain rate in a log-log scale. Grady's, Glenn and Chudnovsky's, and Zhou et al.'s models are displayed.

In addition to their unique law, Zhou et al. [Zhou 2006b] fit the distribution of fragment sizes with the Rayleigh distribution:

$$F(s) = 1 - e^{-(s - s_{min})^2 / 2\sigma^2} \tag{2.50}$$

Therefore, Zhou et al.'s calculations emphasize the need for computational simulations. Analytical models cannot predict accurately the response of the material. Their results, however, only concern very simple geometry and do not account for material heterogeneity. The present thesis stems from Zhou et al.'s observations and aims at generalizing them to heterogeneous materials in multiple dimensions.

2.7   Summary

Eighty years are separating us from the first essential experimental study on fragmentation, achieved by Rosin and Rammler [Rosin 1933]. Since then, several trends of thoughts have emerged.

First trend presented here concerns fragmentation's resulting state (e.g. the fragment mass distribution), without considering the physics leading to it. Based on analytical, experimental, and numerical observations, many distributions have arisen. An exhaustive description would have required more than one chapter of a thesis. This is why we only selected few of them, which seemed relevant for the understanding of the following chapters.

Most analytical models are based either on the Poisson point process (in which fragment do not interact, and which leads to exponential distributions), or on the concept of criticality (which results in power law distributions). However, those analytical predictions do not always represent fragmentation accurately. For instance, experimental and numerical studies have shown that Weibull distribution may fit more adequately distribution of fragment sizes.

The second trend focuses on the physics underlying the fragmentation of homogeneous materials. By deriving energetic and dynamic equations, these models predict characteristic length and time scales. Energy models use energy balance or entropy maximization, while dynamic model are based on Mott's healing wave principle.

In the last trend of thought, microstructural heterogeneity of the material (e.g. defects) is included. Analytical, experimental and numerical models have emerged to understand its role on fragmentation. Using an explicit representation of the defects, or statistical arguments, or continuum damage approach, researchers have been able to relate microstructural defects to some interesting failure features. There remains, however, many misunderstood issues that still needs to be investigated.

Finally, classical experimental and numerical techniques were also reviewed. The expanding ring/cylinder are appropriate devices to reach strain rate lower than $10^5 \ s^{-1}$. To go faster, impacts, explosives, as well as the use of Kolksy bar, are more relevant. Experiments have the advantage of reflecting perfectly the fragmentation

process, but they are expensive, difficult to handle, and do not give access to the time evolution of some characteristic physical parameters. By contrast, numerical simulations are able to track rapidly evolving values. Yet, they remain models and some errors are necessarily made. In the present thesis, since we are interested in the physics governing the evolution and in predicting the final state of fragmentation, numerical simulations appear to be the most appropriate tool.

Modeling and implementing

As pointed out in chapter 2, studying fragmentation can involve many analytical, experimental, or numerical methods. Since the main objective of the thesis is the understanding of the physics underlying fragmentation, the access to time evolving quantities, such as number of fragments and energies, is required. Numerical simulations are the most appropriate tool to achieve this goal. This chapter is dedicated to the modeling and the implementing issues, which must be correctly addressed in order to reflect accurately the physics of the process. The numerical framework is based on the well-known finite element method (section 3.1.2), and fracture is modeled by the cohesive approach (section 3.1.3). Moreover, fragmentation simulations may require high performance computing. The mesh needed to resolve the multiple cracks that might initiate during the fragmentation process, must be very fine. Serial calculations do not necessarily handle such fine meshes (memory and efficiency issues). In collaboration with Pr. Raul Radovitzky and coworkers, we are using the discontinuous Galerkin framework (section 3.2.2) for parallel simulations and improved scalability. Finally, this chapter also tackles the modeling of material heterogeneity. It is described macroscopically by a statistical distribution of failure strengths. As explained in section 3.3, the shape of the distribution has generally a Weibull type.

3.1 Coupled framework 'finite elements - cohesive elements' in dynamics

3.1.1 Motivation

The finite element method (FEM) is a numerical technique that calculates approximate solutions of partial differential and integral equations [Belytschko 2000, Hughes 2000, Zienkiewicz 2005a, Zienkiewicz 2005b]. Those equations have a solution but complexities in geometry, material properties, and boundary conditions make them hard to solve. By discretizing space and time, the FEM generates an approximate solution in a reasonable time frame.

However, although the FEM may solve a diversity of problems that ranges from static elastic problems to dynamic large-deformation visco plastic problems, it hardly tackles fracture. Additional techniques need to be included within the numerical framework. We are using the cohesive element approach whose main advantages

are its simplicity and its ability to handle multiple crack initiations simultaneously. However, it inconveniently leads to mesh dependent solutions (cracks follow the element boundaries). In this section, we develop the numerical framework coupling the FEM and the cohesive approach.

3.1.2   The Finite Element framework in continuum mechanics

3.1.2.1   Strong formulation

Let us consider the dynamic motion of a continuum body occupying the initial configuration $B_0 \subset \mathbb{R}^3$ at time t_0 (figure 3.1). At any time t in $T = [t_0, t_{final}]$, the position $\boldsymbol{x}$ of the material point $\boldsymbol{X}$ is described by the deformation mapping:

$$\boldsymbol{x} = \boldsymbol{\varphi}(\boldsymbol{X}, t) \tag{3.1}$$

Its boundary surface ∂B_0 is partitioned into a Dirichlet part $\partial_D B_0$ and a Neumann part $\partial_N B_0$. Displacements (resp. efforts) are imposed on $\partial_D B_0$ (resp. $\partial_N B_0$). The problem has a solution if:

$$\partial B_0 = \partial_D B_0 \cup \partial_N B_0 \tag{3.2}$$

$$\partial_D B_0 \cap \partial_N B_0 = \emptyset \tag{3.3}$$
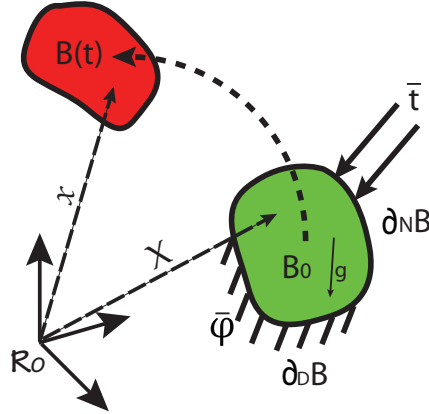
Figure 3.1: Schematic of the Lagrangian deformation of the body B_0, Neumann boundary $\partial_N B_0$, and Dirichlet boundary $\partial_D B_0$.

The deformation gradient, which characterizes the local deformation state is:

$$\boldsymbol{F} = \boldsymbol{\nabla}_0 \boldsymbol{\varphi}(\boldsymbol{X}, t) \quad \forall \boldsymbol{X} \subset B_0 \ \forall t \in T \tag{3.4}$$

The continuum problem is governed by the equation of motion and the boundary conditions:

$$\boldsymbol{\nabla}_0 \boldsymbol{P} + \rho_0 \boldsymbol{b} = \rho \ddot{\boldsymbol{\varphi}} \quad \forall \boldsymbol{X} \subset B_0 \quad \forall t \in T \tag{3.5}$$

$$\boldsymbol{\varphi} = \bar{\boldsymbol{\varphi}} \quad \forall \boldsymbol{X} \subset \partial_D B_0 \quad \forall t \in T \tag{3.6}$$

$$\boldsymbol{P}\boldsymbol{n} = \bar{\boldsymbol{t}} \quad \forall \boldsymbol{X} \subset \partial_N B_0 \quad \forall t \in T \tag{3.7}$$

where $\boldsymbol{P}$ is the first Piola-Kirchoff stress tensor
$\boldsymbol{b}$ are the body forces
$\bar{\boldsymbol{\varphi}}$ are the displacement applied on $\partial_D B_0$
$\bar{\boldsymbol{t}}$ are the forces applied on $\partial_N B_0$
$\boldsymbol{n}$ is the normal unit vector

Initial conditions in displacement and velocity provide enough conditions:

$$\boldsymbol{\varphi}(\boldsymbol{X}, \boldsymbol{t_0}) = \boldsymbol{X} \quad \forall \boldsymbol{X} \subset B_0 \tag{3.8}$$

$$\dot{\boldsymbol{\varphi}}(\boldsymbol{X}, \boldsymbol{t_0}) = \boldsymbol{V} \quad \forall \boldsymbol{X} \subset B_0 \tag{3.9}$$

The last equation is the constitutive law of the material, which links $\boldsymbol{P}$ to the $\boldsymbol{\varphi}$-dependent free energy A:

$$\boldsymbol{P} = \frac{\partial A}{\partial \boldsymbol{F}} \tag{3.10}$$

3.1.2.2 Weak formulation

The momentum equation (eq. 3.5) cannot be discretized directly; a weak form, often called variational form or principle of virtual work, is needed. The weak form is equivalent to the momentum equation 3.5 and the Neumann boundary condition (eq. 3.6). We require trial functions $\boldsymbol{\varphi}$ to satisfy all the displacement boundary conditions and to be smooth enough so that all the derivatives in the momentum equation are well defined. The test functions $\boldsymbol{\delta\varphi}$ are kinetically admissible trial functions, meaning that they are independent of time and they vanish on the Dirichlet boundary. These requirements can be expressed by:

$$\boldsymbol{\varphi}(\boldsymbol{X}, t) \in \mathcal{U} \text{ where } \mathcal{U} = \{\boldsymbol{\varphi}(\boldsymbol{X}, t) \mid \boldsymbol{\varphi}(\boldsymbol{X}, t) \in C^0(\boldsymbol{X}) , \ \boldsymbol{\varphi} = \bar{\boldsymbol{\varphi}} \text{ on } \partial_D B_0\}$$

$$\boldsymbol{\delta\varphi}(\boldsymbol{X}, t) \in \mathcal{U}_0 \text{ where } \mathcal{U}_0 = \{\boldsymbol{\delta\varphi}(\boldsymbol{X}, t) \mid \boldsymbol{\delta\varphi}(\boldsymbol{X}, t) \in C^0(\boldsymbol{X}) , \ \boldsymbol{\delta\varphi} = \boldsymbol{0} \text{ on } \partial_D B_0\}$$

Equations 3.1 to 3.10 are equivalent to finding $\varphi \in \mathcal{U}$ such that, $\forall \boldsymbol{\delta\varphi} \in \mathcal{U}_0$

$$\delta W^{int}(\boldsymbol{\delta\varphi}, \boldsymbol{\varphi}) - \delta W^{ext}(\boldsymbol{\delta\varphi}, \boldsymbol{\varphi}) + \delta W^{kin}(\boldsymbol{\delta\varphi}, \boldsymbol{\varphi}) = 0 \tag{3.11}$$

where δW^{int} is the virtual internal work:

$$\delta W^{int} = \int_{B_0} \boldsymbol{P} : \boldsymbol{\nabla}_0 \boldsymbol{\delta\varphi} \ dV_0 \tag{3.12}$$

δW^{ext} is the virtual external work:

$$\delta W^{ext} = \int_{B_0} \rho_0 \boldsymbol{b} \boldsymbol{\delta\varphi} dV_0 + \int_{\partial_N B_0} \bar{\boldsymbol{t}} \boldsymbol{\delta\varphi} \; dS_0 \tag{3.13}$$

And δW^{kin} is the virtual kinetic or inertial work:

$$\delta W^{kin} = \int_{B_0} \rho_0 \ddot{\boldsymbol{\varphi}} \boldsymbol{\delta\varphi} \; dV_0 \tag{3.14}$$

3.1.2.3   Formulation involving an interface

If the continuum body involves a discontinuity $\partial_I B_0$, such as a fracture line, the equations governing the evolution of the continuum bodies B_0^+ and B_0^- (figure 3.2) are the same as equation 3.5 to equation 3.7. An additional equation ensures that the interface is in equilibrium:

$$[\![\boldsymbol{Pn}]\!] = (\boldsymbol{P}^+ - \boldsymbol{P}^-)\boldsymbol{n} = \boldsymbol{0} \quad \forall \boldsymbol{X} \subset \partial_I B_0 \;\; \forall t \in T \tag{3.15}$$

$\boldsymbol{n}$ is the normal going from B_0^- to B_0^+.
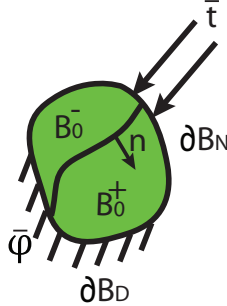
Figure 3.2: Schematic of a continuum body with an interface $\partial_I B_0$.

The interface equilibrium condition results in an additional term in the weak formulation (eq. 3.11). The internal work is now:

$$\delta W^{int} = \int_{B_0^{+-}} \boldsymbol{P} : \boldsymbol{\nabla}_0 \boldsymbol{\delta\varphi} \; dV_0 \; + \int_{\partial_I B_0} [\![\boldsymbol{Pn}\boldsymbol{\delta\varphi}]\!] \; dS_0 \tag{3.16}$$

External (equation 3.13) and kinetic (equation 3.14) works do not change.

3.1.2.4   Space discretization

The geometry of B_0 is approximated by a mesh, consisting of the union of elementary entities named elements (figure 3.3). In the present work, they are triangles in

two dimensions and tetrahedra in three dimensions. The meshed geometry is B_{0h} and the elements are B_0^e:

$$B_0 \approx B_{0h} = \bigcup_{e=1}^{E} B_0^e \qquad (3.17)$$

The bounds of the integrals in equations 3.12 to 3.14 are approximated by considering the meshed volume B_{0h}, rather than the initial volume B_0.
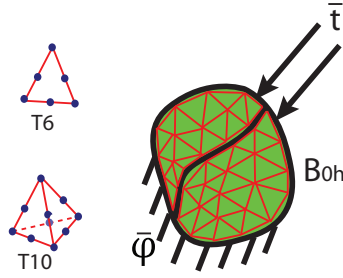
Figure 3.3: Schematic of a structure meshed with boundary conditions. T6 (quadratic triangle) and T10 (quadratic tetrahedra) are the elements used in this thesis.

Moreover, the approximated solution $\boldsymbol{\varphi_h}$ is computed using the following interpolation:

$$\boldsymbol{\varphi_h}(\boldsymbol{X}) = \sum_{a=1}^{N_{nodes}} N_a(\boldsymbol{X}) \boldsymbol{\varphi_a} \qquad (3.18)$$

where N_a is the shape function

$\boldsymbol{\varphi_a}$ is the nodal approximation of the displacement field

We choose a quadratic interpolation, so that the elements have six (resp. ten) nodes in two (resp. three) dimensions (figure 3.3). The shape functions N_a are polynomials of degrees two such that $N_a(\boldsymbol{X_b}) = \delta_{ab}$.

Finally, there remains to compute the integrals of the weak formulation, defined by equations 3.12 to 3.14, formulated in function of the approximated volume B_{0h} and the approximated solution φ_h. Gauss integration provides an efficient framework. It involves quadrature points and weighting functions. First, since we choose a quadratic approximation, elements have three quadrature points. Secondly, the Galerkin (or equivalently the Finite Element) approximation is based on weighting functions equal to the shape functions N_a.

Note that changing the number of quadrature points changes the accuracy of the solution, while changing weighting functions has a deeper impact. Weighting functions determine the type of numerical method. For instance, in the FEM, they

are equal to the shape functions. In point collocation methods (comprising the finite difference method), they are based on Dirac functions at the nodes of the mesh. In subdomain collocation, the weighted functions are the unity in the subdomain, and zero elsewhere.

Once taking into account the discretization, equation 3.11 takes the following simple form:

$$\boldsymbol{M}\ddot{\boldsymbol{\varphi}}_h + \boldsymbol{f}_{int}(\boldsymbol{\varphi}_h) = \boldsymbol{f}_{ext}(\boldsymbol{\varphi}_h) \tag{3.19}$$

where $\boldsymbol{M}$ is the mass matrix

$\boldsymbol{\varphi}$ is the displacement vector

$\boldsymbol{f}_{int}$ is the internal forces array

$\boldsymbol{f}_{ext}$ is the external forces array

This framework is implemented in the library SimulPack, an in-house research code, and which is used in the following chapters to compute the approximations.

3.1.2.5 Explicit time integration

Now, equation 3.19 is discretized in time. The Newmark scheme is a time integration scheme that consists in approximating an exact time differential equation by discrete approximated equations. In our case, the time step between two successive times has a constant value Δt. If the discrete solution at time n is $\boldsymbol{\varphi}^n$, then equation 3.19 becomes:

$$\text{At every time } t^n, \boldsymbol{M}\ddot{\boldsymbol{\varphi}}^n + \boldsymbol{f}_{int}^n = \boldsymbol{f}_{ext}^n \tag{3.20}$$

The general expression of the Newmark scheme is:

$$\boldsymbol{\varphi}^{n+1} = \boldsymbol{\varphi}_p^{n+1} + \beta\Delta t^2\ddot{\boldsymbol{\varphi}}^{n+1} \tag{3.21}$$

$$\dot{\boldsymbol{\varphi}}^{n+1} = \dot{\boldsymbol{\varphi}}_p^{n+1} + \gamma\Delta t\ddot{\boldsymbol{\varphi}}^{n+1} \tag{3.22}$$

where $\boldsymbol{\varphi}_p^{n+1}$ and $\dot{\boldsymbol{\varphi}}_p^{n+1}$ denote the predictor vectors:

$$\boldsymbol{\varphi}_p^{n+1} = \boldsymbol{\varphi}^n + \Delta t\dot{\boldsymbol{\varphi}}^n + \frac{\Delta t^2}{2}(1 - 2\beta)\ddot{\boldsymbol{\varphi}}^n \tag{3.23}$$

$$\dot{\boldsymbol{\varphi}}_p^{n+1} = \dot{\boldsymbol{\varphi}}^n + (1 - \gamma)\Delta t\ddot{\boldsymbol{\varphi}}^n \tag{3.24}$$

In the formulation that we have implemented, $\gamma = 1/2$ and $\beta = 0$, which corresponds to the explicit central difference method. The final formulation is thus:

$$\boldsymbol{\varphi}^{n+1} = \boldsymbol{\varphi}^n + \Delta t\dot{\boldsymbol{\varphi}}^n + \frac{1}{2}\Delta t^2\ddot{\boldsymbol{\varphi}}^n \tag{3.25}$$

$$\dot{\boldsymbol{\varphi}}^{n+1} = \dot{\boldsymbol{\varphi}}^n + \frac{\Delta t^2}{2}(\ddot{\boldsymbol{\varphi}}^n + \ddot{\boldsymbol{\varphi}}^{n+1}) \tag{3.26}$$

Parameters β and γ act upon numerical stability. β determines the type of scheme. $\beta \neq 0$ is associated to implicit schemes, while $\beta = 0$ constitutes explicit schemes. The advantage of implicit method over explicit method is that, for linear problems, suitable implicit integrators are unconditionally stable. For non-linear problems, unconditional stability is not systematic. In such cases, the parameter γ manages artificial viscosity to enforce numerical stability. Experience indicates that the time steps for implicit integrators can be much larger than those for explicit integration. They are suitable for static problems, or permanent regimes. By contrast, explicit schemes, which are nice to implement, require a condition to guarantee stability. They are generally used in dynamic problems, when the time step must be small to represent all the physical mechanisms; they are especially adapted to fragmentation type problems which need an accurate time description of the stress field. The stability condition is expressed by:

$$\Delta t = \alpha \Delta t_c \tag{3.27}$$

$$\Delta t_c = \min_{e \in B_0^h} \frac{l_e}{c_e} \tag{3.28}$$

α is a security coefficient that softens unsteady effects of non-linearities. l_e is the characteristic length of element e, c_e is the wave speed in element e.

3.1.3 Addressing fracture modeling with cohesive crack model

3.1.3.1 Origins of the model

The cohesive crack is the simplest model that describes the progressive fracture process [Bazant 1998]. When it is still closed, a cohesive crack is a fictitious crack, able to fully transfer stress from one surface to the other. Then, as the crack opens, the cohesive zone includes non-linearity and energy dissipation, while the rest of the body behaves as if no crack had appeared. This model was introduced by Dugdale [Dugdale 1960] and Barenblatt [Barenblatt 1962] in the sixties, to represent the crack tip of a preexisting crack.

Barenblatt introduced the cohesive zone to account for the non-linear breaking of the atomic bonds during crack propagation (figure 3.4). He showed that the cohesive approach relieves the crack tip singularity of the linear elastic fracture model, and he related the fracture energy G_c to the interatomic potential. His analysis is limited to cracks whose size is very large compared to the cohesive zone itself. He focused only on the onset of crack growth.

Simultaneously, Dugdale proposed a model to deal with plasticity at crack tip. He assumed that the stress on the crack line, ahead of the crack tip, is limited by yield strength. The plastic deformation concentrates along the crack line. It generates a displacement discontinuity similar to a crack because of the flow of dislocations
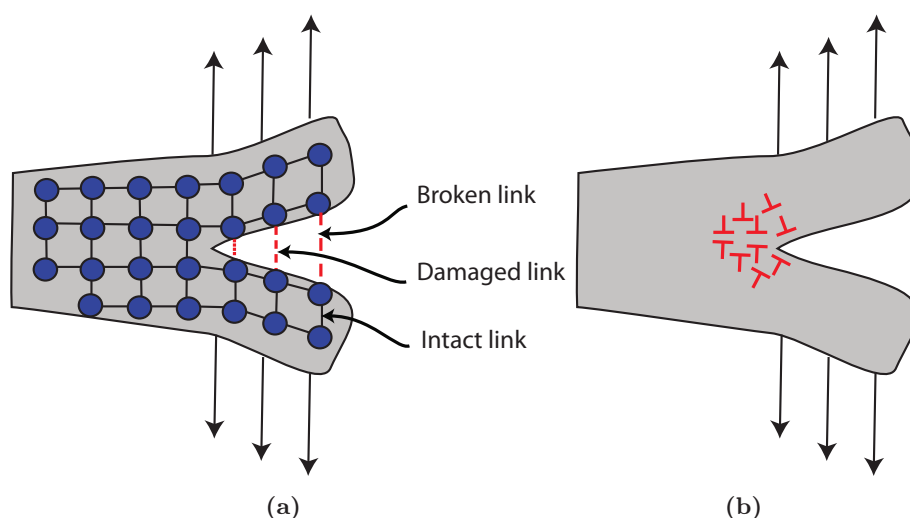
Figure 3.4: Original microscopic cohesive approach. (a) Barenblatt modeled fracture as the result of breaking of atomic bonds. (b) Dugdale was interested in flow of dislocations at crack tip.

gathering around the crack line (figure 3.4). Originally, it was a purely plastic model, which did not involve any fracture criterion.

In the seventies, in the concrete community, Hillerborg et al. [Hillerborg 1976] assumed that cohesive cracks can appear everywhere within the body, even without pre-existing macrocrack. Since then, many researchers have used cohesive cracks to describe the near-tip zone for cracks in diverse materials, such as metals, polymers, ceramics, and geomaterials. Hillerborg's approach is macroscopic; he considered the cohesive crack to be a constitutive relation of the material. He got two key ideas. In the first, he noted that after peak load, all the deformation localizes into the crack. The second is the non-instantaneous description of the evolution of the crack, from intact to fully broken. Various researchers [Hughes 1966, Evans 1968, Heilmann 1987] showed that the evolution law is accessible via suitable experiments. Indeed, if the concrete specimen is small enough and the testing machine is stiff enough, the crack evolves in a stable manner, making it possible to quantify the transition. As pointed out by Elices and Planas [Planas 1995, Planas 2003, Elices 2002], extensions of the cohesive crack model can be very general, including non-linear behavior of the bulk, effect of triaxality on the cracking criterion, and crack evolution law.

The question of the cohesive law has been of interest during the past decades. Two approaches have been competing: the intrinsic and extrinsic approaches. On the one hand, the intrinsic approach (figure 3.5) considers that the cohesive law may include both elastic and softening parts. The cohesive zone belongs intrinsically to
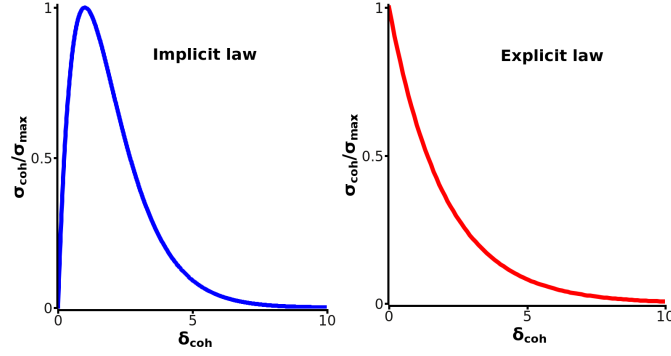
Figure 3.5: Intrinsic (left) and extrinsic (right) cohesive laws.
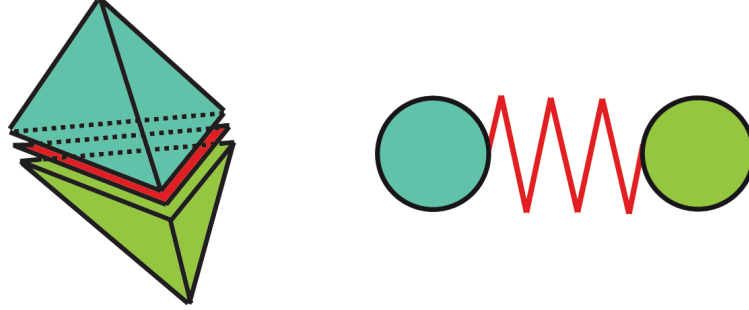
Figure 3.6: Cohesive element within (left) a Finite Element mesh and (right) a Discrete Element mesh.

the specimen, both before and after failure onset. On the other hand, the extrinsic approach (figure 3.5) is based on the idea that the cohesive zone may be modeled right after peak stress; it does not exist before and only includes the softening part.

The cohesive approach is now widely used in numerical simulations to model non-instantaneous and dissipative failure. The basic idea lies in introducing a cohesive interface between two bulk entities (particles in discontinuous frameworks, elements in continuum frameworks) between which a crack may appear.

3.1.3.2 Finite Element implementation of the cohesive methodology

The weak formulation with an interface can be easily adapted to the cohesive element formulation. The cohesive law relates the opening of the crack $\delta\boldsymbol{\varphi}$ to the traction across the interface $\boldsymbol{T} = \boldsymbol{P}\boldsymbol{n}$. Equation 3.16 becomes:

$$\delta W^{int} = \int_{B_0^{+-}} \boldsymbol{P} : \boldsymbol{\nabla}_0\delta\boldsymbol{\varphi} \; dV_0 \; + \; \int_{\partial_I B_0} \boldsymbol{T}\left(\llbracket\boldsymbol{\varphi}\rrbracket\right)\llbracket\delta\boldsymbol{\varphi}\rrbracket \; dS_0 \qquad (3.29)$$

In practice, the implementation in a FE code involves cohesive elements. A cohesive element is an interface element between two adjacent elements of the mesh
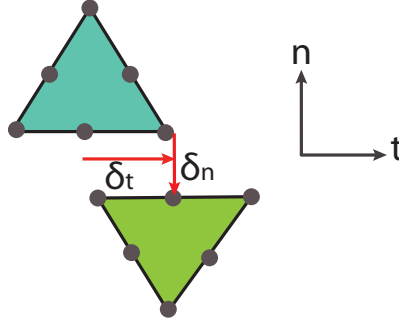
Figure 3.7: Schematic of a crack opening in two dimensions. Normal and tangential openings.

(figure 3.6). In two dimensions, it is a line constituted of six nodes (figure 3.7). In three dimensions, it is a surface constituted of twelve nodes (quadratic elements). The displacement jump across the crack is $\boldsymbol{\varphi}$ and can be decomposed into a normal δ_n and tangential δ_s jump (figure 3.7):

$$[\![\boldsymbol{\varphi}]\!] = \boldsymbol{\varphi}^+ - \boldsymbol{\varphi}^- = \delta_n \boldsymbol{n} + \delta_t \boldsymbol{t} \tag{3.30}$$

In order to resolve properly the cohesive zone, the cohesive elements must be small enough. Derivation of the cohesive zone size l_z can be found in the work of Palmer and Rice [Palmer 1973], Rice [Rice 1980]:

$$l_z = \frac{9\pi E'}{32} \frac{G_c}{\sigma_c^2} \tag{3.31}$$

where $E' = E$ for plane stress and $E' = \frac{E}{1-\nu^2}$ for plane strain. G_c is the toughness, σ_c is the failure strength, E is the Young's modulus, and ν is the Poisson ratio. Typically, $l_m \simeq \frac{l_z}{3}$, where l_m denotes the mesh size.

3.1.3.3   Needleman's exponential intrinsic law

The intrinsic approach results from the physical considerations concerning the delamination processes at material interface under multiaxial loading, in which the location of the crack is well defined before its initiation. By understanding fracture behavior, Needleman and coworkers developed an exponential energy law for imperfect metallic interfaces involving the normal and tangential opening of the crack [Needleman 1990, Miller 1999, Freund 1999].

Let $r, q, \delta_{n,0}$ and $\delta_{t,0}$ be some characteristic input values. We denote $\Delta_n = \frac{\delta_n}{\delta_{n,0}}$ and $\Delta_t = \frac{\delta_t}{\delta_{t,0}}$. The exponential cohesive law from Xu and Needleman [Xu 1994]
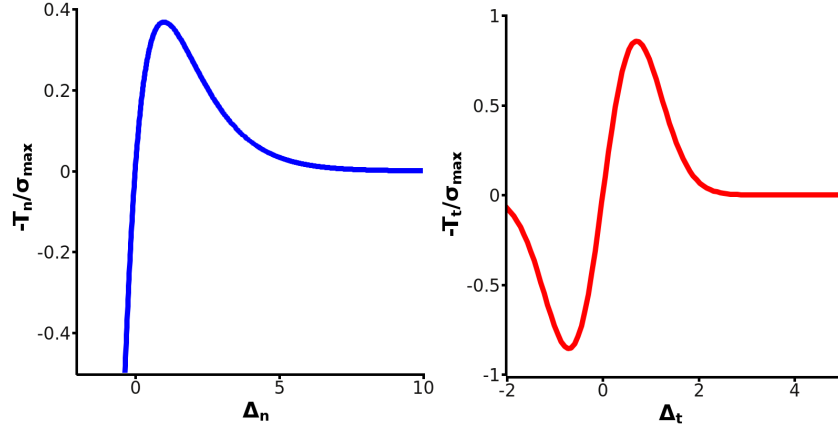
Figure 3.8: Exponential cohesive law. Left: normalized normal traction with $\Delta_t = 0$. Right: Tangential traction with $\Delta_n = 0$. $q = 1$ and $r = 0$.

expresses the normal T_n and the tangential T_t forces at the interface (figure 3.8):

$$T_n = -\sigma_{max} \; e^{-\Delta_n} \left(\Delta_n \; e^{-\Delta_t^2} \; + \; \frac{1-q}{r-1} \left(1 - e^{-\Delta_t^2} \right) (r - \Delta_n) \right) \qquad (3.32)$$

$$T_t = -2\sigma_{max} \; \frac{\delta_{n,0}}{\delta_{t,0}} \Delta_t \left(q \; + \; \frac{r-q}{r-1} \Delta_n \right) e^{-\Delta_n} \; e^{-\Delta_t^2} \qquad (3.33)$$

From a technical point of view, the insertion of the cohesive elements occurs before the dynamic loop begins, at the location of the cracks. This procedure has a main drawback: the non-physical compliance that the initial increasing slope of the law results in. In dynamics, stress waves are not well transmitted across the interface elements [Seagraves 2009]. Klein et al. [Klein 2001] quantified this artificial compliance by studying the effective Young's modulus of a one-dimensional body. They showed that it can be made negligible by enforcing the value of the cohesive law's initial slope to be very large. However, this requirement leads to an additional constraint: the time step in the dynamic calculation must be very low. The loss of efficiency may be considerable. Therefore, the use of the intrinsic approach requires a compromise between low time step (computational efficiency) and artificial compliance (physical accuracy).

To limit this non-accuracy, Falk et al. [Falk 2001] suggest a criterion concerning the mesh size l_m, the cohesive zone size l_z, and the distance between two cohesive interfaces l_d:

$$l_m \; < \; l_z \; < \; l_d \qquad (3.34)$$

This relation guaranties a toughness-controlled failure process. If it is not satisfied, cohesive zones might not be well described and/or failure might be strength con-

trolled (controlled by the failure strength σ_c). Stability in cohesive zone modeling has been investigated by Foulk in [Foulk 2010].

3.1.3.4   Ortiz's linear extrinsic law

The extrinsic approach was motivated by the fact that crack can appear anywhere within the structure. The use of the intrinsic approach in such problems would lead to consider a structure whose volume is fully constrained by the cohesive zone, and the resulting artificial compliance would be penalizing. To face this issue, Ortiz and coworkers [Camacho 1996, Ortiz 1999, Pandolfi 2002] pioneered the extrinsic approach in which the cohesive zones appear dynamically within the body. The main technical difficulty is the dynamic insertion of new cohesive elements. A careful change in the topology of the mesh is necessary.

Despite this difficulty, and motivated by the fact that, in fragmentation simulations, crack can appear anywhere, we chose to use the extrinsic approach. Although several laws have been proposed, we decided to keep Ortiz's original law because of its simplicity (it is linear).

The insertion criterion is based on a stress threshold: if the stress locally reaches the failure strength, also called the cohesive strength, then a cohesive element is inserted. Once inserted, the effective opening is computed at each time step, and the stress across the interface σ_{coh} is updated.

The effective opening is:

$$\delta = \sqrt{\delta_n^2 + \beta^2 \delta_t^2} \qquad (3.35)$$

β is a coefficient which balances the normal and tangential contributions of the displacement jump. We denote the cohesive strength σ_c and the critical opening δ_c (figure 3.9). The cohesive stress σ_{coh} is:

$$\frac{\sigma_{coh}}{\sigma_c} = 1 - \frac{\delta_{coh}}{\delta_c} \text{ , for } \dot{\delta}_{coh} > 0 \text{ , } \delta_{coh} = \delta_{max} \text{ and } D < 1 : \text{opening} \qquad (3.36)$$

$$\frac{\sigma_{coh}}{\sigma_c} = 1 - \frac{\delta_{max}}{\delta_c} \text{ , for } \delta_{coh} < \delta_{max} \text{ and } D < 1 : \text{closing} \qquad (3.37)$$

The first equation controls the opening of the crack; the closing is governed by the second. D is the local damage, whose value is 0 if crack has not opened, and 1 if it is fully broken:

$$D = min\left(\frac{\delta_{max}}{\delta_c}, 1\right) \qquad (3.38)$$

The energy that the failure can dissipate is:

$$G_c = \frac{\sigma_c \, \delta_c}{2} \qquad (3.39)$$

When it is partially opened, the dissipated energy is E_{diss} and it retains the elastic recoverable energy E_{rec} (figure 3.9):

$$E_{diss} = DG_c \tag{3.40}$$

$$E_{rec} = \sigma_{coh}.\delta_{coh} = (1 - D)D\frac{\delta_{coh}}{\delta_c} \tag{3.41}$$

When the crack is on the opening path, $\delta_{coh} = \delta_{max}$ and the recoverable energy is:

$$E_{rec} = (1 - D)DG_c \tag{3.42}$$
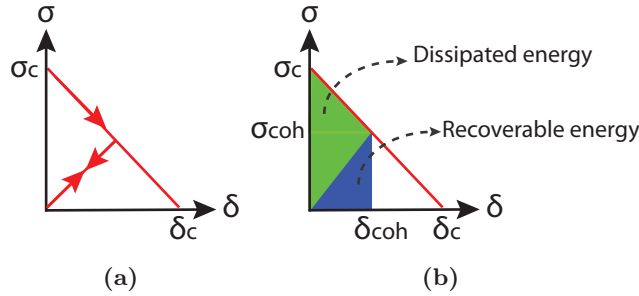
Figure 3.9: (a) Linear irreversible cohesive law and (b) associated energies.

3.2 Handling parallelization: the discontinuous Galerkin method

3.2.1 Motivation for, and origins of the DGM

This section focuses on technical aspects that parallelization rises. Parallelizing the code is necessary to simulate fragmentation at high strain rates, which requires very fine meshes. At some point, the increase in the degrees of freedom cannot be handled by a single processor, serial calculations are limited by the memory of the processor. Parallelizing the code and running it on multiple processors increase available memory and significantly lower the calculation time (c.f. section 3.2.3).

The previous section detailed the numerical framework used to simulate the dynamic evolution of a body undergoing multiple crack initiations. It is based on the FEM coupled to extrinsic cohesive approach, in which elements are inserted into the mesh dynamically. This operation results in the repetitive update of the mesh topology, which is delicate to address in serial codes, and which becomes a challenging issue when it is question of parallelization. Indeed, the severe changes in the mesh topology, occurring regularly during the simulation, are hardly parallelizable in an efficient way. When a cohesive element is inserted by a given processor, it must send

its connectivity map to the other processors. Communication between processors drastically alters the efficiency that the parallelization is supposed to provide. As a result, in order to reduce the communication time between processors, a natural idea consists in avoiding the numerous topology changes by updating the mesh only once.

This interesting idea originated in Pr. Radovitzky's group, in the Massachusetts Institute of Technology, Boston, USA. Pr. Radovitzky and coworkers developed the core of a parallel code based on the discontinuous Galerkin method (DGM). At EPFL, we tested and improved the code in view of fragmentation simulations and implemented functions related to fragment tracking (see appendix A). This collaboration was particularly efficient during the sabbatical year that Pr. Radovitzky spent in our group at EPFL.

The bases of the code are the following. In order to limit processor communication, the mesh update occurs only once, at the beginning of the calculation, e.g. before the dynamic loop begins. The mesh is entirely split during the initialization stage, which amounts to inserting interface elements at every edge of the mesh (figure 3.10). Nodes are duplicated, elements are added, and the number of degrees of freedom naturally increases. Before failure onset, interface elements are controlled by some flux defined in the discontinuous Galerkin method. After failure, they become linear decreasing cohesive elements.

7x2=14 dof   3x6x2=32 dof
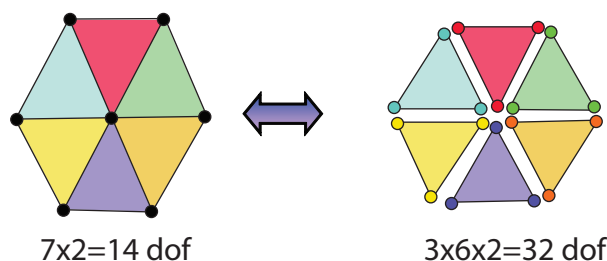
Figure 3.10: Splitting of a mesh. Interface elements are inserted between two adjacent bulk elements (triangle in two dimensions, tetrahedron in three dimensions). Each interface is independently governed by either the DG framework (before failure onset), or the linear cohesive law (after failure onset).

The DGM is a generalization of the usual Galerkin method which constitutes the basis of the widespread finite element method. In the recent years, the discontinuous Galerkin methods have received considerable attention for problems involving advection and diffusion terms [Cokburn 2002]. More recently, it has been used for problems allowing physical discontinuities such as fracture [Mergheim 2004, De Borst 2006] and discontinuities based on constitutive models that incorporate

spatial gradients [Noels 2006, Wells 2004], or numerical discontinuities involving irregular meshes (hanging nodes [Castillo 2000], hp adaptivity [Oden 1998]).

The current formulation of the DGM is the result of a century work during which mathematicians and physicians have improved the formulation [Zienkiewicz 2003]. The name of discontinuous Galerkin seems to appear first in a paper by Lesaint and Raviart [Lesaint 1974] who defined a method to link separate domains in a weak manner. An approximation is computed independently in each domain, weakly connected to the others afterward. Other theories have been derived to link such separate domains, among which the method of domain decomposition [Gosselet 2006]. It adds Lagrange multiplier functions at contiguous interfaces of the various domains in such a manner that the number of unknown variables increases. The essence of the DGM lies in the elimination of the Lagrange multiplier functions so that the total number of unknown variables does not depend on the interfaces. An obvious way to accomplish this elimination is the direct substitution. This idea was developed by Nitsche who derived a new variational principle [Nitsche 1971]. He also discovered that this process could lead to numerical singularities. Hence, he added a further constraint of least-square type, to avoid numerical indefiniteness. The parameter that he introduced can be seen as a stabilization term.

Moreover, the DGM has other significant advantages. Stable and high-order conservative, it is also able to capture highly complex solutions presenting discontinuities, such as shocks and fragmentation problems. It guaranties the proper representation of material parameters, such as the Young's modulus. There is no issue of artificial compliance with the DGM, stress waves are precisely tracked [Radovitzky 2010, Seagraves 2009]. In addition, since the method uses a discontinuous approximation, it produces matrices that are block-diagonal, which renders it highly parallelizable [Noels 2007]. Consequently, the DGM is particularly well suited for our problem: it is an accurate and stable generalization of the FEM, it describes well discontinuities (the interface elements inserted during the initial splitting of the mesh are driven by the DGM), tracks accurately stress waves, and it is highly scalable (it enables to run quick simulations on large meshes). Nonetheless, the main drawback of the method lies in the multiplication of the degrees of freedom (figure 3.10). The memory needed to execute the codes increases. This issue can easily be solved by running the simulations on multiple processors.

3.2.2   New hybrid formulation 'DG - cohesive'

The strong formulation is the same as in section 3.1.2.3. The weak formulation is adapted, based on the idea that the DGM relaxes the equilibrium (eq. 3.5) across the interfaces $\partial_I B_0$ (figure 3.2), and the compatibility equations ($[\![\varphi]\!] = 0$, $\forall \varphi \in \partial_I B_0$), by enforcing them weakly rather than strongly. First, we recall the jump operator

and define the average operator:

$$[\![\bullet]\!] = \bullet^+ - \bullet^- \qquad \langle\bullet\rangle = \frac{\bullet^+ + \bullet^-}{2} \tag{3.43}$$

Equation 3.16 involves the jump across the interface :

$$[\![\mathbf{P}\,\delta\boldsymbol{\varphi}]\!] = [\![\mathbf{P}]\!]\,\langle\delta\boldsymbol{\varphi}\rangle + \langle\boldsymbol{P}\rangle\,[\![\delta\boldsymbol{\varphi}]\!] \tag{3.44}$$

The key point consists of addressing the contribution of the interface discontinuity by introducing a numerical flux $h(\boldsymbol{P}^+, \boldsymbol{P}^-, \boldsymbol{n})$, which depends on the limit values of the stress on the interface surfaces $(\boldsymbol{P}^+, \boldsymbol{P}^-)$. $\mathbf{n}$ the normal vector to $\partial_I B_0$ pointing from B_0^+ to B_0^-. In the case of elliptic equations, Bassi and Rebay [Bassi 1997] proposed that h takes the form:

$$h(\boldsymbol{P}^+, \boldsymbol{P}^-, \boldsymbol{n}) = \langle\mathbf{P}\rangle\boldsymbol{n} \tag{3.45}$$

Following the derivations detailed in [Noels 2006], the weak formulation becomes:

$$\delta W^{int} = \int_{B_0^{+-}} \boldsymbol{P}: \boldsymbol{\nabla}_0\boldsymbol{\delta\varphi}\, dV_0 \;+\; \int_{\partial_I B_0} [\![\boldsymbol{\delta\varphi}]\!]\langle\boldsymbol{P}\rangle\boldsymbol{n}\, dS_0 \tag{3.46}$$

However, experience shows that this formulation is highly unstable. Nitsche showed that the compatibility on the displacements must be enforced weakly by using the quadratic penalty term [Nitsche 1971]. An appropriate expression in solid mechanics involves the tangent moduli $\mathbb{C}$. The final expression of the internal work becomes:

$$\begin{aligned}
\delta W^{int} = &\int_{B_0^{+-}} \boldsymbol{P}: \boldsymbol{\nabla}_0\boldsymbol{\delta\varphi}\, dV_0 \\
&+ \int_{\partial_I B_0} [\![\boldsymbol{\delta\varphi}]\!].\langle\boldsymbol{P}\rangle.\boldsymbol{n}\, dS_0 \\
&+ \int_{\partial_I B_0} [\![\boldsymbol{\varphi}]\!] \otimes \boldsymbol{n}\; : \langle\frac{\beta}{h_s}\mathbb{C}\rangle :\; [\![\boldsymbol{\delta\varphi}]\!] \otimes \boldsymbol{n}\, dS_0
\end{aligned} \tag{3.47}$$

where $\beta > 0$ is the stabilization parameter and h_s is a suitable characteristic length.

The weak formulation of the hybrid discontinuous Galerkin - cohesive method is thus:

$$\begin{aligned}
&\int_{B_0} (\rho_0\,\ddot{\boldsymbol{\varphi}}\,\boldsymbol{\delta\varphi} + \boldsymbol{P}: \boldsymbol{\nabla}_0\boldsymbol{\delta\varphi})\, dV_0 + \alpha \left(\int_{\partial_I B_0} \boldsymbol{T}([\![\boldsymbol{\varphi}]\!])\, [\![\boldsymbol{\delta\varphi}]\!]\, dS_0 \right) \\
&+ (1-\alpha) \left(-\int_{\partial_I B_0} \langle\boldsymbol{P}\rangle\, [\![\boldsymbol{\delta\varphi}]\!]\, \boldsymbol{n}\, dS_0 + \int_{\partial_I B_0} [\![\boldsymbol{\varphi}]\!] \otimes \boldsymbol{n}\; : \langle\frac{\beta}{h_s}\mathbb{C}\rangle :\; [\![\boldsymbol{\delta\varphi}]\!] \otimes \boldsymbol{n}\, dS_0 \right) \\
&= \int_{\partial_N B_0} \bar{\boldsymbol{T}}\,\boldsymbol{\delta\varphi}\, dS_0
\end{aligned}$$

$$\tag{3.48}$$

The first term of the left hand-side of equation 3.48 gathers volumetric terms (dynamic and internal forces). The right hand-side term involves Neumann boundary conditions. These two integrals constitute the usual virtual work principle. The two other terms only apply on interface boundaries $\partial_I B_0$. The term, which is multiplied by α, is related to the cohesive law, while the terms multiplied by $1 - \alpha$ refer to the DG framework. In the DG parenthesis, the first integral is directly computed from the equations; it involves a flux and guarantees the consistency of the numerical scheme. The other integral enforces weakly the interlement compatilibty. It is a quadratic stabilization term, which has been proved to be necessary to guarantee numerical stability [Nitsche 1971].

Hence, the value of α governs the state of the interfaces: they are intact when $\alpha = 0$ and damaged when $\alpha = 1$. Initially, $\alpha = 0$ at each interior boundary. When the fracture criterion is satisfied, α is locally set to 1. We recall that the failure criterion is based on a stress threshold: as soon as the stress locally reaches the cohesive strength σ_c, the cohesive law is activated.

Space discretization and subsequent derivations (nodal approximation and Gauss integration) are nearly similar to section 3.1.2.4. The only differences lie in the expression of the internal forces and in the definition of the interface. Internal forces now involve a DG term, which can be calculated from equation 3.48. The interface boundary is defined by:

$$\partial_I B_0 = \left(\bigcup_{e=1}^{E} \partial B_0^e \right) \setminus \partial B_{0h} \tag{3.49}$$

3.2.3   Scalability and efficiency

The performance test of the parallel version of the DG-cohesive implementation was carried out in a test session on Blue Gene (this type of session limits the number of available processors and is required by the administrators before running on more processors). Figure 3.11 represents the time needed to perform the initialization step (domain decomposition with ParMETIS [Schloegel], splitting of the mesh, determination of the lumped mass matrix, of shape functions and of the time step) for a mesh composed of 18836 tetrahedra, which corresponds to roughly 600000 degrees of freedom. The old code is the one used in all the simulations of this thesis. The new code is an ongoing improvement of the mesh splitting. The third curve corresponds to the initialization plus 2545 steps of the dynamic loop.

The log-log plot highlights a power-like dependence of the execution time on the number of processors. This rapid decrease justifies the use of parallel computing to gain time. Indeed, the best power-law fit of the curve corresponding to the dynamic
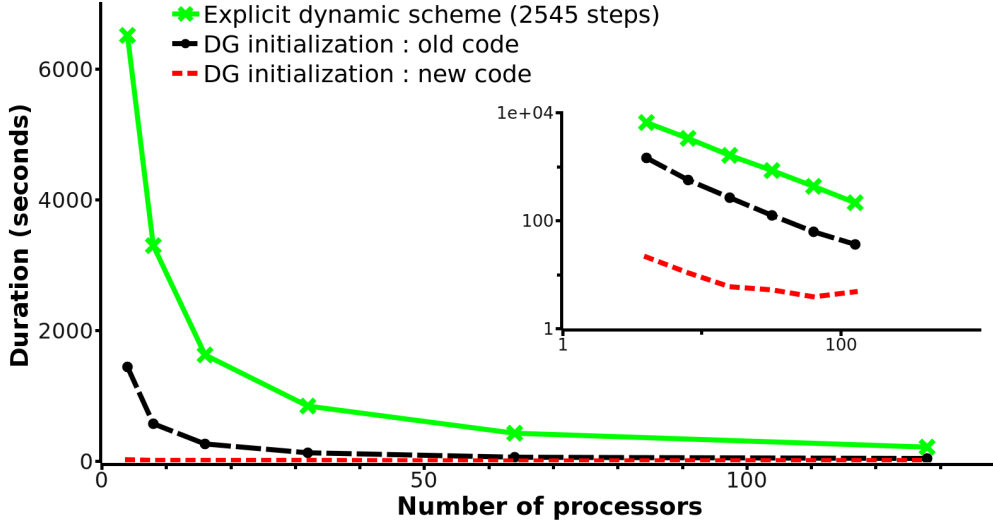
Figure 3.11: Scalability of the DG code in natural and log-log axis. The efficiency is closed to one.

loop is $t_{N_p} = \frac{25718}{N_p^{0.99}}$, where N_p is the number of processors and t_{N_p} is the time required by N_p processors to achieve the job. It corresponds to the efficiency:

$$E = \frac{t_1}{N_p.t_{N_p}} \ \rightarrow \ 1 \tag{3.50}$$

where t_1 is the time required by one processor. The efficiency $E = 1$ is the best achievable, it means that the load is perfectly distributed among the processors and that the communication time tends to be null. Note that, in figure 3.11, the curve associated to the new code does not rigorously display a power law dependence because the time needed by the processors to perform the operations is much smaller than the interprocessor communication time. A mesh constituted of more degrees of freedom, distributed among the same number of processors, would have led to a scalable response. The code used in this thesis is thus highly efficient and scalable.

3.3   Statistical representation of volumetric defects

In the previous sections, we have focused on the numerical frameworks used in this thesis. The FEM and the DGM handle bulk material response, for serial and parallel simulations. Failure is addressed by the Ortiz's linear irreversible cohesive law. The bases of the numerical framework are now set. Characteristic values of the cohesive law (σ_c, G_c) are, however, not given yet. The main objective of this section is to relate microstructure and the value of the cohesive strengths.

Since every material is imperfect, it contains defects, which may constitute the location for failure initiation. A defect is a region where stresses are concentrated by

the microstructure. Under the action of an external loading, stress locally increases and may lead to structural damage. As a result, identifying accurately material flaws is a key issue to predict the failure behavior. However, since most flaws are located within the structure, they are not visible and their explicit description is not obvious. To bypass this difficulty, scientists have been using statistics to give a quantitative representation of the material microstructure.

In the following of the thesis, failure strength and cohesive strength are confounded. A defect is associated to a cohesive element, and they share the same parameters (failure strength and toughness).

3.3.1 Defects in ceramics

Ceramics usually exhibit a dense population of defects, and are thus adequate candidates to list the most probable defects in brittle materials. A ceramic is an inorganic, mostly crystalline, non-metallic solid. It is prepared by the action of heat and subsequent cooling. To highlight some outstanding properties, they have low density, high mechanical strength, high hardness, high working temperature; they are resistant to wear and corrosion, and have excellent electric properties. However, they have a major drawback: their low reliability. Even though substantial advances have been made to improve the quality of the manufacturing process, there remain numerous defects, which cause the ceramic failure.

As illustrated in figure 3.12, ceramics are characterized by many types of defects spanning a wide range, from atomic (in the tenth to the nanometer order) to specimen (in the centimeter order) range. All these defects contribute to the final complex mechanical properties of the material. Naturally, defects differ not only in their size, but also in their shape, orientation, and distribution [Kanzaki 1997]. Today, experimental instruments make the visualization of almost all of these features possible. The pictures exposed in this section are taken from the work of Dusza and Steen [Dusza 1999]. In situ observation of fracture behavior in ceramics has also been carried out by Ii [Ii 2005].

The most common defects can be classified into four categories [Lamon 2007]:

- Microstructural defects have a characteristic length lower than the grain size. They are generally triple joints, grain boundary decohesion sites, inclusions.

- Processing defects appear during the processing stages. Pores of various sizes and shapes are the most frequently observed defects in ceramics. They have different origins [Telle 1995]: poor powder packing, and impurities in the starting powder. Clusters of reinforcing phases are also commonly observed in composite ceramics, and usually arise as a result of poor mixing. Abnormally
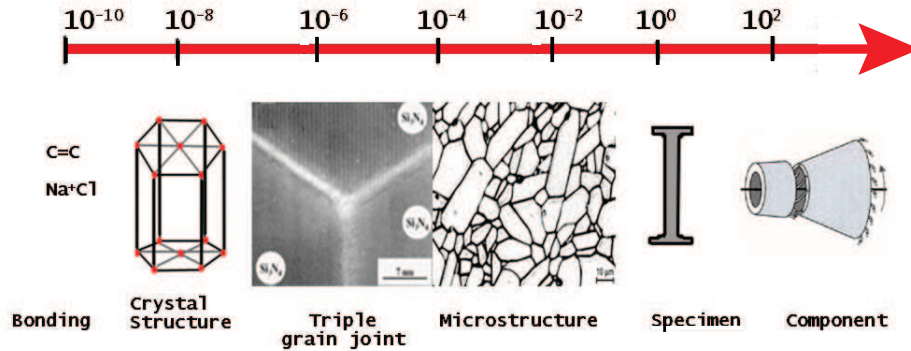
Figure 3.12: Schematic of the characteristic defects in ceramics and their associated length scale [Lamon 2007].

large grains are also often present, their origin is related to inhomogeneous densification during sintering.

- Machining defects stem from inaccurate forming procedure.

- Wear defects, due to corrosion, cavitation, chemical transformation, arise during usage.

These defects strongly influence fracture [Ainscough 1976, Becher 1998]. To illustrate the effect of the microstructure on quasi static failure, figure 3.13 shows a fracture line in silicon nitride which follows predominantly intergranular fracture modes.

Nowadays, it seems obvious to relate microstructural flaws and failure. A century ago, it was not. In the thirties, Weibull got the idea to interpret failure as a mechanism originating at the defects' location.

3.3.2   Weibull's approach of statistical failure in quasi-static

The Weibull theory is by far the world's most popular statistical model for life data. Waloddi Weibull was born on June 18, 1887. His family originally came from Schleswig-Holstein, at that time closely connected with Denmark. His first paper was on the propagation of explosive wave in 1914. He also published many papers on strength of materials, fatigue, rupture in solids, bearings, and of course, on the Weibull distribution. Let us first come back to his original empirical idea (section 3.3.2.1), and then justify theoretically the expression of the Weibull distribution by use of the weakest link theory [Pierce 1936, Wolstenholme 1995] (section 3.3.2.2)
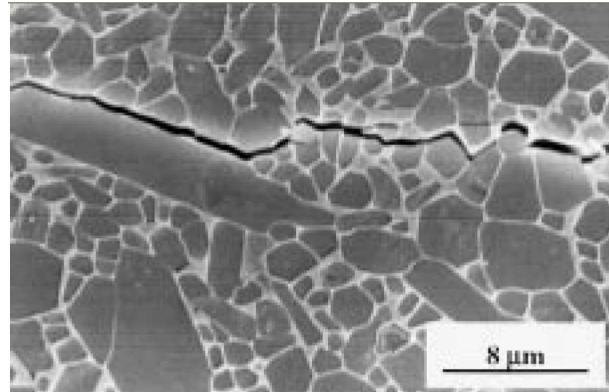
Figure 3.13: Fracture line in silicon nitride to highlight the effect of the microstructure on crack path [Dusza 1999].

and of the extreme value statistics (section 3.3.3.2) [Coles 2001, Leadbetter 1983, Bazant 2007].

3.3.2.1 Empirical distribution

Weibull considered a set of specimens, constituted of the same material, geometry, and loaded in the same configuration. He noted that the same quasi static tensile loading can lead to distinct failure strengths [Weibull 1939]. Following his idea, Abe et al. [Abe 2003] performed four-point bending tests of alumina bulk ceramics to determine fracture strengths of three commercially available alumina bulk ceramics. Their properties are detailed in table 3.1.

Sample Sample	Purity (%)	Density kg/m^3	Average strength(MPa)	Weibull modulus
A	99.7	3.91	260	28
B	99.9	3.91	315	35
C	99.7	3.92	359	33

Table 3.1: Properties of commercial alumina ceramics. Purity quantifies the proportion of defects, density is the proportion of pores. [Abe 2003]

Thirty to forty equally sized and equally shaped specimens, made of materials A, B and C, were broken in tensile quasi statics. For each material, figure 3.14 lists the failure strengths in terms of probability of failure. Taking a logarithmic y-axis reveals that the inverse of the probabilities of failure follow affine functions. Their slopes are identical; the common value is a material parameter called Weibull modulus (table 3.1). Since identical sample geometry and loading condition lead to distinct values of failure strengths, the relation between failure and strength is not deterministic. This is why Weibull developed the concept of probabilistic failure.
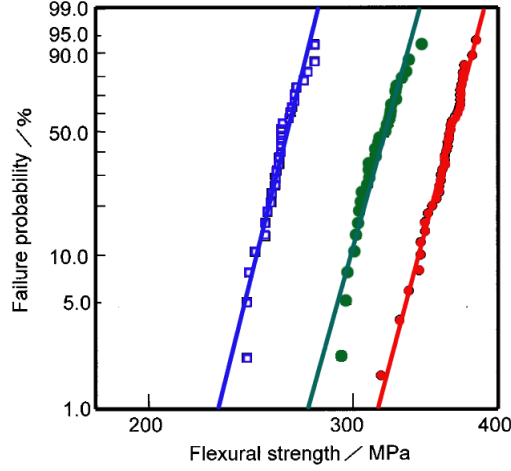
Figure 3.14: Inverse of the probability of failure at a given strength [Abe 2003].

In the thirties, Weibull proposed a macroscopic phenomenological model, which includes the effect of heterogeneities in the failure process. In 1939, he defined the well-known Weibull's distribution. Materials of volume V, with a homogeneous volume-defect density submitted to the homogeneous uniaxial stress state σ, undergo failure with the probability:

$$P_f = 1 - e^{-N(\sigma, V)} \tag{3.51}$$

$N(\sigma, V)$ is a material function assumed to be independent of the position in the specimen and of the direction of the stress σ. Weibull mentioned that $N(\sigma, V)$ is necessarily a monotonically increasing function of σ. He noted that power laws are more representative of life data analysis:

$$N(\sigma, V) = \begin{cases} \frac{V}{V_0} \left(\frac{\sigma - \sigma_{min}}{\sigma_0} \right)^m & if \sigma > \sigma_{min} \\ 0 & otherwise \end{cases} \tag{3.52}$$

where V is the specimen volume,
V_0 is an arbitrary normalizing volume,
σ_{min} is the lower bond of strength,
σ_0 is the scale factor,
m is the Weibull modulus.

m and σ_0 are material parameters. To give a quantitative understanding, m is usually comprised between 1 and 20 for ceramics. It is around 30 for composites, and it reaches values between 50 and 100 for steels.
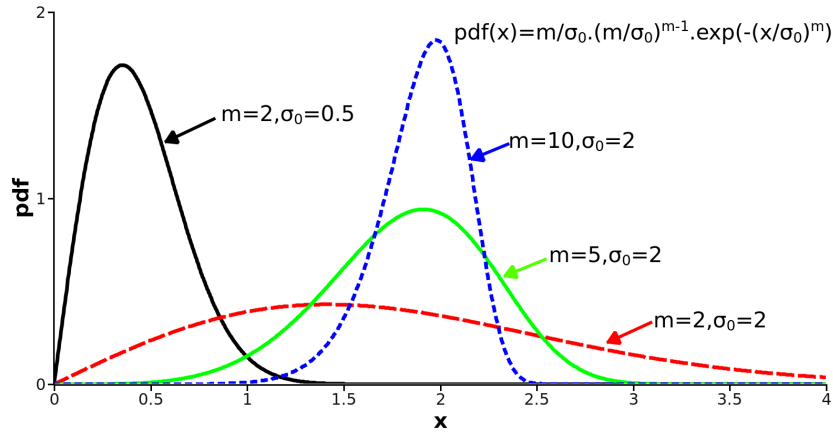
Figure 3.15: Effect of the parameters m and σ_0 on the Weibull distributions. The normalizing volume is such that $V_0 = V$, and $\sigma_{min} = 0$.

3.3.2.2   The weakest link theory

The shape of the Weibull's distribution can be justified by the weakest link theory that we present in this section.

Hypothesis:

First, let us precise the hypothesis of the weakest link theory, which is a fundamental concept of brittle fracture modeling. The material is constituted of a series of elementary volume dV [Pierce 1936, Wolstenholme 1995]. Each dV embodies a defect, and is characterized by a failure strength. Depending on the loading, failure may initiate in the volume dV (figure 3.16).

- Hypothesis 1: The gradient of the stress field is low enough so that each element dV is submitted to a uniform load.

- Hypothesis 2: Failure strengths are independent random variables. This hypothesis guarantees the heterogeneity of the material and assumes that there is no interaction between defects.

- Hypothesis 3: The failure of one elementary volume dV leads to the failure of the whole volume V.

Selection of the probabilistic law

The Poisson point process is a stochastic process in which events occur continuously and independently of one another. Here, an event is the activation of a defect. In the volume V, the population of defects is modeled by the parameter λ, which
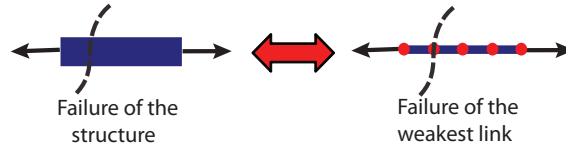
Figure 3.16: Schematic representing the weakest link theory.

corresponds to the density of defect activation. The Poisson process predicts that the probability that k defects are activated is:

$$P_k(V) = e^{-\lambda V} \frac{(\lambda V)^k}{k!} \tag{3.53}$$

k=0 means that no defect is activated, the structure is intact. k=1 represents the activation of one volume dV, which is equivalent to failure of the whole structure V in one dimension. The probability of failure, which is the inverse of the probability of survival can be thus written:

$$P_f(V) = 1 - P_0(V) = e^{-\lambda V} \tag{3.54}$$

Equation 3.54 underlines that defect density λ fully determines the probability of failure. λ can be expressed in terms of either defect failure strength (σ), or the size of the defect (a). Size and strength are indeed related through the toughness K_{Ic} [Anderson 2005, Einav 2006]:

$$K_{Ic} = Y.\sigma.\sqrt{a} \tag{3.55}$$

where Y is a dimensionless constant that depends on the geometry and the mode of loading.
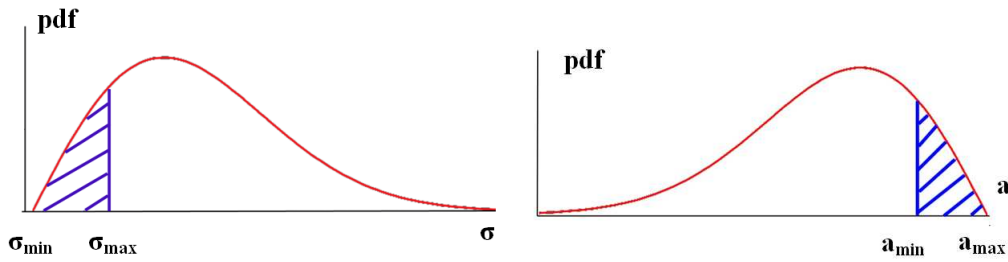
Figure 3.17: Probability density functions (pdf) of a Weibull distribution in the (a) strength approach and (b) size approach.

Influence of the volume: strength approach (figure 3.17(a))

Defect density is described with a function λ that represents the probability density function (pdf) of the probability P. Let us consider the random variable $X : B \to \mathbb{R}$ associated to the event $\{\sigma \in B : X(\sigma) = \bar{\sigma}\}$, where $\bar{\sigma}$ is an elementary strength. Let also $P = P_X(\sigma)$ be the associated probability. The probability density function $\lambda(\sigma)$ verifies:

$$P(\sigma < X < \sigma + d\sigma) = \lambda(\sigma)d\sigma \tag{3.56}$$

The cumulative density function (cdf) is then

$$F(\sigma) = P(X \leq \sigma) = \int_0^\sigma \lambda \tag{3.57}$$

Therefore, the probability of finding a critical defect at σ is the probability that the elementary strength associated to a defect has a value inferior to σ. Thus, the probability of failure of a volume V_{elem}, loaded in a uniform stress field σ is:

$$P_f(\sigma, V_{elem}) = V_{elem} \cdot P(X \leq \sigma) = V_{elem} \int_0^\sigma \lambda \tag{3.58}$$

For a volume V, composed of N identical elementary volume V_{elem}, the probability of failure at a given uniform stress σ is derived from the probability of survival of each elementary volume:

$$P_s(\sigma, V) = (P_s(\sigma, V_{elem}))^N \tag{3.59}$$

this leads to the probability of failure:

$$P_f(\sigma, V) = 1 - (1 - P_f(\sigma, V_{elem}))^N = 1 - \left(1 - V_{elem} \int_0^\sigma f\right)^N \tag{3.60}$$

When the number of elementary volumes N is high, this equation leads to :

$$P_f(\sigma, V) = 1 - e^{-V \int_0^\sigma \lambda} \tag{3.61}$$

where $V = N \cdot V_{elem}$ This expression is valid for a uniform and uniaxial stress field.

Influence of the volume: size approach (figure 3.17(b))

The size approach is similar to the strength approach. Defect density is described with a function g that represents the probability density function (pdf) of the probability P. Let us consider the random variable $X : B \to \mathbb{R}$ associated to the event $\{a \in B : X(a) = \bar{a}\}$, where $\bar{\sigma}$ is an elementary strength. Let also $P = P_X(a)$ be the associated probability. The probability density function $g(a)$ verifies:

$$P(a < X < a + da) = g(a)da \tag{3.62}$$

The cumulative density function (cdf) is then

$$G(a) = P(X \leq a) = \int_a^\infty g \tag{3.63}$$

Therefore, the probability of finding a critical defect of size a is the probability that the characteristic size associated to a defect has a value greater than a. Thus, the probability of failure of a volume V_{elem} is:

$$P_f(a, V_{elem}) = V_{elem} \cdot P(X \leq a) = V_{elem} \int_a^\infty g \tag{3.64}$$

Following the same steps as in the first approach, the probability of failure can be written:

$$P_f(a, V) = 1 - e^{-V \cdot \int_a^\infty f} \tag{3.65}$$

3.3.3   Expressions of the defect density

A large panel of defect density has been proposed since Weibull's weakest link theory [Danzer 1992, Graham-Brady 2010, Jayatilaka 1977, Jeulin 1993, Bazant 1998, Lamon 2007]. We selected two of them.

3.3.3.1   De Jayatilika's model

Jayatilaka proposed an expression of the defect density as a function of failure strength [Jayatilaka 1977]. He based his derivation on the experimental results of Poloniecki et al. [Jeulin 1993, Chudnovsky 1987], who expressed the defect density with a complex function of the defect size. After non trivial developments, Jayatilaka deduced the probability of failure for N cracks, N sufficiently large:

$$P_f = 1 - e^{-N \frac{c^{n-1}}{n!} \left(\frac{\pi \sigma^2}{K_{IC}^2} \right)^{n-1}} \tag{3.66}$$

where c and n are characteristic constants. This expression is similar to Weibull's prediction, which is not surprising when noticing that the tail of the distribution is only considered (N is taken large) and that the Poloniecki's density function involves a power law.

3.3.3.2   Bazant's theory based on the fracture process zone concept: extreme value statistics and central limit theorem

Bazant's main area of interest is quasi-brittle failure (typically concrete-like materials), which behavior is at the frontier of brittle and ductile failure [Bazant 1998, Bazant 2007, Bazant 2002, Bazant 1999, Bazant 2004]. Brittle fracture designates a group of fracture processes, which occur with absence of plastic deformation. On the contrary, ductile materials can be deformed plastically without fracture. Bazant uses the fracture process zone concept (FPZ) to describe the transition between the

two mechanisms. The FPZ is a zone surrounding the crack-tip damaged by crack-bridging and micro-cracking activities. Depending on the sizes of the specimen and the FPZ, the material failure behavior is guided by its brittleness or by its ductility (see figure 3.18).

The body is modeled by a combination of representative volume elements (RVE). Bazant defined the RVE to be the smallest material element whose failure causes the failure of the whole structure (this is the weakest link hypothesis). In the case of brittle failure, FPZ does not interact with the boundary of the specimen. For failure in mode I, the RVE is composed of a single elementary volume. The failure of one element leads to the failure of one RVE and consequently of the structure. The minimum value of the failure strengths thus determines when the structure is broken. Extreme value statistics [Coles 2001, Leadbetter 1983] show that there exist only three types of distributions, which satisfy the weakest link hypothesis [Fisher 1928]: the Fréchet [Fréchet 1927], the Weibull [Weibull 1939] and the Gumbel [Gumbel 1958] distributions. Since it is bounded by a minimum value, Bazant suggests that the Weibull distribution is the only distribution mathematically acceptable for brittle structures [Bazant 1998, Bazant 2007, Bazant 2004].

By contrast, in the case of ductile failure, FPZ does interact with the boundary of the specimen. For failure in mode I, the RVE is a series of elementary volumes in parallel (figure 3.18). The failure of one RVE occurs when all the elements in parallel are broken. The average value of the failure strengths controls the behavior. The central limit theorem applies, which leads to normal distribution.

To summarize, depending on the material properties, one should either consider a Weibull distribution (brittle-like failure) or a normal distribution (ductile-like failure). Doremus [Doremus 1983] confirmed theoretically these distributions, along with other extreme-value type distributions.
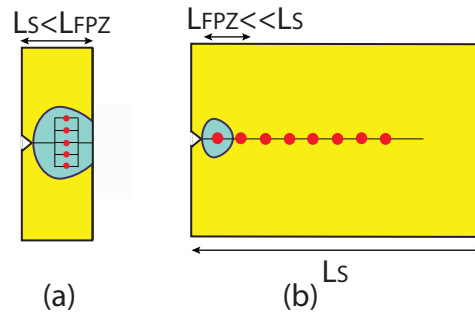
Figure 3.18: Effect of the specimen size (L_s) and the FPZ size (L_{FPZ}) on the failure mechanisms. (a) Ductile process: the RVE is constituted of several elementary volumes in parallel. (b) Brittle process: the RVE is constituted of one elementary volume.

3.4   Summary

In this chapter, the numerical methods used in this thesis were detailed. The serial code is based on the traditional FEM, while the parallelized version is based on the DGM. Both methods are coupled to the cohesive element methodology. In the FEM case, cohesive elements are inserted dynamically into the mesh, which results in regular updates of the mesh. In parallel, since they occur repeatedly, topological changes penalize the communication between processors and the efficiency of the parallelization. This is the reason why the DGM was selected. Indeed, the DG-cohesive framework avoids the dynamic insertion of cohesive elements by inserting interface elements everywhere, during the initialization stage. As long as failure has not initiated, interface elements behave following the DGM. Then, when a critical strength is reached, they switch to the linear irreversible cohesive law. Domain decomposition based on the DGM is highly scalable.

Finally, we modeled the heterogeneity of the material with distribution of cohesive strengths, which corresponds to failure strengths. For brittle materials, the Weibull distribution is the most appropriate. It has been validated by experiments and theoretical analysis (weakest link theory and extreme value statistics). In contrast, normal distributions seem to represent more accurately the behavior of ductile materials.

General physical concepts

This chapter [1] may be considered as a transition between chapter 3, which exposed the physical and numerical modeling employed in numerical simulations, and the following chapters (chapter 5 to chapter 8) that present the main contributions of the thesis. Fragmentation phenomenon is based on non-linear complex physics and its understanding may naturally not be straightforward. As a result, in this chapter, in order to facilitate the reader's understanding, we detail qualitatively two principles: crack interactions that occur through non-linear stress wave interactions, as well as energy balance between potential, kinetic, and fracture energies. Material properties and boundary conditions are shown qualitatively to affect both. The following chapters will detail quantitatively the ideas developed here.

4.1 How stress release waves govern crack interactions

4.1.1 One-dimensional bar

Let us consider a bar of given length L loaded uniformly in tension. The material has a linear elastic response with Young's modulus E, volumetric mass ρ and longitudinal wave speed $c = \sqrt{E/\rho}$. It is heterogeneous and failure may initiate at defect locations. The defect i, characterized by its failure strength $\sigma_{c,i}$, undergoes at time t the longitudinal stress $\sigma_i(t)$. We order the defects depending on their failure strengths such that $\forall i, \sigma_{c,i} \leq \sigma_{c,i+1}$. Boundary conditions involve controlled displacements on the extremities of the bar. Initial conditions consist of a velocity ramp such that the bar is subjected to uniform loading at the strain rate $\dot{\varepsilon}$.

In a first stage, stress is uniform and increases linearly until reaching the value of the weakest link strength $\sigma_{c,min} = \sigma_{c,1}$ at time $t = t_0$. Then, failure begins at the weakest link. For clarity purpose, we first consider a bar with only one defect. Secondly, the bar has two defects, and finally any number of defects.

The bar is here constituted of the elastic bulk and one defect (figures 4.1 and 4.2). Failure can be modeled through two approaches: instantaneous and non instantaneous failures. In the case of instantaneous failure (figure 4.1), stress at the defect location drops instantaneously from $\sigma_{c,min}$ to 0. Since failure is effective as soon as

---

[1]The first part of the chapter will be the topic of a short communication in a physics journal, co-authored by S.Levy, J.F.Molinari, R.Radovitzky

$\sigma = \sigma_{c,min}$, the crack takes no time to open and does not dissipate energy. This failure modeling is associated to an instantaneous drop in stress, which generates a discontinuity in the stress field. To compensate it, two stress waves propagate from the defect in opposite directions. On the one side of the wave front, the stress is null, while on the other side, the stress continues increasing and reaches at time t the value $\sigma = \sigma_{c,min} + E \dot{\varepsilon} (t - t_0)$. The boundaries, where displacements are applied, do not see that failure has occurred yet. As a result, there exists a non null time necessary to broadcast failure information, which depends on the location of the weakest link, the length of the bar, the Young's modulus E, and the strain rate $\dot{\varepsilon}$.
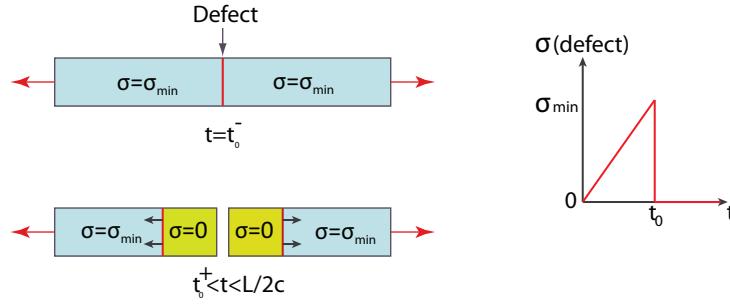
Figure 4.1: Instantaneous fracture. Discontinuous drop in stress and associated propagating waves, with no energy dissipation.

In the case of non-instantaneous failure (figure 4.2), the defect is also activated as soon as $\sigma = \sigma_{c,min}$ but does not drop instantaneously to zero. Failure is effective after some time: the crack opens continuously, the bar is partially damaged until the crack reaches a critical opening. This opening distance is associated to energy dissipation. A traction-separation law governs the evolution of the stress at the defect location as a function of the crack opening. In figure 4.2, we model crack by a spring whose stress decreases when it opens. Let us suppose that this traction-separation law is linear decreasing and reaches zero when crack opening is δ_c. The energy dissipated by failure is the toughness $G_c = \frac{\sigma_{c,min} \cdot \delta_c}{2}$. Large (resp. small) values of the toughness are associated to ductile (resp. brittle) behavior. The time needed to broadcast the information that failure is effective is larger in the non-instantaneous than in the instantaneous case.

Let us now consider a bar with two defects and assume that defects 1 and 2 are far enough so that they both initiate (figure 4.3). While defect 1 initiates and gets damaged, the stress increases in the regions of the bar that have not been encompassed yet by stress waves. Stress rises and reaches $\sigma_{c,2}$. If it has been
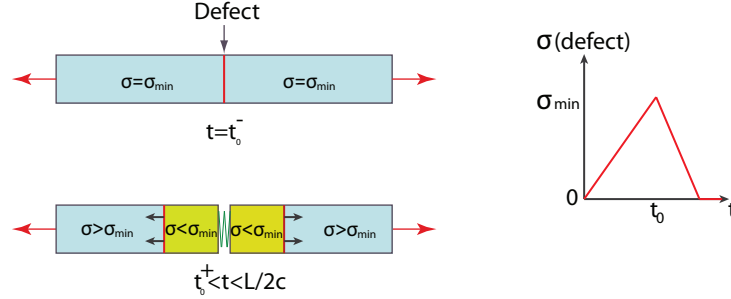
Figure 4.2: Non-instantaneous fracture. Continuous drop in stress governed by a traction-separation law and associated propagating waves, with energy dissipation.

encompassed by stress waves, a region is unloaded. Assuming that defect 2 has not been released, it undergoes the same failure process as defect 1, and it releases its own propagating stress waves. At some point, the waves generated by defects 1 and 2 join and interact. Wave physics show that, depending on the value of their amplitude and phase, two interacting waves may either be constructive or destructive. This means that, when they cross, the two stress waves may generate new wave front with either larger or smaller amplitude. The resulting waves propagate along the bar, reflect on the bar boundaries, and interact again in a constructive or destructive way. This process continues and waves repeatedly go through the two defects. This multiple wave passing is at the origin of the progressive damage of the defects: a defect usually does not break instantaneously, but requires several wave passings to fully break. Naturally, since the location and the value of the failure strength are defined statistically, we cannot predict the behavior of the resulting wave. The solution of such a problem is not obvious, and cannot be calculated analytically when more defects come into play. Numerical simulations are thus required to represent accurately stress wave interactions.

When there are more than two defects, the process is identical. The weakest link is first initiated. Stress waves are propagating and release the encompassed defects. In the regions that have not been encompassed by the weakest link's wave, the stress is rising and other defects initiate. They generate their own stress waves, and a highly non-linear network of stress waves establishes. Their interactions are mostly destructive and sometimes constructive. Some defects are thus initiated, others remain intact.

In quasi statics, the strain rate $\dot{\varepsilon}$ is low compared to the ratio c/L. When the weakest link is activated, stress waves propagate and release the encompassed areas. Since they are propagating fast, in comparison to the increase in stress of the non-
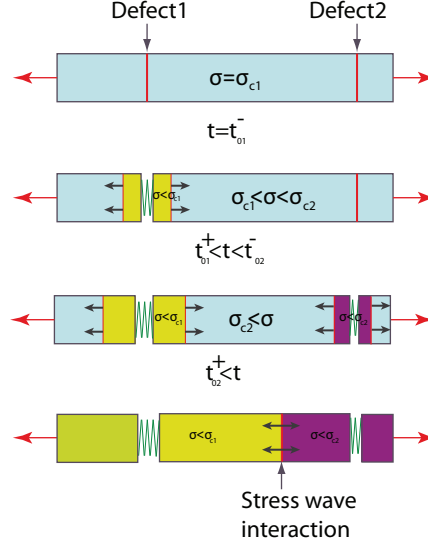
Figure 4.3: Non-instantaneous fracture with two defects. Continuous opening of the cracks, propagating and interacting stress waves.

encompassed areas, no more defect nucleates. Failure only occurs at the weakest link. On the contrary, in dynamics, the strain ratio $\dot{\varepsilon}$ is much higher than the rate c/L. In this case, the waves released by the failure of the weakest link are propagating slowly in comparison to the increase in stress of the non-encompassed areas. Other defects are initiated. Consequently, in quasi-static, the bar fragments at one location, while it fails at multiple points in dynamics. Purely qualitative considerations of the dynamics of stress waves in a one-dimensional problem thus justify that at high strain rates, more fragments are generated than at low strain rates. In the following, we will see that energetic arguments may as well be evoked to justify this intuitive result.

In addition to these wave interaction considerations, another mechanism may take place. When multiple fragments are generated, they are moving: part of the kinetic energy is used for the global motion of the body, the rest locally evolves to ensure energetic equilibrium with potential energy. Fragments may thus impact each other, which leads to additional compression forces. Applied on the fragment's boundaries, these forces generate compressive waves that affect the global response. As shown by Zhao and coworkers [Cai 2000, Zhao 2006b, Zhao 2006a], the interactions between compressive waves and fractures are complicated. Although analytical solutions have been proposed for simple test case, they can hardly handle more complex cases. Once more, numerical simulations seem to be the most appropriate tool to

predict such mechanisms.

In multiple dimensions, the mechanisms are the same although they are more difficult to visualize. Mechanical waves are propagating in every direction around the defects and interact with other waves. Both crack initiation and crack propagation are influenced by the wave network. Some time is necessary for the information to broadcast to boundaries. In quasi static, the fragmentation pattern involves few cracked lines, while it is denser in dynamics.

4.1.2 Quantification of the secondary wave effect

As highlighted in the previous paragraph 4.1.1, when two stress wave fronts interact, the resulting wave has a magnitude that may be either higher or lower than the initial wave magnitudes. However, since they require some restricting conditions, constructive waves are generally less accessible, and wave interactions mostly result in lower magnitudes. Hild and coworkers [Brajer 2003, Denoual 1997, Denoual 2002, Forquin 2003b, Forquin 2003a, Hild 2003] have developed a theory in which constructive waves are neglected. This amounts to assuming that a region of the bar that has been encompassed once is definitively protected from further damage.

However, this strong hypothesis has already been proved to be approximate. Drugan [Drugan 2001] derived the stress field of a bar with three defects and showed that secondary waves play a key role in fragmentation. In order to quantify their effect, we conduct numerical simulations on various brittle materials, at strain rates ranging from $\dot{\varepsilon} = 10^3 \ s^{-1}$ to $\dot{\varepsilon} = 10^5 \ s^{-1}$. Since Hild et al.'s model assumes highly heterogeneous and brittle materials, we selected four materials:

- Mat.1: Highly brittle and homogeneous (Weibull distribution with Weibull modulus 20 and scale parameter 5 MPa) with toughness $G_c = 1 \ N/m$

- Mat.2: Highly brittle and heterogeneous (Weibull distribution with Weibull modulus 2 and scale parameter 500 MPa) with toughness $G_c = 1 \ N/m$

- Mat.3: Brittle and homogeneous (Weibull distribution with Weibull modulus 20 and scale parameter 5 MPa) with toughness $G_c = 50 \ N/m$

- Mat.4: Brittle and heterogeneous (Weibull distribution with Weibull modulus 2 and scale parameter 500 MPa) with toughness $G_c = 50 \ N/m$

For each material and each strain rate, we conduct two simulations. One employs the numerical model presented in chapter 3, which accounts for secondary waves. The other is based on Hild et al.'s theory. In practice, for the second type of simulation, a cohesive element can be in two stages: breakable or unbreakable. Initially, all the cohesive elements may break. Then, at each time step, we verify whether a given cohesive element has a mean effective stress σ_{eff} lower than it was

at previous time (implying that the stress has been unloaded by a propagating stress wave):

$$\text{If (cohesive element i is breakable \&}$$
$$\sigma_{eff}(t_i) \; < \; \sigma_{eff}(t_{i-1}) - \text{tolerance)}$$
$$\text{then (cohesive element i becomes unbreakable)}$$

where the tolerance is set to $1 \; MPa$. In one dimension, this effective stress is the principal stress in the direction of the bar. This framework allows neglecting the effect of secondary waves.

First, strain rate is set to $\dot{\varepsilon} = 10^4 \; s^{-1}$. For each material, we plot the cohesive energies for the two simulations and quantify the difference by focusing on their final values $E_{coh,fin}$ through the ratio:

$$\Delta \; = \; \frac{E_{coh,fin}^{with} - E_{coh,fin}^{without}}{E_{coh,fin}^{with}} \tag{4.1}$$

where *with* stands for 'with secondary wave effect' (usual model), and *without* stands for 'without secondary wave effect' (Hild et al.'s approach).
Figure 4.4 presents the result for material Mat.2. Naturally, since some defects become unbreakable in the second type of simulation, the cohesive energy 'without' can only be smaller than the 'with' secondary waves.
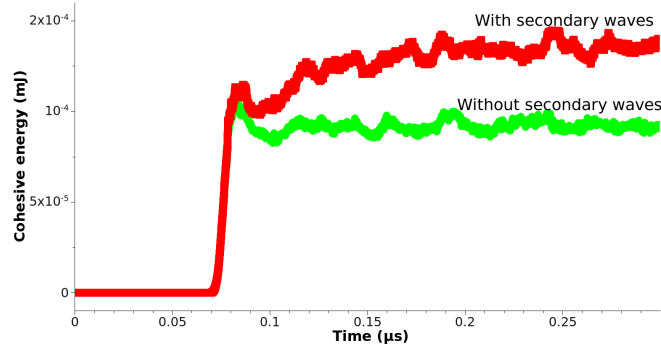
Figure 4.4: Evolution of the cohesive energies at strain rate $\dot{\varepsilon} = 10^4 \; s^{-1}$, for Mat.2 (very brittle and heterogeneous) in two cases: with and without accounting for the secondary waves. Note that cohesive energy fluctuates because it involves recoverable energy.

As highlighted by table 4.1, we observe that the materials selected lead to distinct responses.
In other words,

- Mat.1 and Mat.3: $\Delta \simeq 0$. When the material is homogeneous, secondary waves have a negligible effect at $\dot{\varepsilon} = 10^4 \; s^{-1}$.

Strain rate (s^{-1})	10^3	2.10^3	10^4
Mat.1	0.0573	<0.005	<0.005
Mat.2	0.7243	0.6175	0.333
Mat.3	<0.005	<0.005	<0.005
Mat.4	>0.95	>0.95	0.4173

Table 4.1: Computed values of Δ for several strain rates.

- Mat.2 and Mat.4: $0 < \Delta_2 \leq \Delta_4$. When material is heterogeneous, secondary waves affect failure response at $\dot{\varepsilon} = 10^4 \ s^{-1}$. The less brittle the material is, the more significant the secondary waves effect is.

In order to verify that these observations remain valid at other strain rate, we ran simulations from $\dot{\varepsilon} = 10^3 \ s^{-1}$ to $\dot{\varepsilon} = 10^5 \ s^{-1}$. The trends are identical and accentuated. Indeed, Mat.1 and Mat3. still lead to very close responses ($\Delta \simeq 0$), while Mat.2 and Mat.4 become more sensitive to secondary waves while strain rate decreases. Figure 4.5 plots the evolution of the rate Δ (equation 4.1) for Mat.2, as a function of the strain rate. At very high strain rates, there is at most 2% difference between both cases, while it reaches 80% at the intermediate strain rate $\dot{\varepsilon} = 2.10^3 \ s^{-1}$. Δ displays a logarithmic decay.
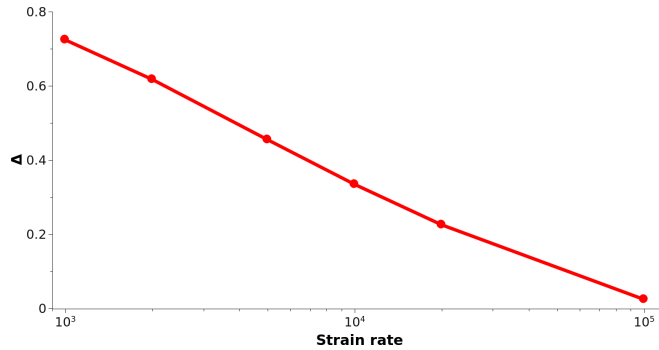
Figure 4.5: Evolution of the ratio Δ that measures the effect of secondary waves in one-dimensional fragmentation, with strain rate. x-axis is logarithmic

In conclusion, secondary stress waves have insignificant effect at very high strain rates for all the studied materials. It is also negligible for the homogeneous materials at every strain rate. However, at intermediate (and low) strain rates, secondary wave effect becomes consequential, as the material becomes more ductile and more heterogeneous. These observations highlight the necessity of taking wave interactions into account. They may change considerably the structural responses. As an illustration, in car crashes, strain rate ranges $100 \ s^{-1}$ and materials are highly heterogeneous (because of the diverse components of the car and the complex geometry)

and ductile (the carter is made of steel): 95% of the damage may stem from wave interactions. Similarly, the most rapid bullets can reach $\dot\varepsilon = 10^5\ s^{-1}$ and gradually slow down and stop. During the beginning of the impact, stress wave interactions may have negligible effect. However, as the bullet penetrates the structure, they may become significant. Since most impacts occur at small or intermediate strain rates, and since most materials are heterogeneous or ductile, neglecting secondary stress waves amounts to underestimating damage by a factor that can reach 95%. Naturally, these observations are only the result of the study of four materials and the bar geometry. More simulations will be run to confirm (or invalidate) them in more complex problems.

4.2   Energy balance arguments

In this section, we focus on the energy evolution during fragmentation. We concentrate on the kinetic, potential, and cohesive energies. If energy is balanced, the variation of external work is equal to the sum of the variations of kinetic, potential, and cohesive energies:

$$\varphi(W_{ext}) \ = \ \varphi(E_{kin} \ + \ E_{pot} \ + \ E_{coh}) \tag{4.2}$$

In any of the simulations presented in this thesis, energy balance has been verified. Moreover, all the following results in this section concern the fragmentation of a rectangular plate of length 0.01 meters and thickness is generally set to 0.15 mm (this value may change; it is chosen to be as small as possible and to ensure the mesh quality). It is constituted of a brittle heterogeneous material (Weibull modulus two, scale parameter 50 MPa, toughness $G_c = 50\ N.m^{-1}$) with Young's modulus $E = 370\ GPa$, Poisson ratio $\nu = 0.22$, and volumetric mass $\rho = 3900\ kg.m^{-3}$. Strain rate is $\dot\varepsilon = 10^4\ s^{-1}$. In the following, we vary these parameters one after the other, to study their effect on the energy evolution.

4.2.1   Effect of boundary conditions

We first compare two types of tensile loading conditions: the impulse and the uniform expansion.

Impulse: The impulse boundary conditions consist of applying a velocity ramp before the dynamic explicit calculation begins (figure 4.6(a)). The body is thus loaded uniformly at onset and released. Thus, initially, kinetic energy is injected, while potential and cohesive energies are null (figure 4.6(b)). Then, kinetic energy is converted into potential energy. Since we assume a linear elastic response of the bulk, the body expands and the potential energy increases quadratically with time:

$$E_{pot} = \frac{V}{2}\ E\dot\varepsilon^2 t^2 \tag{4.3}$$

where V is the volume of the specimen. Two cases arise:

- **With no failure:** The body stretches and stress reaches a peak when kinetic energy is null. Nonetheless, the peak stress does not extend to the minimum value required for fragmenting the body. There is not enough input energy (kinetic energy) in the system to initiate failure. Then, potential energy decreases quadratically, while kinetic energy increases. The conversion of energy only involves kinetic and potential energies.

- **Leading to failure:** Strain rate is high enough to initiate failure. The body stretches, and the stress reaches a value larger than the one required for fragmenting the body (figure 4.6(b)). Then, potential energy is converted into failure; cohesive energy increases. This conversion generates a loss in potential energy, which is compensated dynamically by kinetic energy. After peak stress, two mechanisms are competing: first, potential energy is directly converted into failure; second, kinetic energy is converted into potential energy, which is in turn converted into cohesive energy. Since these two mechanisms occur simultaneously, they cannot be distinguished easily. We will, however, see that depending on strain rate and material properties, the indirect conversion (involving kinetic energy) may dominate.

(a)   (b)

Figure 4.6: Impulse loading: (a) The dashed arrows indicate the amplitude of the velocities applied initially within the whole body. (b) Evolution of the variation of the kinetic, potential, and cohesive energies. Strain rate is $\dot{\varepsilon} = 10^4 s^{-1}$, parameters are detailed in the text.

Uniform expansion: The uniform expansion conditions consist of applying initially an impulse, and of pulling on the boundaries during the explicit dynamic loop (figure 4.7(a)). The advantage is, whatever the strain rate is, the body will break. Quasi static regime is thus accessible. Moreover, as shown in [Zhou 2006a], in the dynamic regime, impulse and uniform expansion lead to the same response. The only drawback lies in the understanding of the results; they are less obvious to interpret. First, potential energy increases quadratically (figure 4.7(b)). Kinetic energy

is constant since we impose a uniform expansion. The sum of both (which is equal to the external work) thus increases quadratically. Then, when the stress is high enough to damage some defects, cohesive energy increases. Failure energy is supplied by potential energy conversion, which is governed by the two mechanisms detailed previously (direct conversion of potential energy and indirect conversion based on kinetic energy). As a result, since we keep pulling, kinetic energy increases, potential energy decreases and cohesive energy increases until the body is fully broken (e.g. when stress waves have fully released the body). Note that the final value of the potential energy is not necessarily zero because failure stops as soon as the stress is low enough in comparison to the failure strengths, and not necessarily when it is null. Each fragment independently possesses global kinetic energy that makes it flies, local kinetic energy that is constantly converted into potential energy, and internal damage. In comparison to the impulse loading, the final cohesive energy is slightly larger because of the constant supply of kinetic energy ($E_{coh,fin} \simeq 0.0556~J$ for the impulse, $E_{coh,fin} \simeq 0.0604~J$ for the uniform expansion).

4.2.2 Effect of the input parameters

4.2.2.1 Strain rate

Let us consider two extreme cases: $\dot{\varepsilon} = 10~s^{-1}$ (quasi-static to intermediate) and $\dot{\varepsilon} = 10^5~s^{-1}$ (dynamic). We select the same specimen plate as in the previous paragraph, and material parameters are detailed at the beginning of the section. Naturally, the mesh is fine in the dynamic case (to ensure convergence) and coarse in the quasi-static case (to ensure reasonable simulation time). In order to maintain the good quality of the mesh, the plate thickness was adjusted. The specimen is loaded in uniform expansion to unable the small velocities imposed by the quasi-static test to reach failure.

Figure 4.8 compares the energetic responses generated by quasi-static and dynamic experiments. Before peak potential energy, the behavior of the potential is slightly identical. The response is not rigorously quadratic because of the activation of some defects. Indeed, in two dimensions, the failure of one defect does not lead to the failure of the whole structure. Crack must propagate through the entire structure. The plate can undergo diffuse damage while potential energy still increases. At some time, the damaged locations interact, cracks are forming and fragmentation process occurs. The transition between diffuse damage and fragmentation is not well-defined. Note, however, that diffuse damage before peak stress is nearly negligible since the cohesive energy remains quasi null. We can thus assume an elastic response before peak stress, which ensures that the value of the peak potential energy is proportional to $\dot{\varepsilon}^2$ (eq. 4.3). We emphasize that the values of peak potential energy in figures 4.8(a) and 4.8(b) cannot be compared directly. The specimen thicknesses are different (0.15 mm at high strain rate and 0.22 mm at
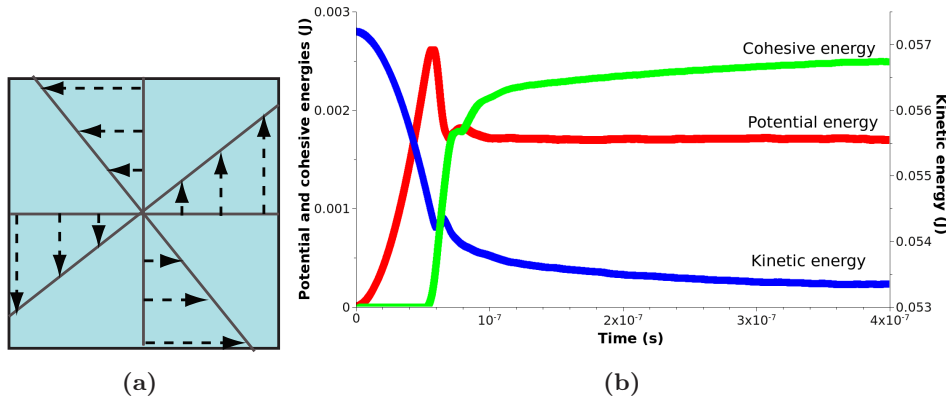
(a)

(b)
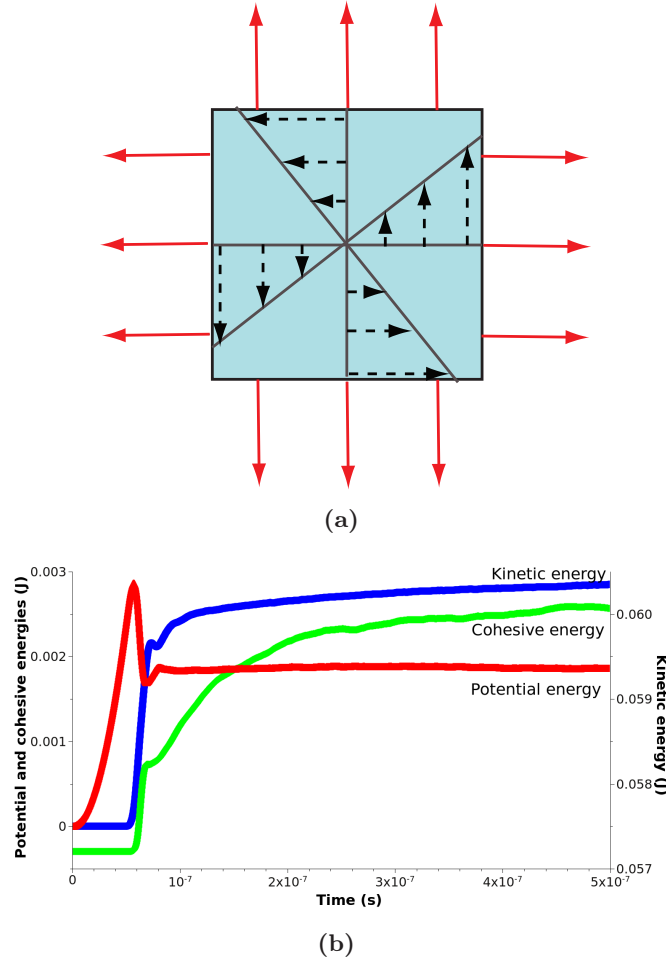
Figure 4.7: Uniform expansion: (a) The dashed arrows indicate the amplitude of the velocities applied initially within the whole body, the plain arrows represent the displacements imposed on the plate boundaries during the whole simulation. (b) Evolution of the variation of the kinetic, potential, and cohesive energies. Strain rate is $\dot{\varepsilon} = 10^4 s^{-1}$, parameters are detailed in the text.

low strain rate), which leads to distinct specimen volumes. From equation 4.3, E_{pot} (and a fortiori peak potential value) involves the specimen volume.

After peak, dynamic and quasi-static behaviors are distinct. In the quasi-static case (figure 4.8(a)), wave velocity is large compared to strain rate ($c/L_{plate} \gg \dot{\varepsilon}$). The 'elastic' phase takes thus much more time than the failure phase. The majority of the cohesive energy comes from potential energy. The increase in kinetic results from the external work, which is constantly applied.

On the contrary, in dynamics (figure 4.8(b)), wave velocity is small compared to strain rate ($c/L_{plate} \simeq \dot{\varepsilon}$). The 'elastic' phase occurs rapidly compared to the failure phase. Therefore, failure occurs 'slowly', which offers some time to use kinetic energy. Indeed, in dynamics, not only peak potential energy is directly converted into failure, but kinetic energy (which is supplied by external work) is also transferred into potential energy, which is in turn employed in failure. Both direct and indirect conversions are significant. The indirect conversion is made possible because of the time required by the waves to reach the boundaries (see section 4.1.1). While the information that failure has occurred within the body and broadcasts via stress waves, we keep pulling and inserting energy into the system.

To summarize, the number of activated defects is an increasing function of the strain rate for two main reasons: the amount of available energy, and the time needed by stress waves to broadcast information that the specimen is fragmenting. This double effect contributes to generating more cracks in dynamics than in quasi-statics.

4.2.2.2   Young's modulus

The Young's modulus mostly affects the behavior before peak stress. Figure 4.9 displays the potential energy evolution for several Young's modulus (same mesh, same other material parameters). Strain rate is $10^4 \ s^{-1}$. Assuming a linear elastic response, time to failure evolves as $1/E$:

$$t_f = \frac{\sigma_{peak}}{E.\dot{\varepsilon}} \tag{4.4}$$

and the rate of increase in potential energy is proportional to E, while peak potential energy is inverse proportional to E (eq. 4.3).

The behavior after peak stress is also affected by the Young's modulus through the wave speed (that is proportional to $\sqrt{E}$). Large Young's moduli result in more rapid response than small Young's moduli.
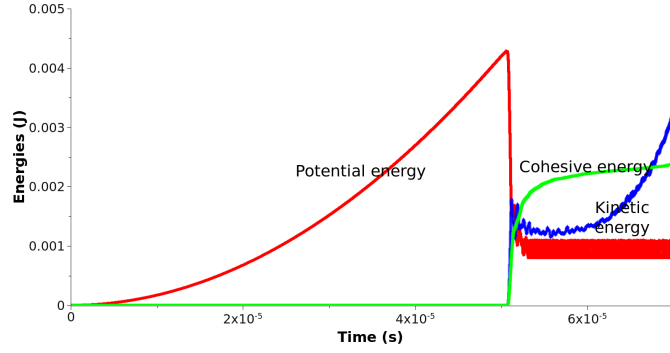
(a)
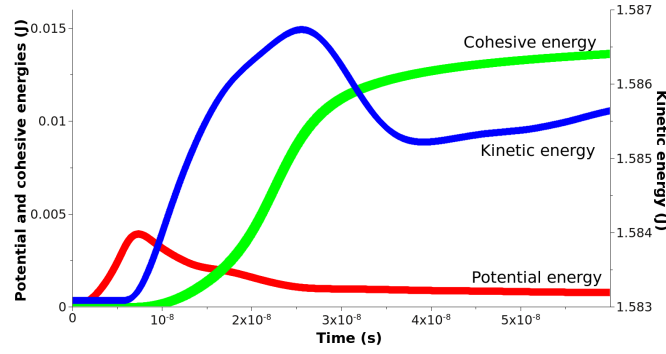
(b)

Figure 4.8: Evolution of the kinetic, potential, and cohesive energies (a) in quasi-statics ($\dot{\varepsilon} = 10 \ s^{-1}$) ,(b) in dynamics ($\dot{\varepsilon} = 10^5 \ s^{-1}$). The left (resp. right) scale is associated to the potential and cohesive energies (resp. kinetic energy).
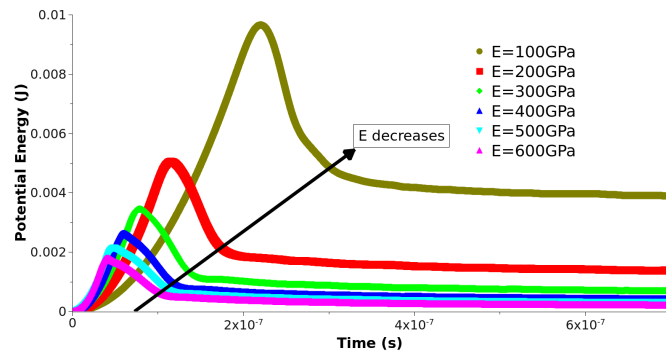
Figure 4.9: Effect of Young's modulus on potential energy. It mostly affects the value of the peak potential energy, and a fortiori, the time needed to reach it.

4.2.2.3   Brittleness/ductility

The mechanisms in brittle and ductile failure are distinct. By varying the tough-
ness G_c, we can simulate both fragmentation responses. Figure 4.10 (identical mesh,
other material properties, and strain rate as in previous paragraph) highlights the
effect of the toughness on potential energy. Naturally, since it is only related to
failure energy dissipation, toughness does not influence pre-peak behavior. Post-
peak behavior is, however, highly dependent upon toughness. For ductile materials,
the process is 'slow', while it is 'rapid' for brittle materials. This trend is pre-
dictable when referring to the characteristic time scale defined by Camacho and
Ortiz [Camacho 1996]:

$$t_0 = \frac{G_c\ E}{c\ \sigma_c^2} \tag{4.5}$$

t_0 is a material parameter, which embodies the time needed by a cohesive element
to fully open. Large toughnesses are associated to high values of t_0 and thus to slow
responses. The demonstration of the expression of t_0 is based on energy balanced
and addressed in chapter 7.
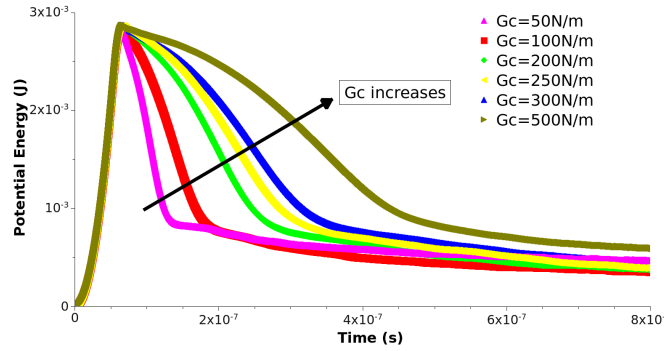
Figure 4.10: Effect of toughness on potential energy. It is mostly significant after
peak stress.

In addition, we compare in figure 4.11 the evolutions of potential, kinetic, and
cohesive energies for brittle ($G_c = 5N/m$) and ductile ($G_c = 500N/m$) materials.
Figure 4.11(a) highlights that brittle failure dissipation equally originates at direct
and indirect conversions of potential energy. We recall that direct refers to the
conversion of stored potential energy into failure, while indirect means that external
work is converted into kinetic energy, which is in turn converted into potential
energy, and into failure. Reversely, in the ductile case, dissipated energy is mostly
due to indirect conversion. Kinetic energy mostly supplies failure because ductile
process is 'slow' enough to allow this process. Moreover, since each crack may
dissipate ten times more energy in ductile than brittle failure, the final value of the
cohesive energy is larger in ductile fragmentation ($E_{coh,fin} = 3\ mJ$ for the brittle
material, and $E_{coh,fin} = 38\ mJ$ for the ductile material). In order to counter this

lack of energy dissipation, brittle fragmentation generally leads to more fragments, but this is insufficient to compensate the difference in energy.

(a)

(b)
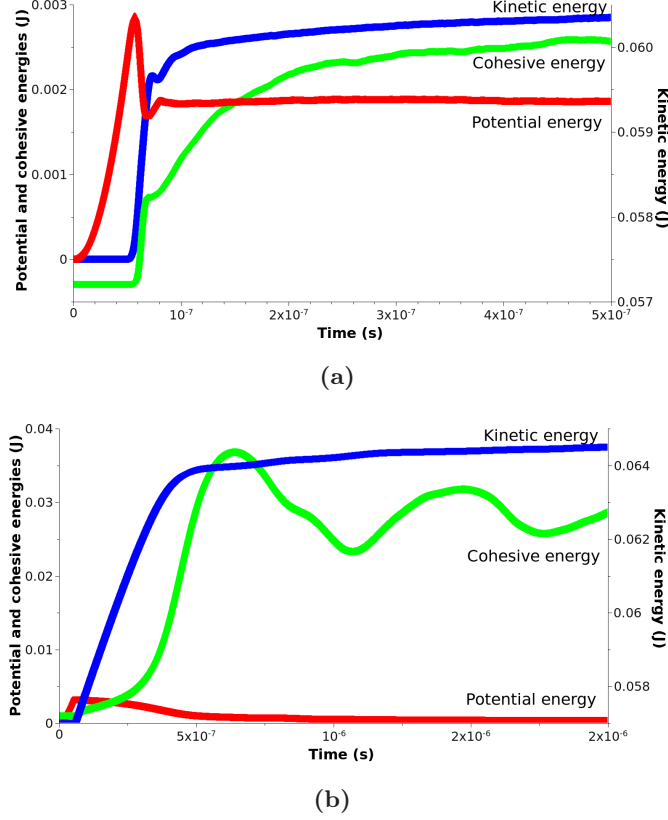
Figure 4.11: Evolution of the kinetic, potential, and cohesive energies (a) for a brittle material ($G_c = 5 \ N/m$), (b) for a ductile material ($G_c = 500 \ N/m$). The left (resp. right) scale is associated to the potential and cohesive energies (resp. kinetic energy).

4.2.2.4 Microstructural heterogeneity

Studying extensively the effect of microstructural heterogeneity on fragmentation will require several full chapters. In this section, we only give a glimpse at the influence of heterogeneity on potential and cohesive energies. One possible way of controlling heterogeneity is to select a Weibull distribution of cohesive strengths, with given minimum value $\sigma_{c,min}$, Weibull modulus m, and variable scale parameter $\sigma_{c,0}$:

$$F(\sigma) = 1 - e^{-\left(\frac{\sigma_c - \sigma_{c,min}}{\sigma_{c,0}}\right)^m} \tag{4.6}$$

For instance, let us select $\sigma_{c,min} = 260 MPa$, $m = 2$, and two values of the scale parameter, $\sigma_{c,0} = 50 \ MPa$ and $\sigma_{c,0} = 500 \ MPa$. This results in two distinct distri-

butions of defects, as highlighted by figure 4.12. To simplify comparison, we name thereafter 'homogeneous' and 'heterogeneous' (although the 'homogeneous' material is not strictly homogeneous). Since they have the same weakest link, fragmentation initiates at the same time in both cases.
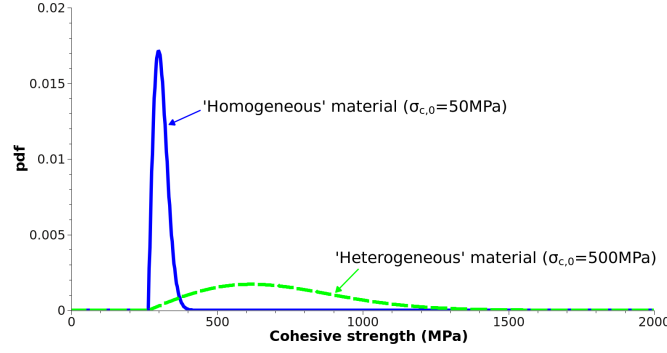
Figure 4.12: Weibull distribution of defects for 'homogeneous' and 'heterogeneous' materials.

Figure 4.13 displays the evolution of the potential and cohesive energies for these two materials. Since the simulations were run for the same mesh and same input parameters (except $\sigma_{c,0}$), the values of these energies can be directly compared to each other. Peak potential energy is higher for the 'heterogeneous' material since its distribution of cohesive strengths reaches larger values. Moreover, the value of the cohesive energy is rather close. It indicates that, in the case of 'heterogeneous' material, dissipation is supplied by potential energy (direct conversion), whereas for 'homogeneous materials', kinetic energy mostly contributes to it (indirect dissipation).

Moreover, the number of broken edges at the end of the simulation is about the same for both material (about 22000), whereas the number of damaged edges is higher for the 'homogeneous' material. For the 'homogeneous' (resp. 'heterogeneous') material, there are 81993 (resp. 42655) damaged but not broken edges. More generally, for a given set of parameters (bulk, strain rate, and toughness), the number of broken edges is roughly independent from the heterogeneity of the material, while the number of damaged edges decreases if scale parameter increases (e.g. if heterogeneity increases). As a result, 'heterogeneous' materials lead to fewer damaged edges but have a larger final cohesive energy than the 'homogeneous' materials ($E_{coh}^{fin} = 6$ mJ for the homogeneous material, while $E_{coh}^{fin} = 9$ mJ for the heterogeneous material). This apparent contradiction suggests that the rate of defect initiation is higher for 'homogeneous' materials (among which many defects are activated simultaneously), and that those initiated defects are barely damaged.
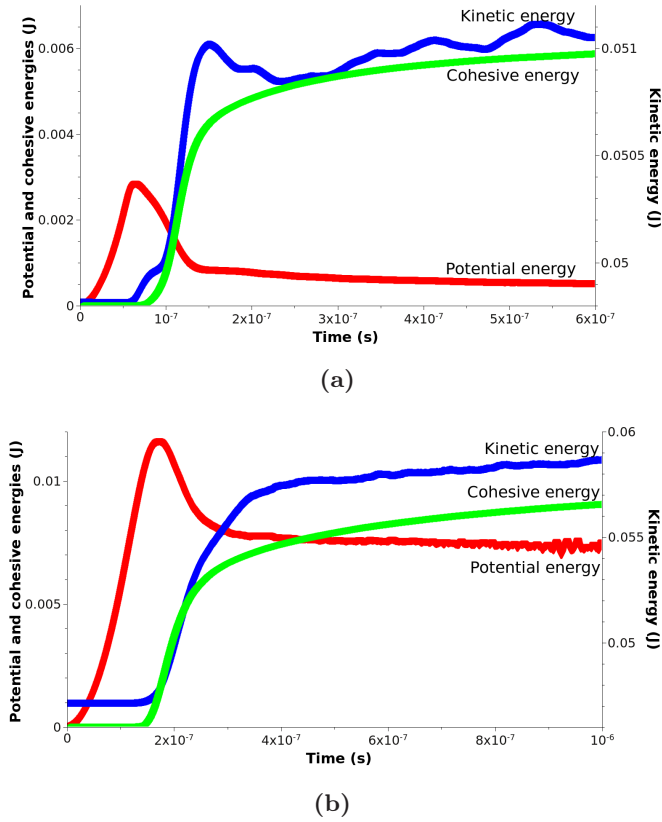
Figure 4.13:   Evolution of the kinetic, potential, and cohesive energies (a) for a homogeneous material ($\sigma_{c,0} = 50\ MPa$), (b) for a heterogeneous material ($\sigma_{c,0} = 500\ MPa$). The left (resp. right) scale is associated to the potential and cohesive energies (resp. kinetic energy).

4.3   Summary

To understand fragmentation mechanisms, both dynamic and energetic arguments must be accounted for. The dynamics of stress waves are highly non-linear and cannot be calculated analytically. We have shown, via numerical simulations and qualitative explanations, that stress wave effects are dependent upon multiple parameters, among them strain rate, wave speed, specimen geometry, toughness, and defects. Stress waves are the vector of crack interactions. They broadcast information concerning the stress field state. Since they need some time to travel, there exists a delay between the time of occurrence of a given event, and the time at which information has been actually transmitted to the rest of the structure. This delay is significant in dynamics and negligible in quasi-statics.

Two interacting waves lead to new waves whose amplitudes can either be larger or smaller than the initial ones. These new waves constitute the secondary wave network. They propagate, interact, and passes several times through the defects. We quantified the role of this multiple passing, e.g. of secondary waves in the fragmentation of a bar. For homogeneous materials at any strain rate, as well as at very high strain rates for any materials, secondary waves have negligible effects. They are significant at intermediate and low strain rates, for heterogeneous materials, though. Consequently, it is essential to include wave mechanics into numerical codes. Obscuration zone models cannot capture the full amount of dissipated energy.

Finally, we also focused on energy conversion. For every boundary conditions, potential energy first increases, reaches a peak, and decreases. Some material parameters mostly affect pre-peak response (Young's modulus), some influence post-peak (toughness), others have clearly an effect on both (strain rate, heterogeneity). When studying energy transfers, two types of response arise. In the first, stored potential energy is sufficient to fragment the body (direct conversion for low strain rate, brittle, 'homogeneous' materials, etc.). In the second, part of the stored potential energy is employed in failure, but the major contribution stems from kinetic energy (indirect conversion for high strain rate, ductile, 'heterogeneous' materials, etc.).

Signature of defects in one-dimensional fragmentation

As pointed out in the previous chapters, defects play a critical role in the dynamic fragmentation of brittle materials. Cracks initiate at seemingly random locations, propagate and coalesce to form fragments. The process is accompanied by stress release waves, whose influence is difficult to account for without numerical analysis. In this chapter [1], we are using the coupled Finite Element - cohesive elements capability detailed in chapter 3 to relate the defect distribution contained in a material with the resulting number of fragments. In order to simplify the problem and focus solely on crack initiation, we consider a one-dimensional geometry. We select Mott's ring, in which contacts between fragments are limited and which periodicity facilitates physical understanding. We show how the left tail of the cohesive strength distribution, e.g. the number of large defects, determines the rate at which cracks are initiated and how it strongly controls the generation of stress release waves and fragmentation process. Our numerical calculations yield a new factor, which we label communication factor. It is used to normalize the average fragment size and to define a new scaling function of material properties, defect statistics and loading rate.

5.1 Synopsis of the study

5.1.1 Objectives

As detailed in chapter 2, a range of phenomenological, theoretical and numerical models have been pursued during the last decades to describe fragmentation. However, most of them consider fragmentation as a macroscopic process, without including the effect of the microstructure. In brittle fragmentation, defects play a key role: fracture sites are usually structural flaws. A defect is activated when the stress is locally high enough to destroy the cohesion of the material.

In quasi statics, the weakest link theory applies (see chapter 3): the weakest flaws initiate and slowly lead to failure with few crack interactions. In dynamics,

---

[1]This chapter has given rise to the journal article *S.Levy, J.F.Molinari, Dynamic fragmentation of ceramics, signature of defects and scaling of fragment sizes, Journal of the Mechanics and Physics of Solids, 58(1), 12-26, 2010*

numerous flaws are activated and interact through a complex network of stress waves. Each damaged defect opens and generates stress release waves that protect the encompassed neighboring regions. When many defects open, stress waves are generated simultaneously, propagate, and interact. The behavior is then highly non linear (see chapter 4).

Hild and coworkers [Hild 2003] derived the expression of the tensile strength-rate corresponding to the transition quasi-statics to dynamics. However, they made a strong assumption: when an area is encompassed by stress waves, it is definitely protected from further damage. We underlined in chapter 4 the importance of the secondary waves. In some cases, they constitute the essential source of damage. The framework used here does account for these wave interactions. It allows us to investigate the role of defects within this network of stress release waves, as well as on fragment sizes.

Our objective is to extend the work of Zhou et al. [Zhou 2006a] by including defect distributions. We wish to analyze how defects influence the average fragment size in an idealized system, consisting of a ceramic ring under uniform expansion. The ring material is initially elastic, and is controlled by cohesive failure as soon as the stress field locally exceeds the strength of local flaws. The adopted numerical framework is the finite element method (chapter 3). The underlying question will be whether or not, despite the statistical complexity, our results can be synthesized in a simple normalized form, in which fragment statistics are made explicitly dependent upon material properties, flaw population, and loading parameters.

The chapter is structured as follows. First, we describe the expanding ring test. We also detail the randomly spaced defect characteristics. Then, we verify the numerical convergence of our results and discuss the influence of the population of defects (density and representative distribution). A full section is devoted to building a theoretical model which aims at describing the communication between microcrack sites. Finally, we propose new scaling parameters for heterogeneous fragmentation.

5.1.2   Description of the test and energy evolution

We study the fragmentation of a ring whose motion is imparted by some radial impulse or strain rate (fig.5.1):

$$\dot{\varepsilon} = \frac{\text{radial velocity}}{\text{ring radius}} \tag{5.1}$$

During the process, the input energy is converted into fracture energy, and into elastic and kinetic energies (due to the propagation of stress waves and to the global motion). In quasi statics, the elastic energy dominates and the weakest link theory

applies. On the contrary, the dynamic regime is governed by kinetic effects, which are arguably more challenging to understand. Therefore, our applications concentrate on strain rates ranging from $10^3 s^{-1}$ to $10^6 s^{-1}$. Moreover, we have chosen this test for its simplicity. The radial and periodic geometry limits boundary effects and contacts between fragments. The small thickness of the ring restricts the fragmentation process to crack initiation. Since crack propagation makes the physical understanding more complex, focusing on initiation rather than propagation is clearly an advantage to complete our objectives (crack propagation will be discussed in chapter 7).
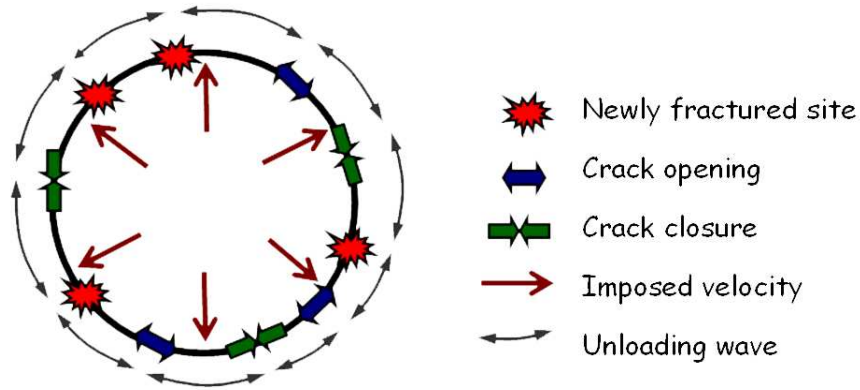
Figure 5.1: Schematic of the expanding ring test showing the development of a complex network of stress wave interactions.

Before fracture, the behavior is linear elastic and controlled by a finite element simulation. When the weakest defects are initiated, cohesive elements are inserted and stress release waves begin their propagation and interactions. Depending on the local stress, cracks may nucleate, grow, or close (chapter 3). As soon as one link is completely broken, the expansion of the ring is not constrained anymore: inertial effects govern the evolution of the fragmentation. While the ring continues expanding, cracks keep evolving and interacting until the fragmentation process is stabilized.

5.1.3   Modeling the initial distribution of defects

Every material is inherently imperfect; defects are distributed among its volume. Each defect is naturally associated to a failure strength, which we refer to as its cohesive strength σ_c (see chapter 3). It designates the stress activation threshold required to initiate fracture, and its value depends on its shape, size and orientation. A defect with low failure strength is weak, while a defect with large failure strength has a low probability of failure. Since each defect is affiliated to a value of σ_c,
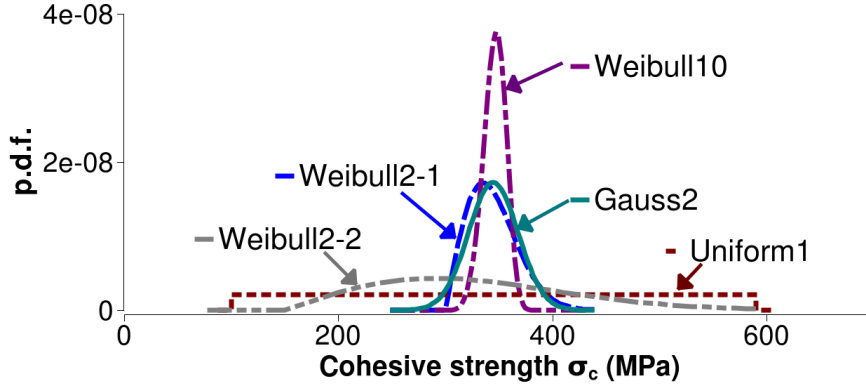
Figure 5.2: Some realizations of cohesive strengths (p.d.f.).

statistical heterogeneity is introduced with a distribution of σ_c. A population of defects is thus characterized by:

1. the number of defects N_{def}, or the defect density L_{ring}/N_{def}

2. the type of the distribution of defects (normal, uniform, ...)

3. the mean μ and the standard deviation υ of the distribution

Choosing an adequate distribution is not obvious. We have focused on the uniform distribution which is not realistic, but whose simple shape helps build a physical understanding. Then, we have compared our results to Gaussian and Weibull distributions, which have been shown to be a physical representation of the defects (chapter 3). These choices were made in respect to the weakest link theory and to extreme value statistics [Leadbetter 1983]. The cumulative density function of the Weibull distribution is defined by:

$$F(\sigma_c) = 1 - e^{-\left(\frac{\sigma_c - \sigma_{c,min}}{\lambda}\right)^m} \tag{5.2}$$

where λ is the scale parameter, m is the shape parameter or Weibull modulus, and $\sigma_{c,min}$ is the minimum value of the cohesive strengths.

In this chapter, several distributions of defects are thus tested. Table 5.1 details their mathematical characteristics. Figure 5.2 illustrates some of the probability density functions (p.d.f.). The chosen Weibull distributions, which are considered by the community to be realistic mathematical models for defects, cover a wide range of standard deviations and Weibull moduli.

Distribution	Gauss2	Weibull2-1	Weibull2-2	Weibull10	Weibull20	Uniform1	Uniform20
Mean μ	345	345	327	347	348	345	348
Standard deviation v	23.2	23.2	95.7	5.7	3.0	140.0	3.0
Minimum value	x	300	150	300	300	102.5	342.8
Weibull modulus m	x	2	2	10	20	x	x
Scale parameter λ	x	5	200	5	5	x	x

Table 5.1: Theoretical characteristics of the defect distributions. Stresses are expressed in MPa.

5.2 Brief review of prior theories

In this section, we recall the theory derived by Grady [Grady 1982], extended by Glenn and Chudnovsky [Glenn 1986a], and the recent numerical results of Zhou et al. [Zhou 2006c]. Other models are detailed in chapter 2. The three selected models propose a law relating the number of fragments and the strain rate in the case of the fragmentation of a homogeneous material. The fracture energy G_c and the cohesive strength σ_c are thus independent from the spatial coordinates, and each fracture site dissipates the same amount of energy G_c.

Grady, and Glenn and Chudnovsky had recourse to an energy argument to derive the expression of the average fragment size. Employing the cohesive methodology, Zhou et al. detailed the effect of wave interactions and normalized their results, making implicit the dependence on material parameters in a simple equation [Zhou 2006c]. The normalization involves three relevant parameters: s_0, t_0 and $\dot{\varepsilon}_0$. The characteristic length s_0 represents *the size of a fragment in quasi statics*, when the applied potential energy is fully converted into fracture energy. This length s_0 is directly related to the characteristic time t_0 defined by Camacho and Ortiz [Camacho 1996]. This time t_0 expresses *the time needed by the waves, released by a cohesive element, to fully encompass s_0*. Another relevant parameter is the characteristic strain rate $\dot{\varepsilon}_0$ defined by Drugan [Drugan 2001]. A possible interpretation relates $\dot{\varepsilon}_0$ and t_0: t_0 *is the time needed by the cohesive element to fully open when submitted to $\dot{\varepsilon}_0$*. The analytical expressions of these three representative parameters are:

$$t_0 = \frac{E\,G_c}{\sigma_c^2\,c} \tag{5.3}$$

$$s_0 = c\,t_0 \tag{5.4}$$

$$\dot{\varepsilon}_0 = \frac{\sigma_c}{E\,t_0} \tag{5.5}$$

Note that t_0 has the same expression as in equation 2.35. Figure 5.3 represents Grady's , Glenn and Chudnovsky's, and Zhou et al.'s models with normalized axes. The normalized strain rate and the normalized average fragment size are defined in [Zhou 2006c] by:

$$\bar{s} = \frac{s}{s_0} \quad \text{and} \quad \bar{\dot{\varepsilon}} = \frac{\dot{\varepsilon}}{\dot{\varepsilon}_0} \tag{5.6}$$

Using this notation, our reference equations are the two theoretical models based on energy conservation (eq.5.7 and eq.5.8) and the numerical model, which includes wave propagation and dynamic effects (eq.5.9):

$$\text{Grady's model}: \quad \bar{s}_G = \left(\frac{24}{\bar{\dot{\varepsilon}}^2}\right)^{1/3} \tag{5.7}$$

$$\text{Glenn and Chudnovsky's model}: \quad \bar{s}_{GC} = \frac{4}{\bar{\dot{\varepsilon}}} sinh\left(\frac{1}{3}sinh^{-1}\left(\frac{3}{2}\bar{\dot{\varepsilon}}\right)\right) \tag{5.8}$$

$$\text{Zhou et al.'s model}: \quad \bar{s}_{ZMR} = \frac{4.5}{1 + 4.5\,\bar{\dot{\varepsilon}}^{2/3}} \tag{5.9}$$
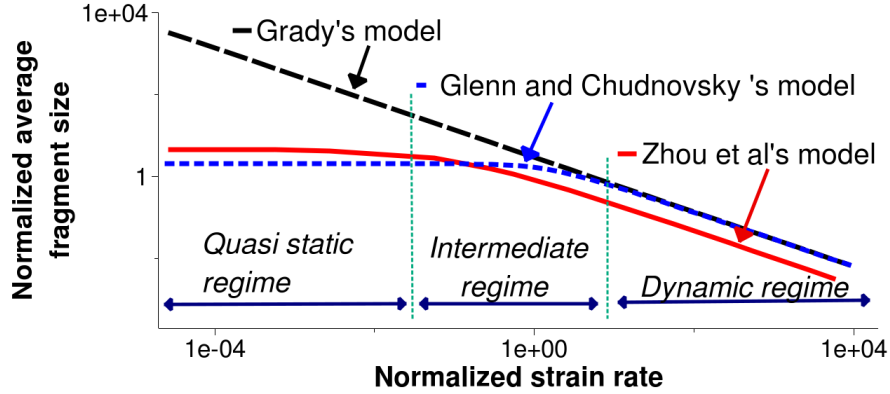
Figure 5.3: Reference models for homogeneous fragmentation.

Nevertheless, these normalizations only address the homogeneous case. Since we are dealing with a distribution of fracture toughnesses and a distribution of cohesive strengths, the parameters G_c and σ_c are not clearly defined anymore. In order to simplify the problem, we have constrained the parameter t_0 to be identical for every cohesive element. This implies that all the cohesive elements have the same intrinsic opening time. This choice facilitates the understanding of the phenomenon

without a too severe loss of generality. We still account for a distribution of σ_c and a distribution of G_c; the only difference is that they are linked to one another by:

$$\sigma_c = \sqrt{\frac{E}{s_0} G_c} \qquad (5.10)$$

To determine s_0, we have chosen the reference values $\sigma_{c0} = 300 \ MPa$ and $G_{c0} = 100 \ N.m^{-1}$.

5.3 Numerical convergence and defect density

5.3.1 Influence of the number of elements N_{FE}

Our finite elements discretization is controlled by two independent parameters: the number of elements of the finite element computation N_{FE}, and the number of defects N_{def}. Contrary to the number of defects N_{def} which is a physical parameter standing for the density of defects, the number of elements N_{FE} is purely numerical. It determines the numerical convergence of the simulations. In this section, we focus on the effect of N_{FE}. The next section is dedicated to studying the effect of N_{def}.

Verifying the numerical convergence usually consists in setting the number of defects N_{def} to given values and varying the number of elements N_{FE}. This convergence issue has already been addressed for homogeneous materials in [Gao 2004, Raghupathy 2006], but, as far as we know, has not be dealt for heterogeneous materials. The following figure 5.4 underlines that, for a given number of defects N_{def}, the number of fragments N_{frag} is a slightly decreasing function of the number of elements, as long as the mesh is fine enough. For instance, when $N_{def} = 8000$, the number of fragments varies from 1485 ($N_{FE} = 20000$) to 1461 ($N_{FE} = 35000$). Each point corresponds to one simulation carried out at the strain rate $10^6 s^{-1}$ for a Gaussian distribution with mean $\mu = 345 \ MPa$ and standard deviation $\upsilon = 23.2 \ MPa$ (*Gauss2* in table 5.1).

As a result, we have set the number of elements N_{FE} to 30000, which guarantees the convergence for every strain rate lower than $10^6 s^{-1}$. Besides, one should note that, when the number of elements N_{FE} and the number of defects N_{def} have close values, the numerical simulations are very unstable and generally lead to the full explosion of the ring, breaking all the cohesive elements. In general, it is advised to set:

$$N_{FE} > 2.5 \ N_{def}$$

Convergence can also be verified by varying the number of elements N_{FE}, while keeping the ratio N_{def}/N_{FE} constant. Figure 5.5 underscores that the convergence is guaranteed for the four tested ratios. The rate of convergence is lower for small
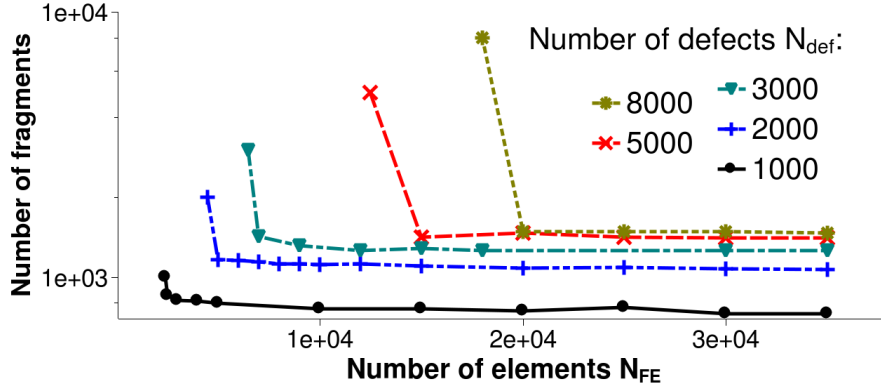
Figure 5.4: Numerical convergence of the number of fragments N_{frag} for a constant number of defects N_{def}. For every N_{def}, if N_{FE} is not large enough, N_{frag} depends on N_{FE}.

ratios because the number of defects increases slower. As explained in the following section 5.3.2, the converged number of fragments depends on the ratio because of defect density effect.
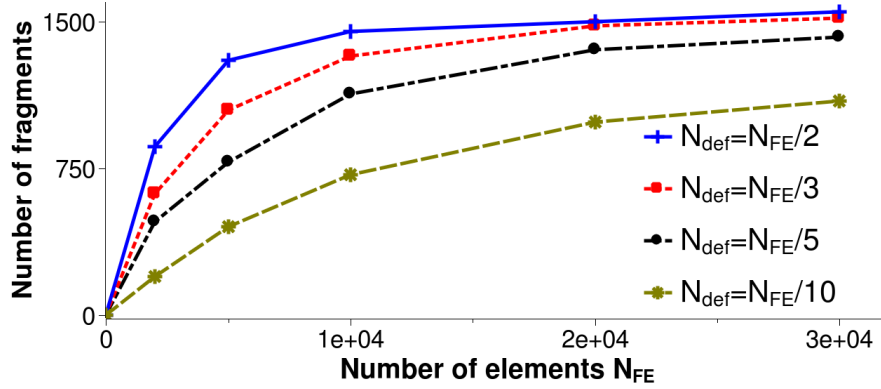
Figure 5.5: Numerical convergence of the number of fragments N_{frag} for a constant ratio N_{def}/N_{FE}. If the proportion of the defects (in comparison to the elements) is low, the increase in N_{frag} is slow. To have a sufficiently rapid convergence, we suggest to take $N_{FE} > 2.5\, N_{def}$.

5.3.2   Influence of the number of defects N_{def}

5.3.2.1   Proportion of the broken defects N_{def}^{broken}

In this section, we look at the influence of the number of defects on the fragmentation process. We set the number of elements to 30000, and the p.d.f. of the

initial distribution to be Gaussian, with mean $\mu = 345\ MPa$ and standard deviation $\upsilon = 23.2\ MPa$ (*Gauss2* in table 5.1). We let the number of defects N_{def} vary, and we count the number of fragments N_{frag}. If there are few initial defects in the ring, they will all break. However, if we consider a higher defect density, only a part of the defects will break while the rest will get partially damaged or will remain fully intact.

Figure 5.6 plots the number of fragments N_{frag} versus the number of defects N_{def}. As there is only one element in the thickness, we can easily relate the number of fragments and the number of broken defects:

$$N_{frag} = N_{def}^{broken} + 1 \tag{5.11}$$
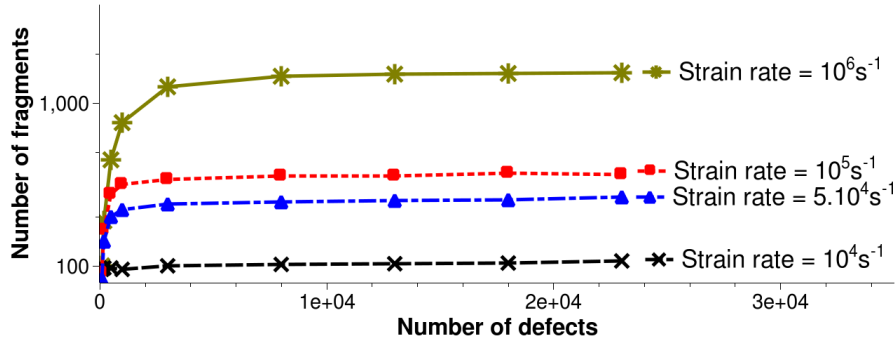
Figure 5.6: Evolution of the number of fragments with the number of defects.

Figure 5.7 represents the evolution of the ratio $\frac{E_{diss}}{E_{diss}+E_{rec}}$ with the number of defects. The *total cohesive energy* stands for the sum of dissipated and recoverable energies ($E_{diss} + E_{rec}$). Obviously, the curves in figure 5.6 are monotonically increasing, while they are monotonically decreasing in figure 5.7. The proportion of the dissipated cohesive energy with respect to the total cohesive energy gets smaller as the number of defects, or number of potential dissipative links, increases. Three phases arise:

i. All the defects break: $N_{def} \simeq N_{def}^{broken}$. The total cohesive energy takes mainly the form of dissipated energy, which means that there are only a few cohesive elements that store recoverable energy, or that only a few defects are partially damaged. Most of them are fully broken.

ii. Defects are either broken or damaged: $N_{def} \simeq N_{def}^{broken} + N_{def}^{damaged}$. The cohesive energy is divided into recoverable and dissipated energies.

iii. Defects are either broken, damaged, or intact: $N_{def} = N_{def}^{broken} + N_{def}^{damaged} + N_{def}^{intact}$. Rising N_{def} does not affect significantly N_{def}^{broken} anymore. Figure 5.7

underlines that the proportion of the recoverable and the dissipated energies is also stable. This steady value depends on the strain rate, which appears to be a decreasing function of the strain rate. For instance, when $\dot{\varepsilon} = 10^4 s^{-1}$, it is about 0.70, while $\dot{\varepsilon} = 10^6 s^{-1}$ leads to a value of 0.62. At a given strain rate, it guarantees that raising the number of defects in the ring has no effect neither on N_{def}^{broken} nor on $N_{def}^{damaged}$.

The steady regime *iii* is a consequence of stress wave relaxation. Indeed, each damaged fracture site releases a wave that unloads partially the encompassed regions. The fragmentation process reaches its final state when the waves have sufficiently unloaded the body. As a result, with increasing number of defects, more sites possibly become damaged and release stress waves. This amounts to a faster fragmentation process. Since it cannot be infinitely short, the process characteristic time reaches a lower value, irrespective to the number of defects. Hence, in this regime, increasing the number of defects does not alter the final stage.

In practice, working on the steady phase *iii* requires to have enough defects on the ring. The transition value between phase *ii* and phase *iii* depends on the strain rate. In phase *iii*, any rise in the number of initial defects will have no consequence in the results, in terms of number of fragments and cohesive energies. In the following sections, the number of defects is set such that we are certain to work in phase *iii*, keeping in mind that the simulation duration increases with the number of initial defects.
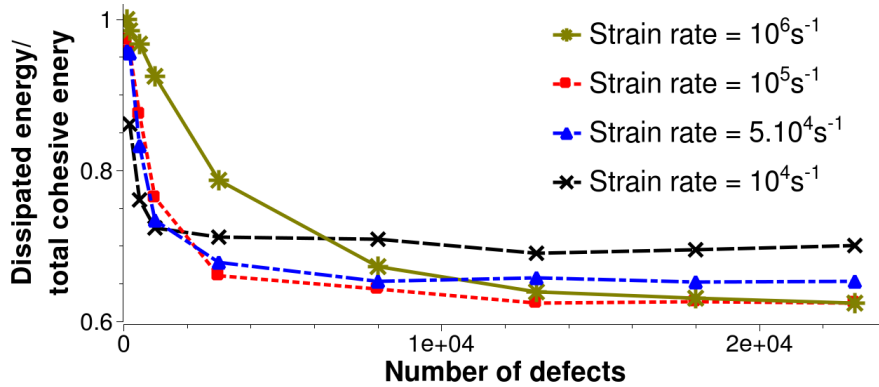
Figure 5.7: Evolution of the rate of the dissipated cohesive energy and the total cohesive energy, with the number of fragments.

5.3.2.2 Representation in terms of average fragment size

In order to compare our results to Grady's and Zhou et al.'s models, we have normalized the axes following section 5.2, *considering that the material is homo-*

geneous. This hypothesis is evidently wrong, but is a priori necessary to compare results. The issue of normalization for heterogeneous materials is handled in section 5.5. Figure 5.8 represents the evolution of the normalized average fragment size versus the normalized strain rate, for different values of N_{def}.
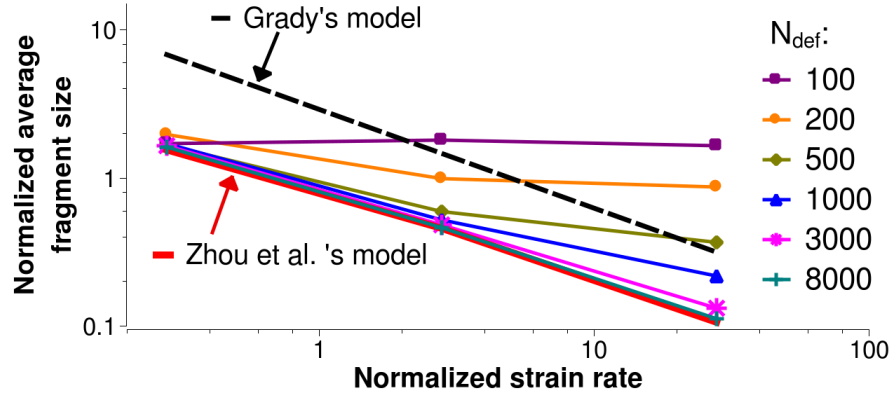
Figure 5.8: Normalized representation of the average fragment size for several numbers of defects.

We underline the influence of N_{def} by computing the average slope of each plot, and compare it to Grady's model. Figure 5.9 illustrates that it is a monotonically decreasing function with an asymptotic limit. For $N_{def} = 100$, the slope is close to zero which expresses that all the defects are broken (phase *i*). As N_{def} increases, the slope decreases (phase *ii*) until it reaches the steady region for $N_{def} \geq 10000$ (phase *iii*). Although this asymptotic value is slightly different from Grady's, his minus two-thirds theoretical prediction appears to be a very good approximation for the present one-dimensional test.
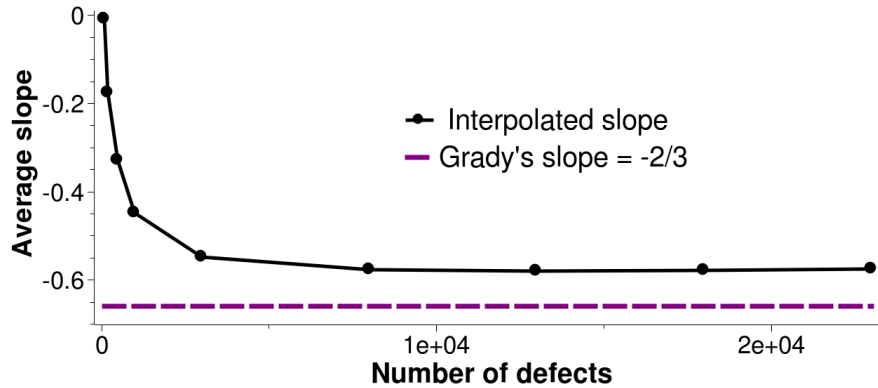
Figure 5.9: Evolution of the average slope of the plots in fig.5.8 in the dynamic regime, with the number of defects.

5.4   Keys to understand communication between defects

5.4.1   Qualitative understanding

Being able to predict how crack interactions affect fragmentation is challenging. In this chapter, we take advantage from the simplicity of the expanding ring test to develop a comprehensive measure of crack interactions. When the ring fragments, some defects are initiated, they open and release stress waves that propagate and protect the encompassed regions. An opening defect interacts with its neighbors through these waves. If they propagate fast, the waves encompass a large region which may prevent numerous defects from getting damaged. Hild et al. [Hild 2003] went further by considering that once a defect is encompassed by a wave, it is definitively protected and cannot get damaged anymore. In this case, the communication between defects is then prevailing. We call it the *extremely communicative* process. On the contrary, if they propagate slowly, fewer defects are encompassed, and little interactions take place: the communication is inconsequential. This *without communication* approach was derived by Grady whose pioneering energy theory [Grady 1982, Grady 1988] does not include any crack interactions. The next paragraphs are dedicated to compare these two extreme behaviors in order to quantify the degree of communication for any non-extreme case.

5.4.1.1   Characterization of the communication extreme cases

Without communication: The stress waves are propagating slowly, compared to the crack opening, and do not have time to transmit the information. Consequently, each fracture site behaves independently from the others. The time associated to the crack opening t_0 is much smaller than the characteristic wave propagation time L_{ring}/c. In the *non communicative* fragmentation case, the weakest flaw first is initiated; then, since they do not interact, the second weakest flaw gets initiated, then the third. The process continues until all the fracture energy is dissipated. Only the weakest defects are damaged (fig.5.10). Instantaneous crack opening, extremely slow wave propagation, fragility, and absence of communication are thus directly related. Moreover, when a weak defect breaks, it releases a small amount of energy which is proportional to its associated σ_c (eq.5.10). Dissipating totally the input strain energy will thus require the activation of numerous flaws. The *non communicative* process may consequently generate "numerous" fragments.

With intense communications: Defects communicate intensively through stress waves that are propagating fast in comparison to the crack opening. The time associated to the crack opening t_0 is thus much larger than the characteristic wave propagating time L_{ring}/c. When the stress waves propagate fast enough, they encompass defects that are associated to any critical failure strength σ_c. Weakest and strong defects may either be protected or damaged, depending on whether or not they have been encompassed by a stress release wave (fig.5.10). Slow crack opening, fast wave

propagation, ductility, and high communication rate are thus associated. Moreover, considering that a strong defect breakage releases a large amount of energy, this *intensely communicative* process may result in a "small" number of fragments.

Effective wave speed: Hence, the same opening time t_0 and the same wave speed c can lead to two opposite behaviors. One possible way of taking this remark into account is to define an effective wave speed c_{eff}. It measures the interactions between defects during any fragmentation process. The following paragraphs are dedicated to define and quantify it.
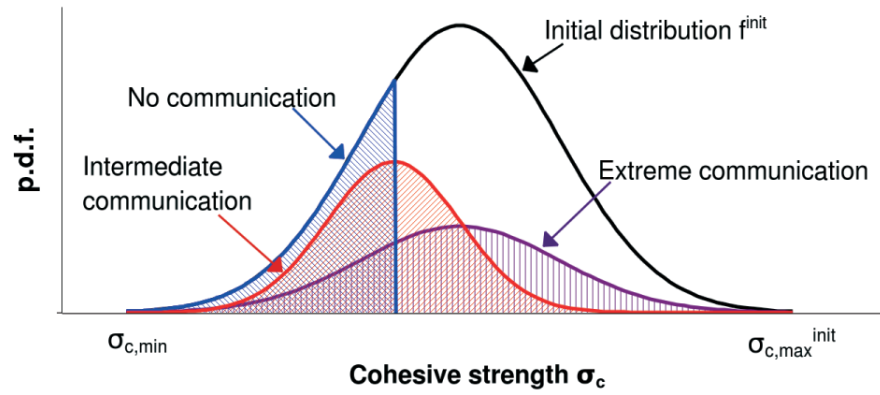
Figure 5.10: Schematic of the broken defects, within the same initial distribution: the *extremely communicative*, the *without communication* and one possibly real cases. Note: $\sigma_{c,min} = \sigma_{c,min}^{init} = \sigma_{c,min}^{broken}$ and $\sigma_{c,max}^{init} \neq \sigma_{c,max}^{broken}$.

5.4.1.2 Definition of relevant parameters

Figure 5.10 illustrates an initial probability density function f^{init}, the two extreme cases previously detailed, and an intermediate possibly real one (the hatched curves do not represent p.d.f. because their area is smaller than one) . The hatched areas represent the proportion of the broken defects, and are related to the number of defects N_{def} and the number of fragments N_{frag}. We denote these areas by α:

$$\alpha = \frac{N_{frag}}{N_{def}} \tag{5.12}$$

Contrary to the weakest link which is always activated, the communication affects the average and the maximum failure strengths of the broken defects, respectively denoted μ^{broken} and $\sigma_{c,max}^{broken}$. A small $\sigma_{c,max}^{broken}$ expresses a low communication rate, while a large one underscores that interactions are prevailing. The two extreme cases follow therefore the properties:

Without communication process:
$$\begin{cases} \sigma_{c,min}^{broken} = \sigma_{c,min}^{init} = \sigma_{c,min} \\ \mu^{broken} \ < \ \mu^{init} \\ \sigma_{c,max}^{broken} \ < \ \sigma_{c,max}^{init} \\ f^{broken} = \begin{cases} \frac{f^{init}}{\alpha} & if \quad \sigma_c < \sigma_{c,max}^{broken} \\ 0 & otherwise \end{cases} \\ \alpha = \int_{\sigma_{c,min}}^{\sigma_{c,max}^{broken}} f^{init} \end{cases}$$

Extremely communicative process:
$$\begin{cases} \sigma_{c,min}^{broken} = \sigma_{c,min}^{init} = \sigma_{c,min} \\ \mu^{broken} \simeq \mu^{init} \\ \sigma_{c,max}^{broken} \simeq \sigma_{c,max}^{init} \\ f^{broken} \simeq f^{init} \end{cases}$$

$$(5.13)$$

In the following section, we will therefore focus on α, $\sigma_{c,min}$, μ^{init} and μ^{broken} by studying the evolution of the function Ψ defined by:

$$\begin{aligned} \Psi : \quad [0 \ , \ 1] \quad &\to \quad [0 \ , \ 1] \\ \alpha \quad &\to \quad \frac{\mu^{broken} - \sigma_{c,min}}{\mu^{init} - \sigma_{c,min}} \end{aligned} \qquad (5.14)$$

The variation of the parameter α can be achieved either by changing the number of initial defects N_{def}, or by changing the strain rate $\dot{\varepsilon}$ which affects the number of fragments N_{frag}. We have also studied the evolution of the maximum and the standard deviation of the broken distribution, and have drawn similar conclusions than the ones detailed in the following.

5.4.2   Quantitative measure of the communication between defects

5.4.2.1   Studied distributions

We now vary the initial p.d.f. and compare the degree of communication they result in. For each of initial p.d.f. f^{init}, we expect the numerical simulations to lead to a p.d.f. of the broken defects f^{broken} with a communication rate between the two previously described extreme cases. The results obtained for three different initial p.d.f. f^{init} (figure 5.2) are presented here:

- A uniform distribution with a large standard deviation $v^{init} = 140 \ MPa$ and a mean $\mu^{init} = 345 \ MPa$. It corresponds to the case *Uniform1* in table 5.1. The slope of the p.d.f. is zero everywhere, except at the minimum and the maximum values $\sigma_{c,min}^{init}$ and $\sigma_{c,max}^{init}$ where it is infinite. This high slope at $\sigma_{c,min}^{init} = 102.5 \ MPa$ should lead to the activation of many defects at the

same instant, so that they may not have time to communicate. This large activation rate should thus result in a low communication rate.

- A Gaussian distribution with a standard deviation $v^{init} = 23.2\ MPa$ and a mean $\mu^{init} = 345\ MPa$. It corresponds to the case *Gauss2* in table 5.1. Since the slope at $\sigma_{c,min}^{init} \simeq 245\ MPa$ is nearly zero, it tends to smooth the fragmentation process, and the interactions should have time to establish. This low activation rate of defects should thus result in a large communication rate.

- A Weibull distribution with a standard deviation $v^{init} = 23.2\ MPa$ and a mean $\mu^{init} = 345\ MPa$. It corresponds to the case *Weibull2-1* in table 5.1. This p.d.f. should lead to an intermediate behavior since the slope at $\sigma_{c,min}^{init} = 300\ MPa$ is comprised between zero and infinity.

Besides, in order to justify more rigorously the influence of the slope of f^{init} at $\sigma_{c,min}^{init}$, we have also tested the distributions represented in figure 5.11. Although they do not probably correspond to any real distribution of defects, these p.d.f. highlight the qualitative trend which relates the communication behavior to the rate of insertion of cohesive elements, and to the slope of f^{init} at $\sigma_{c,min}^{init}$. We set $\sigma_{c,min}^{init} = 307\ MPa$, $\sigma_{c,max}^{init} = 381\ MPa$ and vary the intermediate $\sigma_{c,intermediate}^{init}$ such that:

$$\sigma_{c,intermediate}^{init} = \sigma_{c,min}\ +\ \beta\ \left(\sigma_{c,max}^{init} - \sigma_{c,min}\right) \qquad \text{where } \beta \in [0\ ,\ 1] \qquad (5.15)$$
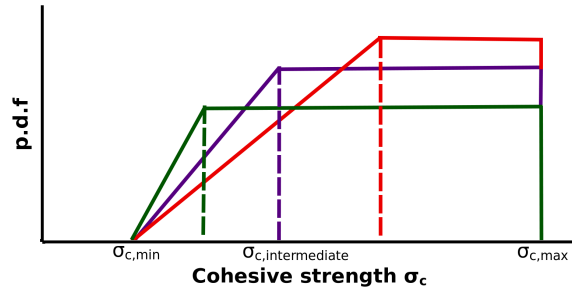
Figure 5.11: Schematic of the initial distributions of defects generated to control the influence of the slope at $\sigma_{c,min}$ on the communication behavior.

5.4.2.2 Definition and determination of the communication parameter

Our main concern is the study of the monotonously increasing function Ψ (eq. 5.14) with the aim at determining a relevant communication parameter. Evidently, $\Psi(0) = 0$ and $\Psi(1) = 1$. Figure 5.12 underlines that, depending on the communication rate, several curves may link these two points. In the case of *intense communication*, we have shown that $\sigma_{c,max}^{broken} \simeq \sigma_{c,max}^{init}$, which corresponds to a Heaviside

step function . Reversely, the case *without communication* links directly the value of α with the p.d.f. f^{init} (eq.5.13). For instance, a uniform p.d.f. f^{init} theoretically coincides with the bisector function (fig. 5.12).
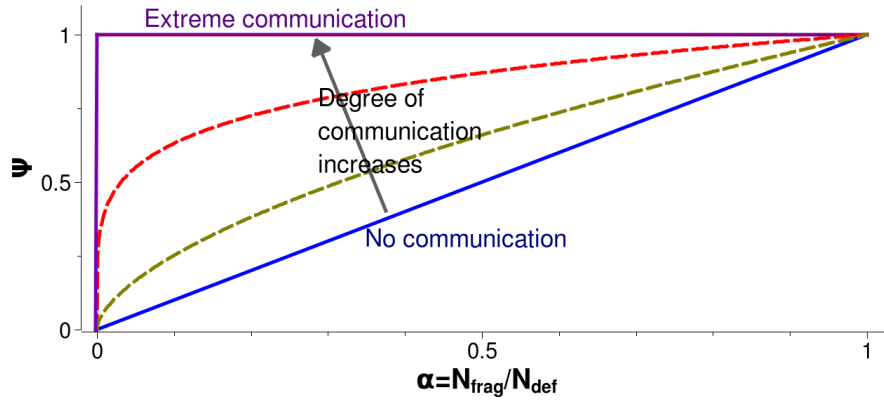
Figure 5.12: Schematic of the theoretical effect of the communication rate on the function Ψ for a uniform initial distribution of defects f^{init}.

From a mathematical point of view, monotonically decreasing p.d.f. can lead to convex curve. However, such p.d.f. seem to have no physical meaning: a monotonically decreasing p.d.f f^{init} refers to a material which has more weakest links than strong ones. Since brittle materials usually exhibit more macroscopic than microscopic defects, we have limited our study to p.d.f leading to concave curves, as shown in figure 5.12.

Intermediate behaviors are situated between these two extreme cases. In order to characterize the function Ψ, several tests are carried out for the same initial distribution f^{init} and several values of α. In figure 5.13, the initial distribution is Gaussian with mean $\mu^{init} = 345\ MPa$ and standard deviation $v^{init} = 23.2\ MPa$ (*Gauss2* in table 5.1). $\alpha = 1$ represents the initial distribution f^{init}, and the three other values ($\alpha = 0.1, \alpha = 0.05, \alpha = 0.02$) result from a change in the strain rate and hence, in the number of fragments N_{frag}.

Figure 5.14 plots the functions Ψ associated to the four distributions *Uniform1*, *Weibull2-1*, *Gauss2* (table 5.1) and $\beta = 0.4$ (eq.5.15). Each numerical test results in one point, the dotted lines are the fitting functions. Power laws appear to be
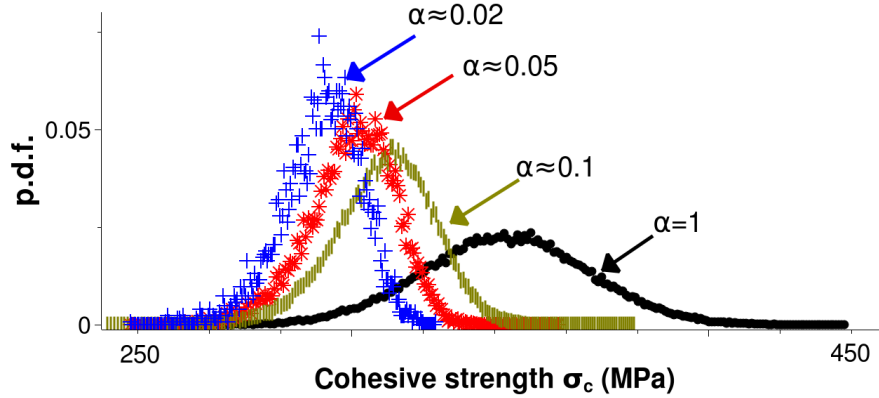
Figure 5.13: Influence of $\alpha = \frac{N_{frag}}{N_{def}}$ on the broken p.d.f., for an initial Gaussian p.d.f..

adequate approximations and lead to:

$$\forall f^{init}, \ \exists \, a \in [0,1], \ \forall \, \alpha \in [0,1], \ \Psi(\alpha) = \alpha^a$$

$$\text{where } a = \begin{cases} 0.20 & \text{for Gauss2} \\ 0.30 & \text{for } \beta = 0.4 \\ 0.65 & \text{for Weibull2-1} \\ 0.75 & \text{for Uniform1} \end{cases} \tag{5.16}$$

The distribution *Gauss2* leads thus to a more communicative process than the *Weibull2-1* and the *Uniform1* distributions. Since the values of the *Gauss2* weakest links vary regularly, their activation is not instantaneous, the stress waves have time to propagate and influence the neighboring defects. The slope of the p.d.f. f^{init} appears to be essential in the communication process. This is confirmed by the $\beta = 0.4$ distribution (eq.5.15) which slope at $\sigma_{c,min}$ is comprised between the *Gauss2*'s and the *Weibull2-1*'s slopes.

In conclusion, the p.d.f. strongly influences the fragmentation process. The slope at $\sigma_{c,min}$ plays a prevailing role in the activation of weak cohesive elements and a fortiori in the communication process. It can be quantified by the communication parameter a which low values represent highly interactive processes.

5.5   Scaling of the average fragment size

In this section, we focus on heterogeneous materials with a high density of defects, such that the number of defects and the number of fragments are independent (plateau region described in section 5.3.2). We look at the influence of the distribution of defects and the strain rate on the average fragment size. Figure 5.15 plots
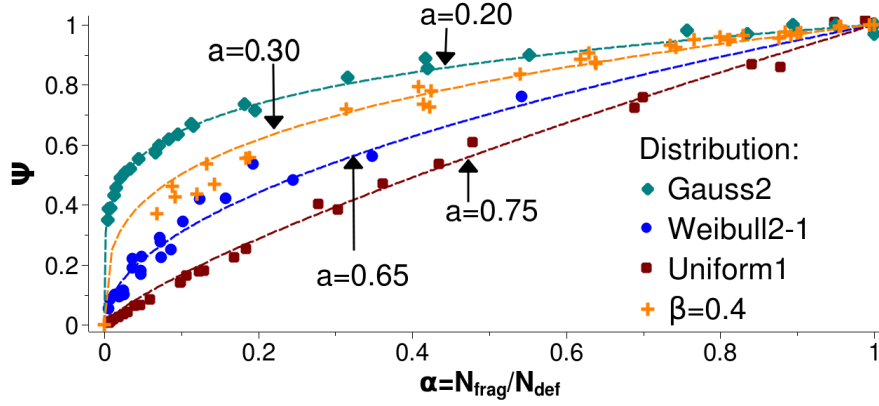
Figure 5.14: Numerical evaluation of the communication parameter a for four distinct initial p.d.f..

the average fragment size for different initial distributions and for several strain rates. The scattering of the points underlines that defects play a prevailing role in the fragmentation process.
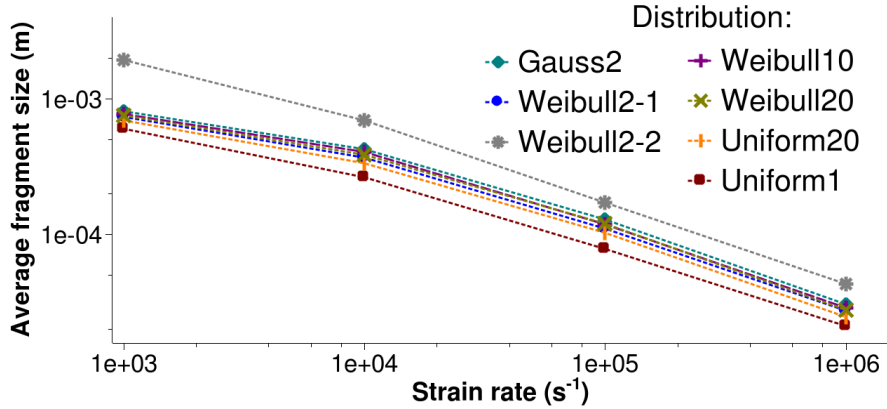
Figure 5.15: Dispersion in the average fragment size when the strain rate and the microstructure vary.

The idea of normalizing the axes to gather all these points into a single curve arises. In the normalization proposed by Zhou et al. for homogeneous materials, the normalization parameters were expressed in terms of σ_c and G_c. Now, since the material is heterogeneous, σ_c and G_c are defined through their distributions instead of being a single value. The homogeneous normalization is not adequate anymore. With the aim at understanding separately the effect of the initial p.d.f. and the communication parameter a, we propose two normalizations. The first one only depends on the initial p.d.f. and not on the communication, while the second accounts for both. Thus, we define new semi-empirical normalization parameters:

$$\dot{\varepsilon}_{0,new} = \frac{\mu_{init}}{E\,t_0} \tag{5.17}$$

$$s_{0,new} = c_{eff}\,t_0 \tag{5.18}$$

$$\text{where} \quad c_{eff} = \begin{cases} c\,\left(\frac{\sigma_{c,min}}{\mu_{init}}\right)^{1/5} & \text{first normalization} \\ c\,\sqrt{\frac{2}{a+1}}\left(\frac{\sigma_{c,min}}{\mu_{init}}\right)^{1/5} & \text{second normalization} \end{cases} \tag{5.19}$$

μ_{init} is the average of the initial distribution of defects, $\sigma_{c,min}$ is the cohesive strength associated to the weakest link, t_0 is the characteristic opening time of the cohesive elements, and a is the communication factor defined in section 5.4.

Multiplying the wave speed c by a function depending on the communication factor a is necessary to include the influence of the interactions between cracks, on the average fragment size. For a homogeneous material, the p.d.f. tends to be a Dirac function, for which the function Ψ is not defined anymore. If one considers that the Dirac function, associated to uniform distribution, yields no communication, then $a \rightarrow 1$. It directly leads to $c_{eff} \rightarrow c$. When the material is heterogeneous, the communication time affects the number of fragments. A low value of a is associated to a process during which cracks strongly interact. Stress waves propagate fast compared to the crack opening time t_0, which justifies that the effective wave speed is a decreasing function of a. Note that the exponent 1/5 in equation 5.19 was obtained to fit best our results.

In the figures 5.16 and 5.17, the x-axis and y-axis are respectively $\bar{\dot{\varepsilon}}_{new} = \frac{\dot{\varepsilon}}{\dot{\varepsilon}_{0,new}}$ and $\bar{s}_{new} = \frac{s_{average}}{s_{0,new}}$. The effect of the first normalization is illustrated in figure 5.16. It brings the curves into three distinct groups: the *Gaussian*, the *Weibull*, and the *Uniform*. The shape of the p.d.f. appears to affect the gathering and needs thus to be included. Therefore, we propose to use the communication parameter a defined in section 5.4, which is directly linked to this shape and to the rate of insertion of cohesive elements. Figure 5.17 compares the final normalization to Grady's and Zhou et al.'s laws for homogeneous materials. The log-log plot underscores that our results exhibit a characteristic exponent which is much close to Grady's minus two-thirds exponent, and that we predict approximately the same non-dimensional number of fragments that Zhou et al. obtained for homogeneous materials.

Although empirical, our second normalization successfully merges the initially scattered points into a single curve. Following the shape of the function proposed by Zhou et al. (section 5.2), the present curve can be fitted by:

$$\bar{s}_{new} = \frac{3}{1 + 4.5(\bar{\dot{\varepsilon}}_{new})^{2/3}} \tag{5.20}$$
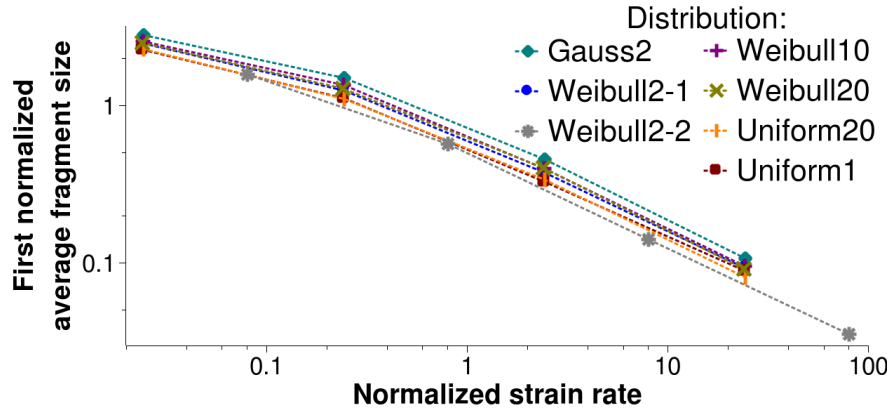
Figure 5.16: Effect of the first normalization which only includes the minimum cohesive strength $\sigma_{c,min}$ and the average of the initial distribution of defects μ_{init}.
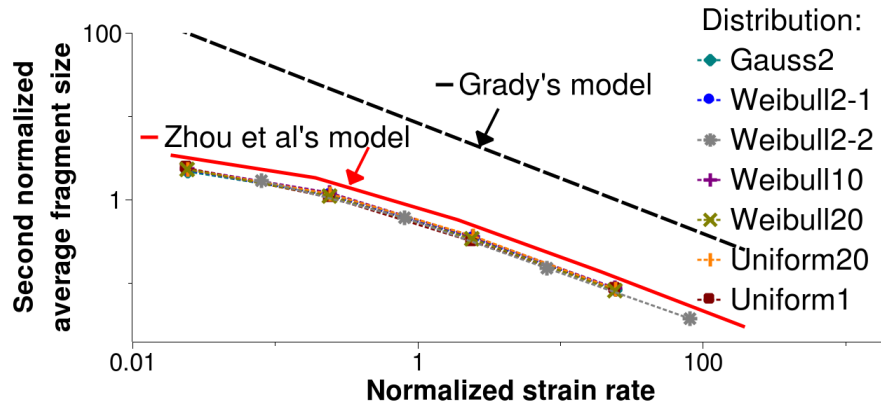
Figure 5.17: Effect of the second normalization which includes $\sigma_{c,min}$, μ_{init} and the communication parameter a, and comparison to Grady's and Zhou et al.'s laws.

Its developed form is:

$$s = t_0 \, c_{eff} \, \frac{3}{1 + 4.5 \left(\frac{E \, t_0}{\mu_{init}}\right)^{2/3} \dot{\varepsilon}^{2/3}}$$

$$\text{where} \quad c_{eff} = c \left(\frac{2}{a+1}\right)^{1/2} \left(\frac{\sigma_{c,min}}{\mu_{init}}\right)^{1/5}$$

(5.21)

The parameters used in the simulations are:

- Young's modulus $E = 275 \, GPa$

- Wave speed $c = 10^4 \, m.s^{-1}$

- Reference opening time $t_0 = 300 \, \mu s$

along with defect distribution dependent parameters:

- Average of the initial distribution of defects μ_{init}

- Weakest link $\sigma_{c,min}$

- Communication parameter: $a = \begin{cases} 0.20 & \text{for Gaussian distribution} \\ 0.65 & \text{for Weibull distribution} \\ 0.75 & \text{for Uniform distribution} \end{cases}$

The resulting effective wave speeds are: $c_{eff} = c \, . \begin{cases} 1.21 & \text{for Gauss2} \\ 1.07 & \text{for Weibull2-1} \\ 0.94 & \text{for Weibull2-2} \\ 1.08 & \text{for Weibull10} \\ 1.09 & \text{for Weibull20} \\ 0.84 & \text{for Uniform1} \\ 1.06 & \text{for Uniform20} \end{cases}$

The proposed scaling law matches the initially scattered points, but highlights differences to prior analytical and numerical models. For rather defect-free materials (such as Uniform20 in table 5.1), we predict slightly more fragments than the one-dimensional numerical model of Zhou et al. (e.g. our average fragment size is about 22% smaller). It may stem from the specific implementation of the two-dimensional contact algorithm. Our computed average fragment size is also smaller by a factor of 10 than Grady's energy predictions in which the process is energy-equilibrium. While valid for ductile materials, this assumption appears incomplete for the presently tested brittle solids. Indeed, in his first papers [Grady 1982, Grady 1988], Grady considers that the local kinetic and the elastic strain energies are converted into fracture energy at the onset of failure. In more recent

work [Grady 2008], Grady underlines that brittle solids undergo a non-equilibrium fragmentation. Indeed, since the onset of the fragmentation process is a nearly instantaneous, the damaged and the non-damaged regions barely communicate; at first, damage stays local. Hence, the non-damaged parts of the structure continue accumulating elastic strain energy, which is eventually converted into fracture energy, generating more fragments. Our simulations confirm Grady's second hypothesis [Grady 2008]. We have quantified that at high strain rates, most fragments result from the conversion of the potential energy accumulated in the damaged structure. In other words, kinetic energy is being converted into strain energy for a "long" period after peak strength. Since Grady's initial energy equilibrium law does not include this excess of strain energy, it predicts less fragments than our explicit numerical calculations.

Despite these dissimilarities, both the reference models and the present fitting curve exhibit a similar trend. Dynamic fragmentation tends asymptotically to a power-law with exponent equal to the inverse two-thirds. Ultimately, this suggests that the energetic criterion governs the dynamic regime. Indeed, statistical predictions would have inferred a dependence of the power exponent to the initial distribution of defects [Hild 2003], and an impulse criterion would have lead to an inverse one-third exponent [Grady 2006a, Tuler 1984]. Our results confirm that, even though dynamic brittle fragmentation is not energy-equilibrium, its asymptotic behavior is energy controlled.

5.6   Summary

In this chapter, we have modeled the fragmentation of a heterogeneous brittle ring submitted to radial expansion. Numerical simulations underscore the prevailing role of defects in the fragmentation physical process and in the resulting fragment sizes. They also emphasize the importance of accounting for stress release waves, which propagate away from crack initiation sites and may prevent damage nucleation at other defects.

We have investigated crack initiation through the degree of interactions between defects. It has led us to define a new communication parameter, which depends on the left tail of the initial probability density function of defects, and which accounts for the rate of insertion of cohesive elements. This communication parameter has been used to construct scaling laws of both the average fragment size and the strain rate. They successfully unify the initially scattered fragment size data into a unique curve. By efficiently scaling the behavior of homogeneous and heterogeneous materials, it highlights that dynamic fragmentation is characterized by a unique asymptotic behavior. The power-law with exponent minus two-thirds, predicted by Grady's energy-equilibrium theory, adequately fits our results. This indicates that the asymptotic limit of dynamic fragmentation is dominated by an energy criterion.

Predictable mass distribution in one-dimension

Similarly as in chapter 5, we simulate the fragmentation of an expanding ring and focus our study on the distribution of fragment masses and on the heaviest fragments. The computational framework is similar as in chapter 5: it employs a finite element procedure to simulate the elastic bulk response, and the cohesive methodology to model material decohesion. Here, we vary material heterogeneity, fracture energy, loading rate and ring circumference in order to quantify their influence on the generation of fragments. The computed fragment mass distributions are best summarized by generalized gamma density functions with shape parameter two, regardless of the model parameters. Contrary to the mean of the distribution that is determined by the average fragment mass, its shape appears to be unique. The heaviest fragments, however, do manifest a dependence upon these physical parameters. Extreme value statistics reveal that toughness, size, and dynamic effects play an important role[1].

6.1 Fragment mass distribution: power or exponential form?

Due to its violent nature, fragmentation has first been described through its resulting state: the number and mass of the fragments. Historically, two plausible forms for the fragment mass distribution have been used: the exponential and the power functions.

Distributions for the fragment mass distribution are often expressed in terms of the inverse cumulative distribution or survivor function [Grady 1985] (c.f. chapter 2):

$$N(m) = \exp\left\{-\int_0^m h(m)\,dm\right\} = \exp\{-H(m)\}, \quad m > 0, \tag{6.1}$$

where m is the fragment mass, $h(m)$ is a hazard function and $H(m)$ is the associated cumulative hazard function. The constant hazard function $h(m) = 1/\mu$, where

---

[1]This chapter has given rise to an article submitted in Physics Reviews E, by *S.Levy, J.F.Molinari, I.Vicari, A.Davison*, and entitled *Dynamic fragmentation of a ring: predictable fragment mass distribution*

μ is a relevant characteristic mass (such as the average mass), is associated to a Poisson point process and yields the exponential fragment mass distribution, whose applicability has been discussed at length by Grady and Kipp [Grady 2006b]. Note that the units of h are kg^{-1} and that H is dimensionless. Mott and Linfoot also assumed a constant hazard function [Mott 1943b], but believed that this assumption was only valid for one-dimensional problems. Hence, since the fragment mass and the fragment size are proportional in one-dimension, $h(s) = \rho \ h(m) = \rho/\mu$ and $H(s) = \rho \ s/\mu$, where ρ is the volumetric mass. In order to generalize this form to two-dimensional and shell geometries, Mott remarked that $s \propto (m/\rho)^{1/2}$ and wrote $H(m) \propto (m/\mu)^{1/2}$. More generally, one can extend this power law dependence to the general form $H(m) \propto (m/\mu)^{\beta}$, which corresponds to the Weibull distribution:

$$N(m) = \exp\left\{-(m/\mu)^{\beta}\right\}, \quad m > 0, \quad \mu, \beta > 0, \tag{6.2}$$

where β is the Weibull modulus. Note that $\beta = 1$ corresponds to the distribution suggested by Grady and Kipp [Grady 1985], while $\beta = 1/2$ refers to that of Mott and Linfoot [Mott 1943b].

In addition to the Weibull modulus, both authors defined a physical characteristic length scale, that one can relate to μ using the volumetric mass ρ. Mott considered a perfectly plastic material with yield stress Y and defined the typical size $s_0 \sim \left(Y/\rho\dot{\varepsilon}^2\gamma\right)^{1/2}$ adequate to fit his experimental results on steel [Mott 1947]. There, γ is the Mott statistical fracture activation parameter, $\dot{\varepsilon}$ is the strain rate, and ρ is the volumetric mass. Instead of considering specific materials, Grady derived a general theory based on energy balance [Grady 1982]. The toughness G_c and the volumetric mass ρ are the key parameters of his length scale, $s_0 \sim \left(G_c/\rho\dot{\varepsilon}^2\right)^{1/3}$ (chapter 2).

In these two approaches, the input energy is totally invested into fracture; this behavior is typically ductile. In ductile failure, the opening of cracks is a slow and energy consuming process, so most of the input energy is converted into fracture energy. Energy arguments can thus legitimately be associated to ductile behaviors and incorporated into the Weibull distribution. Nonetheless, since this theoretical framework does not include statistical variability, its validity may still be questioned for real fragment distributions, resulting from the fragmentation of complex loadings, geometries, and material heterogeneities. There is, however, some empirical evidence for the accuracy of the Weibull distribution, which has been widely used in fitting data from experimental and numerical tests [Gilvarry 1961a, Gilvarry 1961b, Rosin 1933, Zhou 2006b]. Exponential forms have thus proved their validity; they indicate the existence of a characteristic length and suggest ductile-like behaviors.

In contrast, a wide variety of experimental investigations, theoretical derivations, and numerical simulations have revealed that power laws more accurately describe brittle processes, during which the energy supplied is not entirely converted into

fracture energy [Capaccioni 1986, Schuhmann 1941, Turcotte 1986b, Wittel 2005]. While the fragmentation process evolves, failure does not dissipate enough strain energy (thus, the body continues accumulating it), leading to a self-similar behavior: each fragment successively splits into smaller fragments. Schuhmann's law, which is the limiting form of the Weibull distribution for small fragments, gives [Schuhmann 1941]:

$$N(m) = 1 - (m/\mu)^\beta, \quad 0 < m < \mu, \quad \mu, \beta > 0 \tag{6.3}$$

where μ and β are characteristic of the experiment. Turcotte [Turcotte 1986b] has listed objects whose fragment sizes behave according to equation (6.3), with β falling in the range 1.5 to 3.5. Hence, power laws indicate self-organized criticality and are usually associated to fragile behaviors.

However, several authors have pointed out that these two general frameworks may not fit experimental data. For instance, Englman [Englman 1991] suggested that power laws predict the behavior of small fragments while the exponential decay includes finite-size effects, which are related to heavier fragments. The idea of mixing exponential and power laws to decouple the behavior of heavy and small fragments thus arises. Grady [Grady 2008] proposed a Cauchy-like distribution that is equivalent to a power law for small fragments, and has a slower decay in the heavy fragment range:

$$N(m) = \left\{1 + (m/\mu)^\beta\right\}^{-1}, \quad m > 0, \quad \mu, \beta > 0. \tag{6.4}$$

Similarly, based on the theory of percolation [Stauffer 1985], Aström et al. studied the explosion of a two-dimensional structure [Åström 2000], and used the empirical fragment mass distribution for which:

$$N(m) = (m/\mu)^{-\beta} \exp\{-m/\mu\}, \quad m > 0, \quad \mu, \beta > 0. \tag{6.5}$$

Finally, a one-dimensional Voronoi tessellation argument yields cells whose masses follow a survivor function [Grady 1985] of the form:

$$N(m) = (1 + m/\mu) \exp\{-m/\mu\}, \quad m > 0, \quad \mu, \beta > 0, \tag{6.6}$$

corresponding to the gamma distribution with shape parameter two. In order to enable comparisons, its representative curve is plotted in figure 6.1, along with other fragment mass distributions associated to previously described theories.

Despite this large body of work, the governing physical laws are not yet been clearly understood (see chapter 3 for more details). In this chapter, we use a finite element framework, coupled to cohesive elements [Camacho 1996], to simulate the fragmentation of an expanding ring. The loading, material properties and size of the ring characterize the experiment. The framework is detailed in chapter 3.
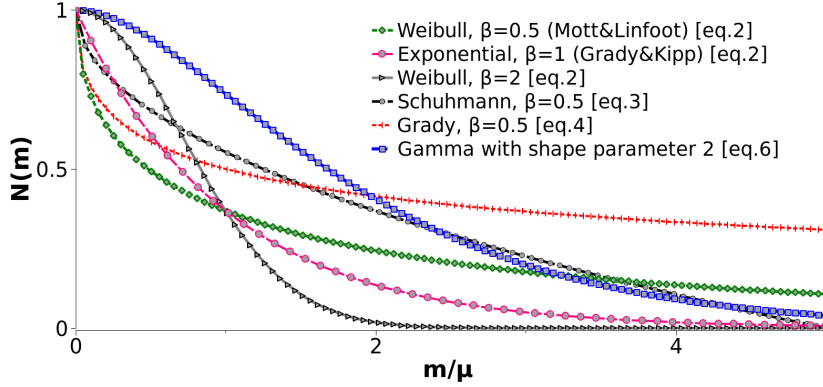
Figure 6.1: Survivor functions of fragment masses proposed in earlier works. The slope at the origin and the decrease in the right tail are essential for comparison of the distributions. The exponential distribution and the gamma distribution with shape parameter two rely on one-dimensional theoretical proofs.

The contribution of the present chapter lies in establishing the usefulness of another distribution, namely the generalized gamma distribution with shape parameter two, through numerical calculations. The formulation follows Mott's argument for the exponential distribution (equation (6.2)), in which the proportionality between fragment mass and fragment size depends on spatial dimension ($s \propto m^\beta$).

6.2 Brief overview of the model and useful results

6.2.1 Expanding ring test and implementation

Similarly as in chapter 5, we study the motion of a ring submitted to a radial outward velocity. We use a finite-element framework along with an explicit time integration scheme to simulate the elastic evolution of the body (see chapter 3). The mesh is composed of quadratic triangles. In order to recover one-dimensional response with a two-dimensional mesh, we impose the thickness of the ring to be constituted of a single element (of dimension $2\mu m$). N_{FE} denotes the number of radial edges of the finite-element mesh (e.g. about half of the total number of elements).

The imposed strain rate $\dot{\varepsilon}$ varies from $10^4 s^{-1}$ to $10^6 s^{-1}$. The ring is originally of length $L = 0.05m$ and is composed of an elastic material (Young's modulus $E = 275GPa$ and longitudinal wave speed $c = \sqrt{E/\rho} = 10^4 m.s^{-1}$) in which material defects are randomly distributed. These defects are weak sites where cracks may initiate.The expansion is first purely elastic, and the stress increases linearly until it reaches a critical threshold, corresponding to the value of the weakest link's failure strength, or cohesive strength σ_c. Then, a cohesive element [Camacho 1996] is

inserted dynamically into the mesh, at the location of the weak link. It relates linearly the local stress σ to the opening displacement δ, and controls the evolution of damage. When it is completely broken (e.g. when $\delta = \delta_c$), the cohesive element has consumed the energy $G_c = \frac{\sigma_c \delta_c}{2}$, called toughness. While the weakest link is getting damaged, the stress continues increasing in the rest of the structure. Other defects nucleate and possibly break. The process ends when no more defects are initiated.

The microstructure is defined by the cohesive strength (σ_c) and toughness (G_c) distributions. We choose a number of defects N_{def} large enough ($N_{\text{def}} = 0.8 \, N_{FE}$) so that there is no influence of the number of possible crack nucleation sites on the numerical results (chapter 5 and [Levy 2010]). Generally, we set the distribution of σ_c to follow a Weibull function [Weibull 1939] defined by:

$$F(\sigma_c) = 1 - \exp\left\{ -\left(\frac{\sigma_c - \sigma_{c,\text{min}}}{\lambda} \right)^{m_w} \right\}, \quad \sigma_c > \sigma_{c,\text{min}}, \quad \sigma_{c,\text{min}}, \lambda, m_w > 0, \quad (6.7)$$

where λ is the scale parameter, m_w is the Weibull modulus, and $\sigma_{c,\text{min}}$ is the minimum value of the cohesive strengths. Concerning the toughness, there is no experimental evidence of the existence of a representative distribution. The quasi-static macroscopic toughness G_c can be measured, but an arbitrary choice must be made to assign the full toughness distribution. We have selected two cases: G_c is either a Dirac centered at values $\{1, 50, 100, 500\}$ (Condition 1, named C1), or it is deduced from the relation $G_c = c \, t_0 \, \sigma_c^2 / E$, that guarantees that all the defects have the same crack opening duration t_0 (Condition 2, named C2) [Camacho 1996]. If Condition 1 is selected, all the defects release the same amount of energy during failure, while with Condition 2, weaker defects dissipate fewer energy.

$$G_c \in \{1, 50, 100, 500\} \, N.m^{-1} \quad \rightarrow \quad \text{C1} \tag{6.8}$$

$$G_c = \frac{c \, t_0}{E} \, \sigma_c^2 \quad \rightarrow \quad \text{C2} \tag{6.9}$$

We chose $t_0 = 30ns$ and $t_0 = 7.6ns$. In the following, we analyze the results of a series of parametric studies. Tables 6.1 and 6.2 detail the parameter values. In order to get reliable statistics, we conducted several simulations for each case. To give a quantitative characterization of the ring fragmentation, we study the average fragment mass, the survivor function of fragment masses and the heaviest fragments.

6.2.2 Convergence and material properties

We first verified that numerical parameters have no influence on the distribution of fragment masses. Table 6.1 shows that the number of fragments is mesh independent. The mass distribution invariance was also verified, but is not shown here. Then, we varied the physical parameters, keeping the number of elements constant ($N_{FE} = 3.10^4$). Several distributions of cohesive strengths σ_c, values of strain rates,

ring lengths and toughnesses were tested in order to quantify material heterogeneity, dynamic, and size effects, and to compare brittle and ductile behaviors (table 6.2).

Test	Cohesive strength distribution (MPa)	Toughness mean value ($N.m^{-1}$)	$\dot{\varepsilon}$ (s^{-1})	N_{FE}	N_{exp}	N_{frag}
1	$\sigma_c \sim W(2, 50, 150)$	C2:$G_c \simeq 35$	10^5	3.10^4	15	630 ± 6
2	$\sigma_c \sim W(2, 50, 150)$	C2:$G_c \simeq 35$	10^5	6.10^4	3	637 ± 5
3	$\sigma_c \sim W(2, 50, 150)$	C2:$G_c \simeq 35$	10^5	9.10^4	3	640 ± 5
4	$\sigma_c \sim W(2, 50, 150)$	C2:$G_c \simeq 35$	10^5	12.10^4	2	642 ± 1

Table 6.1: Parameters chosen to verify the mesh independence. N_{FE} is the number of triangles. N_{exp} is the number of numerical experiences. N_{frag} is the number of fragments. C2 refers to the condition detailed in equation (6.9). $W(2, 50, 150)$ stands for the Weibull distribution with Weibull modulus 2, scale parameter $50MPa$, and minimum value $150MPa$. The convergence in terms of number of fragments is verified in the last column.

6.2.3 Average fragment size

In the ring configuration, the average fragment size, s_{aver}, strongly depends on the strain rate and the material properties. Figure 6.2 underscores this scattering, in the case of uniform, normal and Weibull distributions of defects, whose standard deviations are distinct. The defect distribution has a key role in the fragmentation process. In [Levy 2010] and chapter 5, we established the following equation, which predicts the average fragment size as a function of the strain rate and the material properties:

$$\frac{s_{\mathrm{aver}}}{s_{\mathrm{charac}}} = \frac{3}{1 + 4.5(\frac{\dot{\varepsilon}}{\dot{\varepsilon}_0})^{2/3}}, \tag{6.10}$$

$$\text{where} \begin{cases} s_{\mathrm{charac}} = c \, t_0 \, f(\text{defects}), \\ \dot{\varepsilon}_0 = \frac{\sigma_{c,mean}}{E \, t_0}. \end{cases} \tag{6.11}$$

where $s_{\mathrm{ch}} = c \, t_0 \, f(\text{defects})$ and $\dot{\varepsilon}_{\mathrm{ch}} = \sigma_{c,\mathrm{aver}}/(E \, t_0)$. Here s_{ch} and $\dot{\varepsilon}_{\mathrm{ch}}$ are respectively a characteristic length scale and a characteristic strain rate. They can be fully determined by material properties: $\sigma_{c,\mathrm{aver}}$ is the average value of the defect cohesive strengths, E is the Young's modulus, t_0 is the defect opening time, and c is the wave speed. The function $f(\text{defects})$ is a semi-empirical function, expressed as the product of two independent functions f_1 and f_2 (see chapter 5 and in [Levy 2010]).

The first function f_1 is associated to the shape of the cohesive strength distribution. It quantifies the effect of stress wave interactions. For instance, when the left tail has an infinite slope (such as the uniform distribution), numerous cracks initiate simultaneously when the stress reaches the weakest link's strength $\sigma_{c,min}$. This

Test number	Cohesive strength distribution (MPa)	Toughness mean value ($N.m^{-1}$)	Strain rate $\dot{\varepsilon}$ (s^{-1})	Number of experiments	Length of the ring
5	$\sigma_c \sim W(2, 200, 300)$	C2:$G_c \simeq 100$	10^4	298	L
6	$\sigma_c \sim W(2, 200, 300)$	C2:$G_c \simeq 100$	10^5	299	L
7	$\sigma_c \sim W(2, 200, 300)$	C2:$G_c \simeq 100$	10^6	299	L
8	$\sigma_c \sim W(2, 50, 150)$	C2:$G_c \simeq 100$	10^5	277	L
9	$\sigma_c \sim W(10, 200, 300)$	C2:$G_c \simeq 100$	10^5	299	L
10	$\sigma_c \sim W(20, 200, 300)$	C2:$G_c \simeq 100$	10^5	322	L
11	$\sigma_c \sim W(2, 50, 150)$	C2:$G_c \simeq 1$	10^5	249	L
12	$\sigma_c \sim W(2, 50, 150)$	C1:$G_c = 1$	10^5	112	L
13	$\sigma_c \sim W(2, 50, 150)$	C1:$G_c = 50$	10^5	83	L
14	$\sigma_c \sim W(2, 50, 150)$	C1:$G_c = 100$	10^5	52	L
15	$\sigma_c \sim W(2, 50, 150)$	C1:$G_c = 500$	10^5	117	L
16	$\sigma_c \sim W(2, 50, 150)$	C2:$G_c \simeq 100$	10^5	295	0.5 L
17	$\sigma_c \sim W(2, 50, 150)$	C2:$G_c \simeq 100$	10^5	296	1.5 L
18	$\sigma_c \sim U(345, 3)$	C2:$G_c \simeq 100$	10^5	1	L
19	$\sigma_c \sim U(345, 140)$	C2:$G_c \simeq 100$	10^5	1	L
20	$\sigma_c \sim G(345, 23)$	C2:$G_c \simeq 100$	10^5	1	L

Table 6.2: Physical sets of parameters used in the simulations. C1 and C2 refer to the conditions detailed in equations (6.8) and (6.9). $W(2, 50, 150)$ stands for the Weibull distribution with Weibull modulus 2, scale parameter $50MPa$, and minimum value $150MPa$. $U(345, 3)$ and $G(345, 3)$ respectively stand for uniform and normal distributions with mean $345MPa$ and standard deviation $3MPa$.

leads to a rapid response during which stress waves do not have time to establish; many fragments are generated independently. On the contrary, when the left tail has a null slope (such as the normal distribution), cracks are initiated smoothly, one after the other. Stress waves have time to interact and to release the structure; fewer fragments are generated. Therefore, similarly as the fragment size s_{ch}, which is inverse proportional to the number of fragments, f_1 is a decreasing function of the left tail's slope of the cohesive strength distribution. Empirical arguments have shown that f_1 is comprised between 1 and $\sqrt{2}$ [Levy 2010]. The second function f_2 is a decreasing function of the ratio between $\sigma_{c,\mathrm{aver}} - \sigma_{c,\mathrm{min}}$ and $\sigma_{c,\mathrm{aver}}$, and is comprised between 0 and 1. It quantifies the amount of breakable defects. Given the peak stress (which depends on the strain rate and distribution of defects), the maximum number of defects that may break is the probability of finding a cohesive strength smaller than peak stress times the number of defects. For instance, while peak stress remains lower than $\sigma_{c,aver}$, two distributions with the same $\sigma_{c,aver}$ may not result in the same number of fragments. Distributions with large standard deviation may generate many small fragments because they contain more breakable defects. Hence, f_2, and a fortiori s_{ch}, are decreasing with $\sigma_{c,\mathrm{aver}} - \sigma_{c,\mathrm{min}}$. To summarize, the function $f(\mathrm{defects})$ conveys the idea that variations of the tail of the left slope of the distribution of cohesive strengths yield distinct fragmentation behavior, and that the minimum and the average cohesive strengths constrain the maximum number of breakable defects.
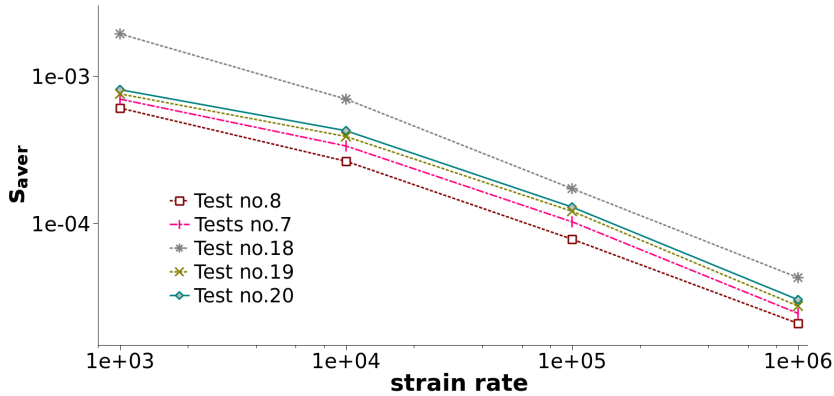
Figure 6.2: Scattering of the average fragment size, due to microstructural properties. Test numbers 7 and 8 refer to Weibull distributions, numbers 18 and 19 to uniform distributions, and number 20 to a normal distribution (table 6.2). s_{aver} is expressed in meters and the strain rate units are s^{-1}. For this figure, the strain rate parameter of table 6.2 has been expanded to cover the range $10^3 \ s^{-1}$ to $10^6 \ s^{-1}$.

6.3 Predictable distribution of fragment sizes

Apart from the number of fragments, which only quantifies the process on average, the distribution of masses has a meaningful additional representation. Several simulations were conducted in order to get reliable parameters characteristic of this distribution. Figure 6.3 displays the survivor functions of fragment masses obtained for a set of parameters reflecting extreme values of strain rate $\dot{\varepsilon}$, toughness G_c, and ring length L_{ring} (table 6.2). Although clearly distinct, the distributions shown have identical shapes. Astonishingly, a simple normalization of the x-axis by the average fragment mass gathers all the initially scattered data into a single curve (figure 6.4). It is noteworthy that all tests listed in table 6.2 (including those not represented in figure 6.4) lie on this single curve, though for clarity most tests are not shown on the figure.
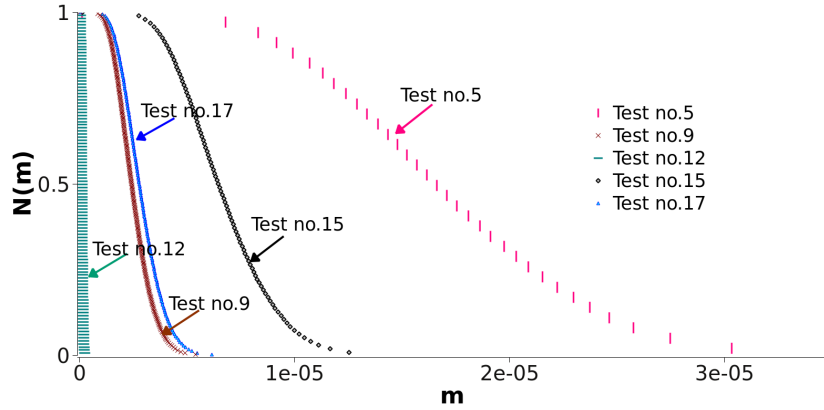
Figure 6.3: Survivor functions of fragment masses obtained for a set of parameters reflecting extreme values of strain rate $\dot{\varepsilon}$, toughness G_c, and ring length L_{ring} (table 6.2). The masses m are in kilograms.

We propose to fit this curve with the generalized gamma distribution with shape parameter two [Johnson 2005]:

$$N(m) = \left(1 + (m/\mu)^{\beta}\right) \exp\{-(m/\mu)^{\beta}\}, \quad m > 0, \quad \mu, \beta > 0, \tag{6.12}$$

where β (representative exponent) and μ (representative mass) are determined by fitting to the data. Our best fit is obtained for $\beta \simeq 2.2$ and $\mu \simeq 0.77 m_{\text{aver}}$ (we recall that m_{aver} is the average fragment mass). These values are remarkably precise: the mean of the β parameters among the thirteen tests detailed in table 6.2 is 2.195 with standard deviation 0.0113, and the mean of the μ parameters is $0.768 m_{\text{aver}}$ with standard deviation $0.0113 m_{\text{aver}}$. Figure 6.5 is a box plot generated for 50 intervals and combines the 299 experiments associated to test5. It also shows the survivor function of test5 and the proposed fitting curve.
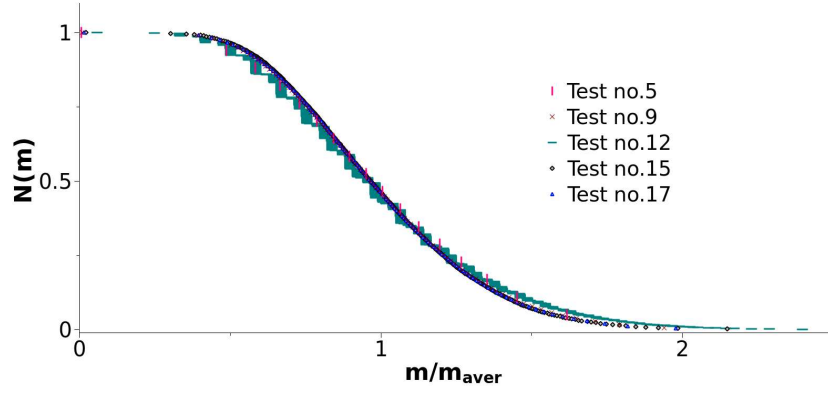
Figure 6.4: Survivor functions of normalized fragment masses obtained for a set of parameters reflecting extreme values of strain rate $\dot{\varepsilon}$, toughness G_c, and ring length L_{ring} (table 6.2). Note that the fragment masses are now normalized by the average fragment mass obtained from equation (6.10) ($m_{\text{aver}} = \rho\, s_{\text{aver}}$).
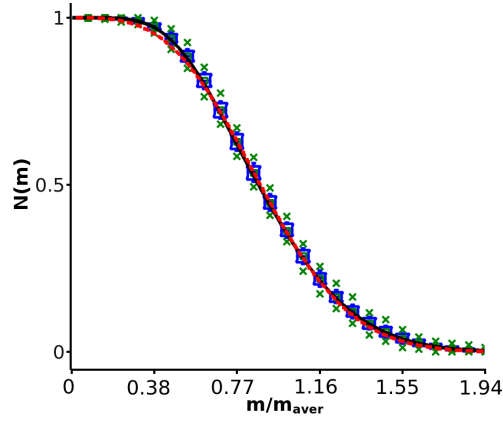
Figure 6.5: Survivor function associated to test5 (dashed red curve) (table 6.2), along with that of the inverse of the generalized gamma distribution with shape parameter 2 (thin dark curve). Box plots of the survivor functions underline the scattering of the distributions calculated independently over the 299 experiments. The x-axis involves normalized masses.

Generalized gamma distributions are a group of widely used functions. In its original form, the generalized gamma distributions conveys two shape parameters d and p. The probability density function of the generalized gamma distribution is:

$$f(m) = \frac{\beta}{\mu\Gamma(\frac{d}{\beta})} \ (m/\mu)^{d-1} \ \exp\{-(m/\mu)^\beta\}, \quad m > 0, \quad \mu, d, \beta > 0, \qquad (6.13)$$

where Γ is the gamma function. The shape parameter d reflects the physical process; it infers details about the occurrence of an event. The second shape parameter β has secondary importance [Lienhard 1967]; in fragmentation, it is usually associated to finite size effects of the structure [Åström 2000]. Depending on the values of the shape parameters, the distribution can take the form of the Weibull ($d = \beta$, equation 6.2), the exponential ($d = \beta = 1$), the gamma ($\beta = 1$), the Rayleigh ($d = \beta = 2$) distributions, among others. We propose here to use $d = 2\beta$ and we fit $\beta \simeq 2.2$.

Figure 6.6 compares our fit to the exponential (Poisson process) and the gamma (Voronoi tessellation) distributions. Since the exponential distribution has a negative slope at the origin, and since the gamma distribution does not have enough parameters, they cannot fit accurately our data. As shown by figure 6.6, the generalized gamma distribution is an appropriate candidate to fit the survivor function obtained for test no.17. Because they are so similar, the other survivor functions may also be well-approximated by the generalized gamma distribution. Figure 6.6 also displays experimental data obtained from expanding ring tests [Grady 1983, Grady 2003, Zhang 1999] that closely fit our numerical results.
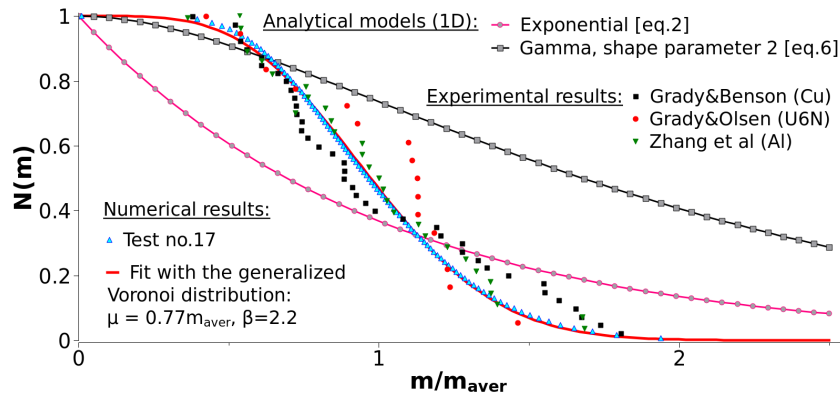
Figure 6.6: Numerical and experimental distributions of fragment masses, proposed generalized gamma distribution with shape parameter two, and comparison to analytical models derived in one dimension (Poisson process and Voronoi tessellation).

To underline the differences between our fit and prior models, two comparisons are made. First, many models behave as a generalized gamma distribution and

the scale parameter d is the statistical relevant parameter. As highlighted in the introduction, the Weibull distribution with exponent $\beta = d$ has been widely used. A theoretical derivation of the expanding ring test leads to $\beta = 1$ [Grady 2006b], e.g. to the exponential distribution. Zhou et al. [Zhou 2006b] computed $\beta = 2$, which amounts to the Rayleigh distribution.

The second comparison concerns the behavior of the smaller (or lighter) fragments, which reflects the governing mechanisms of fragmentation. The light fragment range can be studied through the representative exponent d in equation 6.13 and β in equations 6.4 and 6.12. Oddershede et al. [Oddershede 1993] carried out impact experiments on gypsum structures of diverse shapes. For the bar geometry, they found the exponent 1.05. Similarly, Meibom et al. [Meibom 1996] considered the one-dimensional fragmentation resulting from the impact of dry clay structures on the ground, and found the exponent 1 ± 0.1. Åström et al. [Åström 2004b] computed the exponent 0.5 for the explosive fragmentation of two-dimensional structures. Wittel [Wittel 2006] simulated shell fragmentation and noticed that the exponent is closed to 1.55. Therefore, many models have been proposed to fit the fragment mass distributions. The differences in the exponent values are related to the geometry, the type of loading, and more generally, to the physical mechanisms underlying fragmentation.

Our fitted value 2.2 is above all the previous fits, which infers that we obtain a narrower mass distribution. This can be explained by the simple loading test, which involves pure tensile loading with few contacts. Impact tests include more complex mechanisms such as bending and shearing, that lead to more disperse fragment mass distributions. We plan to investigate the issue of impact in future work. The proposed distribution and its parameters μ and β therefore fully characterize the fragment masses. Contrary to the average fragment mass, which is determined by material parameters (equation (6.11)), the shape of the distribution appears to be a common characteristic of the fragmentation of a uniformly expanding thin ring (equation 6.12). We stress, however, that the predictable behavior of the fragment mass distribution is a strong result, which is only known to be valid for the problem studied here.

We stress however that the universality of the fragment mass distribution is a strong result which is only known to be valid for the problem studied here. Changing the geometry of the structure and the boundary conditions may result in different observations. The expanding ring problem focuses on the initiation of defects rather than the propagation of cracks. Therefore, if field experiments reveal a relation between physical parameters and fragment mass distribution (and deviate from our model), we may conjecture that this is due to crack propagation and coalescence mechanisms. We expect to observe these deviations in two and three-dimensional problems, the topic of chapters 7 and 8.

6.4   Heaviest fragment behavior

Although our proposed function fits the fragment population as a whole, it fails to accurately characterize the heaviest fragments. The statistics of extremes provide a suitable framework for studying the heaviest fragments [Beirlant 2004, Coles 2001]. In this section, we do not study the heaviest fragment masses quantitatively, but simply highlight some relations between the largest fragments and physical parameters.

As the experiments are independent (one microstructure and one mesh have been generated for each test), we can apply the statistics of extremes, and try to find the distribution type that characterizes the right tail of the fragment mass distribution. For each experiment, we computed the ratio between the maximum and the average fragment masses. Then, we studied the cumulative density function of these values ($cdf_{\max}$)) and compared it to the generalized extreme value distributions. In the present case, Gumbel distributions provide the best fit to the numerical results:

$$\mathrm{cdf}_{max}(m) = \exp\left[-\exp\left\{-\frac{(m/m_{\mathrm{aver}} - a)}{b}\right\}\right],$$
$$-\infty < m < \infty, \quad -\infty < a < \infty, b > 0 \tag{6.14}$$

where a and b are parameters of the distribution. This is coherent with the standard theory of extremes, which suggests that the largest values of independent samples drawn from equation (6.12) will follow equation (6.14). Figure 6.7 shows some test results and the associated Gumbel distributions.
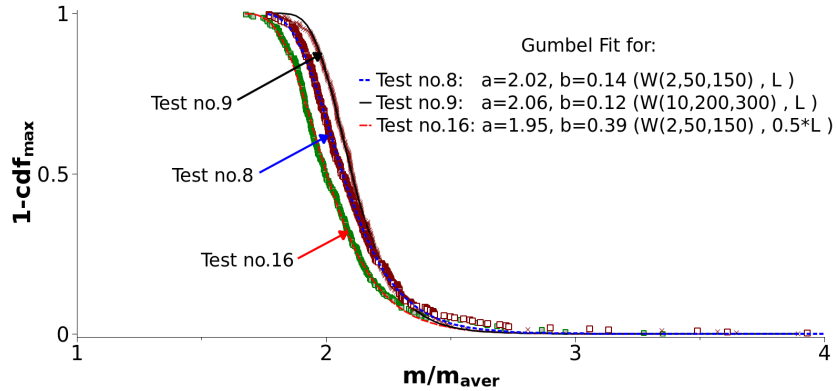
Figure 6.7: Survivor functions of the heaviest fragment mass and their fit with a Gumbel distribution. For each test, m corresponds to the heaviest fragment mass and m_{aver} refers to the average fragment mass. W(2, 50, 150) stands for the Weibull distribution with Weibull modulus 2, scale parameter 50MPa, and minimum value 150MPa. L is the reference length of the ring.

Although all the heaviest fragment masses seem to follow the same type of extreme distribution, the parameters a and b vary. Their distinct values emphasize that physical parameters affect the behavior of the heaviest fragments. Figures 6.8 display the survivor functions of the 'heaviest' masses (note that 'heavy' has here a specific sense since the x-axis is normalized by the average fragment mass). Unlike the uniqueness of the mass distribution (equation (6.12)), the extreme fragments depend on the length of the ring, the brittleness of the material, and the defect distribution. Figures 6.8 highlight that long bars generate 'heavier' fragments than short bars, and that brittle materials yield 'heavy' fragments. The dependence on the defect distribution underscores that the scale parameter of the Weibull distribution exerts an influence, while changing the Weibull modulus seems to have little impact.

6.5 Summary

The fragmentation of a uniformly expanding ring has been simulated within a finite element framework, coupled to linear cohesive elements. Statistics on fragment masses have been analyzed for different configurations. The ring geometry does not change, whereas its length, the loading rate, the defects, and the toughness vary. After having verified the numerical convergence, we focused on the effect of these physical parameters on fragment generation. We showed that they strongly affect the average fragment mass in a predictable way. The average fragment mass can be computed following a simple formula (see chapter 5). We also show that the distribution of fragment masses follows a unique curve, which depends only on the average fragment mass, and which behaves like the generalized gamma distribution with shape parameter two. Finally, despite this apparent universality, extreme value statistics show that physical parameters do affect fragmentation. Although all the distributions of the heaviest fragments seem to follow a Gumbel law, its parameters depend upon these physical parameters. Defects, toughness, ring size, and loading rate influence fragmentation through the heaviest fragments.
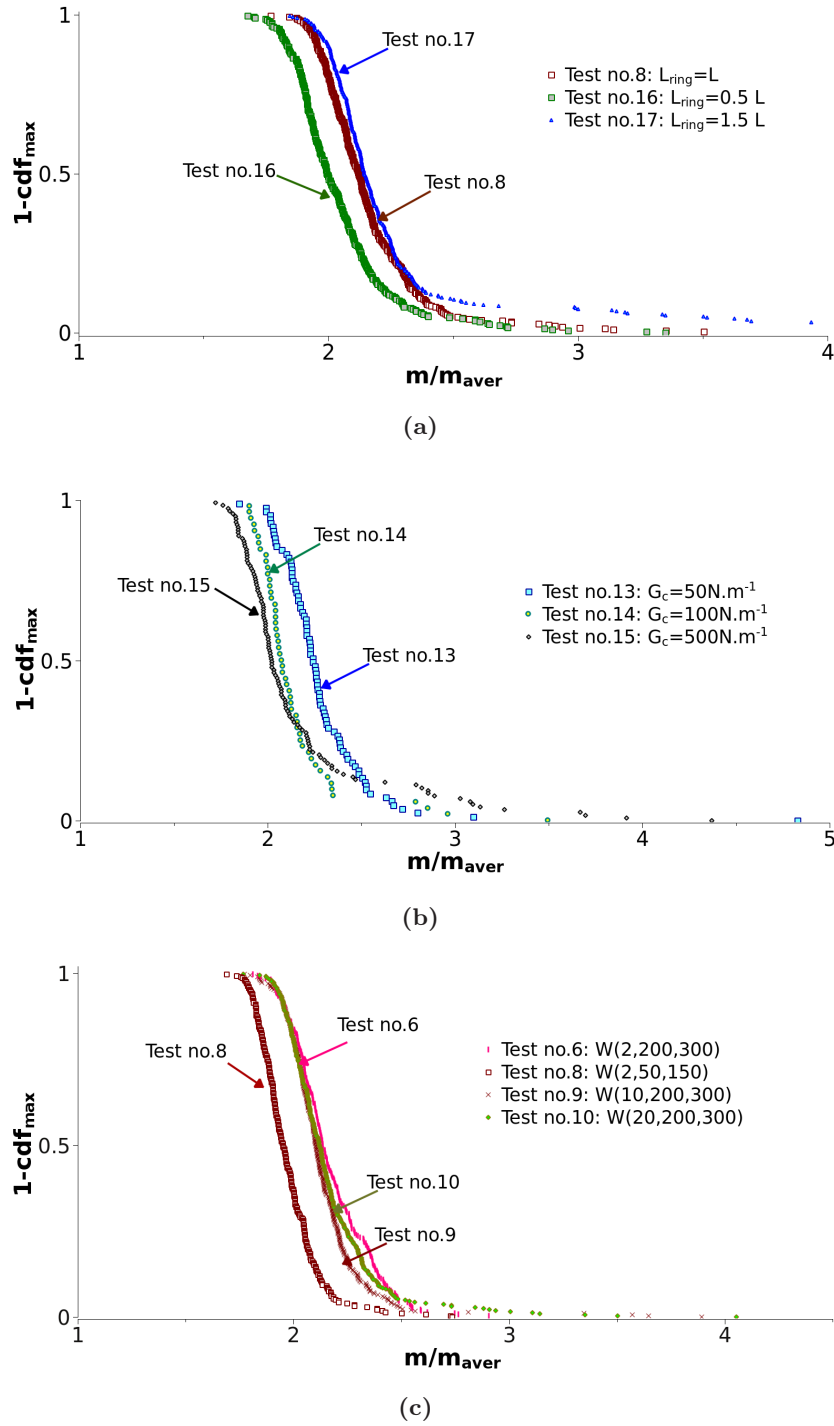
Figure 6.8: Survivor functions of the heaviest fragments. Influence of: (a) the length of the ring, (b) the toughness, (c) the distribution of defects. For each test, m corresponds to the heaviest fragment mass and m_{aver} refers to the average fragment mass. W(2, 50, 150) stands for the Weibull distribution with Weibull modulus 2, scale parameter 50MPa, and minimum value 150MPa. We note that (a) longer bars generate heavier fragments, and (b) lower toughness generates heavier fragments (in terms of normalized mass).

Fragmentation of a plate

In this chapter[1], we investigate the fragmentation of a thin plate in biaxial tension with the aim at understanding and predicting better the physical mechanisms underlying fragmentation in multiple dimensions (crack initiation and crack propagation). We base our interpretations on Grady's model [Grady 1982, Grady 2009] in which a characteristic length scale is derived. We enrich Grady's model by introducing a distribution of defects, and by including non-linear stress wave interactions. In order to handle this added complexity, we choose to use parallel numerical tools to simulate the plate's response. We are using an original hybrid numerical framework, which couples the discontinuous Galerkin approach and the cohesive zone fracture model (see chapter 3). Highly scalable, it allows us to conduct parallel simulations of very fine meshes. We also vary material parameters and strain rate, and show that, depending on their values, fragmentation can either be strength or toughness controlled. Fragmentation at low strain rates is controlled by defects and generate irregular patterns, whereas fragmentation at high strain rates is governed by energy arguments and leads to Weibull-type fragment mass distribution.

7.1 Definition of the problem and objectives

7.1.1 Description of the test

We consider a thin square plate of dimension $L_{plate} = 10$ cm (figure 7.1(a)) and thickness 0.15 mm. The value of the thickness can, however, change and be adapted to the element size to ensure the good quality of the mesh. Since the plate remains very thin in all the simulations, varying the thickness does not affect the fragmentation pattern. The material is aluminum oxide AD-995 with Young's modulus $E = 370$ GPa, Poisson ratio $\nu = 0.22$, volumetric mass $\rho = 3900$ $kg.m^{-3}$, static failure strength $\sigma_c = 262$ MPa and toughness $G_c = 50$ N/m. These parameters will be modified in the following sections in order to understand their influence on the fragmentation process (c.f. table 7.1). The plate is subjected to biaxial tension during the entire duration of the test. Initial displacements and velocities are set so that the plate undergoes uniform expansion with no initial propagating stress waves. We vary the strain rate from 10 s^{-1} to 10^5 s^{-1}.

---

[1]The first part of this chapter is about to be submitted in the International Journal of Fracture. The article by *S.Levy, J.F.Molinari, R.Radovitzky* will be entitled *Dynamic fragmentation of a brittle plate under biaxial loading: strength or toughness controlled?*. The second part dealing with fragment size statistics will be submitted in a physics journal.

	Young's modulus (GPa)	Volumetric mass (kg/m^3)	Poisson ratio	Toughness (N/m)	$\sigma_{c,min}$ (MPa)	Weibull modulus	Scale parameter (MPa)
Mat.1	370	3900	0.22	50	264	2	50
Mat.2	275	3750	0.22	50	264	2	50
Mat.3	260	3690	0.22	50	299	20	50
Mat.4	260	3690	0.22	50	305	2	50
Mat.5	370	3900	0.22	500	264	2	50
Mat.6	370	3900	0.22	250	264	2	50
Mat.7	370	3900	0.22	50	142	2	50
Mat.8	600	3900	0.22	50	264	2	50
Mat.9	370	6327	0.22	50	264	2	50
Mat.10	370	1054	0.22	50	264	2	50
Mat.11	370	3900	0.22	50	69	2	50
Mat.12	370	3900	0.22	50	284	20	30
Test1	[100;600]	3900	0.22	50	264	2	50
Test2	[100;600]	[2405;14430]	0.22	50	264	2	50
Test3	[100;600]	[1054;6324]	0.22	50	264	2	50
Test4	370	[1054;6324]	0.22	50	264	2	50
Test5	370	3900	0.22	50	[112;715]	2	50
Test6	370	3900	0.22	50	264	2	[50;500]
Test7	370	3900	0.22	[10;500]	50	2	50

Table 7.1: Material and test parameters used in the simulations

In any case, fragmentation occurs in two stages: the elastic and the failure stages. Since we impose initial velocities to avoid spurious wave propagation, kinetic energy is originally non null. During the first stage, we pull on the boundaries so that velocities do not evolve. The plate stretches and potential energy is accumulated (figure 7.1(c)). We assume a linear elastic response before failure onset. At time t_{min}, the critical threshold $\sigma_{c,min}$ is reached and the first cohesive element is activated. Potential energy continues increasing because both of inertial effects and material heterogeneity (defects initiate at $\sigma \geq \sigma_{c,min}$). Peak stress is reached at time t_f, corresponding to the transition to the failure phase. During the failure phase, potential energy is dissipated into fracture energy. First, the amount of potential energy, which may be used for fracture, is related to the value of the peak stress. Secondly, since we keep pulling on the boundaries, kinetic energy is constantly added into the system. This kinetic energy is partially converted into potential energy, which in turn may be converted into fracture energy. Consequently, there are two causes of fracture energy: the direct conversion of peak potential energy and the use of input kinetic energy (see section 4.2). The final fragmented state (figure 7.1(b)) involves complex physics mostly driven by stress wave interactions, characterized by the elastic wave speed $c = \sqrt{E/\rho}$. Potential energy has not necessarily a final null value because damage evolution stops as soon as stress is locally low enough (in comparison to the cohesive strengths σ_c).

Impulse boundary conditions (initial velocity solely) were tested as well. The response is close to the uniform expansion (see chapter 4). In the elastic phase, kinetic energy decreases because it is consumed by potential energy. In the failure phase, the same mechanisms occur: the direct conversion of peak potential energy, as well as the indirect conversion of kinetic energy. The difference between impulse and uniform expansion lies in the amount of each energetic contribution. In the impulse case, the direct conversion of potential energy significantly dominates, while it is less obvious in the uniform expansion (it actually depends on strain rate and material properties). We chose to use uniform expansion conditions because it allows accessing the quasi-static regime. In dynamics, impulse and uniform expansion lead to very similar responses [Zhou 2005a].

7.1.2 Modeling of material heterogeneity

Every material is inherently heterogeneous. It may contain pores, inclusions, grain boundaries, crystal imperfections. Since they have tendency to concentrate stresses, these entities are favorable locations for fracture initiation, and we name them defects. Experimental evidence [Weibull 1939] has shown that failure strengths of most materials follow a Weibull distribution (see chapter 3). We associate the failure strength of a defect to the cohesive strength of its associated cohesive element. The distribution of cohesive strengths is thus given by:
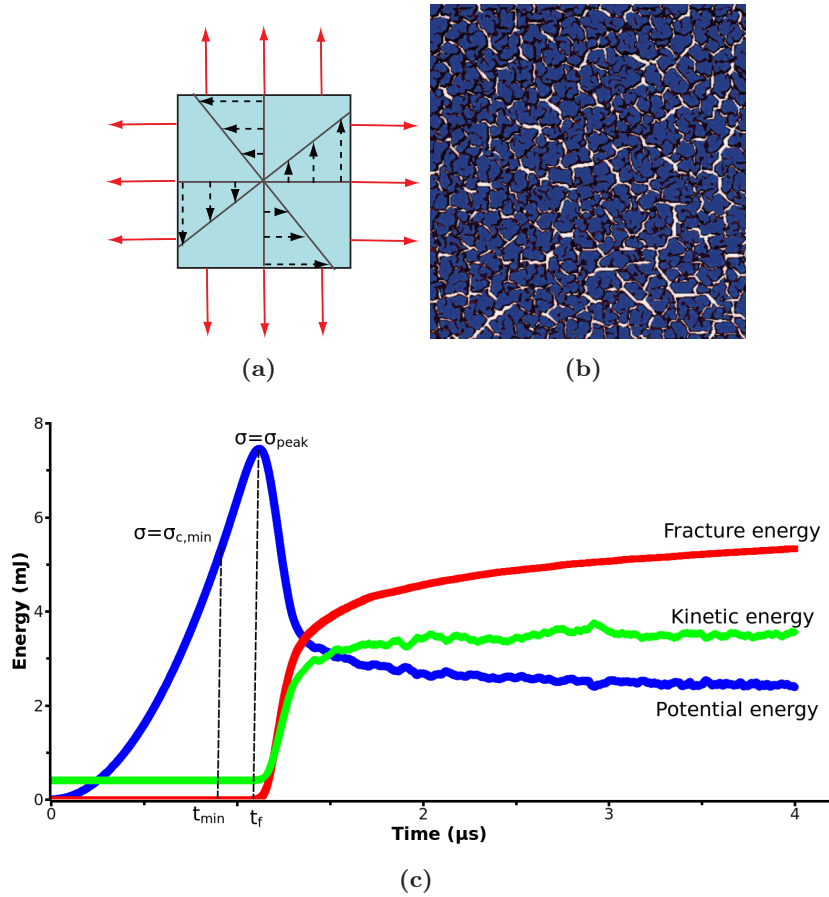
Figure 7.1: (a) Plate under biaxial tension. Dashed arrows indicate the extent of initial velocity amplitudes. Plain arrows indicate boundary conditions in displacements. (b) Fragmented plate from which we can extract the mass of the fragments. (c) Kinetic, potential and fracture energies evolving with time, for material Mat.1 (see table 7.1) at strain rate $\dot{\varepsilon} = 500s^{-1}$. t_{min} corresponds to the time when the first cohesive element is activated. t_f is the time to failure associated to peak potential energy.

$$F(\sigma_c) = 1 - e^{-\left(\frac{\sigma_c - \sigma_{c,min}}{\lambda}\right)^{m_w}} \tag{7.1}$$

$\sigma_{c,min}$ is the minimum cohesive strength, which corresponds to the quasi-static failure strength. m_w is a material parameter called Weibull modulus. λ is the scale parameter, and depends on the material and on the geometry of the structure. In the present chapter, we have tested the response of several distributions of defects plotted in figure 7.2.
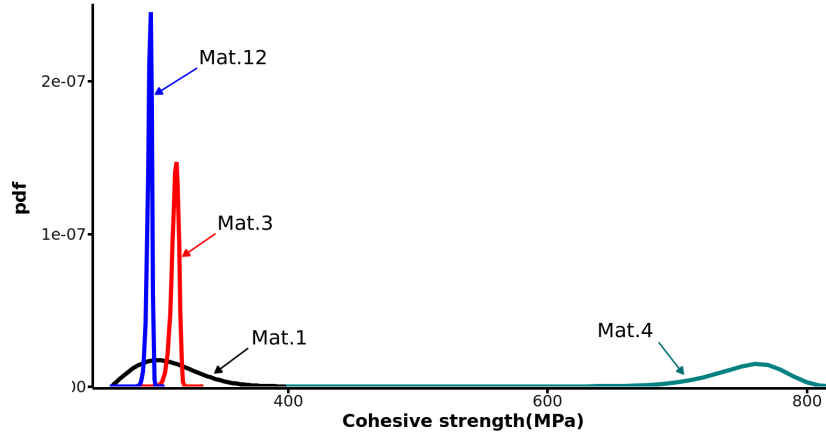
Figure 7.2: Probability density function of some of the distributions of cohesive strengths studied (see table 7.1).

7.1.3 Synopsis of the study

Material parameters: Our objective is to vary bulk material parameters and defect parameters to understand their influence on fragmentation. Table 7.1 details each set of parameters used in the simulations. A line of the table can be associated both to a material (Mat. in the first column) or a test campaign (Test in the first column). Each material (Mat.1 to Mat.12) is defined by seven material parameters. However, since defects are defined statistically, one material can be associated to distinct values of cohesive strengths, even though material parameters are kept constant. This will be useful to study the distribution of fragment masses in the last section.

As a guideline, here are the useful associations that one should make, to compare material properties:

- Effect of Young's modulus is studied through Mat.1, Mat.8, and Test1.

- Effect of volumetric mass is studied through Mat.1, Mat.9, Mat.10, and Test4.

- Effect of toughness is studied through Mat.1, Mat.5, Mat.6, and Test7.

- Effect of the minimum cohesive strength is studied through Mat.1, Mat.7, Mat.11, and Test5.

- Effect of the scale parameter is studied through Mat.1, Mat.4, and Test6.

- Mat.3 and Mat.12 involve higher Weibull modulus, they are nearly homogeneous materials.

In test2 (respectively test3), the product $E.\rho$ (respectively E/ρ) is kept constant. The seven test campaigns are conducted at the strain rate $\dot{\varepsilon} = 10^4 s^{-1}$. Mat.2 was selected for comparison purpose with the results obtained in one-dimension (chapter 5).

Computed values: During the simulation, we compute the time evolution of potential energy and fracture energy (e.g. energy dissipated by the cohesive elements), as well as the mass of each fragment. We deduce some useful parameters:

- the time at which the first cohesive element is activated t_{min} (see figure 7.1(c)).

- the time at which potential energy reaches a peak t_f (which stands for time to failure) (see figure 7.1(c)).

- the value of the peak stress σ_{peak}, assuming a linear elastic response before peak stress $\sigma_{peak} = E \, \dot{\varepsilon} \, t_f$. The value of σ_{peak} is approximated analytically, based on the computed value t_f. The elastic assumption is accurate for most strain rates (if $\dot{\varepsilon} \geq 2.10^4 \ s^{-1}$, the true peak stress is slightly, but not exactly, equal to the analytical one).

- the number of fragments, and the average fragment size s_{aver}.

- the distribution of fragment masses.

Computing fragment sizes in a parallel code is not direct. Once a processor detects fragment boundaries, it must communicate them to other processors. That may lead to heavy and penalizing inter-processor communication. From a technical point of view, to address this issue, we created a class containing tetrahedra and facets. Within the body, each tetrahedron (resp. facet) is related to four facets (resp. two tetrahedra). The lack of neighbor indicates a physical or processor boundary. A damage number is associated to each facet, which is broken when damage reaches one. Fragments are detected by looping over the facets, and are constituted of a list of tetrahedra. In the parallel version of the code, each processor computes its fragment class, then they are assembled using ghost tetrahedra on the processor boundaries. The code has been written to minimize inter-processor communication; a processor exchanges only once with its neighbors (see appendix A).

Main issues: The chapter shed light on several technical and physical issues:

- Convergence (section 7.2): We reach steady values (e.g. independent from the mesh) of the number of fragments and the distribution of fragment masses which guarantees the validity of the following studies. As far as we know, this is the first proof of numerical convergence in multi-dimensional fragmentation simulations.

- Energy conversion and characteristic time and length scales (section 7.3): We first present Grady's theory of equilibrium and non-equilibrium fragmentation [Grady 2009]. Then, we enrich Grady's model by adding new time and length scales. We show that two cases arise: at high strain rates, Grady's equilibrium is verified, while at low strain rates fragmentation occurs in a non-equilibrium state. These cases infer very distinct physical mechanisms.

- Scaling of average fragment size and strain rate (section 7.4): We apply the normalization proposed Levy and Molinari [Levy 2010], which has been proved to be valid in one dimension. We show that this normalizations is mostly valid, expect for some tests. We also compare the plate results to Grady's and Glenn and Chudnovsky's models. We argue that Grady's length scale [Grady 1982] is larger than the computed average fragment size because of wave propagation.

- Distribution of fragment masses (section 7.5): We qualitatively underline the role of strain rate and material parameters on the scattering of the distributions.

7.2 Numerical convergence

We first verify the validity of the computed results through a convergence study. In the case of fragmentation, convergence can either concern the number of fragments or the distribution of fragment sizes. Reaching convergence may, however, be technically challenging since fine meshes are usually required to capture the smallest fragments. We benefit from the efficiency of the parallel implementation that the hybrid formulation provides. Running codes on many processors allows us to increase the degrees of freedom significantly and obtain converged results at high strain rates (up to $10^5 s^{-1}$). The simulation of fragmentation at higher strain rates is a simple extension of the work done so far.

A plate made of aluminum oxide AD-995 with nearly no defects (Mat.12 in table 7.1) is meshed with 8.000 to 6.000.000 degrees of freedom. We compute the average fragment size and distribution of fragment masses. Figure 7.3 displays the evolution of the number of fragments with degrees of freedom, obtained for $\dot{\varepsilon} = 10^4 \ s^{-1}$, in two cases: with and without dust. We name dust the fragments composed of one or two tetrahedra. To compare numerical results to experiments,

this elimination would be necessary, since techniques used to uncover fragment sizes,
have a minimum size that can be resolved. The curves in figure 7.4 first increase,
suggesting that every edge of the mesh is at least damaged. Then, they slightly de-
crease until reaching their final value. Some edges of the mesh are broken, others are
damaged or intact. Convergence in terms of number of fragments is thus achieved
for meshes with at least 200000 degrees of freedom. To the best of our knowledge,
convergence has been reached in one dimension [Molinari 2007], but this is the first
hard evidence of fragment convergence in three dimensions.
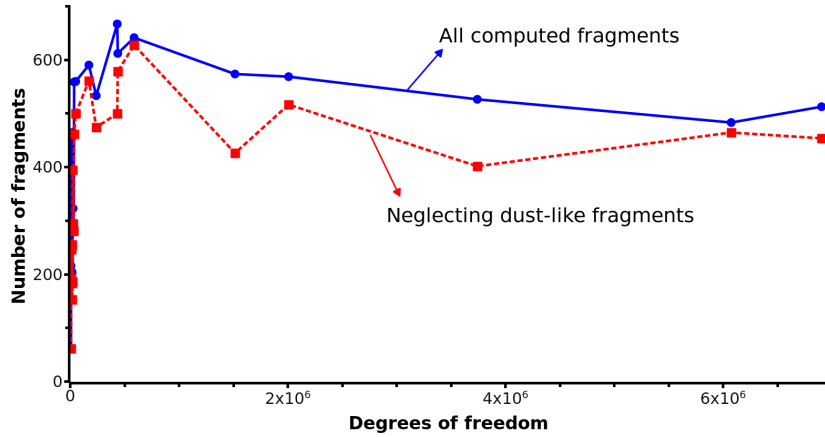
Figure 7.3: Evolution of the number of fragments with the degrees of freedom, for
the strain rate $\dot{\varepsilon} = 10^4 \ s^{-1}$.

Besides, distribution of fragment masses can also be independent from the mesh
if dust is neglected. This simplification may have a counterpart: the left tail of the
distribution may not well represent the physics of fragmentation and we may miss
some self-similar behavior. Figure 7.4 plots the inverse of the cumulative density
function of the normalized fragment masses in two cases: accounting for all the
fragments, and neglecting dust. Note that, in figure 7.4, the x-axis involves the
average fragment mass in order to compare only the shape of distribution of fragment
mass (and not the number of fragments, already achieved previously). When dust
is included in statistics, the curves do not superimpose. Coarse meshes generate
heavier fragments than fine meshes. When dust is neglected, the plots are very
close. This observation suggests that the shape of the distribution of fragment
masses is substantially more sensitive to dust than to mesh fineness.

We also investigate convergence in terms of dissipated energy. Comparing fracture
energy computed for two different plates is not straightforward. Indeed, each plate
contains a given amount of surface energy, which may be converted into fracture
energy. This surface energy is the product of the toughness with the surface of
all the facets. Available energies are thus quantities characteristic of the mesh.
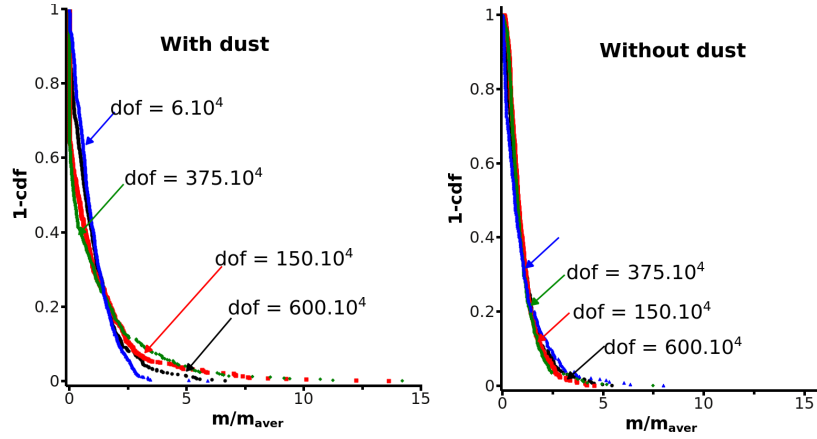
Figure 7.4: Inverse of the cumulative density function of the fragment mass in two cases: with and without accounting for dust (fragments composed of one or two tetrahedra). The x-axis is normalized by the average fragment mass. Strain rate is $\dot{\varepsilon} = 10^4 \ s^{-1}$.

Figure 7.5 displays the available energies of the specimens. Wide variations can be observed because the thickness of the plate is not fixed, it changes from one specimen to the other such that mesh has a good quality and the number of tetrahedra is minimal. Among this available energy, a part is consumed by fully broken facets (broken in figures 7.5 and 7.6), another part is dissipated in the partially damaged facets (damaged in figures 7.5 and 7.6), the rest is not used. Figure 7.6 shows the proportion of the available energy that is dissipated. For small meshes, nearly all the available energy is used, which suggests that all the faces are broken. Then, as the number of degrees of freedom increases, the proportion decreases, first abruptly, than more slowly. More and more facets are either damaged or intact. The proportion does not evolve drastically for fine enough meshes. Figure 7.5 also underlines that the dissipated energy has little dependence upon the degrees of freedom, irrespective to the available energy, for fine enough meshes. This is, however, not a proof of convergence in energy; we can only claim that steady values of the dissipated energy are observed for fine enough meshes.

In summary, for fine enough meshes, the number of fragments and the shape of the fragment mass distribution are independent from the number of degrees of freedom. We also computed the energy dissipated into failure and observed that fine meshes are associated to dissipative features independent from the number of degrees of freedom. The issue of dissipated energy is less obvious, but it seems that a steady state can be reached.
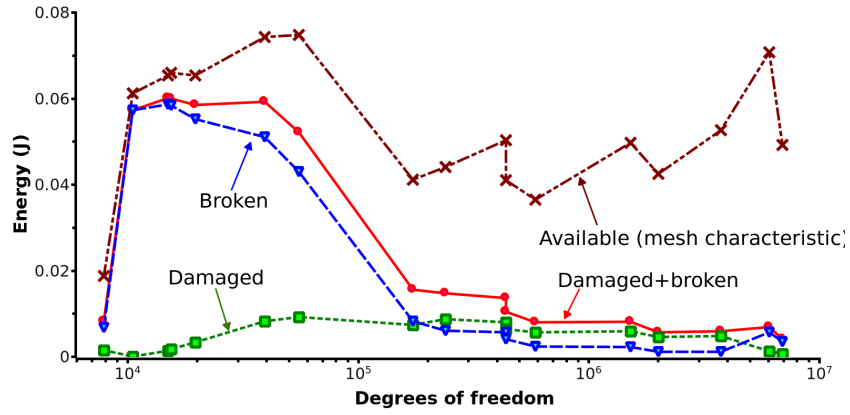
Figure 7.5: Evolution of fracture energy with degrees of freedom, for the strain rate $\dot{\varepsilon} = 10^4 \ s^{-1}$. Energies invested into complete and partial failure are distinguished. The maximum energy that the mesh can provide is also plotted.
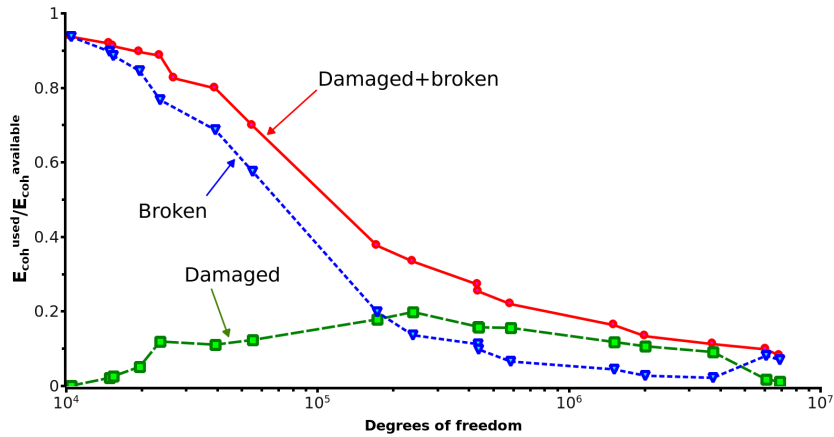

Figure 7.6: Proportion of the available energy dissipated by the fully broken and partially damaged faces, as function of the degrees of freedom. Strain rate is $\dot{\varepsilon} = 10^4 \ s^{-1}$.

7.3 Analysis of Grady's model and its application to heterogeneous materials

7.3.1 Fundamental concepts

7.3.1.1 Grady's theory of fragmentation: a question of energy balance

Based on energy principles, Grady's theory of fragmentation predicts the behavior of materials subjected to dynamic fragmentation. Its fundamental contribution lies in the derivation of local equilibrium (at the fragment scale), rather than global equilibrium (at the structure scale). Indeed, in his key paper [Grady 1982], by deriving the equality between local kinetic energy and fracture energy, he proposed a general expression of the characteristic length scale (the coefficient of proportionality depends on the dimension of the problem):

$$s_{Gr} \propto \left(\frac{G_c}{\rho \, \dot{\varepsilon}^2} \right)^{1/3} \tag{7.2}$$

where ρ is the volumetric mass, G_c is the toughness and $\dot{\varepsilon}$ is the strain rate.

Grady went deeper into the physical understanding of fragmentation [Grady 1988, Grady 2009]. He considered the symmetric expansion of a spherical shell, subjected to an initial outward impulse. The imposed kinetic energy is converted into strain energy, which is, in turn, converted into fracture energy. The volumetric potential energy for an elastic response evolves with time according to:

$$e_{pot} = \frac{1}{2} \rho \, c^2 \, \dot{\varepsilon}^2 \, t^2 = \frac{\sigma(t)^2}{2 \, E} \tag{7.3}$$

where c is the elastic wave speed. Besides, assuming that the fragments constitute a square lattice, the fragment size satisfies the inequality:

$$s \leq 2 \, c \, t \tag{7.4}$$

Equality occurs when cracks evolve independently and are regularly distributed among the body. Strict inequality favorably occurs, because of both stress release waves and the irregular location of defects. Note that the same time t is used in the expressions of the volumetric potential energy e_{pot} and the fragment size s. We comment this assumption at the end of the subsection.

Finally, we denote e_Γ the fracture energy per unit volume, required to generate a rectangular fragment of size s. If we assume that all the fragments have the same size and considering that the problem is two-dimensional, the volumetric fracture energy is:

$$e_\Gamma = \frac{2 \, G_c}{s} = \frac{G_c}{c \, t} \tag{7.5}$$

Fragmentation occurs in equilibrium when $e_{pot} = e_\Gamma$. Equating eq. 7.3 and eq. 7.5 directly provides the characteristic time:

$$t_{Gr} = \left(\frac{2\, G_c}{\rho\, c^3\, \dot{\varepsilon}^2} \right)^{1/3} \tag{7.6}$$

When fracture is in equilibrium, it occurs at the junction of the potential and fracture energy curves, and is, therefore, fully characterized by the time t_{Gr} (figure 7.7). However, Grady explained in [Grady 2009] that some materials subjected to dynamic fragmentation accumulate more potential energy than required. This excess of energy is invested into fracture and leads to smaller fragments than predicted.

Besides, to fully understand Grady's theory, one should note that fracture is assumed to occur since process onset. Indeed, potential energy increases from zero to a value depending on time t (eq. 7.3). The same time t is used to express the length s (eq. 7.4). By assimilating both times, Grady suggests that a stress release wave propagates as soon as potential energy has a non null value, which amounts to considering that fracture occurs since the onset of the process. However, we will show that this assumption may only be valid at high strain rates. In nature, failure does not occur at process onset, but after some time, which is fully determined by failure strength. At high strain rates, the time required to reach failure strength is negligible, whereas at low strain rates, it can be significant. Therefore, we expect Grady's prediction to be accurate at high strain rates, and imprecise at low strain rates. In the following, we adapt Grady's theory to our problem by defining other characteristic times.

7.3.1.2 Adaptation to the plate problem and definition of relevant characteristic times

First, as pointed out by Grady in [Grady 2009], characteristic times and scales are proportional if equality in equation 7.4 is verified. Working with time scales is thus equivalent to working with length scales. In the following, we assume equality in equation 7.4, and we choose to work with time scales.

In addition to the equilibrium time t_{Gr} (equation 7.6), we focus on t_{min} and t_f. t_{min} corresponds to the time when the global stress equals the minimum cohesive strength $\sigma_{c,min}$. t_f corresponds to the time when global potential energy (or equivalently stress) reaches a maximum. In our model, since failure is activated when stress reaches the given threshold $\sigma_{c,min}$, t_f is necessarily larger than t_{min}:

$$t_f \geq t_{min} \text{ where } t_{min} = \frac{\sigma_{c,min}}{E\, \dot{\varepsilon}} \tag{7.7}$$

Note that t_{min}, depending on $\sigma_{c,min}$, can be larger or smaller than t_{Gr}. We will
see in the following that these two possibilities result in very distinct fragmentation
mechanisms. Assuming that the response is elastic until peak stress, equation 7.7 is
equivalent to:

$$\sigma_{peak} \geq \sigma_{c,min} \text{ where } \sigma_{peak} = E \dot{\varepsilon} t_f \tag{7.8}$$

After reaching its peak at t_f, potential energy decreases. It is converted into
fracture energy, generating fragments. The most efficient process would convert
entirely peak potential energy into fracture energy. This leads to the definition of
the characteristic size s_0 and equivalently to the fourth characteristic time $t_{s,0}$:

$$t_{s,0} = \frac{s_0}{2 \, c} = \frac{2 \, G_c \, E}{c \, \sigma_{peak}^2} \tag{7.9}$$

However, peak potential energy may not be fully converted into fracture. Because
of the cohesive element approach, failure occurs if the stress is high enough ($\sigma \geq \sigma_c$).
In fact, failure stops as soon as stress is low enough everywhere, in comparison to the
cohesive strengths. Consequently, the average fragment size s_{aver} is not necessarily
equal to $2 \, c \, t_{s,0}$. This leads to the definition of the time t_s, which is associated to
the actual computed average fragment size:

$$t_s = \frac{s_{aver}}{2 \, c} \tag{7.10}$$

In summary, we have identified five characteristic times t_{Gr}, t_{min}, t_f, $t_{s,0}$, and t_s.
t_{Gr}, t_{min}, and t_f are physical times, whereas $t_{s,0}$, and t_s are associated to the physical
length scales s_0 and s_{aver} (eq. 7.9 and 7.10). In figure 7.7 , we update Grady's
schematic [Grady 2009], which represents energy conversion and equilibrium state,
by adding the other characteristic times and scales.

7.3.2 Toughness or strength controlled?

In this section, we evaluate some of the characteristic times defined previously.
Let us first recall them:

- t_{Gr} is the Grady's equilibrium time. Its expression is given by equation 7.6.

- t_f is the computed time at which potential energy reaches a peak. t_f is not
  necessarily equal to t_{Gr} because of the distribution of cohesive strengths and
  the time needed by the cracks to propagate through the structure.

- $t_{s,0}$ is the theoretical time associated to the size of a fragment s_0(eq. 7.9), if
  peak potential energy is fully converted into fracture energy.

- t_s is the time associated to the computed average fragment size s_{aver}. t_s is not
  necessarily equal to $t_{s,0}$ because potential energy may not be fully converted
  into fracture energy.
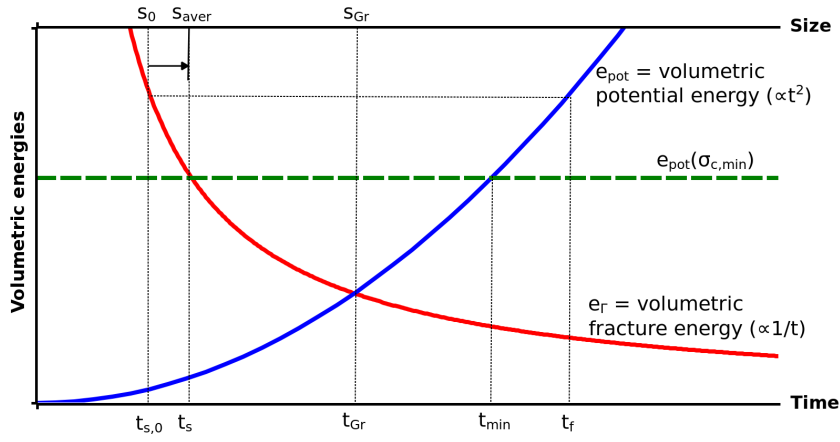
Figure 7.7: Evolution of the volumetric potential energy and fracture energy per unit volume, and display of the characteristic times and sizes in the case $t_{min} \geq t_{Gr}$[Grady 2009]. The volumetric potential energy increases with time, following equation 7.3. The evolution of the dissipated energy per unit volume (eq. 7.5) decreases with fragment size, or equivalently time. Their intersection corresponds to the equilibrium process, which occurs at time t_{Gr}. However, since $t_{min} \geq t_{Gr}$, an excess of potential energy is accumulated. Peak potential energy is reached at t_f. If it is fully converted into fracture energy, the resulting fragment size is $s_0 = 2\,c\,t_{s,0}$. Since peak potential energy may not be entirely used to create new fracture surfaces, the effective fragment size $s_{aver} = 2\,c\,t_s$ is not necessarily equal to s_0.

In this section, we evaluate four of the characteristic times defined previously (t_{Gr}, t_f, $t_{s,0}$, and t_s), leaving t_{min} aside. We have focused on the response of material Mat.1 (c.f. table 7.1) and have conducted simulations at strain rates ranging from $\dot{\varepsilon} = 10 \ s^{-1}$ to $\dot{\varepsilon} = 10^5 \ s^{-1}$. Figure 7.8 illustrates the evolution of these times with strain rate. It underlines that the two theoretical curves associated to t_{Gr} and $t_{s,0}$, as well as the computed curve associated to t_f, cross at the same point $\dot{\varepsilon}_{cross}$:

$$\dot{\varepsilon}_{cross} \ = \ \frac{\dot{\varepsilon}_0}{2} \ \text{where} \ \begin{cases} \dot{\varepsilon}_0 = \frac{\sigma_{peak}}{E \, t_0} \\ t_0 = \frac{G_c \, E}{c \, \sigma_{peak}^2} \end{cases} \tag{7.11}$$
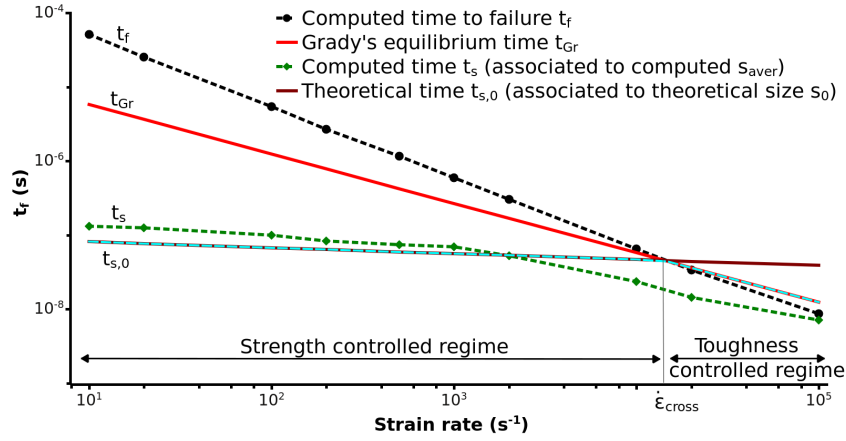
Figure 7.8: Evolution of the four characteristic times with the strain rate, in log-log axes.

This cross point is fundamental in the understanding of the physics of fragmentation. It is the limit between two distinct regimes. Note that $\dot{\varepsilon}_{cross}$ is a function of material parameters and measured peak stress. Its value is half the value of $\dot{\varepsilon}_0$ which is a parameter first defined by Camacho and Ortiz in [Camacho 1996] and reused several times [Drugan 2001, Zhou 2006c, Levy 2010]. $\dot{\varepsilon}_0$ is a characteristic loading rate which scales the fragmentation behavior. A cohesive element, characterized by the toughness G_c and the cohesive strength σ_{peak}, which is subjected to $\dot{\varepsilon}_0$ will break in the amount of time t_0. During the same t_0, stress waves propagate, from the fracture place to the surrounding areas. The encompassed regions are characterized by the length scale is $s_0 \ = \ 2 \, c \, t_0$. Note the similitude between t_0 and $t_{s,0}$ defined in equation 7.9. The time required to generate a fragment of size s_0 (derived from energy equilibrium) is twice the time required to open a cohesive element (derived from dimensional analysis). We also emphasize that the time and length scales derived by Camacho and Ortiz [Camacho 1996] were originally material parameters. Here, they are function of the peak stress, which depends on strain rate.

Let us now detail the two regimes, $\dot{\varepsilon} \leq \dot{\varepsilon}_{cross}$ and $\dot{\varepsilon} \geq \dot{\varepsilon}_{cross}$, by focusing both on the quantity of potential energy stored in the body and the quantity of energy dissipated into failure.

Case $\dot{\varepsilon} \leq \dot{\varepsilon}_{cross}$**:**   As pointed out by figure 7.8, time to failure t_f is larger than equilibrium time t_{Gr}. This case corresponds to figure 7.7. The governing mechanisms of this regime are:

- Stored energy: Potential energy stored in the body is larger than the Grady's equilibrium energy, and fragmentation occurs at a level of energy which overpasses equilibrium.

- Most efficient release of energy: In the most efficient scenario, potential energy is fully converted into fracture energy and generate fragments of size s_0 (which corresponds to time $t_{s,0}$).

- Effective release of energy: In the actual scenario, stored energy is only released partly into fracture. The conversion is indeed not complete because the fracture process stops when the structure is sufficiently released (e.g. when the stress is low enough everywhere in comparison to the cohesive strengths, see section 7.3).

- Consequence on s_{aver}: At small strain rates, the average size s_{aver} is larger than the theoretical size s_0 (and equivalently $t_s \geq t_{s,0}$). Moreover, as schematically explained by figure 7.7, the average size s_{aver} is smaller than the equilibrium size s_{Gr} (and equivalently $t_s \leq t_{Gr}$).

In summary, the range $\dot{\varepsilon} \leq \dot{\varepsilon}_{cross}$ is associated to non-equilibrium fragmentation, and is mainly controlled by the value of the cohesive strengths. Low enough strain rate behaviors are thus strength controlled (and consequently probabilistic), and are associated to non-equilibrium processes.

Case $\dot{\varepsilon} \geq \dot{\varepsilon}_{cross}$**:**   As pointed out by figure 7.8, time to failure t_f is a bit smaller than equilibrium time t_{Gr}. The governing mechanisms of this regime are:

- Stored energy: Contrary to the previous case, peak potential energy is insufficient to lead to such a fine breakage of the structure. The reason for this limitation lies in the finite values of the cohesive strengths. Within the cohesive elements, stresses cannot exceed the cohesive stress. As a result, global potential energy is also constrained, and peak potential energy cannot reach Grady's equilibrium energy. Failure time t_f is thus lower than t_{Gr}. A natural question that may arise is: if peak potential energy is not high enough, how can the structure fragment? This is made possible by the duration of the fragmentation process. Indeed, since it is not instantaneous, energy conversion has time to establish and to supply more potential energy than initial

peak. In dynamics, kinetic energy is accumulated in large excess within the structure. In parallel to the direct conversion of potential energy into failure energy, an additional transfer takes place. Kinetic energy is converted into potential energy, which is in turn used in failure. Therefore, the sum of the two contributions (peak potential and converted kinetic energies) over time can reach Grady's prediction. This mechanism is also described in section 4.2. The process is in equilibrium.

- Post-peak stress behavior: After peak stress, two mechanisms cohabit. On the one hand, we keep pulling on the plate boundaries and potential energy keeps increasing. On the other hand, fracture is initiated at many places and dissipate energy. Both mechanisms are evolving 'independently'. This state can occur because of the 'low' velocity at which stress waves are propagating. Indeed, information that fracture happens is broadcast at the elastic wave speed c, while we are pulling on the plate boundary at the velocity $\dot{\varepsilon}.L_{plate}/2$. In this regime, failure information is not broadcast fast enough in comparison to the applied velocity ($c \ll \dot{\varepsilon}.L_{plate}$). Note that this competition also occurs in the other regime, but it is not significant since wave speed is much larger than boundary velocity.

- Consequence on s_{aver}: Since potential energy is stored both before and after peak stress, the total stored potential energy reaches Grady's equilibrium energy. This regime evolves in quasi-equilibrium and the average fragment size tends to Grady's prediction.

Therefore high enough strain rates lead to fragmentation processes which are not instantaneous, smoother, less random, and in equilibrium. Highly dynamic fragmentation is toughness controlled.

These two cases can be distinguished easily in figure 7.8 : t_s is collinear to t_{Gr} is the toughness controlled regime, whereas t_s behaves similarly as $t_{s,0}$ in the strength controlled regime.

7.3.3 A measure of the equilibrium

What naturally comes to mind is whether there exists a way of quantifying how balanced fragmentation is. In the previous section, we have shown that quasi-static fragmentation is probabilistic (e.g. controlled by defect failure strengths) and does not behave in equilibrium, while dynamic fragmentation is controlled by toughness and occurs in a more equilibrium state. Updating the idea of Grady in [Grady 2009], we use the non-dimensional number F in order to characterize more accurately energy conversion of fragmentation:

$$F = max \left(\frac{t_f}{t_s} \; ; \; 1 \right) \tag{7.12}$$

Large values of F are associated to strength controlled fragmentation. $F = 1$ is the equilibrium case.

If peak potential energy is fully converted into fracture energy, then $t_s = t_{s,0}$. The use of eq. 7.8 and eq. 7.9 leads to the analytical form of the ratio F:

$$F_{theo} = max \left(\frac{c \, \sigma_{peak}^3}{2 \, E^2 \, G_c \, \dot{\varepsilon}} \; ; \; 1 \right) \tag{7.13}$$

where σ_{peak} is a function of the distribution of defects, the strain rate, and the Young's modulus. Its value is here deduced from the time to failure and equation 7.8.

Figure 7.9 displays the evolution of the numerical and analytical ratios F_{num} and F_{theo} with strain rate. For $\dot{\varepsilon} \ll \dot{\varepsilon}_{cross}$, both ratios are decreasing as power laws. The theoretical expression predicts values of F slightly larger than the computed ones because the assumption that potential energy is fully converted into fracture is not exact (c.f. paragraph 7.3.2). Large values of F are associated to non-equilibrium processes during which an excess of potential energy is accumulated (large value of the time to failure t_f). On the contrary, F gets close to one when strain rate is larger than $\dot{\varepsilon}_{cross}$, which suggests that exceeding potential energy is inconsequential. In this case, fragmentation process behaves in a quasi-equilibrium state. The value of F is thus a representative ratio of how energetically balanced is fragmentation.
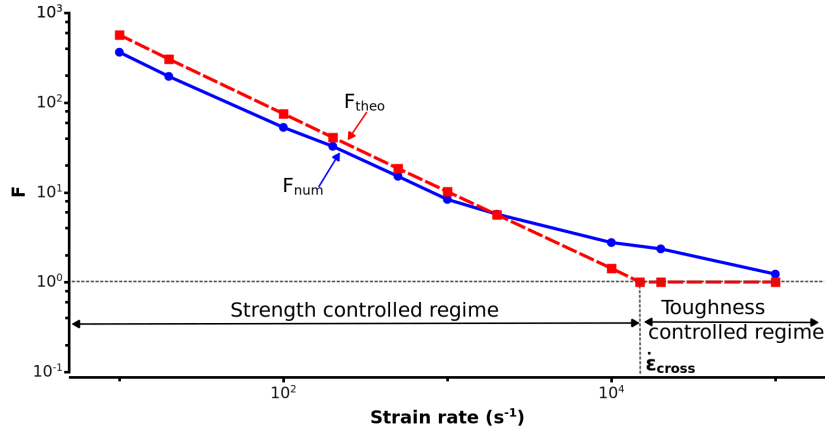

Figure 7.9: Numerical and theoretical ratio F in log-log axes for Mat.1.

7.4   Normalization of average fragment size and strain rate

We are here interested in verifying whether the scaling defined in chapter 5 in one dimension is valid in multiple dimensions. In Levy and Molinari [Levy 2010] and

chapter 5, we defined the normalization:

$$\bar{\dot{\varepsilon}}_{LM} = \frac{\dot{\varepsilon}}{\dot{\varepsilon}_0} \text{ and } \bar{s}_{LM} = \frac{s_{aver}}{c \, t_0 \, f(\text{defects})} \tag{7.14}$$

$\dot{\varepsilon}_0$ is expressed in terms of the average cohesive strength, rather than peak stress. $f(\text{defects})$ is a function of the left tail of the cohesive strength distribution, as well as the minimum and average cohesive strengths ($\sigma_{c,min}$ and μ_{init}):

$$f(\text{defects}) = \sqrt{\frac{2}{a+1}} \left(\frac{\sigma_{c,min}}{\mu_{init}} \right)^{1/5} \tag{7.15}$$

a is a number that quantifies the rate of failure initiation and is comprised between 0 and 1. $a = 0$ suggests that no defect activation occurs, while $a = 1$ indicates that all the defects are initiated simultaneously.

This unique empirical law describes the evolution of the normalized average fragment size with normalized strain rate for one-dimensional fragmentation:

$$\bar{s} = \frac{3}{1 + 4.5 \, \bar{\dot{\varepsilon}}} \tag{7.16}$$

This expression results in a representative curve that is close to Glenn and Chudnovsky's model. Glenn and Chudnovsky [Glenn 1986a] derived an analytical expression of the average fragment size, using balance energy. Contrary to Grady, they took into account failure strength and they explained that potential energy is prevailing in quasi-static, whereas kinetic effects are dominant in dynamics. Figure 7.10 displays these two models, along with Grady's prediction and numerical results for the plate under biaxial tension.

As highlighted in figure 7.10, at high strain rates, all points fall into a reasonably narrow range. Average fragment size values are all smaller than Grady's prediction. This is due to dynamics effects. Indeed, at high strain rates, the velocity at which plate boundaries are pulled is high compared to elastic wave speed. Broadcasting information from failure location to plate boundaries thus required some time during which potential energy continues to be accumulated. This excess of potential energy explains why we compute more fragments than Grady's prediction. Although high strain rates are associated to equilibrium processes, the resulting fragment size is smaller than the predicted one because of dynamic effects. Moreover, still in the high strain rate range, the -2/3 power law exponent predicted by Grady (equation 7.2) seems to be valid. In summary, in the toughness controlled regime, we predict smaller fragments than Grady because of dynamics effects, and we observe the same -2/3 exponent than Grady.
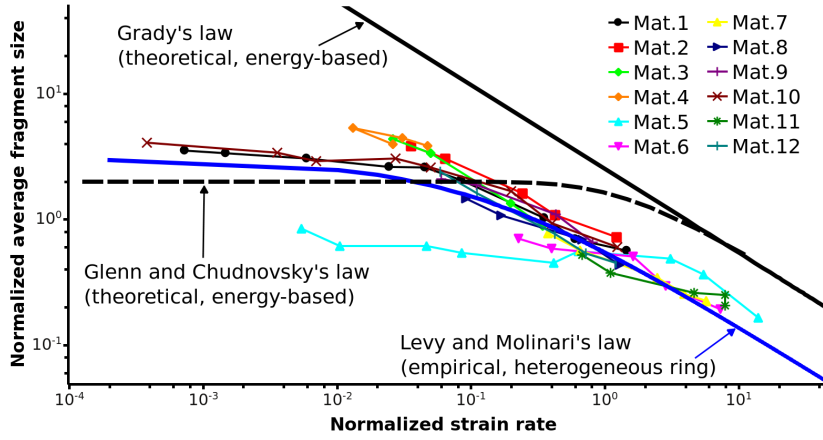
Figure 7.10: Normalized average fragment size function of normalized strain rate in log-log axes. Comparison of the present results to Grady's, Levy and Molinari's, and Glenn and Chudnovsky's models.

By contrast, in the strength controlled regime, normalization seems not adequate in every case. Indeed, while for most materials the one-dimensional normalization is still valid, for Mat.5, Mat.6, it looks inaccurate. In quasi-static, their representative curves are below the predicted ones because of size effects. Mat.5 and Mat.6 are both ductile and generate a few fragments in quasi-statics. For instance, let us consider Mat.5. At strain rate $\dot{\varepsilon} = 10 \ s^{-1}$, e.g. $\bar{\bar{\varepsilon}} \simeq 0.01$, we compute 3 fragments. To fall close to Levy et al.'s models, we should have computed 0.2 fragments, which is obviously impossible. At low strain rate, the specimen size strongly influences the normalization efficiency. If we had considered a larger specimen, the normalized average fragment size would have followed the global trend and could have been predicted by equation 7.16. Glenn and Chudnovsky's law, which is based on energy arguments is neither adequate since the regime is not governed by energy balance but defect strength. It is thus more complex to predict the number of fragments at low strain rates than at high strain rates.

7.5   Distribution of fragment masses

In sections 7.3 and 7.4, we assumed that all the fragments have the same size s_{aver}, which is naturally not true. Fragments have distinct sizes and shapes. In this section, we are interested in the effect of strain rate and material parameters on the distribution of fragment masses. In order to focus solely on the shape of the distribution (its average is related to s_{aver} and has been studied in section 7.4), we normalize the fragment masses with the average fragment mass. Dust-like fragments (one or two tetrahedra) are neglected.

7.5.1 Influence of strain rate

When fragmentation occurs in perfect equilibrium, each fragment is generated independently from the others. It corresponds to $F = 1$ in section 7.3.3. This asymptotic case is characterized by the absence of crack interactions and is mainly governed by energetic arguments, the problem remains local. In such perfect regimes, theory predicts exponential distribution of fragment masses for one dimension geometries [Grady 1985, Lienau 1936]. Equilibrated fragmentation may thus lead to exponential fragment distribution, e.g. Weibull distributions with modulus one (equation 7.17).

$$\text{Weibull distribution}: cdf = 1 - e^{-\left(\frac{m}{\lambda\, m_{aver}}\right)^{m_w}} \text{ with } m_w > 0 \text{ and } \lambda > 0$$
$$\text{Exponential distribution}: cdf = 1 - e^{-\left(\frac{m}{\lambda\, m_{aver}}\right)} \text{ with } \lambda > 0$$
$$(7.17)$$

Fragmentation without crack interaction is the simplest model. Nonetheless, in real experiments, fragment size distributions exhibit more complex features. There exists experimental evidence that fragment mass distribution follows Weibull distribution (equation 7.17) with Weibull modulus varying typically from 0.5 to 2.5 [Gilvarry 1961a, Grady 1990, Mott 1947]. Other types of distributions, combining power and exponential laws have also been considered [Åström 2004b] (see chapters 2 and 6). Naturally, since F never reaches unity in our simulations, but only gets close to it at very high strain rates (see figure 7.9), we expect toughness controlled fragmentation to generate fragments whose masses tend to follow Weibull distribution with exponent close to one (e.g. exponential distribution).

Conversely, at low strain rates, crack interactions cannot be neglected. Stress waves are propagating fast in comparison to the loading, and fragments are not generated independently. As a result, their masses strongly depends upon both the stress field, which in turn depends upon the geometry of the structure and the defects. Thus, we expect strength controlled fragmentation to generate fragments with more disperse sizes. Figure 7.11 displays the fragmentation patterns of a plate subjected to the strain rates $\dot{\varepsilon} = 2.10^3 s^{-1}$ and $\dot{\varepsilon} = 2.10^4 s^{-1}$. It underscores that high strain rates induce more fragments than low strain rates. It is, however, not obvious to draw any conclusion on the fragment size distributions from these visual representations.

Consequently, in order to verify whether this intuition is true, we plot in figure 7.12 the inverse of the cumulative distribution function of the fragment masses. Each curve is the combination of ten Monte Carlo simulations with same mesh, same material Mat.1 (c.f. table 7.1), and distinct random seeds of cohesive strengths. Figure 7.12 underlines that small strain rates generate more disperse fragment distributions than large strain rates (the standard deviation of the masses for $\dot{\varepsilon} = 2.10^3 s^{-1}$ is
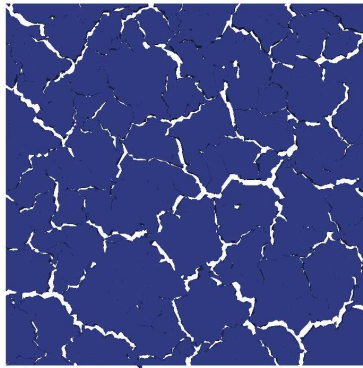
(a)
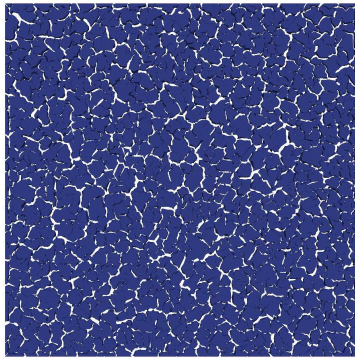
(b)

Figure 7.11: Fragmentation patterns computed for the strain rate (a) $\dot{\varepsilon} = 2.10^3 s^{-1}$, (b) $\dot{\varepsilon} = 2.10^4 s^{-1}$. High strain rates lead to more fragments and more regular patterns than low strain rates.

2.38, while it is 0.98 for $\dot{\varepsilon} = 2.10^4 s^{-1}$). Figure 7.12 also represents the best Weibull fits for $\dot{\varepsilon} = 2.10^3 s^{-1}$ and $\dot{\varepsilon} = 2.10^4 s^{-1}$. As it is obvious from figure 7.12, low strain rates cannot be represented by Weibull distributions, whereas higher strain rates may be. At strain rate $\dot{\varepsilon} = 2.10^3 s^{-1}$, the Weibull fit resolves the behavior of the lighter fragments, but clearly not the heavier. By contrast, at strain rate $\dot{\varepsilon} = 2.10^4 s^{-1}$, a single Weibull distribution fits accurately both the light and heavy fragments. Besides, the associated Weibull modulus is one, e.g. fragment mass distribution tends to be exponential.

In summary, the exponential function, which has been proved to be associated to Poisson process (no interaction between cracks), appropriately reflects distribution of fragment masses for high strain rates. At low strain rate, Weibull fit is not relevant. These observations convey the idea that high strain rates are associated to regular processes, while low strain rates generate more chaotic response.
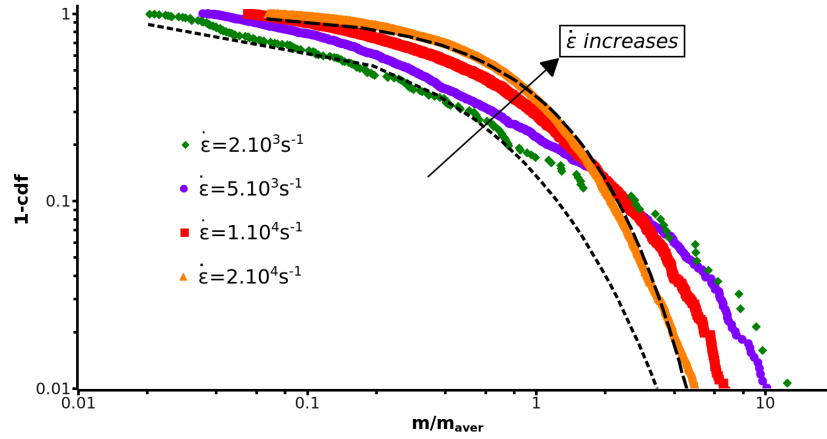
Figure 7.12: Inverse of the cumulative density function of the normalized fragment mass in log-log axis. Influence of the strain rate and best Weibull fits for $\dot{\varepsilon} = 2.10^3 s^{-1}$ and $\dot{\varepsilon} = 2.10^4 s^{-1}$ (dashed curves), for Mat.1. The x-axis is normalized by the average fragment size.

7.5.2 Influence of material parameters

We first focus on bulk parameters (Young's modulus and volumetric mass). Figures 7.5.2, 7.5.2, 7.5.2 underline the role of the Young's modulus on the fragment size distribution for test1, test2, and test3. Small Young's moduli lead to more scattered distributions than large moduli. Note that the shape of the distributions look different from figure 7.12 because the axes are not logarithmic. To quantify the scattering of the distribution, we compute their standard deviations. Figure 7.17 displays the curves associated to test1(volumetric mass ρ constant), test2 ($E.\rho$ constant), test3 (wave speed constant), and test4 (Young's modulus constant). Standard deviation

of the masses is decreasing with Young's modulus, and is almost independent from volumetric mass. Contrary to volumetric mass, Young's modulus is thus a governing parameter of the fragment masses.

Figure 7.13: Effect of bulk properties on fragment mass distributions for Test1: ρ is constant. See table 7.1 for more details about the tests.

Figure 7.14: Effect of bulk properties on fragment mass distributions for Test2: $\rho.E$ is constant. See table 7.1 for more details about the tests.

Then, effects of defect parameters are investigated via test5 (minimum cohesive strength varies), test6 (scale parameter varies), and test7 (toughness varies). In test5 (figure 7.5.2), we study the response of six distinct minimum cohesive strengths. For each simulation, we computed the distribution fragment masses and their standard deviation. To verify whether minimum cohesive strength affects fragment masses, we verify that all the standard deviations are very close (average value of the standards deviation = 1.44 and standard deviation of the standard deviations = 0.068, which
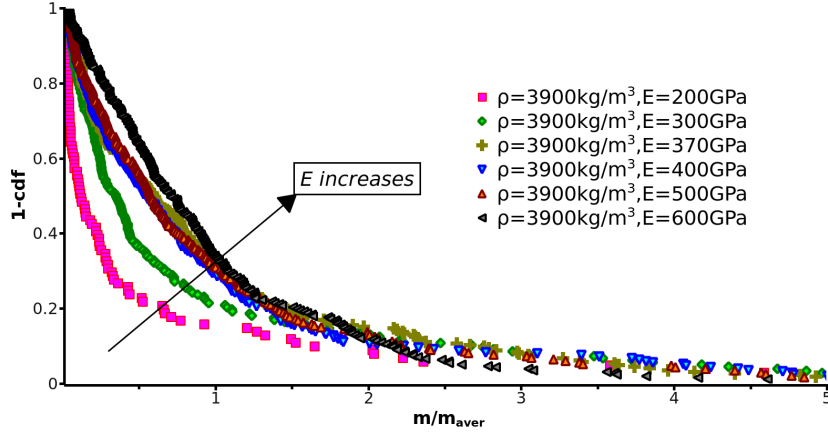
Figure 7.15: Effect of bulk properties on fragment mass distributions for Test3: E/ρ is constant. See table 7.1 for more details about the tests.
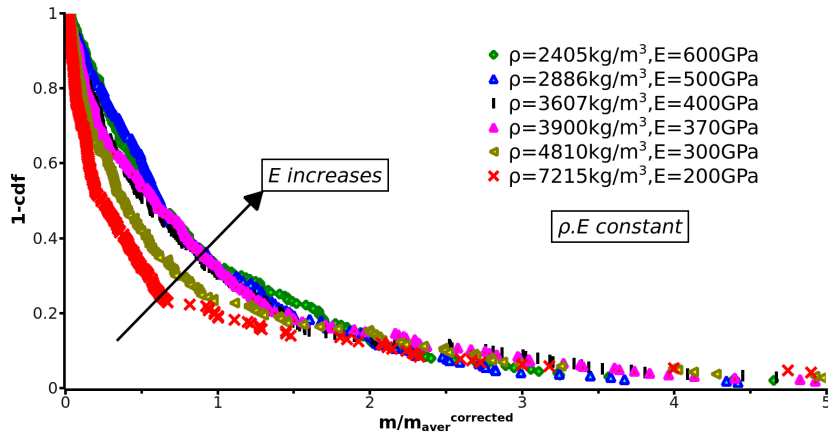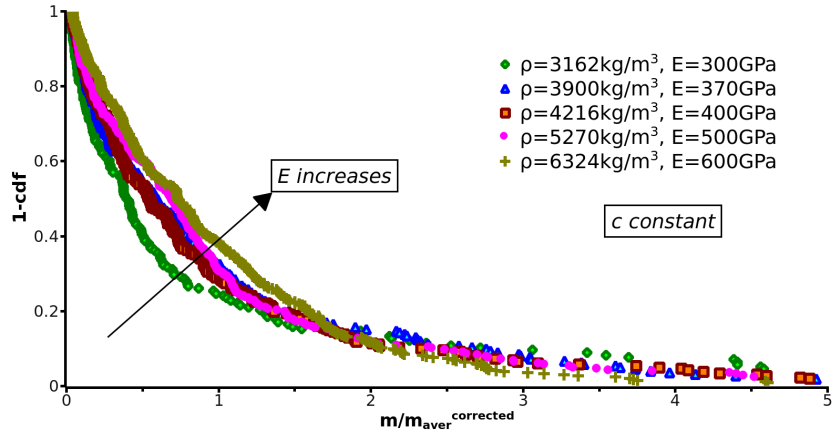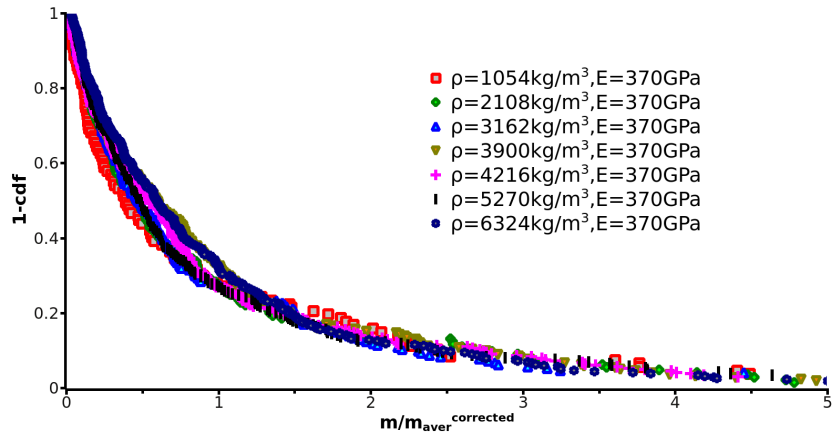

Figure 7.16: Effect of bulk properties on fragment mass distributions for Test4: E is constant. See table 7.1 for more details about the tests.
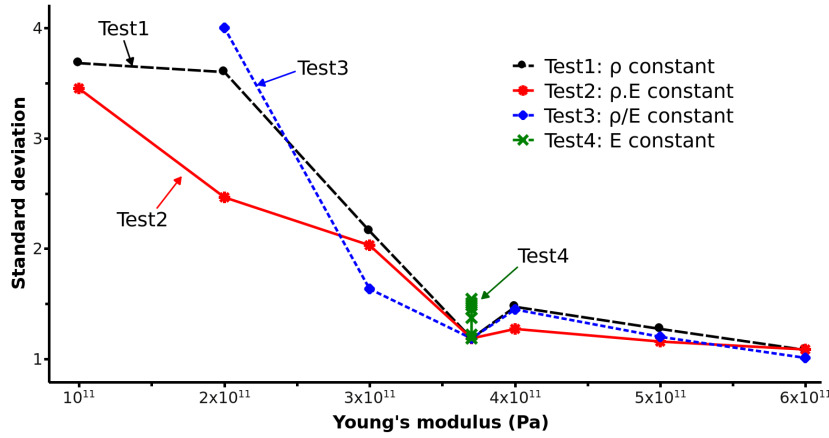
Figure 7.17: Standard deviations of the fragment masses, normalized by the average fragment mass. Small Young's modulus E generates scattered distributions. Volumetric mass ρ has little impact on the fragment masses. Tests are referenced in table 7.1.

is very low). It suggests that, for the cases chosen here, the minimum cohesive strength has little influence on the shape on the distribution. We proceed similarly with test6 and test7 (figures 7.5.2 and 7.5.2). Toughness also has negligible effect (average=1.254 and standard deviation=0.146). By contrast, the scale parameter of the Weibull distribution has a significant role (standard deviation increases from 1.18 for $\lambda = 50 MPa$ to 4.01 for $\lambda = 500 MPa$). Distributions of defects with a large scale parameter (which corresponds to highly heterogeneous materials) lead to scattered fragment mass distributions. In other words, the more homogeneous the material is, the more equally-sized the fragments are. When the material is nearly homogeneous, all the defects tend to be nucleated simultaneously. Since the defects are randomly distributed in space, fragments should have about the same size. On the contrary, when the material is heterogeneous, defect activations are distributed in time and are more sensitive to stress wave healing effects. There is thus less chance to obtain regular fragmentation patterns.

7.6   Conclusion

We simulated the fragmentation of a thin plate subjected to biaxial tension, for a wide range of strain rates. A hybrid numerical framework, coupling discontinuous Galerkin and cohesive approaches, has been used. In the context of fragmentation, the main advantage of the discontinuous Galerkin framework is its ability to handle naturally discontinuities like fracture lines, and to be easily parallelized. Cohesive elements are activated dynamically, as soon as local stress reaches the cohesive strength. By defining Weibull distributions of cohesive strengths, we modeled the micro-structural heterogeneity of the material. Varying the parameters used in
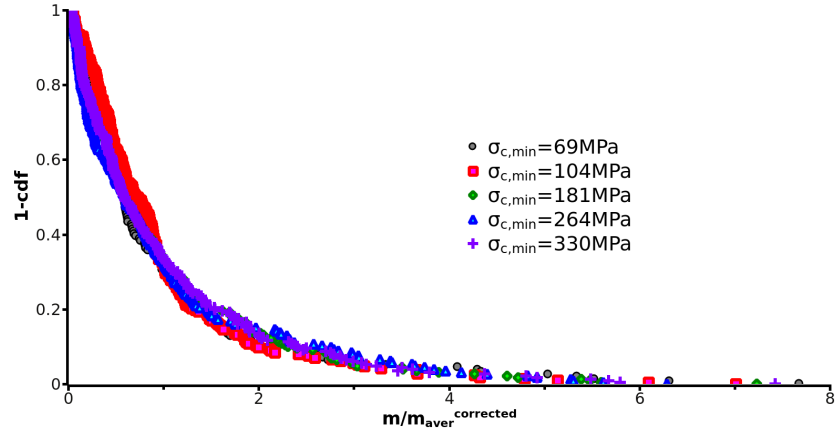
Figure 7.18: Effect of defect properties on fragment mass distributions for Test5: only $\sigma_{c,min}$ varies. See table 7.1 for more details about the tests.
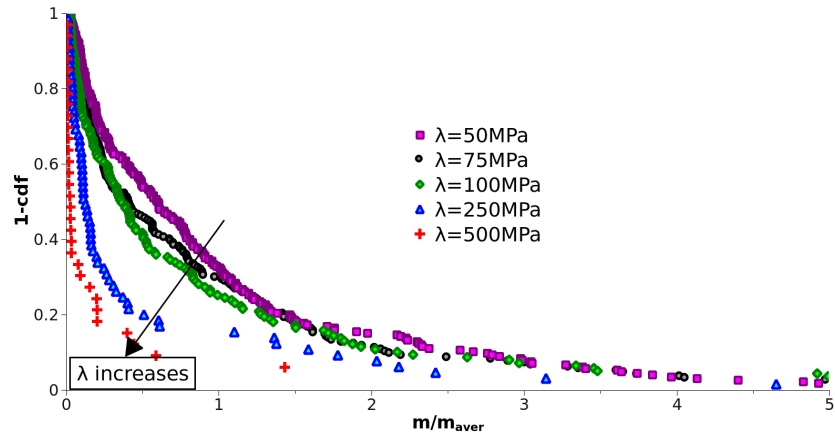
Figure 7.19: Effect of defect properties on fragment mass distributions for Test6: only λ varies. See table 7.1 for more details about the tests.
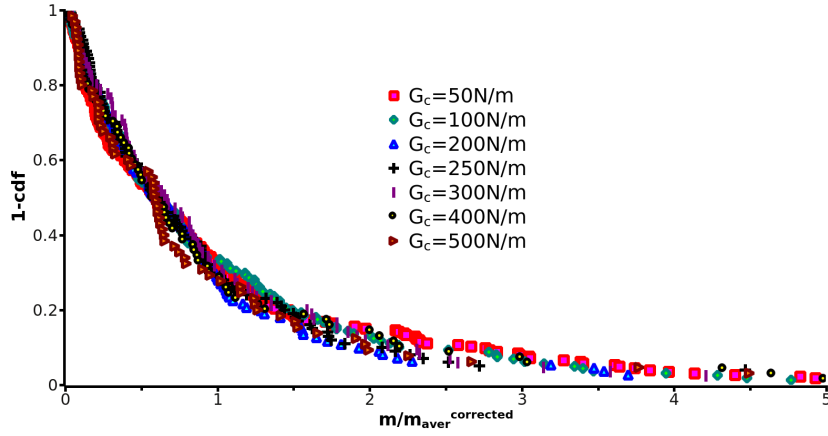
Figure 7.20: Effect of defect properties on fragment mass distributions for Test6: only λ varies. See table 7.1 for more details about the tests.

the Weibull distribution (minimum cohesive strength, scale parameter, and Weibull modulus), as well as material parameters (Young's modulus, volumetric mass, and toughness) allowed us to quantify their influence on fragmentation. We tackled the issue of convergence and showed that, for fine enough meshes, the number of fragments, and the distribution of fragment masses are independent from the degrees of freedom.

First, we questioned the meaning of convergence, which may be dependent upon the evaluation criterion. It can either be dissipated energy, or average fragment size, or distribution of fragment masses. We show that for fine enough meshes, we reach steady values for any of these criteria. In the case of the distribution of fragment masses, we neglected fragments made of one or two tetrahedra. By selecting adequate meshes, we thus guarantee the independence of our results respectively to the mesh.

We detailed Grady's model in which he defined equilibrium time and length scales. Fragmentation occurs in equilibrium when potential energy is locally converted into fracture energy. Crack interactions and time needed to reach the minimum cohesive strength are thus neglected in Grady's theory. In our model, since we included both effects, we defined new characteristic time and length scales that account for the distribution of defects and the dynamics of fragmentation. We showed that, depending on material parameters, two regimes arise: the strength controlled and the toughness controlled. The strength controlled regime corresponds to low strain rates. It is mainly governed by the microstructure, and the geometry of the body; fragmentation occurs in a non-equilibrium state. Reversely, fragmentation at high strain rate is in equilibrium and thus behaves following energy arguments. The transition between these two regimes, as well as asymptotic values of the average

fragment size have been theoretically determined. At high strain rates, we predict more fragments than Grady because of the dynamics of stress waves by a factor of three, but we recover the -2/3 slope that his analytical model predicts.

Concerning the distribution of fragment masses, we have underlined that high strain rates generate distributions tending to be driven by Weibull-like laws. Conversely, low strain rates lead to more disperse distributions which are less predictable. Moreover, besides strain rate, we have identified that only Young's modulus and material heterogeneity affect fragment mass distribution. Other parameters studied (volumetric mass, toughness, minimum failure strength) seem to have no significant effect.

In summary, for strain rates and material parameters such that fragmentation is strength controlled, defects and geometry are prevailing; probabilistic and dynamics effects dominate, which generate irregular fragment patterns. On the contrary, in the highly dynamic regime, fragmentation is toughness controlled, and energy arguments govern the physical mechanisms, which generate predictable and more regular fragmentation patterns.

From two- to three-dimensional fragmentation

Since very recently, simulations of dynamic fragmentation have had access to three-dimensional geometries. The increase in computational power and the development of efficient parallel codes are offering new opportunities. As an illustration, this chapter [1] glances at the fragmentation of a hollow sphere, constituted of a heterogeneous material. The influence of strain rate effect on fragment mass distributions is studied and compared to the ring and plate tests (see chapters 6 and 7). The thickness of the sphere ranges extreme values, e.g. from the very thin thickness (which amounts to quasi two-dimensional fragmentation) to the plain sphere. The fragmentation of six distinct geometries is studied and induces fragments whose shapes exhibit two- and/or three-dimensional features.

8.1 Description of the numerical simulations

8.1.1 Hollow sphere geometry and mesh

The geometry is a hollow sphere with variable thickness. We selected six geometries, with same external radius $R_{ext} = 0.01$ meters and variable internal radius $0 \leq R_{int} \leq 0.0099$. We classify the spheres depending on R_{int}:

Geometry (Geom.)	1	2	3	4	5	6
Internal radius (R_{int})	0	0.00375	0.006	0.0085	0.00925	0.0099
Degrees of freedom	13.352.787	12.349.098	5.428.845	2.667.972	2.744.544	818.928

Table 8.1: Classification of the studied geometries as function of the internal radius, and number of degrees of freedom of the associated mesh. Radii are in meters.

In practice, since a sphere is highly symmetric, we only consider $1/8^{th}$ of a sphere and adapt boundary conditions to enforce the symmetry. This spatial simplification

---

[1]This chapter constitutes the base of an article in preparation, dealing with fragment shapes, and co-authored by S.Levy, J.F.Molinari, R.Radovitzky.

allows us conducting simulations on finer meshes, and therefore, to reach higher strain rates. Meshes are generated with the free software Gmsh [Geuzaine], and are constrained so that they all have the same element size. Figure 8.1 displays three of the six meshes.

8.1.2   Heterogeneous material

The material is an aluminum oxide, named AD-995 or Al_2O_3 99.5%. The bulk is elastic and characterized by its Young's modulus $E = 370\ GPa$, Poisson ratio $\nu = 0.22$, and volumetric mass $\rho = 3900\ kg.m^{-3}$. Failure parameters are set to $G_c = 50\ N.m^{-1}$ and $\sigma_{c,min} = 264\ MPa$. In addition, we assume the cohesive strengths to follow a Weibull distribution with Weibull's modulus two and scale parameter 50 MPa.

8.1.3   Loading conditions

The specimens are loaded uniformly via an initial impulse. Strain rate varies from $\dot{\varepsilon} = 10^3\ s^{-1}$ to $\dot{\varepsilon} = 10^5\ s^{-1}$. Since the sphere is centered on the origin, the initial velocities are:

$$v_x(x, y, z) = \dot{\varepsilon}\ x \tag{8.1}$$
$$v_y(x, y, z) = \dot{\varepsilon}\ y \tag{8.2}$$
$$v_z(x, y, z) = \dot{\varepsilon}\ z \tag{8.3}$$

8.1.4   Objectives

In the next sections, we study the fragmentation of the hollow spheres and focus on the following issues:

1. **Strain rate effect:** How does the loading affect the distribution of fragment masses?

2. **Dimensionality effect:** Does the average fragment size depend on the internal radius R_{int}? To what extent does dimensionality affect the shape of the fragments?

8.2   Influence of strain rate

8.2.1   Minimum strain rate leading to fragmentation and fragmentation patterns

The values of the strain rate were chosen to respect some energetic and numerical constraints. The highest value ($\dot{\varepsilon} = 10^5\ s^{-1}$) is set so that the computed results display converged features, keeping the same mesh for every strain rate. The smallest value ($\dot{\varepsilon} = 10^3\ s^{-1}$) is limited by energy arguments. Indeed, because of the
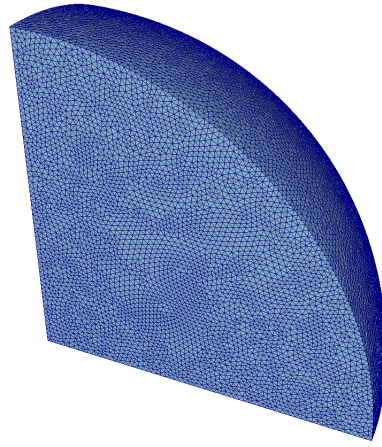
(a)
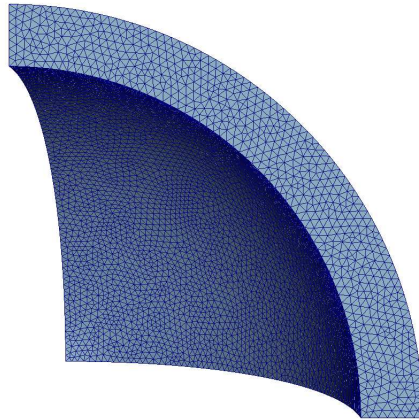
(b)
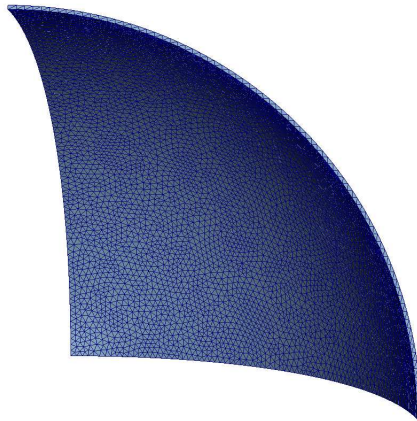
(c)

Figure 8.1: Three meshes employed in the numerical simulations: (a) Geom.1 ($R_{int} = 0$), (b) Geom.4 ($R_{int} = 0.0085$), (c) Geom.6 ($R_{int} = 0.0099$)

impulse boundary conditions, the total energy injected into the system is exactly
the impulse energy E_{in}, which is applied through the velocity conditions detailed
by equations 8.1 to 8.3. As highlighted by figure 8.2(c), the initial kinetic energy
(which equals E_{in}) is converted into potential energy. The body expands elastically
and the stress reaches the peak value σ_{peak}. If $\sigma_{peak} \leq \sigma_{c,min}$, failure cannot take
place. The condition for failure to initiate is thus:

$$E_{in} = \frac{\Pi}{20}\rho\dot{\varepsilon}^2\left(R_{ext}^5 - R_{int}^5\right) \tag{8.4}$$

$$E_{pot,peak} = \frac{\Pi}{12}\frac{\sigma_p^2}{E}\left(R_{ext}^3 - R_{int}^3\right) \tag{8.5}$$

$$E_{int} > E_{pot,peak} \Leftrightarrow \text{failure} \tag{8.6}$$

Given the distribution of defects, this condition leads to the strain rate $\dot{\varepsilon} \simeq 700 \; s^{-1}$
for the thinnest geometry (Geom.5), and to the strain rate $\dot{\varepsilon} \simeq 880 \; s^{-1}$ for the
thickest geometry (Geom.1) . Figure 8.2 displays the case of the geometry Geom.6
subjected to the strain rate $\dot{\varepsilon} = 10^3 \; s^{-1}$. Figure 8.2(c) represents the evolution of
the kinetic, potential, and cohesive energies with time. Since kinetic energy never
reaches zero, the body accumulates a sufficient amount of energy to fail completely.
Figures 8.2(a) and 8.2(b) show the associated fragmentation pattern: in figure 8.2(a)
one color is associated to one fragment, and in figure 8.2(b) the red (resp. the blue)
color corresponds to the broken (resp. non broken) edges. The comparison of the
two pictures emphasizes that some broken edges delimit two fragments, whereas
others are internal to a fragment and constitute diffuse damage.

Naturally, the number of fragments increases with strain rate. Figure 8.3 focuses
on the geometry Geom.6. For $\dot{\varepsilon} = 10^3 \; s^{-1}$ (figure 8.3(a)), there are 132 only
fragments, which is not enough to get statistics on fragment sizes. On the opposite,
if $\dot{\varepsilon} = 10^5 \; s^{-1}$ (figure 8.3(d)), 7426 fragments are generated and distributions of
fragment masses can be computed.

8.2.2   Evolution of the distribution of fragment masses

The effect of strain rate is studied through the distribution of masses. We selected
Geom.4 and Geom.6, and plotted (figure 8.4) the inverse of the cumulative density
function (cdf) of the dimensionless masses (m/m_{aver}), at three strain rates: $\dot{\varepsilon} = 10^4 s^{-1}$, $\dot{\varepsilon} = 2.10^4 s^{-1}$, and $\dot{\varepsilon} = 10^5 s^{-1}$. Intermediate strain rates generate disperse
distributions, whereas higher strain rates lead to less scattered masses. In other
words, when the strain rate increases, fragments tend to have similar masses. This
trend has already been observed in two dimensions with the plate test (chapter 7),
but has not been observed in one-dimension (chapter 6). This difference between
one- and multi-dimensional fragmentations underlines the role of crack propagation.
Indeed, in one-dimension, crack initiation is the main mechanism, while in multiple
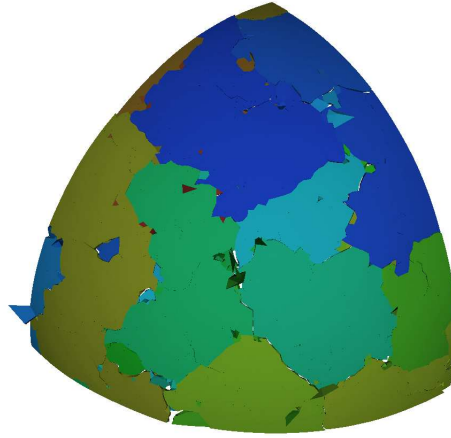
(a)
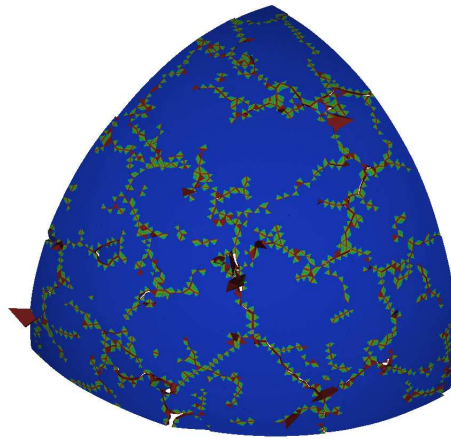
(b)
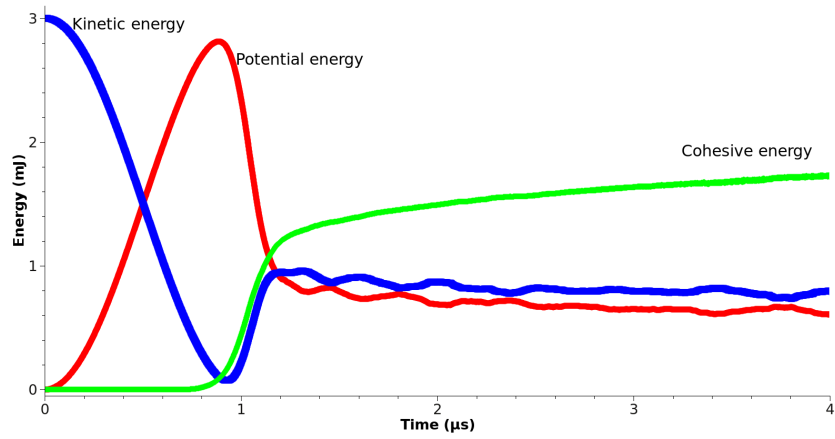
(c)

Figure 8.2: Fragmentation of the geometry Geom.6 at strain rate $\dot{\varepsilon} = 10^3 \ s^{-1}$. (a) Each color constitutes one fragment. (b) Red (resp. blue) color corresponds to broken (resp. non broken) edges. (c) Evolution of the kinetic, potential and cohesive energies.
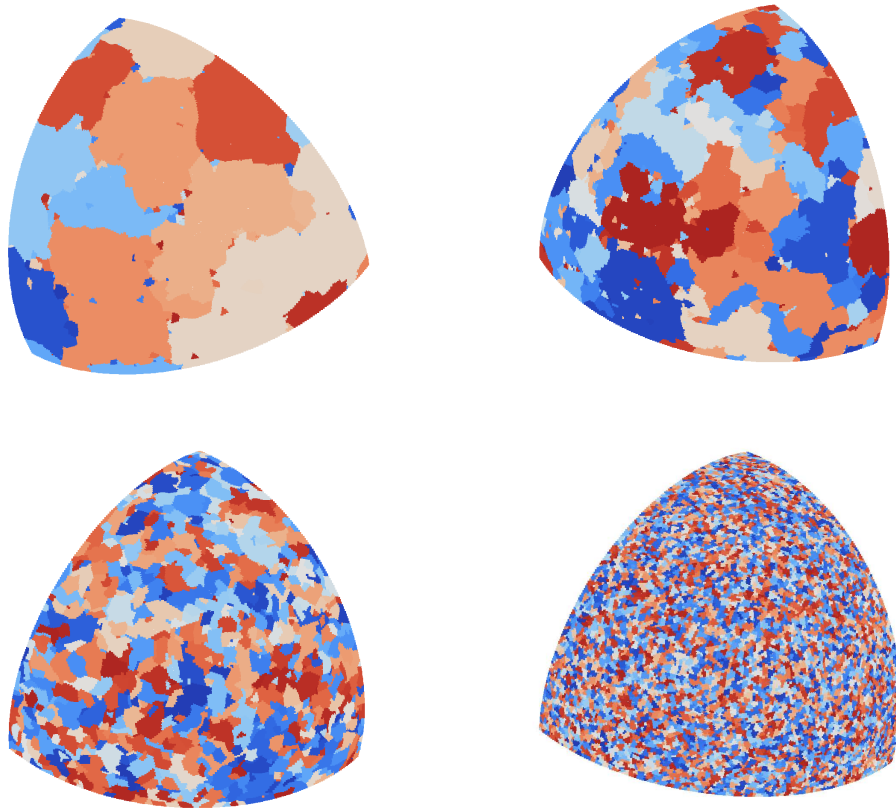
Figure 8.3: Fragmentation pattern associated to Geom.6 for several strain rates: (a) $\dot{\varepsilon} = 10^3 \ s^{-1}$, (b) $\dot{\varepsilon} = 2.10^3 \ s^{-1}$, (c) $\dot{\varepsilon} = 10^4 \ s^{-1}$, (d) $\dot{\varepsilon} = 10^5 \ s^{-1}$. Fragments are represented by distinct colors. More fragments are generated at high strain rates.

dimensions, crack propagation also takes place. The observed dependence of mass distribution upon strain rate seems thus to be the result of crack propagation and branching mechanisms, which are more dominant at low and intermediate strain rates.

Moreover, figure 8.4 also displays some thin curves that are the best Weibull fits[2] (the absence of fitting curve for $\dot{\varepsilon} = 10^4 \ s^{-1}$ and $\dot{\varepsilon} = 2.10^4 \ s^{-1}$ in figure 8.4(b) indicates that the Weibull fit was evidently not suitable). At high strain rates, both Geom.4 and Geom.6 can be approximated by Weibull distributions. Nonetheless, the fit accuracy is different. On the one hand, Geom.6 leads to fragments exhibiting Weibull-type distribution. Since Geom.6 is nearly a two-dimensional geometry, it can be compared to the plate test, conducted in chapter 7. Indeed, in section 7.5, we showed that at high strain rates, the distribution tends to be exponential (e.g. it is Weibull with modulus one). In three dimensions, the Weibull modulus is 2.4. This difference underscores that, although they can be both approximated accurately by Weibull distributions, the plate and the very thin sphere exhibit some differences. Three-dimensional mechanisms affect the value of the Weibull modulus rather than the type of distribution. On the other hand, for Geom.4, the Weibull fit is obviously imprecise. The heavier fragments are badly resolved. Consequently, when dimensionality increases (e.g. when R_{int} decreases), Weibull fit is not necessarily adequate anymore. This observation still requires validation: the issue of mesh convergence has not been handled yet, and there might exists some mesh dependency in the light fragment range.

The comparison of these observations to prior models is not straightforward; only few experimental and numerical studies have been performed in three dimensions. Moreover, as far as we know, they concern impact rather than expansion loadings. Oddershede et al. [Oddershede 1993] were interested in the effect of dimensionality in impact fragmentation of brittle materials. They observed that, in the small range, the mass distribution follows a power law whose exponent increases with dimensionality and ranges from 1.0 to 1.55. Similarly, Meibom and Balslev [Meibom 1996] carried out impact experiments on dry clay at relatively low strain rates. They observed the same trend: the power exponent increases from 1.5 to 2.0 when dimensionality goes from 1 to 3. In three dimensions, they show (experimentally and theoretically) that mass distributions exhibit two characteristic exponents: small fragments are governed by three-dimensional mechanisms, while large fragments follow two-dimensional laws. The transition mass between the two regimes is 0.44-0.76 times the plate thickness.

---

[2]Fits are computed using the Levenberg-Marquardt algorithm. It constitutes an interpolation between the Gauss-Newton algorithm and the method of gradient descent. It is slower than the Gauss-Newton algorithm, but it provides a solution, even if the starting point is far from the final point.
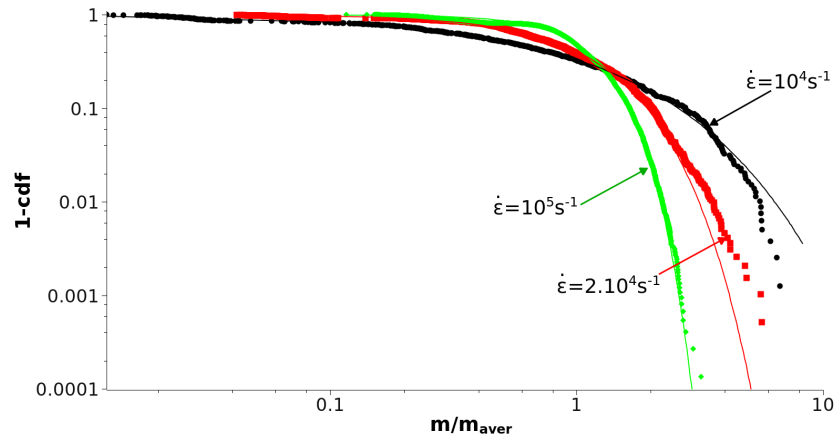
(a)
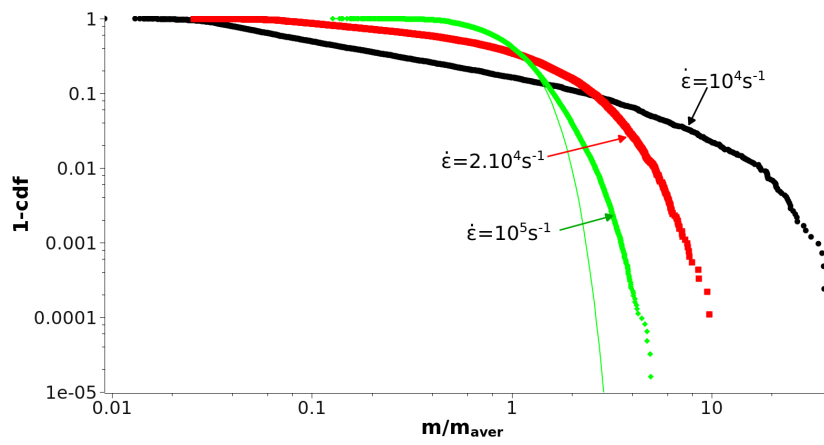
(b)

Figure 8.4: Influence of the strain rate on the inverse of the cumulative density functions of the normalized fragment masses: (a) for Geom.6 and (b) for Geom.4. Thin curves represent best Weibull fits.

These experimental results have been confirmed by theoretical and numerical models. The Gilvarry's theory [Gilvarry 1961a] concerns expansion loadings and integrates three-dimensional effects (see section 2.4.2). It distinguishes between one-, two-, and three-dimensional flaws, and affects a Poisson process to each of them. Fragment size distributions are shown to exhibit exponential distribution. Besides, based on Gilvarry's proof, Åström et al. [Åström 2004b] derived another representative fragment mass distribution, which decouples small and large fragment behaviors. Crack branching and merging mechanisms produce power law in the small size range, whereas Poisson process controls the large size range and leads to exponential cutoff at a system-dependent length scale (see section 2.4.3). Similarly, Carmona et al. [Carmona 2008, Wittel 2008] decoupled the behavior of small and large fragments. They simulated the fragmentation of a plain sphere submitted to impact loading and observed that, for large enough velocities, mass distributions follow a power law in the small fragment range, while large fragments are represented by an exponential cutoff of the power law.

Although impact and explosive loadings involve distinct mechanisms, the distribution of fragment masses that they result in, has been shown to exhibit the same shape [Åström 2000]. For impact loadings, fragmentation is located close to the impact boundary and energy is used locally in compression. By contrast, for explosive loadings, fragments are distributed over the entire body and energy is used in tension. In both cases, Åström emphasizes that the distribution of fragment sizes combine a power law for the small fragments and a finite cut-off generally represented by an exponential. The difference between the two loadings lies in the value of the constants, among which the exponent of the power law. Impacts should lead to higher values than explosions.

In order to verify whether our numerical simulations also lead to scale-invariant distribution for small fragments and exponential distribution for large fragments, we focus on the numerical experiment conducted for the geometry Geom.4 at strain rate $\dot{\varepsilon} = 10^5 s^{-1}$. As highlighted by figure 8.4(b), the Weibull fit does not represent accurately the whole distribution. Light and heavy fragment ranges are thus decoupled. Figure 8.5 displays power and Weibull fits calculated independently for each range. Apparently, in both ranges, the Weibull approximation is better. The idea of decoupling the fit depending on fragment ranges is thus valid, but we do not recover any scale-invariant mechanism in three dimensions, for uniform expansion. This lack of criticality in the small range is probably due to the mesh element size. The precision of the lighter fragments can be improved by considering finer meshes.
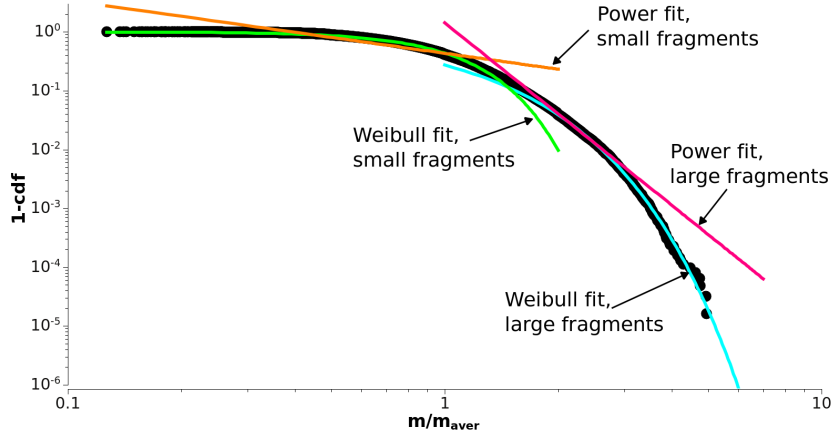
Figure 8.5: Inverse of the cumulative distribution of the normalized masses computed at strain rate $\dot{\varepsilon} = 10^5 s^{-1}$ for the geometry Geom.4. Best fits of type power-law and Weibull are displayed; heavy and light fragment ranges are decoupled.

8.3　Influence of the hollow sphere thickness

8.3.1　Evolution of the average fragment size

We now focus on the effect of dimensionality on fragmentation. We compute the number of fragments N_{frag} and deduce the average fragment size s_{aver} assuming that fragments exhibit cubic shapes. Writing that the total volume of the sphere equals N_{frag} times the average volume of the fragments leads to the average fragment size:

$$s_{aver} = \left(\frac{\Pi.(R_{ext}^3 - R_{int}^3)}{6.N_{frag}} \right)^{1/3} \tag{8.7}$$

Figure 8.6 represents the evolution of the average fragment size with internal radius R_{int} for various strain rates. Note that for the strain rate $\dot{\varepsilon} = 10^5 s^{-1}$ some points associated to the small R_{int} are missing due to lack of convergence. Surprisingly, the curves are not monotonous. Very thin spheres (Geom.6) lead to many fragments, or to an equivalently small average fragment size. Then, as dimensionality increases (e.g. R_{int} decreases), s_{aver} first increases until a peak, after which it slowly decreases. Therefore, we define three stages:

- Fully 2D: (Geom.6): There is no propagation in the thickness, all the energy is used for 2D-fragmentation (see figure 8.7(a)).

- Transition from 2D to 3D (Geom.5 and Geom.4): Propagation through the thickness takes place, but the thickness is not large enough to allow crack merging, and a fortiori the nucleation of several fragments. Part of the input energy is consequently lost into crack propagation (see figure 8.7(b)).

- Fully 3D (Geom.3, Geom.2 and Geom.1): The thickness is sufficiently large to induce multiple fragments through it. Energy is dissipated into crack propagation and crack branching, which results in more fragments (see figures 8.7(c) and 8.7(d)).
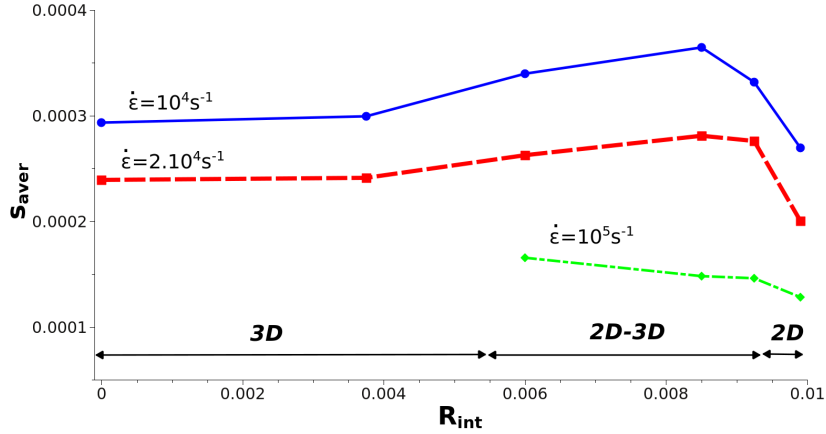
Figure 8.6: Evolution of the average fragment size distribution with internal radius of the sphere R_{int} at various strain rates.

Figure 8.7 displays the fragmentation patterns associated to Geom.1, Geom.3, Geom.5, and Geom.6 at strain rate $\dot{\varepsilon} = 10^4 s^{-1}$. It highlights that the shape of the fragments depends on the internal radius R_{int}. In 2D, fragments are very thin. During the transition 2D-3D, crack merging cannot take place and fragments are elongated in the radial direction. In 3D, cracks are able to propagate through the thickness, which is large enough to allow fragment nucleation. Nonetheless, there exists a difference in the shape of fragments formed close to the boundaries and within the body: fragments are more elongated when crack propagation interacts with boundary, and are more equally shaped within the bulk. Consequently, three-dimensional fragmentation results in failure patterns that exhibit both bulk and boundary features.

The idea that fragments need a minimum thickness to be generated can be understood schematically. In figure 8.8, fragments are represented by circles whose size is set by strain rate. In 2D, there is no crack propagation through the thickness and, fragments are quasi two-dimensional. By contrast, in 3D, there is crack propagation and several fragments can be generated through the thickness. During the transition between 2D and 3D, crack propagation also occurs, but since they are too large, several fragments cannot fit through the thickness.
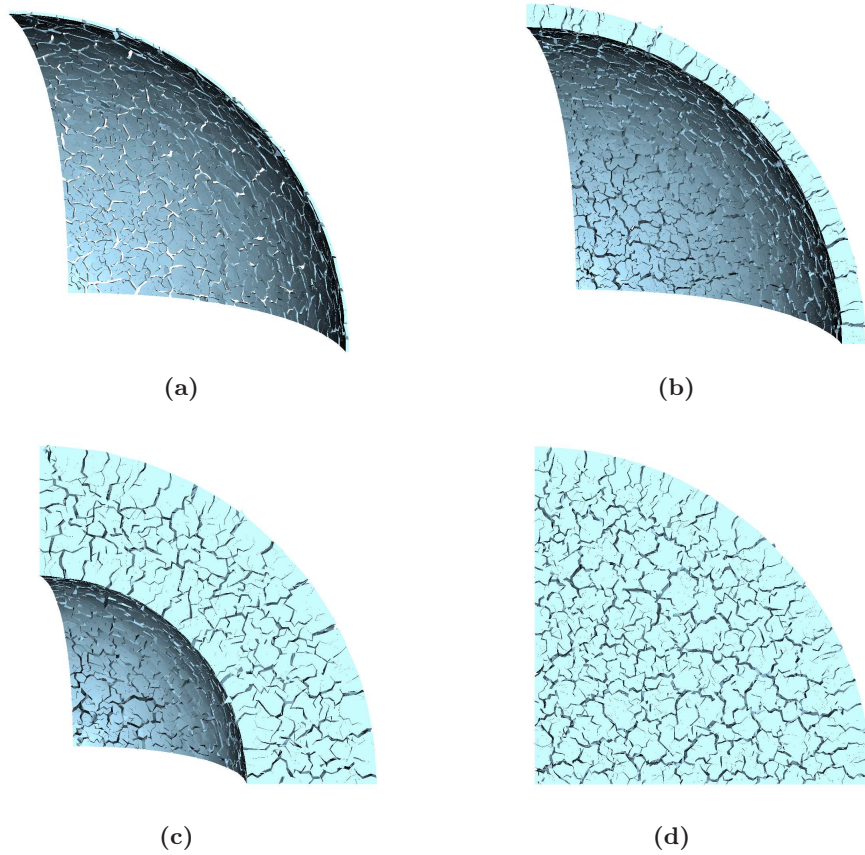
Figure 8.7: Fragmentation patterns computed for (a) Geom.6, (b) Geom.5, (c) Geom.3, and (a) Geom.1 at strain rate $\dot{\varepsilon} = 10^4 s^{-1}$. (a) No crack propagation through the thickness. (b) Crack propagation and slight branching through the thickness, but no fragment generation. (c) and (d) Crack propagation and fully developed branching, with fragment generation through the thickness. Fragments close to the boundaries are more elongated than the ones within the body.
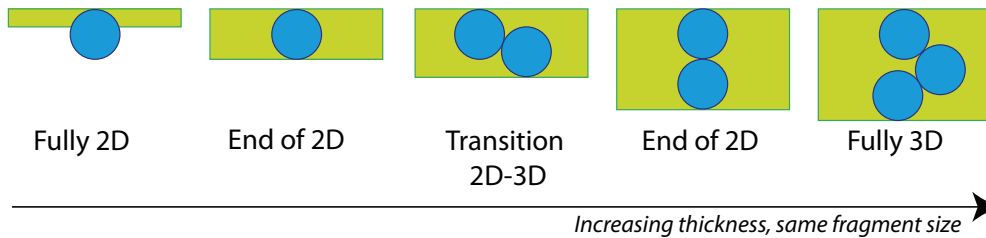
Figure 8.8: Schematic of the transition between 2D and 3D fragmentations. Fragments are represented by blue spheres (the view is a cut through the thickness). Thickness of the body (in green) increases from left to right. In 2D, the thickness is not large enough to allow the generation of several fragments through it. By contrast, in 3D, multiple fragments fit easily through the thickness.

8.3.2 Evolution of the shape of the fragments

To confirm whether three-dimensional fragmentation leads both to 2D- and 3D-like fragments, we study the shape of the fragments. One way of addressing this issue consists in computing the fragments' momenta of inertia. To handle this, we first determine the center of mass (CM) and the inertial tensor of each fragment in the reference basis at the center of mass I_{CM}:

$$I_{CM} = \begin{pmatrix} I_{xx} & -I_{xy} & -I_{xz} \\ -I_{xy} & I_{yy} & -I_{yz} \\ -I_{xz} & -I_{yz} & I_{zz} \end{pmatrix} \sim \begin{pmatrix} I_0 & 0 & 0 \\ 0 & I_1 & 0 \\ 0 & 0 & I_2 \end{pmatrix} \tag{8.8}$$

If the center of mass of the fragment has the coordinates (x_{CM}, y_{CM}, z_{CM}), then the component of the matrix of inertia are:

$$I_{xx} = \rho \int_{volume} \left((y - y_{CM})^2 + (z - z_{CM})^2 \right) dV \tag{8.9}$$

$$I_{yy} = \rho \int_{volume} \left((x - x_{CM})^2 + (z - z_{CM})^2 \right) dV \tag{8.10}$$

$$I_{zz} = \rho \int_{volume} \left((x - x_{CM})^2 + (y - y_{CM})^2 \right) dV \tag{8.11}$$

$$I_{xy} = \rho \int_{volume} (x - x_{CM})(y - y_{CM}) dV \tag{8.12}$$

$$I_{xz} = \rho \int_{volume} (x - x_{CM})(z - z_{CM}) dV \tag{8.13}$$

$$I_{yz} = \rho \int_{volume} (y - y_{CM})(z - z_{CM}) dV \tag{8.14}$$

Since the inertia tensor is symmetric positive, it has necessarily three eigenvalues. We compute them by equalizing the characteristic polynomial to zero. This leads to an equation of order three that we solve using the Cardan technique. The eigenvalues I_0, I_1, and I_2 are the momenta of inertia (equation 8.8), and are ordered so that $I_0 \leq I_1 \leq I_2$. They are defined in a local basis attached to a given fragment. Large momentum of inertia in a given direction represents a fragment with large dimension in that direction. As a result:

$\frac{I_0}{I_2} \simeq \frac{I_1}{I_2} \simeq 1 \Rightarrow$ The fragment is 3D and has a spherical or cubic shape (equiaxed)

$\frac{I_0}{I_2} \ll \frac{I_1}{I_2} \simeq 1 \Rightarrow$ The fragment is 2D and has a circular or square shape

$\frac{I_0}{I_2} \ll 1$ and $\frac{I_1}{I_2} \ll 1 \Rightarrow$ The fragment is 1D and has a bar shape if $I_0 \simeq I_1$

For each fragment, we compute the ratios $\frac{I_0}{I_2}$ and $\frac{I_1}{I_2}$, and we plot the points of coordinates $(\frac{I_0}{I_2}, \frac{I_1}{I_2})$ in figure 8.9, for the geometries Geom.2, Geom.5, and Geom.6. Naturally, these ratios are positive, smaller than one, and since $I_0 \leq I_1$, all the points are in the upper quadrant. Red crosses are associated to Geom.6 and are mainly on the left size of the figure. It expresses that the largest dimension is large compared to the two others. Fragments of type A and B (see figure 8.9) are susceptible to be generated. By contrast, Geom.2 (dark points) leads to fragments characterized by inertial ratios that are mostly located on the right side of the figure, which suggests that they tend to be equally sized. Fragments of type C are more likely to be encountered, especially near the boundary. Finally, Geom.5 (green points), which corresponds to the transition 2D-3D, displays ratios ranging from 2D (red crosses of Geom.6) to 3D (black points of Geom.2). Consequently, during the transition, fragment shapes combine 2D and 3D types of fragments. In 3D, both types are also present, but the 2D fragments are not easily visible, hidden by the numerous 3D fragments.
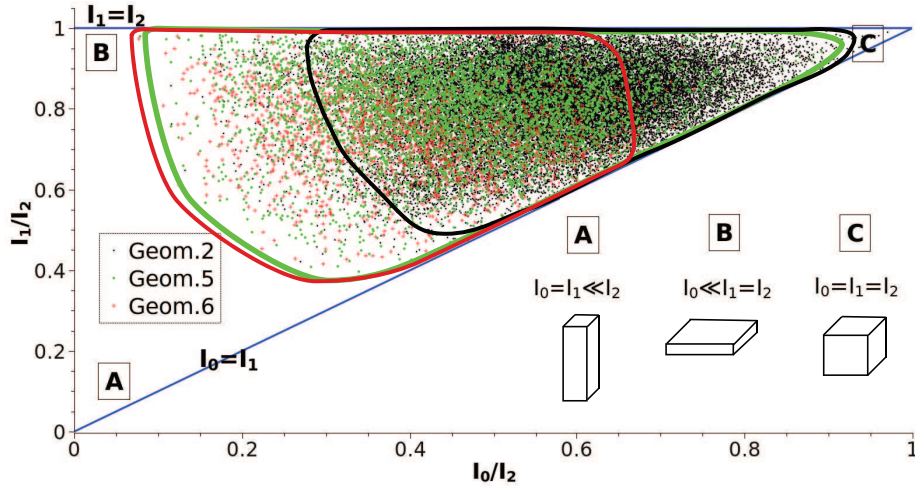
Figure 8.9:   Ratios I_0/I_2 and I_1/I_2 computed for each fragment, resulting from the fragmentation of the geometries Geom.2 (thin dark points), Geom.5 (green points), and Geom.6 (red crosses), at strain rate $\dot{\varepsilon} = 2.10^4 \ s^{-1}$.

This trend can also be highlighted by considering the cumulative density function associated to the ratios $\frac{I_0}{I_2}$ and $\frac{I_1}{I_2}$. Figure 8.10(a) (respectively figure 8.10(b)) plots the distribution of the ratio $\frac{I_0}{I_2}$ (respectively $\frac{I_1}{I_2}$) associated to the fragmentation of the geometries Geom.3, Geom.4, Geom.5, Geom.6 at strain rate $\dot{\varepsilon} = 2.10^4 s^{-1}$. As dimensionality increases (e.g. R_{int} decreases) the curves are shifted to the right and are thus getting nearer to one. It indicates that the largest and the two smaller dimensions of the fragments become closer when dimensionality increases. In other words, fragments exhibiting three equal dimensions may be encountered as dimen-

sionality increases (this observation is only a trend since most fragments remain characterized by $\frac{I_0}{I_2} \simeq 0.5$ and $\frac{I_0}{I_2} \simeq 0.8$ and are thus not equally sized).
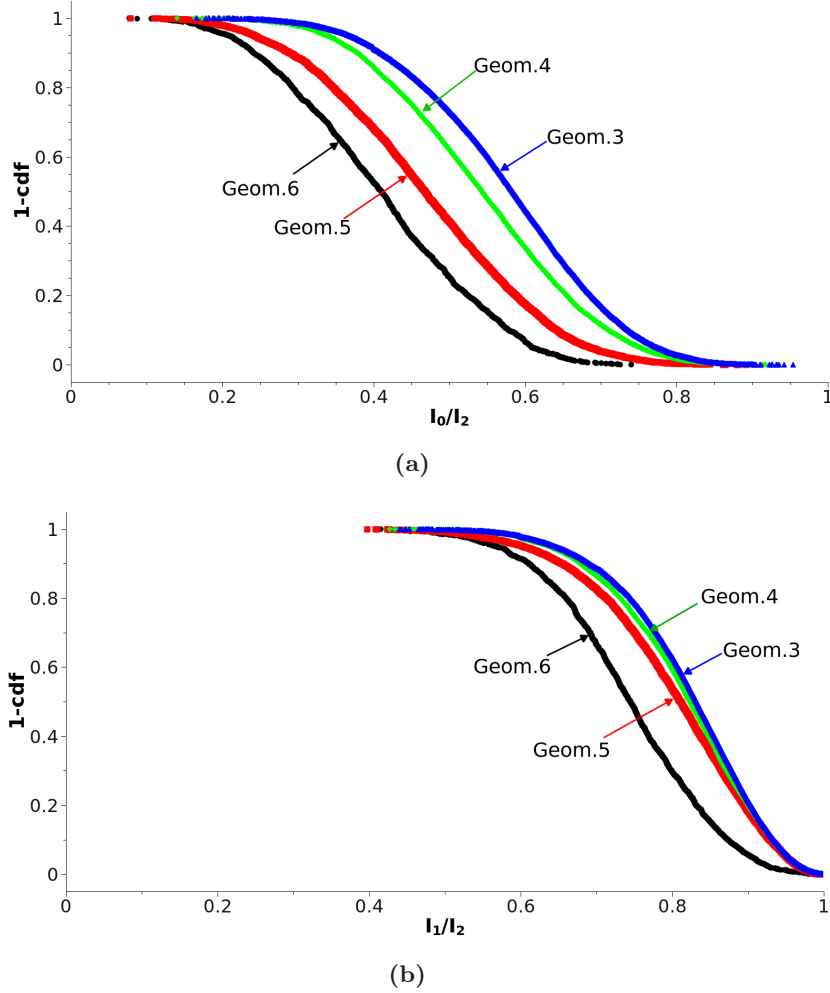
Figure 8.10: Inverse of the cumulative distributions of the ratios (a) I_0/I_2 and (b) I_1/I_2. The curves are getting closer to one another when dimensionality increases.

In summary, in three dimensions, most fragments have 3D-type shape (e.g. the three dimensions are approximately equal). Naturally, the smaller the internal radius R_{int} is, the more 3D-fragments are generated. However, 2D fragments (e.g. one or two dimensions are small compared to the largest) can be encountered.

8.4 Summary

The fragmentation of $1/8^{th}$ of a hollow sphere has been simulated for various strain rates and sphere thicknesses. The impulse boundary conditions require a

minimum strain rate to initiate failure. Once this limit passed, we have computed fragment mass distributions as well as fragments' momenta of inertia, in order to study strain rate and dimensionality effects.

When the thickness of the sphere membrane is small enough (2D fragmentation), mass distributions can be approximated by a Weibull distributions. Small strain rates lead to disperse distributions. These observations confirm the ones proposed in chapter 7 for the plate test. By contrast, when the plate is thick, Weibull distribution cannot resolve both light and heavy fragments. These two ranges have thus been decoupled and fitted independently using the Levenberg-Marquardt algorithm. In three dimensions, small and large fragments appears to be governed by distinct mechanisms.

In order to understand better the reasons for this decoupling, a geometrical justification of the transition between two- and three-dimensional fragmentation has been proposed. If the thickness of the hollow sphere is large enough, multiple fragments can be generated through it (3D fragmentation). On the contrary, if it is very thin, at most one fragment can be encountered (2D fragmentation). During the transition 2D-3D, cracks propagate through the thickness but do not merge.

Finally, the shapes of the fragments have been analyzed. For each fragment, momenta of inertia were computed to quantify the three principal dimensions of the fragment. As the hollow sphere thickness increases, the number of fragments that are nearly equally-shaped (e.g. the three dimensions are very closed to each other) increases. We named them '3D fragments'. Naturally the proportion of '1D' or '2D fragments' (e.g. one or two dimensions are very small compared to the largest one) decreases with the sphere thickness, although they remain present in every simulation. These 1D or 2D fragments are mainly formed closed to the internal and external sphere boundaries where crack propagation interferes.

As far as we know, apart from the ones presented here, few simulations of three-dimensional fragmentation involving complex physics have been run [Carmona 2008]. This computational capability allows us accessing features that have been little described. The study of fragment shapes in three dimensions through inertia momenta certainly constitutes a new topic of research. Despite the novelty of these results, more simulations should be run with different mesh size in order to quantify the role of the mesh on the fragment shape, and to go deeper in the understanding of the mechanisms underlying three-dimensional fragmentation.

Conclusion

9.1 Summary

This thesis has been dedicated to improving the physical understanding and the predictability of the fragmentation of brittle materials using advanced numerical tools. Each chapter attempted to shed light on some difficulties that we might recall, along with the main conclusions reached in each chapter.

9.1.1 Chapter 2: A collection of fragmentation models in dynamics

Compiling prior models of fragmentation into a state of the art chapter was challenging. Indeed, since fragmentation is a transverse subject, it has attracted scientists from many domains. Gathering and ordering their contributions was not a simple process. In the thirties, mining engineers were the first to become interested in fragment mass distributions [Rosin 1933]. They were followed by mathematicians with statistical tools [Lienau 1936]. During World War II, since military research was intensively concentrated on the area of explosions, a large amount of experimental data on ductile materials was produced [Mott 1943b]. Besides experiments, Mott put the emphasis on understanding the physics underlying fragmentation. Proposing empirical laws of fragment mass distributions did not satisfy him; he produced a complex statistical theory. Mott understood that fracture originates at defects and that failure is accompanied by propagating stress waves that protect the structure from further damage [Mott 1947]. These advanced developments have modified the perception of fragmentation. Since then, defect and stress wave effects have been the driving forces in this research.

The first statistical theories accounting for defects were proposed in the sixties [Gilvarry 1961a]. With the emergence of computers in the seventies, various numerical frameworks were formulated (element-based and particle-based) and were used to simulate fragmentation. In the early nineties, models of failure were integrated into numerical codes, making them an efficient, safe, and cheap tool to study fragmentation. They naturally handle stress wave effects that theoretical models could not account for, because of their high non-linearity. They can also include an explicit description of defects. Compared to experiments, which involve high technology devices to investigate the time evolution of the fragmentation process, and which require a certain precaution to control high velocity impacts and explosions,

numerical simulations are undoubtedly safer and cheaper. However, statistical models have the advantage of being simple and therefore convenient, and experiments are the only possible way to reproduce reality exactly.

Finally, the invaluable publications of Grady [Grady 1990] based on energy arguments, the self-similarity concept developed by Turcotte and others [Turcotte 1986b], have provided complementary points of view. Seminal contributions based on energy equilibrium, entropy maximization, cascade processes, etc., have led to elegant principles that represent quite accurately reality. One aim of this thesis has been to bridge those arguments through numerical simulations in order to understand better the physics of fragmentation.

9.1.2   Chapter 3: Modeling and implementing

The numerical framework used in this thesis is based on Galerkin methods and cohesive zone approach. The novelty lies in the parallelism of the code, based on the discontinuous Galerkin method, as well as in its ability to represent accurately the physics of fragmentation. Originally, we investigated expanding ring fragmentation. This test did not require very fine meshes, and serial computation was sufficient. Consequently, we simply used the finite element method that provides an approximation of the displacement at the nodes of a continuous mesh. However, since it cannot capture fracture evolution, coupling with other concepts is necessary. Among them, the cohesive zone model has widely spread during the past decades. Developed in the seventies, it has been adapted to numerical frameworks via both the implicit and the explicit approaches. In the implicit approach, cohesive elements are inserted at every edge of the mesh where failure is expected to occur. In the explicit approach, cohesive elements are inserted dynamically as soon as a failure criterion is satisfied. The major advantage of the former is its rather simple implementation. However, adding cohesive elements from the onset adds an artificial compliance which alters elastic wave speed. To limit this effect, the time step must be reduced as much as possible; a compromise between physical accuracy and numerical efficiency must thus be made. Therefore, to counter this difficulty, dynamic insertion (or explicit approach) was developed by Ortiz and coworkers [Camacho 1996, Ortiz 1999]. This dynamic insertion and Ortiz's linear irreversible law have been used during this thesis for serial simulations of the ring fragmentation.

Nonetheless, the explicit cohesive approach has a major drawback that makes it hardly parallelizable. Changing the mesh topology repeatedly is costly and quite difficult to implement. Parallelizing the initial numerical framework would have required significantly impairing operations, and would have consequently rendered the framework inefficient. Nonetheless, parallelization appeared to be mandatory to handle large meshes and to reach high dimensionality (because of the limited memory of a processor). Another technique ought to be found.

First developed in the Massachusetts Institute of Technology, Boston, USA by Pr. Raul Radovitzky and coworkers, the discontinuous Galerkin method (DGM) can naturally be parallelized and be coupled to cohesive elements. We thus initiated a close collaboration with this research group. In particular, we carried out fruitful investigations with Pr. Raul Radovitzky during his sabbatical in the LSMS laboratory of EPFL, that tested and improved the initial parallel code. We also added new functions specific to the problem of fragmentation. Besides this code, we have had access to efficient machines available at EPFL (the LSMS cluster, Pleiades2, Callisto, and BlueGene). Combining these two capabilities has allowed us to conduct massively parallel simulations, and to reach convergence in multi-dimensional problems.

The basic idea of the DGM is as follows: parallelizing a code naturally generates communication between processors. In fragmentation problems, since failure occurs at many locations, mesh topology changes constantly. This results in heavy communications, which drastically limit the efficiency of the calculations. The main goal is thus to find a method in which mesh topology does not evolve. The DGM, which is mostly used in fluid mechanics and transport equations, appeared to be an adequate response. It deals with discontinuities by relaxing the compatibility equations between elements. Every face of the mesh is weakly in equilibrium (whereas it was strongly in equilibrium in the finite element method), which provides additional degrees of freedom at the nodes. The displacements of the nodes of a face now have the possibility to be different at each adjacent element. This amounts to having interface elements between two adjacent elements with a condition on their equilibrium. By inserting interface elements everywhere, at each face of the mesh, cracks can nucleate everywhere and the mesh topology does not change.

In the implementation, before the dynamic loop begins, the mesh is split (nodes are decoupled and interface elements are inserted everywhere). Each face is controlled either by the DG framework (elastic response), or by the cohesive law (failure response). The switch between the two laws occurs as soon as the failure criterion is verified. This failure criterion concerns the local value of the stress: when it goes beyond the cohesive strength threshold, the switch is effective and definitive.

However, this switch is accompanied by a local discontinuity in stress (that depends on the difference between the cohesive strength and the stress before the switch occurs). To limit its effect, the time step is chosen small enough, and the Gauss points are treated independently. An other drawback of the numerical scheme stems from the mass matrix lumping. It may filter high frequency modes, and sudden variations (such as a propagating wave front) may not well be represented. Although they may generate some instabilities in some sensitive cases, these limitations have secondary effect and do not affect the quality of the results. Besides, the major drawback of the DG framework lies in the multiplication of the degrees

of freedom. The multiplication of nodes and the insertion of interface elements at each edge of the mesh require significant memory increase.

Finally, in order to model material heterogeneity, we selected distributions of cohesive strengths. The issue here was to choose representative distributions. Based on the weakest link principle and the probability of failure in quasi static, we showed that the Weibull distribution is the most appropriate for brittle materials. Extreme value statistics confirmed this result. In the other chapters, we thus mostly considered Weibull distributions of defects. Besides, the cohesive parameters (cohesive strength and toughness) are only representative of the defects, their values do not involve rate dependency. As long as the mesh is fine enough, microcracks are explicitly represented and rate dependency is a natural consequence of this exhaustive description.

Consequently, the advantages of this method are numerous:

- The DGM is a consistent, accurate and converging method.

- Large scale simulations can be run.

- Fracture is not instantaneous and dissipates energy.

- Energy balance is verified.

- Young's modulus is not altered by the presence of interface elements, and stress waves are accurately represented.

- Weibull distribution of defects can be naturally included.

9.1.3 Chapter 4: General physical concepts

This chapter constituted a transition between the technical issues raised in chapter 2 and the main contributions of the thesis of the following chapters. It was devoted to explaining to capital mechanisms that arise in fragmentation: crack interactions and energy transfer. Crack interactions occur through stress waves, which are released because of the discontinuity in the stress field that the crack opening generates. When numerous defects nucleate, they induce multiple stress waves that propagate and interact. Wave interaction can be constructive or destructive. When it is constructive, the amplitude of the resulting wave is higher than the initial ones. This scenario requires restricting conditions that makes it relatively rare. By contrast, destructive interactions create waves with lower amplitude. The resulting waves propagate along the structure and interact again. Defects are thus encompassed several times by stress waves, which gradually damage them. The final state of a defect (e.g. intact, damage, or fully broken) strongly depend upon this multiple passing waves. The network of secondary waves is shown to be negligible if the

material is homogeneous, as well as if the strain rate is very high. On the contrary, it is significant for heterogeneous materials, and its effect increases with material ductility.

Besides stress wave dynamics, energy arguments underline the energy conversions occurring during the process. In explosive fragmentation, the structure stretches, accumulates potential energy until it reaches a peak. After this peak, whose value is determined by material parameter and strain rate, potential energy is mostly converted into failure. This direct conversion takes place in the first stage. If it is not sufficient, kinetic energy that is in excess in the body, is converted into failure energy, which is in turn used in failure. This indirect conversion is slower and generally occurs at high strain rates as well as for ductile and heterogeneous materials. Therefore, material properties, defects, and loading are key parameters influencing the dynamics and the energy transfers underlying fragmentation. Energy conversions are time dependent processes. Writing solely the energy balance equation, which relates kinetic, potential, and failure energies, does not give access to their dynamic evolutions. In order to understand fully energy transfers and the effect of the key parameters, an exhaustive temporal description must thus be achieved.

9.1.4 Chapter 5: Signature of defects in one-dimensional fragmentation

The main objective of this chapter was to understand and quantify the role of defects in failure initiation. In order to avoid crack propagation, we selected a one-dimensional geometry and loaded it in tension (Mott's expanding ring test). The ring has the advantage of limiting contacts between fragments and avoiding boundary difficulties. We thus pursued numerical simulations on Mott's test. As Mott predicted, when failure occurs at a defect, stress waves propagate in both directions around the defect. Since each defect is able to be initiated, several waves propagate and interact. We showed that the rate of failure initiation depends on the left tail of the distribution of cohesive strengths. The extreme cases are uniform and normal distributions. Indeed, the left tail of the normal distribution is flat (slope tends to be null), while it is infinitely steep in the uniform distribution. This difference results in very distinct behaviors.

When the weakest link is activated, the ring is in a state of uniform tensile stress. For a normal distribution, scarcely any weakest links are present along the ring. The stress continues increasing everywhere but at the weakest link, until the second weakest link nucleates. Then, the stress increases everywhere except around the two weakest links. The process continues smoothly. On the contrary, for uniform distributions, there are numerous weakest links and they nucleate simultaneously. This results in many propagating and interacting stress waves. The response is more disordered and generates more fragments. We quantified the amount of stress

wave interactions with a new parameter, which only depends upon the shape of
the left tail of the cohesive strength distribution. The value of this parameter was
determined empirically through a series of tests.

We also generalized the scaling that Zhou et al. [Zhou 2006c] proposed and had
verified for homogeneous materials in one-dimensional. They defined material de-
pendent characteristic length scale and strain rate, which efficiently scaled their
results. However, when materials are heterogeneous, material parameters are de-
fined through distributions instead of single values. Zhou et al.'s scaling is no longer
up to date; we thus enriched it using our newly defined parameter. By normalizing
the average fragment size and the strain rate with the updated characteristic param-
eters, we managed to gather all the initially scattered results into a single curve. In
quasi static, the average fragment size exhibited independent response from strain
rate, whereas in dynamics, it followed a power law with exponent -2/3, which was
predicted by Grady's energy-balance theory.

9.1.5   Chapter 6: Predictable mass distribution in one dimension

The numerical results of the expanding ring test also provided fragment mass
distributions. We studied them and compared them to prior models. Statistics,
physics and experiments have given rise to a wide range of predictions of fragment
mass distributions. On the one hand, the derivation of Poisson point statistics and
hazard functions lead to exponential forms. On the other hand, physical arguments
indicated that fragment masses have a self-similar behavior and that power laws
should describe them better. Other arguments have been employed, but in the end,
most distributions combine exponential and power laws.

In order to focus solely on the shape of the fragment mass distribution, we nor-
malized masses by the average fragment mass. This efficient scaling resulted in a
unique law irrespective of material parameters and strain rate. We proposed to fit
the unique distribution with the generalized gamma distribution with shape param-
eter two. This uniqueness is a very strong result that we emphasize is only valid for
one-dimensional geometries, in which crack propagation is negligible.

We also focused on the behavior of the heaviest fragments. Extreme value statis-
tics predicted that the heaviest fragments follow Gumbel distributions. We verified
it numerically. By contrast to the prior unique behavior, heaviest fragments exhibit
a dependence upon strain rate, defect parameters and length of the ring. In one-
dimension, the fragment mass distribution is thus unique, but the heaviest fragment
distribution depends upon input parameters.

9.1.6 Chapter 7: Fragmentation of a plate

One-dimensional geometries have the advantage of being simple and of giving access to interesting physics of crack initiation. However, they do not provide information about crack propagation. As a result, we considered a thin plate loaded in biaxial tension. Since it involves large meshes, we used parallel computations to simulate the plate fragmentation response. The numerical framework is the discontinuous Galerkin method coupled to cohesive zone model. Post processing gives access to fragment masses. We first verified numerical convergence in terms of number of fragments and distribution of fragment masses. Once convergence was reached, results were analyzed.

Few computational results dealing with multi-dimensional fragmentation are available. Our objective was to provide a better understanding of the role of material parameters, defect distribution and strain rate. Because of the complexity of the process, we decided to think in terms of energy and we enriched 'Grady's model' of equilibrium fragmentation. It assumes that energy equilibrium is verified at the fragment scale. The derivation of the balance between input energy and fracture energy yields characteristic time and length scales. Nonetheless, Grady acknowledged that equilibrium fragmentation is generally not representative of brittle fragmentation, in which an excess of potential energy is accumulated in the body and leads to more fragments. By defining additional characteristic times in Grady's model, we showed that two regimes exist. The limit between these two regimes has been derived theoretically and is highly dependent upon material parameters.

In quasi static, fragmentation is governed by the value of the failure strengths. We call it the strength controlled regime. Before failure onset, the body 'slowly' accumulates energy in excess (the minimum cohesive strength is higher than the peak stress associated to Grady's equilibrium theory). This results in more fragments than Grady's prediction. When the cohesive strengths are reached, failure initiates. Since stress waves propagate fast (the relative velocity between stress waves and material points is high), the fragmentation process occurs very 'rapidly' in comparison to the loading phase and involves extensive stress wave interactions. Therefore, quasi-static loadings lead to highly dynamic fragmentation processes.

By contrast, in dynamics, fragmentation is governed by energy equilibrium. We call it the toughness controlled regime. Little input energy is accumulated in excess and the response occurs almost in Grady's equilibrium. Moreover, since the elastic wave speed is close to the velocity at which the plate is pulled, stress waves barely propagate and interact. The information that failure has occurred does not have time to broadcast and reach the body boundaries. A non-negligible amount of time is thus necessary for the stress waves to establish steadily. During this time, we keep pulling on the plate, which accumulates energy. As a result, slightly more fragments

than Grady's prediction are computed. In this regime, the loading phase is 'rapid', whereas fragmentation is a 'slow' process involving few stress wave interactions. Dynamic loadings are thus associated to smooth fragmentation processes.

We also investigated whether the scaling defined in one-dimension was still valid in multiple dimensions. For all the material studied, the normalization is rather efficient. It gathers all the computed points around the one-dimensional prediction. Therefore, it seems that crack propagation does not significantly affect the efficiency of the scaling. Besides, in the high strain rate regime, we compute more fragments than Grady (by a factor of three), but we recover its -2/3 characteristic exponent. Therefore, Grady's concept of equilibrium constitutes of good and simple approximation. However, it does not include all the physical mechanisms occurring during fragmentation. Benefiting from the accuracy of the numerical framework, we have been able to underline Grady's model limitations and have quantified the error made, when the dynamics of stress waves and energy transfers are not taken into account.

Finally, we also studied fragment mass distributions and showed that strain rate, material parameters, and microstructural parameters do affect the shape of the distribution. In the toughness controlled regime, the fragment mass distribution exhibits a regular behavior which can be fitted with a Weibull distribution, with modulus close to one (suggesting that interactions are limited). In the strength controlled regime, fragment mass distributions are more disordered and no adequate fitting was found. Contrary to one dimensional observation, there is no unique distribution of fragment masses in the plate test.

9.1.7   Chapter 8: From two- to three-dimensional fragmentation

Three-dimensional fragmentation involves mechanisms that could not be investigated with the ring nor the plate geometries. The fragmentation of a hollow sphere has thus been simulated, and fragment mass distributions and fragment shapes have been analyzed. The breakage of a very thin sphere induces fragments whose masses follow a Weibull distribution. When it becomes thicker, a single fitting function cannot resolve precisely the behavior of all the fragments. Light and heavy fragments were thus considered independently, and we showed that in both ranges, Weibull distributions approximate accurately the computed results. This decoupling highlights that distinct mechanisms control three-dimensional fragmentation.

In order to understand this observation better, we focused on fragment shapes. In two dimensions, fragments are mostly flat, whereas in three dimensions, the majority tends to exhibit equal dimensions in the three directions. When the sphere is thick, cracks interfere with boundaries and fragments that are generated close to the boundaries are more elongated. The transition between two- and three-dimensional

fragmentation has been explained schematically. If the thickness is very small, no crack propagation occurs in the third dimension (2D fragmentation). Conversely, if it is large, the cracks can propagate, branch, and merge (3D fragmentation). During the transition, cracks propagate through the thickness but do not have space to merge; fragment nucleation through the thickness is improbable.

9.1.8 Ideas that need to be emphasized

Among these results, here are the seven major contributions of this thesis for the understanding of fragmentation:

1. The use of High Performance Computing in fragmentation simulations based on cohesive elements is necessary to simulate accurately fragmentation mechanisms.

2. Both the dynamics of stress waves and energy arguments govern fragmentation.

3. The left tail of the cohesive strength distribution (e.g. the largest defects or equivalently the weakest defects) determines the rate of failure initiation, and the level of interaction between stress waves.

4. Depending on material properties and strain rate, fragmentation can either be strength controlled (low strain rates, dynamic fragmentation process, extensive stress wave interactions, probabilistic) or toughness controlled (high strain rates, smooth fragmentation process, few stress wave interactions, deterministic).

5. The -2/3 exponent in Grady's model seems always valid, but we predict more fragments by a factor of three than Grady, because of the time dependence of energy transfers and stress wave interactions.

6. The distribution of fragment masses is dependent upon strain rate and material parameters. Crack propagation mechanisms are the origin of this dependence.

The originality of this thesis lies in the alliance of high performance computing and physical interpretation. In the past, the topic of fragmentation has mostly been tackled separately by engineers, physicists, statisticians, experimentalists, or computer scientists. Few investigations have attempted to relate these different disciplines. Future advances in fragmentation will have to keep combining them to provide a deeper understanding of fragmentation.

9.2 Perspectives ...

Understanding the physics underlying fragmentation is a great challenge; many years of hard work and collaboration between scientific fields will probably be nec-

essary to become truly predictive. Here are some interesting possible developments, in the field of numerical simulation of fragmentation.

9.2.1 ... in line with the present thesis

In order to extend the work done so far, a few topics could be explored:

- **Explosion in three dimensions:** To continue the work achieved with the sphere, other three-dimensional geometries should be considered to answer the questions: Are the strength and toughness controlled regimes still observable? What is the average fragment size behavior? Can it be predicted?

- **Size effects:** Does the size of the geometries affect our conclusions? Must a critical behavior be emphasized while changing the dimensions of the geometries? Is it related to the distribution of defects?

- **Fragment velocity:** What is the distribution of fragment velocities and kinetic energies [Grady 2001]? This is a matter of security since kinetic energy is the characteristic value that determines whether the flying fragments are harmful to their surroundings (including of course human beings).

- **Influence of the loading on fragment shapes:** How does the loading affect fragment shapes? Instead of considering a plate in biaxial tension, it could be loaded differently along the two axes. Investigating the effect of confinement on the fragment shapes would also be interesting. More detailed studies in three dimensions induce a deeper understanding of the three-dimensional mechanisms. Can a scaling of fragment shape be defined? [Kun 2006].

All these studies could immediately be carried out immediately. The code is available to compute fully three-dimensional response on multiple processors. Post processing for fragmentation is also ready: it counts the number of fragments, determines the fragment masses, as well as the three momenta of inertia (to study fragment shape).

9.2.2 ... broader impact

In this thesis, we have studied fragmentation through explosions, we considered a simple elastic response before fracture onset, materials were mostly brittle, and we have represented defects statistically. These hypotheses can be enriched:

- **Impacts:** In daily life, fragmentation generally results from impact loadings, rather than explosions. At first, we chose explosions because simulations are easier to perform. Indeed, in impacts, the loading is compressive at first, tension occurs after some wave reflections, and contact issues may arise. In explosions, the structure is directly loaded in tension which limits contacts. However, the DG framework seems to handle compression efficiently:

Radovitzky and coworkers are currently able to run simulations of compressive responses at high strain rate. New simulations may thus be performed to study impact fragmentation. Then, a comparison of exploding and impacting behaviors would be fair [Åström 2000]. Relating angle of impact to physical mechanisms would also be worthwhile [Grady 2001]. It is our belief that simulations of impact fragmentation is a promising field, and efforts should mainly be focused on the issues it raises.

- **Fundamental concepts:** A crack branching criterion, based on microstructural properties rather than energy arguments, could be proposed. Crack tip velocity in diverse materials and crack configurations, could be measured. The failure of a three-dimensional structure generates free surfaces, whose shapes could be characterized using fractal theory for instance.

- **Explicit microstructure:** Instead of modeling microstructure statistically at the mesoscale, an explicit representation at the microscale is a possible direction. The scalability of the DG framework would be used to go to small scales, rather than high strain rates. Diverse microstructures could be tested (concrete, composites, etc) and compared. Non-local approaches might also be used. Fragmentation would then be a multiscale problem. Definition of a representative volume element of the microstructure and its homogenization could give rise to the definition of a damage parameter and a new multiscale continuum formulation [Denoual 2002, Kun 1999].

- **Transition from brittle to ductile:** It is well known that materials subjected to fragmentation will behave differently, depending on whether they are brittle or ductile. These concepts could be investigated by simply changing the coefficients in the cohesive law (large toughness for ductile materials). Bulk plasticity could also be included in the modeling of ductile fragmentation.

- **Multiphysics:** Inserting heat transfer would give access to a wider range of applications such as electronics (semi-conductors), space science (re-entrance of objects or asteroid entrance into the Earth's atmosphere), industrial applications involving heating and rapid cooling, etc.

- **Damage evolution in composite materials:** In many industrial applications in which weight and strength are optimized, composite materials are selected. Slender structures (airplane fuselage, helicopter rotor blades, submarine vessels, ...) are typically made of composites and designed to resist dynamic loadings. A physical-based modeling of the damage in large scale structures can be accurately achieved using the framework presented in the thesis.

- **Design of new materials:** Microstructure may be adapted, depending on whether the material should dissipate a lot of energy (bullet proof) or be resistant (car windshield). The size of the defects, as well as their spatial location

and density are design parameters that lead to very distinct fragmentation responses. Playing with them could induce new materials that would enforce fragmentation to occur at a given strength and a given place.

All of the aforementioned research topics might intertwine the three scientific fields of fundamental mechanics, high performance computing, and experimental science. Taking advantage of these three cores of modern mechanical sciences would broaden our understanding, provide relevant characteristic models and, more practically, would guide the design of innovative materials and structures.

Parallel code for fragmentation

This appendix is dedicated to those willing to use the functions developed for the fragmentation post-processing. The serial version is rather simple whereas the parallel algorithms are more subtle. The objective consists in indicating, for each node or tetrahedron of the mesh, the fragment that they belong to. The methodology used to delimit the fragments' boundaries is composed of two steps:

1. Construction of the facet and the element lists, which are fully related to the mesh topology and independent from the damage variables. It occurs when the function CreateLists(char*) is called (can be done at any time after mesh split).

2. Construction of the fragment list, which needs the facet and the element lists, as well as the damage variables computed during the dynamic loop. It is achieved during the function FragmentProcedure(char*) (should be called each time information on the fragments is required, usually at the end of the simulation).

A.1 Useful linked lists

Three linked lists are constructed: FacetElemList (for the facets corresponding to interface elements composed of 12 nodes), TetraElemList (for the tetrahedra corresponding to bulk elements composed of 10 nodes), and FragmentList (for the fragments). We briefly detail these lists' components.

A.1.1 The Facet

int el : number of the corresponding interface element in the mesh
double damage: value of the damage at the interface
int N[12] : connectivity
Pointers which link to the two adjacent elements

A.1.2 The Tetrahedron

int el : number of the corresponding bulk element in the mesh
int proc : name of the processor that contains the tetrahedron
int N[10] : connectivity
Pointers which link to the four adjacent facets

A.1.3   The Fragment structure

int namelocal : name of the fragment in the processor numbering
int nameglobal : name of the fragment in the global numbering
int NbulkElem : number of tetrahedra in the fragment
int *BuklElem : array of the tetrahedra in the fragment
int Ngluedelem : number of tetrahedra that will be used to glue the fragment
(non null if it is distributed among several processors)
int *TobegluedElem : array containing the tetrahedra that will be glued

A.2   Construction of the facet and element lists

If the code is run in serial, step 1 is called. When it is executed in parallel, the four steps are called.

A.2.1   Step1

Each processor constructs its own lists. The FacetElemList is first built by looping over all the interface elements. Then, the TetraElemList is constructed by looping over the bulk elements. At this stage, $Tetra \rightarrow proc = myPId$. A tetrahedron has at most four neighboring facets. There exist two cases which lead to the absence of a facet:

1. The tetrahedron is on a physical boundary.

2. The tetrahedron is on a processor boundary and the identity of the neighbor has a lower value. Indeed, during the construction of the interface elements, a choice was taken: at inter-processor boundaries, the interface elements belong to the processor with lower identity.

For each tetrahedron, the adjacent facets are searched. When they are found, the structure tetrahedron is updated. Similarly, each of the (at most) four structures associated to the adjacent facets are completed.

A.2.2   Step2

This step is called in the parallel execution. Each processor works independently from the others. The communication map is read via the file pcom-myPId, where myPId is the processor identity.

Figure A.1 gives an example of a mesh distributed among three processors. The associated files pcom-myPId display the arrays:

$$\text{pcom-0: } [2, 1, 2, a, b, 2, 4, c, d, e, f]$$
$$\text{pcom-1: } [2, 0, 2, f, e, 2, 4, a, b, c, d] \qquad\text{(A.1)}$$
$$\text{pcom-2: } [2, 0, 4, d, c, b, a, 1, 4, g, e, f, d]$$

The first number corresponds to the number of neighboring processors. The second number is the name of one of the neighbor, the third is the number of shared nodes, followed by their names. The sequence 'name of the processor, number of shared nodes, name of the shared nodes' continues until the end of the file. Note that the ordering of the processors is not important, while the ordering of the nodes is.
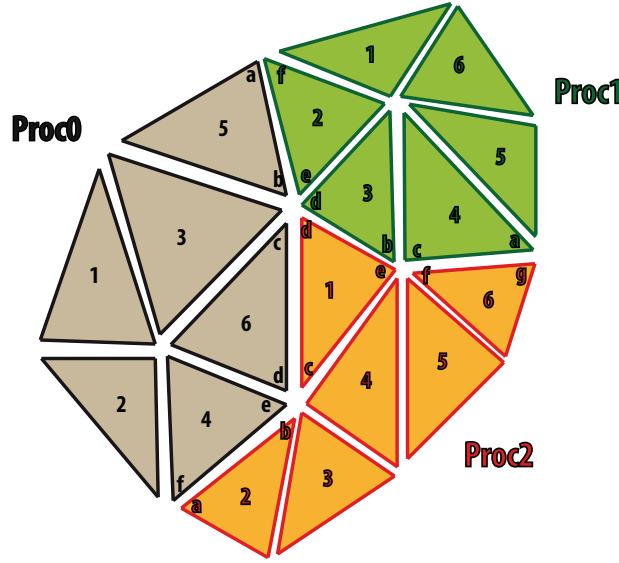
Figure A.1: (color online) Scheme of a mesh distributed among the three processors Proc0 (colored in gray), Proc1 (colored in green), and Proc2 (colored in orange). The elements' numbers and the nodes' names refer to the processor numberings. Interface elements are not represented for clarity.

Then, the integers nbofMaps, *MapOffset, *MapNode, *MapProc are filled in. Let us consider Proc1 in figure A.1. It contains:

$$
\begin{aligned}
nbofMaps &= 2 \\
MapOffset &= [0, 2, 6] \\
MapProc &= [0, 2] \\
MapNode &= [f, e, a, b, c, d]
\end{aligned}
\tag{A.2}
$$

Proc2 contains:

$$
\begin{aligned}
nbofMaps &= 2 \\
MapOffset &= [0, 4, 8] \\
MapProc &= [0, 1] \\
MapNode &= [d, c, b, a, g, e, f, d]
\end{aligned}
\tag{A.3}
$$

A.2.3   Step3

Each processor builds the pointer **TBS (standing for To Be Sent). Its size is equal to the number of processors, and it contains the number of shared nodes and their line number. To construct TBS, the processor loops over its interface elements (FacetElemList). If the facet has only one neighbor, it is on an inter-processor boundary, and the neighboring processor has a higher identity (see section A.2.1).

In our example, Proc1 contains the array:

(*TBS)[0] = NULL   because Proc1 has no interface elements in relation
with Proc0 (1>0)
(*TBS)[1] = NULL   because Proc1 will not send to itself any node to share
TBS[2] = [0, 2, 1, 3]   because Proc1 does have interface elements in relation (2>1)
$$(A.4)$$

The nodes in TBS[2] are ordered two by two in the example (because two nodes define one edge); in the code they are ordered six by six (because simulations are three-dimensional with quadratic elements). Besides, the couple (0,2) that corresponds to the nodes (a,c) is associated to the tetrahedron 4 in Proc1. After, the couple (1,3) is associated to the tetrahedron 3 in Proc1. The reason for tetrahedron 4 to be called before tetrahedron 3 lies in the construction of the FacetElemList.

A.2.4   Step4

It is the communication step. One after the other, each processor (processor I) scatters its TBS array. The other processors (processors J) receive it. Then, they read their MapOffset, MapProc, and MapNode arrays to find the name of the corresponding nodes in their own numbering. They search for the corresponding elements within their TetraElemList and send it back to processor I. Processor I constructs new tetrahedra such that $Tetra \rightarrow proc = J$ (and not $Tetra \rightarrow proc = I$ like in the initial TetraElemList). Therefore, the new TetraElemList of processor I contains tetrahedra belonging to itself, as well as tetrahedra belonging to other processors. The latter are often called ghost tetrahedra.

Let us go back to the example. Here is the corresponding sequence of actions:

- Proc2 receives from Proc1 the array [0,2,1,3].

- Proc2 reads in MapProc that he communicates with Proc1 after Proc0.

- Proc2 reads the second term in MapOffset, which is 4.

- Proc2 reads MapNode[4+0]=g, MapNode[4+2]=f, MapNode[4+1]=e, MapNode[4+3]=d. We recover that the nodes a, c, b, d in Proc1 are called g, f, e, d in Proc2.

- Proc2 finds that f and g (resp. d and e) are part of element 6 (resp.1).

- Proc2 sends to Proc1 the array [6,1].

- Proc1 receives the array [6,1] and constructs two new tetrahedra.

In the end, Proc1 has 8 tetrahedra in its TetraElemList, as highlighted by figure A.2.
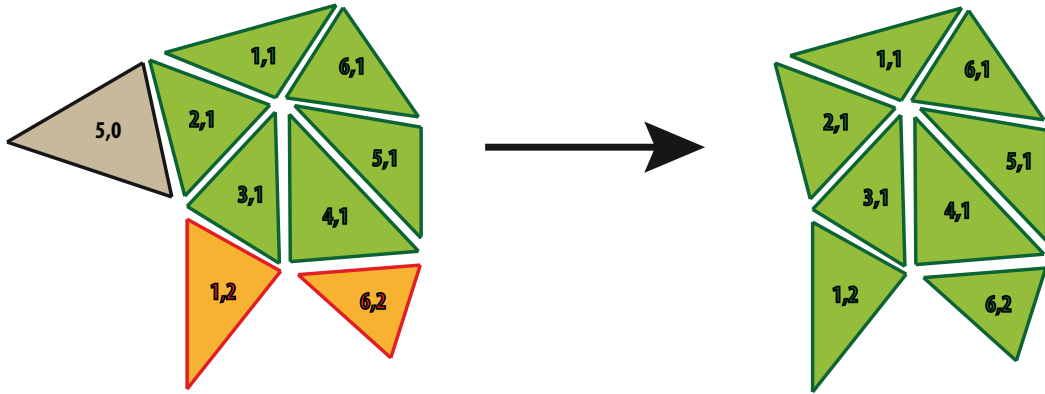
Figure A.2: Tetrahedra associated to the processor Proc1 without ghost elements (right) and with ghost elements (left).The numbers contained in the elements consist of two figures: before the coma, it is the number of the element in the local numbering, whereas after the coma, it is the name of the processor that the elements physically belong to.

A.3 Construction of the fragment list

Similarly as in the previous section, the serial execution calls step 1, while the parallel version executed steps 1 to 4.

A.3.1 Step1

Each processor constructs its FragmentList. The array visited-elem has the size of the number of bulk elements and is initialized at 0. When the tetrahedron I is visited, visit-elem[I-1] is incremented. At the end, we verify that all the tetrahedra have been visited only once.

To construct the FragmentList, the processor loops over its TetraElemList. If the tetrahedron has not been visited yet and if it belongs to itself ($Tetra \rightarrow proc = myPId$), a new fragment is constructed. Then, if the neighboring facets are not broken, the adjacent tetrahedra are added into the fragment. The process continues until the fragment is fully surrounded by broken facets, processor boundaries, or physical boundaries. If a tetrahedron does belong to the fragment but not to the processor ($Tetra \rightarrow proc \neq myPId$), it is also added into the tobegluedElem array.

A.3.2   Step2

From now, the functions are specific to the parallel version. Each processor has its own FragmentList and its own number of fragments. First, fragments are renumbered in the global numbering. For instance in figure A.3, Proc0 has 4 fragments, Proc1 has 3 fragments, Proc2 has 3 fragments. The local numbers are crossed out, while the global ones are not. The maximum number of fragments is 10.
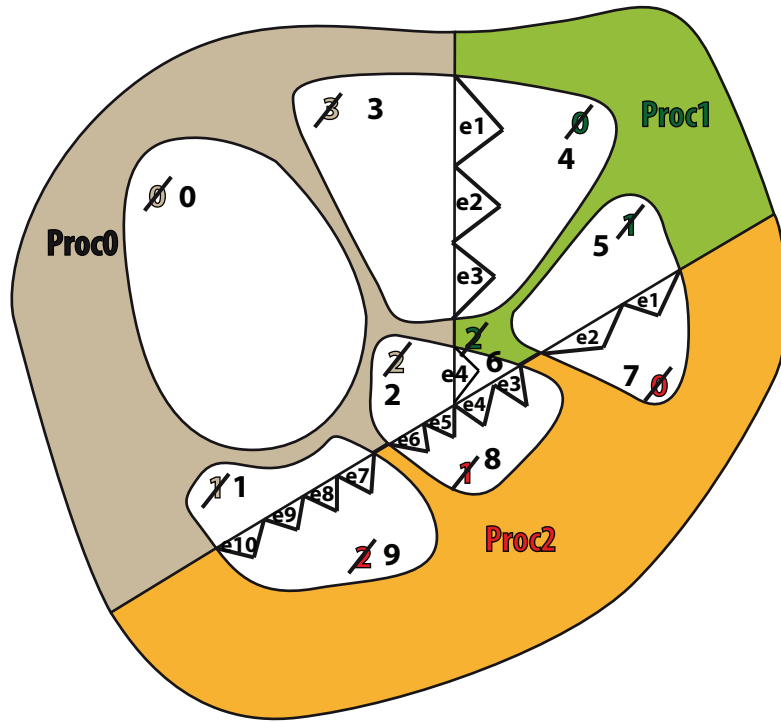

Figure A.3: Fragments distributed among three processors with their local (crossed out numbers) and global numbers. Ghosts elements are named e1 to e10, in the local numbering.

A.3.3   Step3

Each processor constructs its **TBS pointer (standing for To Be Sent). It consists of a series of 'global fragment number - element number'. In the example of

figure A.3, this leads to:

- Proc0:
$$(*TBS)[0] = NULL$$
$$TBS[1] = [3, 1, 3, 2, 3, 3, 2, 4] \tag{A.5}$$
$$TBS[2] = [2, 5, 2, 6, 1, 7, 1, 8, 1, 9, 1, 10]$$

- Proc1:
$$(*TBS)[0] = NULL$$
$$(*TBS)[1] = NULL \tag{A.6}$$
$$TBS[2] = [5, 1, 5, 2, 6, 3, 6, 4]$$

- Proc2:
$$(*TBS)[0] = NULL$$
$$(*TBS)[1] = NULL \tag{A.7}$$
$$(*TBS)[2] = NULL$$

A.3.4 Step4

This is the communication step. Each processor has a MapFragment array, initialized by MapFragment[i]=i, for i smaller than the maximum number of fragments computed in step 2 (10 in the example). Then, one after the other, each processor I sends its TBS array to the other processors J. Processor J searches within its TetraElemList the tetrahedron corresponding to the sent one. When it finds it, it also has access to the fragment that it belongs to.

For instance, Proc1 receives from Proc0: [3,1,3,2,3,3,2,4]. Proc1 finds that element1 belongs to fragment 4, as well as elements 2 and 3 (see figure A.3). Similarly, Proc1 finds that element4 is in fragment6. It signifies that fragments 3 and 4, as well as 2 and 6, are the same. Proc1 updates its MapFragment which becomes:

$$MapFragment = [0, 1, 2, 3, 3, 5, 2, 7, 8, 9]$$

Each processor does so and sends its MapFragment to the master, which updates its own MapFragment by keeping the smallest fragment values. In the example Proc0 is the master and finds:

$$MapFragment = [0, 1, 2, 3, 3, 5, 2, 5, 2, 1]$$

The master sends this final MapFragment to all the processors that can now update the effective fragment number.

Additional study on the plate fragmentation

In this appendix, we present additional results concerning the plate study in chapter 7. We first describe qualitatively how material parameters influence the average fragment size. Then, an empirical expression of the peak stress is derived.

B.1 Qualitative description of material effects on the average fragment size

Fragmentation terminates when no more cohesive energy is dissipated, and the number of fragments N_{frag} does not evolve anymore. We compute the average fragment size $s_{aver} = \frac{L_{plate}}{\sqrt{N_{frag}}}$ in order to quantify the role of material parameters on the fragmentation of the plate. We analyze the role of bulk parameters, microstructure and loading rate. Figures B.1 and B.2 illustrate the dependence of the average fragment size s_{aver} on these parameters. No unique obvious law seems to describe accurately the evolution of s_{aver}. However, some general comments may be drawn:

- Naturally, higher loading rates generate more fragments. s_{aver} is a decreasing function of the strain rate $\dot{\varepsilon}$ (figure B.1).

- Figure B.2(a) highlights that materials with high volumetric mass generate small fragments. This is due to the stress wave healing effect. Indeed, when ρ increases, elastic waves propagate slower, encompassing less defects. More cracks are initiated which results in more fragments. The fragmentation patterns of two different materials with distinct volumetric mass are displayed in figure B.3. Figure B.3(a) illustrates the fragmentation pattern for a material with the volumetric mass $\rho = 1054 \ kg/m^3$ (material Mat.10 in table 7.1), submitted to the strain rate $\dot{\varepsilon} = 10^4 \ s^{-1}$. Figure B.3(b) is associated to material Mat.9 with volumetric mass $\rho = 6327 \ kg/m^3$ and displays a finer fragmentation pattern.

- Concerning the Young's modulus E, the argument used for the volumetric mass is not sufficient. Indeed, increasing E amounts to increasing c; the average fragment size should then be an increasing function of E. However,

figure B.2(b) underlines the reverse trend. Two mechanisms are here competing: the stress wave healing effect and the storable elastic energy (which increases with E). Our results show that strain energy effect is prevailing.

- During the failure process, when a crack opens, tougher materials release more fracture energy. s_{aver} is thus an increasing function of the toughness G_c (figure B.2(c)).

Zhou et al. [Zhou 2004], who studied the one-dimensional fragmentation of homogeneous materials, observed numerically the same trends: at high enough strain rate, the average fragment size decreases with Young's modulus at constant volumetric mass (equivalent to test1), and it increases with wave speed at constant Young's modulus (equivalent to test4) and toughness (equivalent to test7). One-dimensional trends are consequently valid in two dimensions. By contrast, Grady's energy-balance model does not convey all the trends. Its prediction (eq. 7.2) is indeed independent from the Young's modulus.
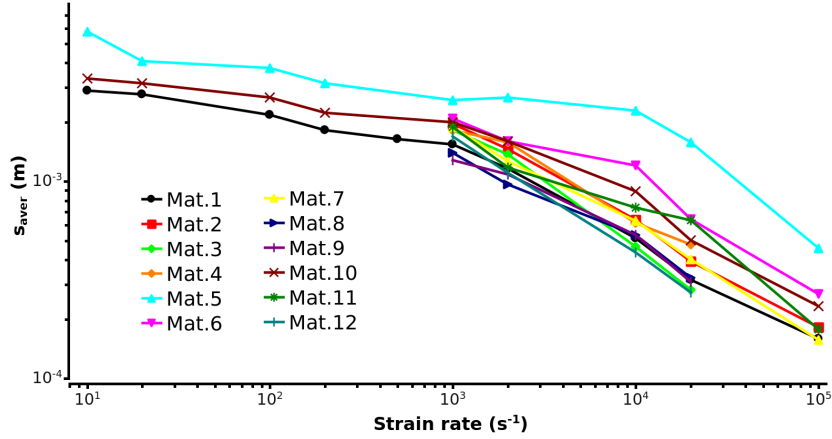
Figure B.1: Evolution of the average fragment size with strain rate. Twelve materials fragmented over the range $\dot{\varepsilon} = 10^3 s^{-1}$ to $\dot{\varepsilon} = 10^5 s^{-1}$, while only three materials are fragmented over the range $\dot{\varepsilon} = 10 s^{-1}$ to $\dot{\varepsilon} = 10^5 s^{-1}$. The materials are detailed in table 7.1.

B.2 Numerical identification of the time to failure and peak stress

In this section, we establish empirical expressions of the peak strength σ_{peak} and the time to failure t_f, which corresponds to the time at which potential energy is maximum. Their analytical determination is not obvious. Indeed, failure initiates when the stress reaches the cohesive strength of the weakest defect $\sigma_{c,min}$. A non null time is necessary to complete fracture of this weakest link, during which the
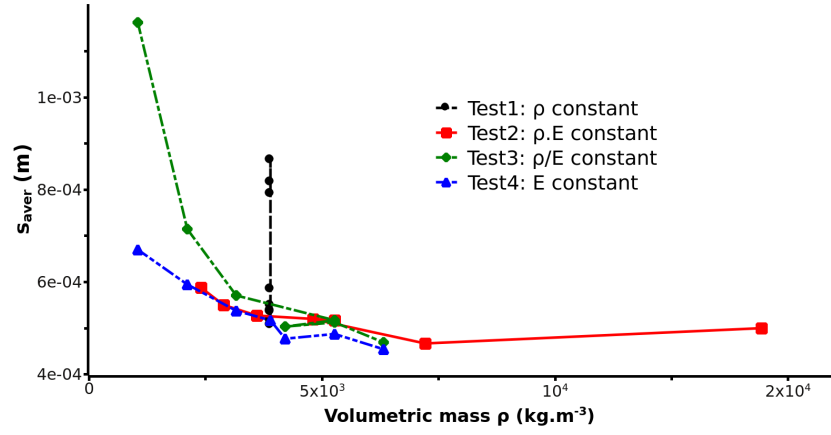
(a)
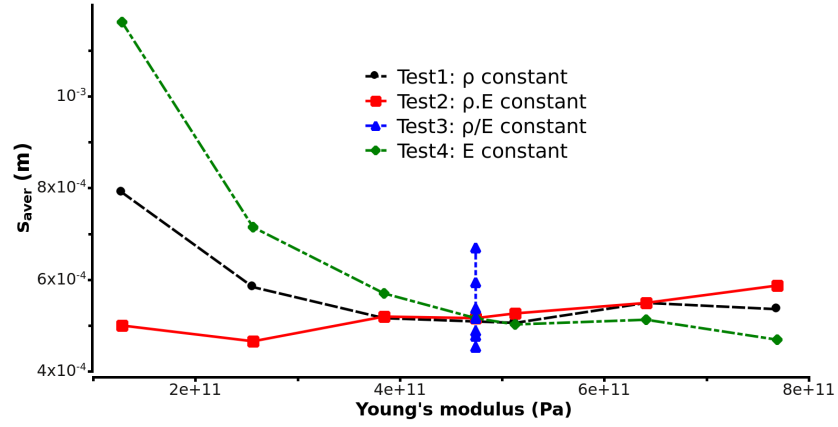
(b)
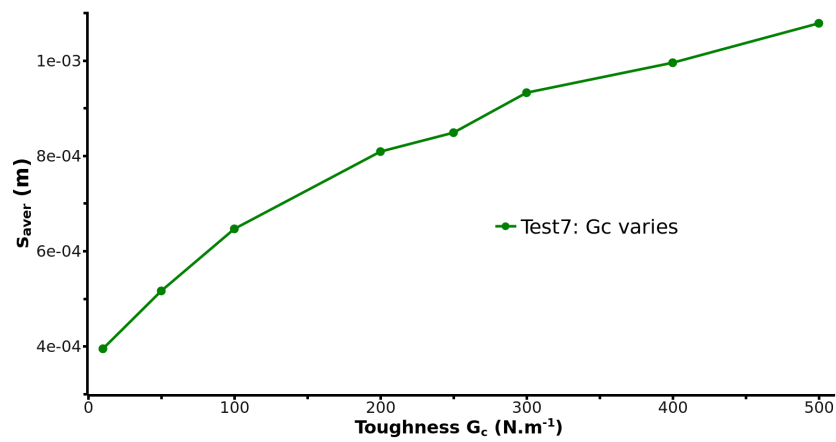
(c)

Figure B.2: Evolution of the average fragment size with (a) volumetric mass, (b) Young's modulus, (c) toughness. The tests are detailed in table 7.1.

(a)   (b)
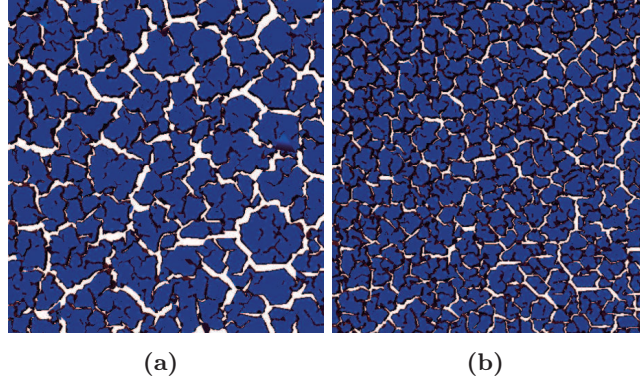
Figure B.3: Fragmentation patterns computed for different materials with volumetric mass (a) $\rho = 1054\ kg/m^3$ and (b) $\rho = 6327\ kg/m^3$, at strain rate $\dot{\varepsilon} = 10^4\ s^{-1}$ (Mat.9 and Mat.11 in table 7.1). Small volumetric mass generates less fragments.

stress continues increasing. Other cracks initiate and need time to break during which stress still increases. The stress waves released by crack opening may have a healing effect, preventing other defects from further damage. As a result, some defects are fully broken, other are partially damage, and the rest is intact. Because of the high non-linearity of the process, the prediction of the peak stress, which is related to the distribution of cohesive strengths, can hardly be achieved analytically. Moreover, besides the distribution of cohesive strengths, other parameters may affect σ_{peak} and t_f. Therefore, we conduct several tests, detailed in table 7.1, in order to quantify the effect of bulk properties (Young's modulus E and volumetric mass ρ), defect properties (distribution of cohesive strengths, toughness G_C), and strain rate $\dot{\varepsilon}$.

First, we set the strain rate to be $\dot{\varepsilon} = 10^4 s^{-1}$ and we investigate the evolution of time to failure with respect to the Young's modulus in four test campaigns. In test 1, the volumetric mass ρ is constant, and the Young's modulus E varies. In test 2, we set $\rho.E$ constant, while in test 3, E/ρ is constant (which is equivalent to insuring a constant wave speed). Finally, in test 4, the Young's modulus E is constant, and the volumetric mass ρ changes. Strain rate and microstructure are identical for each test. Figure B.4 displays the difference between time to failure t_f and minimum time t_{min} (eq. 7.7) in a log-log plot. All the curves nearly superimpose. We fit the curves with power laws, whose exponents are slightly equal. In test 4, the variations of t_f are negligible in comparison to the others. As a result, we conclude that the time to failure t_f displays a small dependence on the volumetric mass ρ which can thus be neglected without severe loss of accuracy. On the contrary, $t_f - t_{min}$ depends strongly on the Young's modulus, which can be traced back its dominant role in potential energy. We fit the numerical results with the function $t_f = t_{min} + 1143/E^{0.90}$.
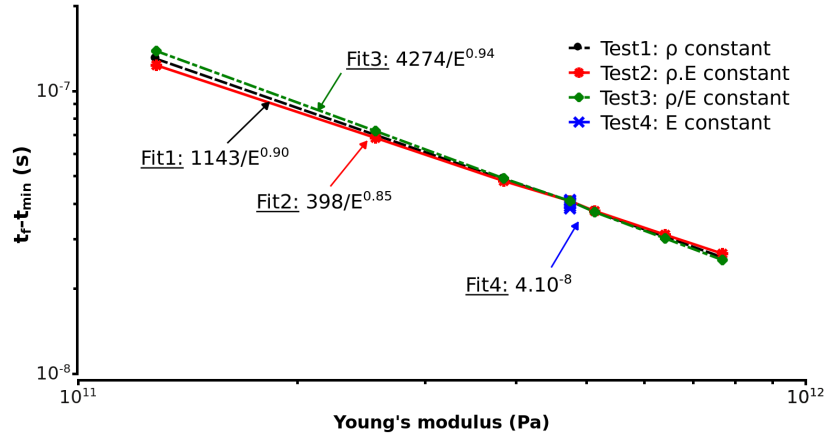
Figure B.4: Evolution of the difference between time to failure and minimum time with the Young's modulus, for the strain rate $\dot{\varepsilon} = 10^4 \ s^{-1}$. The tests are detailed in table 7.1.

Secondly, we keep the strain rate to be $\dot{\varepsilon} = 10^4 s^{-1}$ and we analyze the influence of the microstructure. In test 5 and test 6, the toughness G_c is constant and the distribution of cohesive strength changes through respectively, the smallest cohesive strength $\sigma_{c,min}$ and the scale parameter λ (eq. 7.1). In test 7, the toughness varies and the distribution of cohesive strengths is kept identical. Figure B.5 plots the time to failure with respect to the average failure strength $\sigma_{c,aver}$. It illustrates that toughness has negligible effect, in comparison to $\sigma_{c,min}$ and λ, and that the average cohesive strength is a relevant characteristic strength. Figure B.5 indicates that the evolution of the difference between time to failure and minimum time $(t_f - t_{min})$ is exponential with respect to $\sigma_{c,aver}$. We fit the numerical results with $t_f = t_{min} + 1.566 \ 10^{-8} \ . \ \exp\left(\sigma_{c,aver} \ / \ 320.10^6\right)$. Although there is no analytical proof, intuition relates the exponential shape and the value of the fitted parameters to the distribution of defects, namely a Weibull distribution with Weibull modulus two. The value 320.10^6 may be associated to an average failure strength, while $1.566 \ 10^{-8}$ may be linked to a weakest link. Changing the distribution of defects may thus alter the validity of this expression.

Finally, we consider several materials detailed in table 7.1 and study the effect of the strain rate on $t_f - t_{min}$. Figure B.6 underlines that, in any of the twelve material tested, the dependence follows a power law characterized by the common exponent 0.92.

In conclusion, time to failure only depends upon strain rate $\dot{\varepsilon}$, Young's modulus E, minimum and average cohesive strengths ($\sigma_{c,min}$ and $\sigma_{c,aver}$). Combining the previous fittings yields to the general empirical formula:
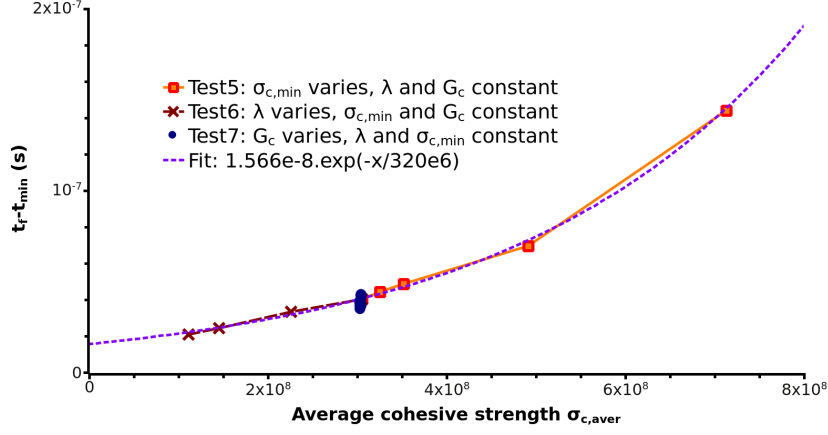
Figure B.5: Evolution of the difference between time to failure and minimum time with the average cohesive strength, for the strain rate $\dot{\varepsilon} = 10^4 \ s^{-1}$. The tests are detailed in table 7.1.

$$t_{f,emp} = t_{min} + \frac{2.4.10^6 \ \exp\left(\frac{\sigma_{c,aver}}{320.10^6}\right)}{\dot{\varepsilon}^{0.92} \ E^{0.90}} \tag{B.1}$$

Since the quantification of the damage before peak stress is not obvious, we prefer to simplify the formulation by keeping a linear reversible response: $\sigma_{peak} = E \dot{\varepsilon} \ t_{f,emp}$. Softening before failure onset is therefore not included (this assumption will be questioned further). The effective peak strength is:

$$\sigma_{peak} = \sigma_{c,min} \ + 2.4.10^6 \ \exp\left(\frac{\sigma_{c,aver}}{320.10^6}\right) \dot{\varepsilon}^{0.08} \ E^{0.10} \tag{B.2}$$
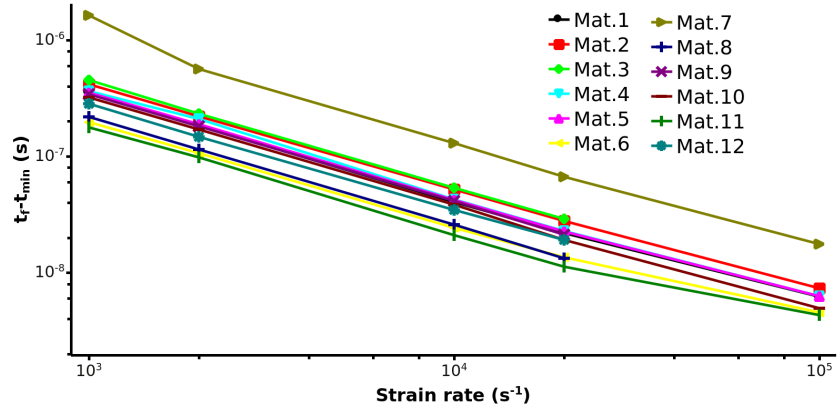
(a)
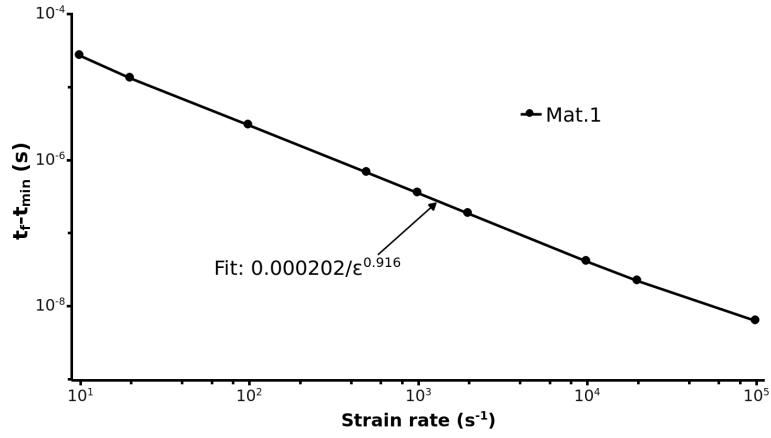
(b)

Figure B.6: Evolution of the difference between time to failure and minimum time with the strain rate for: (a) several materials in the range $\dot{\varepsilon} = 10^3 s^{-1}$ to $\dot{\varepsilon} = 10^5 s^{-1}$, (b) only Mat.1 in the range $\dot{\varepsilon} = 10 s^{-1}$ to $\dot{\varepsilon} = 10^5 s^{-1}$. Fitting law is only displayed in (b). Materials are referenced in table 7.1.

Bibliography

[Abe 2003] H. Abe, M. Naito, T. Hotta, N. Shinohara and K. Uematsu. *Flaw size distribution in high-quality alumina.* Journal of the American Society, vol. 86, no. 6, pages 1019–1021, 2003. 57, 58

[Ainscough 1976] J.B. Ainscough and P.F. Messer. *The room temperature fracture strength of sintered UO2 rings containing deliberately introduced impurities.* Journal of Materials Science, vol. 11, pages 767–775, 1976. 56

[Alava 2006] M.J. Alava, P.K.V.V. Nukala and S. Zapperi. *Statistical models for fracture.* Advances in Physics, vol. 55, no. 3-4, pages 349–476, 2006. 23

[Allen 2001] D.H. Allen and C.R. Searcy. *A micromechanically-based model for predicting dynamic damage evolution in ductile polymers.* Mechanics of Materials, vol. 33, pages 177–184, 2001. 26

[Allix 1992] O. Allix and P. Ladevèze. *Interlaminar interface modeling for the prediction of delamination.* Composite Structures, vol. 22, no. 4, pages 235–242, 1992. 31

[Andersen 1997] J.V. Andersen, D. Sornette and K.T. Leung. *Tricritical behavior in rupture induced by disorder.* Physical Review Letters, vol. 78, no. 11, pages 2140–2143, 1997. 12

[Anderson 2005] T.L. Anderson. Fracture mechanics: fundamentals and applications. CRC Press, 2005. 60

[Andersons 2000] J. Andersons, U.A. Handge, I.M. Sokolov and A. Blumen. *Analysis of brittle coating fragmentation under uniaxial tension for Weibull strength distributions.* The European Physical Journal B, vol. 17, pages 261–268, 2000. 23

[Ari 1993] N. Ari and J.S. Wilbeck. *Debris fragment characterization in oblique hypervelocity impacts.* International Journal of Impact Engineering, vol. 14, pages 37–48, 1993. 29

[Ashby 1990] M.F. Ashby and C.G. Sammis. *The damage mechanics of brittle solids in compression.* Pure and Applied Geophysics, vol. 133, pages 189–521, 1990. 26

[Åström 2000] J.A. Åström, B.L. Holian and J. Timonen. *Universality in fragmentation.* Physical Review Letters, vol. 84, no. 14, pages 3061–3065, 2000. 25, 107, 115, 159, 177

[Åström 2004a] J.A. Åström, R.P. Linna and J. Timonen. *Exponential and power-law mass distributions in brittle fragmentation.* Physical Review E, vol. 70, no. 2, pages 026104–026111, 2004. 25

[Åström 2004b] J.A. Åström, F. Ouchterlony, R.P. Linna and J. Timonen. *Universal dynamic fragmentation in D dimensions.* Physical Review Letters, vol. 92(24), page 245506(4), 2004. 25, 116, 141, 159

[Åström 2006] J.A. Åström. *Statistical models of brittle fragmentation.* Advances in Physics, vol. 55, pages 247–278, 2006. 22, 25

[Aurenhammer 1991] F. Aurenhammer. *Voronoi diagrams - A survey of fundamental geometric data structure.* ACM Computing Surveys, vol. 3, no. 23, pages 345–405, 1991. 15

[Barenblatt 1962] G.I. Barenblatt. *Mathematical theory of equilibrium cracks in brittle fracture.* Advances in Applied Mechanics, vol. 2, pages 55–129, 1962. 43

[Bassi 1997] F. Bassi and S. Rebay. *A high-order accurate discontinuous finite element method for the numerical solution of the compressible Navier-Stokes equations.* Journal of Computational Physics, vol. 131, pages 267–279, 1997. 52

[Bazant 1998] Z.P. Bazant, and J. Planas. Fracture and size effect in concrete and other quasibrittle materials: concrete and other quasibrittle materials. CRC press, 1998. 43, 62, 63

[Bazant 1999] Z.P. Bazant. *Size effect on structural strength: a review.* Archive of Applied Mechanics, vol. 69, pages 703–725, 1999. 62

[Bazant 2002] Z.P. Bazant and M. Jirasek. *Nonlocal integral formulation of plasticity and damage: survey of progress.* Journal of Engineering Mechanics, pages 1119–1149, 2002. 62

[Bazant 2004] Z.P. Bazant. *Probability distribution of energetic-statistical effect in quasibrittle fracture.* Probabilistic Engineering Mechanics, vol. 19, pages 307–319, 2004. 62, 63

[Bazant 2007] Z.P. Bazant and S.D. Pang. *Activation energy based extreme value statistics and size effect in brittle and quasibrittle fracture.* Journal of the Mechanics and Physics of Solids, vol. 55, pages 91–131, 2007. 57, 62, 63

[Becher 1998] P.F. Becher, E.Y. Sun, K.P. Plucknett, K.B. Alexander, C.H. Hsueh, H.T. Lin, B. Waters and C.G. Westmoreland. *Microstructual design of silicon nitride with improved fracture toughness: effects of grain shape and size.* Journal of the American Ceramic Society, vol. 46, pages 1909–1942, 1998. 56

[Beirlant 2004] J. Beirlant, Y. Goegebeur, J. Teugels and J. Segers. Statistics of extremes: theory and applications. John Wiley, New York, 2004. 117

[Belytschko 1994] T. Belytschko, Y.Y. Lu and L. Gu. *Element-free Galerkin methods for static and dynamic fracture.* International Journal of Numerical Methods, vol. 37, no. 2, pages 229–256, 1994. 32

[Belytschko 2000] T. Belytschko, W.K. Liu and B. Moran. Nonlinear finite elements for continua and structures. Wiley, 2000. 30, 37

[Bennett 1936] J.G. Bennett. *Broken coal.* Journal of the Institute of Fuel, vol. 10, pages 22–39, 1936. 11, 12

[Bershadskii 2000] A. Bershadskii. *Some classification of fragmentation processes related to fracture.* Journal of Physics A, pages 2179–2183, 2000. 12

[Bird 2009] N.R.A. Bird, C.W. Watts, A.M. Tarquis and A.P. Whitmore. *Modeling dynamic fragmentation of soil.* Vadose Zone Journal, vol. 8, no. 1, pages 197–201, 2009. 12

[Bishop 2009] J.E. Bishop. *Simulating the pervasive failure of materials and structures using randomly close-packed Voronoi tesselations.* Computational Mechanics, vol. 44, no. 4, pages 455–471, 2009. 15

[Blackman 2003] B.R.K. Blackman, H. Hadavinia, A.J. Kinloch and J.G. Williams. *The use of a cohesive zone model to study the fracture of fibre composites and adhesively-bonded joints.* International Journal of Fracture, vol. 119, no. 1, pages 25–46, 2003. 30

[Blum 1973] H. Blum. *Biological shape and visual science (part I).* Journal Theoretical Biology, vol. 38, pages 205–287, 1973. 15

[Botet 1996] R. Botet and M. Ploszajczak. *Delayed failure in shocked silicon carbide.* Physical Review E, vol. 54, pages 3320–3333, 1996. 22

[Bouzid 2001] S. Bouzid, A. Nyoungue, Z. Azari, N. Bouaouadja and G. Pluvinage. *Fracture criterion for glass under impact loading.* International Journal of Impact Engineering, vol. 25, pages 831–845, 2001. 29

[Brajer 2003] X. Brajer, P. Forquin, R. Gy and F. Hild. *The role of surface and volume defects in the fracture of glass under quasi-static and dynamic loadings.* Journal of Non-Crystalline Solids, vol. 316, pages 42–53, 2003. 26, 69

[Butcher 1975] B.M. Butcher and A.L. Stevens. *Shock wave response of window rock coal.* Internation Journal of Rock Mechanics and Mining Science & Geomechanics Abstracts, vol. 12, pages 147–155, 1975. 28

[Cai 2000] J.G. Cai and J. Zhao. *Effects of multiple parallel fractures of apparent attenuation of stress waves in rock masses.* Journal of Rock Mechanics and Mining Science, vol. 37, pages 661–682, 2000. 68

[Camacho 1996] G.T. Camacho and M. Ortiz. *Computational modelling of impact damage in brittle materials.* International Journal of Solids and Structures, vol. 33, no. 20-22, pages 2899–2938, 1996. 21, 30, 48, 78, 87, 107, 108, 109, 135, 168

[Capaccioni 1986] F. Capaccioni, P. Cerroni, M. Coradini, M. Di Martino, P. Farinella, E. Flamini, G. Martelli, P. Paolicchi, P.N. Smith, A. Woodwrs and V. Zappala. *Asteroidal catastrophic collisions simulated by hypervelocity impact experiments.* Icarus, vol. 66, pages 487–514, 1986. 29, 107

[Carmona 2008] H.A. Carmona, F.K. Wittel, F. Kun and H.J. Herrmann. *Fragmentation processes in impact of spheres.* Physical Review E, vol. 77, no. 5-1302, 2008. 159, 166

[Castillo 2000] P. Castillo, B. Cockburn, I. Perugia and D. Schötzau. *An a priori error analysis of the local discontinuous Galerkin method for elliptic problems.* SIAM Journal on Numerical Analysis, vol. 38, pages 1676–1706, 2000. 51

[Cazes 2009] F. Cazes, M. Coret, A. Combescure and A. Gravouil. *A thermodynamic method for the construction of a cohesive law from a non-local damage model.* International Journal of Solids and Structures, vol. 46, pages 1476–1490, 2009. 26

[Chaboche 1988a] J.L. Chaboche. *Continuum damage mechanics. 1. General concepts.* Journal of applied mechanics - Transactions of the ASME, vol. 55, no. 1, pages 59–64, 1988. 31

[Chaboche 1988b] J.L. Chaboche. *Continuum damage mechanics. 2. Damage growth, crack initiation, and crack-growth.* Journal of applied mechanics - Transactions of the ASME, vol. 55, no. 1, pages 65–72, 1988. 31

[Chen 1996] W. Chen and G. Ravichandran. *Static and dynamic compressive behavior of aluminum nitride under moderate confinement.* Journal of the American Ceramics Society, vol. 79, pages 579–584, 1996. 23, 29

[Chudnovsky 1987] A. Chudnovsky and B. Kunin. *A probabilistic model of brittle crack formation.* Journal of Applied Physics, vol. 62, no. 10, page 4124, 1987. 62

[Cirak 2005] F. Cirak, M. Ortiz and A. Pandolfi. *A cohesive approach to thin-shell fracture and fragmentation.* Computer Methods in Applied Mechanics and Engineering, vol. 194, no. 21-24, pages 2604 – 2618, 2005. 30

[Clifton 1997] R.J. Clifton, M. Mello and N.S. Brar. *Effect of shear on failure waves in soda lime glass.* Proceedings of the Conference of the American Physical Society Topical Group on Shock Compression of Condensed Matter held at Amherst, MA, USA, pages 521–524, 1997. 29

[Cokburn 2002] B. Cokburn. *Discontinuous Galerkin methods.* Plenary lecture presented at the 80th annual GAMM conference, Augsburg, Germany, 2002. 50

[Coles 1991] P. Coles. *Voronoi cosmology.* Nature, vol. 349, no. 288, pages 461–472, 1991. 15

[Coles 2001] S. Coles. An introduction to statistical modeling of extreme values. Springer, 2001. 57, 63, 117

[Combescure 1990] A. Combescure and J. Yin. *Finite element method for large displacement and large strain elasto-plastic analysis of shell structures and some application of damage mechanics.* Engineering Fracture Mechanics, vol. 36, no. 2, pages 219–231, 1990. 31

[D'Addetta 2001] G.A. D'Addetta, F. Kun, E. Ramm and H.J. Herrmann. From solids to granulates - discrete element simulations of fracture and fragmentation processes in geomaterials. Springer Berlin / Heidelberg, 2001. 32

[Danzer 1992] R. Danzer. *A general strength distribution function for brittle materials.* Journal of the European Ceramic Society, vol. 10, pages 461–472, 1992. 62

[Daphalapurkar 2010] N.P. Daphalapurkar and K.T. Ramesh. *Predicting variability in the dynamic failure strength of brittle materials.* Journal of the Mechanics and Physics of Solids, vol. submitted, 2010. 23

[De Borst 2006] R. De Borst. *Modern domain-based discretization methods for damage and fracture.* International Journal of Fracture, vol. 138, pages 241–262, 2006. 50

[De Oliveira 2007] P.M.C. De Oliveira, C.A.F. Leite, C.V. Chianca, J.S. Sa Martins and C.F. Moukarzel. *Fragmentation experiment and model for falling mercury drops.* Physica A, pages 375–380, 2007. 29

[Delannay 1996] R. Delannay, G. Le Caer and R. Botet. *A simple soluble model of discrete sequential fragmentation.* Journal of Physics A, vol. 29, page 6693, 1996. 22

[Denoual 1997] C. Denoual, G. Barbier and F. Hild. *A probabilistic approach for fragmentation of brittle materials under dynamic loading.* Mechanics of Solids and Structures, vol. t.325, Serie II b, pages 685–691, 1997. 26, 69

[Denoual 2002] C. Denoual and F. Hild. *Dynamic fragmentation of brittle solids: a multi-scale model.* European Journal of Mechanics and Solids, vol. 21, pages 105–120, 2002. 26, 69, 177

[Doremus 1983] R.H. Doremus. *Fracture statistics: a comparison of the normal, Weibull and Type I extreme value distributions.* Journal of Applied Physics, vol. 54, no. 1, pages 193–198, 1983. 63

[Drugan 2001] W.J. Drugan. *Dynamic fragmentation of brittle materials: analytical mechanics-based models.* Journal of the Mechanics and Physics of Solids, vol. 49, no. 6, pages 1181–1208, 2001. 21, 69, 87, 135

[Dugdale 1960] D.S. Dugdale. *Yielding of steel sheets containing slits.* Journal of the Mechanics and Physics of Solids, vol. 8, no. 2, pages 100–104, 1960. 43

[Dusza 1999] J. Dusza and M. Steen. *Fractography and fracture mechanics property assessment of advanced structural ceramics.* International Materials Reviews, vol. 44, no. 5, pages 165–216, 1999. 55, 57

[Einav 2006] I. Einav. *Breakage mechanisms-Part I: theory.* Journal of the Mechanics and Physics of Solids, vol. 55, pages 1274–1297, 2006. 60

[Elek 2005] P. Elek and S. Jaramaz. *Modeling of fragmentation of rapidly expanding cylinder.* Journal of Theoretical and Applied Mechanics, vol. 32, no. 2, pages 113–130, 2005. 32

[Elices 2002] M. Elices, G.V. Guinea, F.J. Gomez and J. Planas. *The cohesive zone model: advantages, limitations and challenges.* Engineering Fracture Mechanics, vol. 69, pages 137–163, 2002. 44

[Englman 1991] R. Englman. *Fragments of matter from a maximum-entropy viewpoint.* Journal of Physics: Condensed Matter, vol. 3, pages 1019–1053, 1991. 23, 107

[Espinosa 1998] H.D. Espinosa, P.D. Zavatierri and S.K. Dwivedi. *A finite deformation continuum discrete model for the description of fragmentation and damage in brittle materials.* Journal of the Mechanics and Physics of Solids, vol. 46, pages 1909–1942, 1998. 26, 30

[Espinosa 2003a] H.D. Espinosa and P.D. Zavatierri. *A grain level model for the study of failure initiation and evolution in polycristalline brittle materials. PartI: theory and numerical implementation.* Mechanics of Materials, vol. 35, pages 333–364, 2003. 26

[Espinosa 2003b] H.D. Espinosa and P.D. Zavatierri. *A grain level model for the study of failure initiation and evolution in polycristalline brittle materials. PartII: numerical examples.* Mechanics of Materials, vol. 35, pages 365–394, 2003. 26

[Evans 1968] A.G. Evans and M.S. Marathe. *Microcracking and stress-strain curves for concrete in tension.* Materials and Structures Journal, vol. 1, pages 61–64, 1968. 44

[Eymard 2000] R. Eymard, T. Gallouët and R. Herbin. Handbook of numerical analysis, volume 7. 2000. 30

[Fahrenthold 2001] E.P. Fahrenthold and B.A. Horban. *An improved hybrid particle-element method for hypervelocity impact simulation.* International Journal of Impact Engineering, vol. 26, no. 1-10, pages 169–178, 2001. 32

[Falk 2001] M.L. Falk, A. Needleman and J.R. Rice. *A critical evaluation of cohesive models of dynamic fracture.* Journal of Physique IV (5th European Mechanics of materials conference in Delft, Netherlands, pages 5.43–5.50, 2001. 47

[Fineberg 1991] J. Fineberg, S.P. Gross, M. Marder and H.L. Swinney. *Instability in dynamic fracture.* Physical Review Letters, vol. 67, no. 4, pages 457–460, 1991. 5

[Fisher 1928] R.A. Fisher and L.H.C Tippett. *Limiting forms of the frequency distribution of the largest and smallest member of a sample.* Proceedings of the Cambridge Philosophical Society, pages 180–190, 1928. 63

[Forquin 2003a] P. Forquin, C. Denoual, D.E. Cottenot and F. Hild. *Experiments and modelling of the compressive behaviour of two SiC ceramics.* Mechanics of Materials, vol. 35, pages 987–1002, 2003. 26, 29, 69

[Forquin 2003b] P. Forquin, L. Tran, Loubigne P.F., L. Rota and F. Hild. *Effect of aluminum reinforcement on the dynamic fragmentation of SiC ceramics.* International Journal of Impact Engineering, vol. 28, pages 1061–1076, 2003. 26, 69

[Foulk 2010] J.W. Foulk. *An examination of stability in cohesive zone modeling.* Computational methods in Applied Mechanics and Engineering, vol. 199, pages 465–470, 2010. 48

[Fréchet 1927] M. Fréchet. *Sur la loi de probabilité de l'écart maximum.* Annales de la société polonaise de mathématique, vol. 6, pages 93–116, 1927. 63

[Freund 1999] L.B. Freund. *Dynamic behavior of brittle materials.* Rapport technique, 1999. 46

[Fujiwara 1980] A. Fujiwara. *Experimental study on the velocity of fragments in collisional breakup.* Icarus, vol. 44, pages 142–153, 1980. 29

[Gao 2004] Y.F. Gao and A.F. Bower. *A simple technique for avoiding convergence problems in finite element simulations of crack nucleation and growth*

on cohesive interface. Modelling and Simulation in Materials Science and Engineering, vol. 12, pages 453–463, 2004. 89

[Geuzaine] C. Geuzaine and J.F. Remacle. *http://geuz.org/gmsh/.* -. 152

[Gilvarry 1961a] J.J. Gilvarry. *Fracture of brittle solids: 1. Distribution function for fragment size in single fracture (Theoretical).* Journal of Applied Physics, vol. 32, no. 3, pages 391–399, 1961. 3, 24, 106, 141, 159, 167

[Gilvarry 1961b] J.J. Gilvarry and B.H. Bergstrom. *Fracture of brittle solids: 2. Distribution function for fragment size in single fracture (Experimental).* Journal of Applied Physics, vol. 32, no. 3, pages 400–410, 1961. 25, 106

[Gilvarry 1962a] J.J. Gilvarry and B.H. Bergstrom. *Fracture of brittle solids: 3. Experimental results on the distribution of fragment size in single fracture.* Journal of Applied Physics, vol. 33, no. 11, pages 3211–3213, 1962. 25

[Gilvarry 1962b] J.J. Gilvarry and B.H. Bergstrom. *Fracture of brittle solids: 4. Two-dimensional distribution function for fragment size in single fracture (theoretical).* Journal of Applied Physics, vol. 33, no. 11, pages 3214–3217, 1962. 25

[Gilvarry 1962c] J.J. Gilvarry and B.H. Bergstrom. *Fracture of brittle solids: 5. Two-dimensional distribution function for fragment size in single fracture (experimental).* Journal of Applied Physics, vol. 33, no. 11, pages 3218–3224, 1962. 25

[Gingold 1977] R.A. Gingold and J.J. Monaghan. *Smooth particle hydrodynamics - Theory and application to non-spherical stars.* Monthly notices of the royal astronomical Society, vol. 181, no. 2, pages 378–389, 1977. 32

[Glenn 1986a] L.A. Glenn and A. Chudnovsky. *Strain-energy effects on dynamic fragmentation.* Journal of Applied Physics, vol. 59, no. 4, pages 1379–1380, 1986. 19, 32, 87, 139

[Glenn 1986b] L.A. Glenn, B.Y. Gommerstadt and A. Chudnovsky. *A fracture mechanics model of fragmentation.* Journal of Applied Physics, vol. 60, no. 3, pages 1224–1226, 1986. 19

[Gold 2008] V. Gold and E.L. Baker. *A model for fracture of explosively driven metal shells.* Engineering Fracture Mechanics, vol. 75, pages 275–289, 2008. 32

[Gosselet 2006] P. Gosselet and C. Rey. *Non-overlapping domain decomposition methods in structural mechanics.* Archives of Computational Methods in Engineering, vol. 13, pages 515–572, 2006. 51

[Goto 2008] D.M. Goto, R. Beckera, T.J. Orzechowskia, H.K. Springera, A.J. Sunwooa and C.K. Syna. *Investigation of the fracture and fragmentation of explosively driven rings and cylinders.* International Journal of Impact Engineering, vol. 35, pages 1547–1556, 2008. 28, 32

[Gourdin 1989] W.H. Gourdin, S.L. Weinland and L.M. Boling. *Development of the electromagnetically launched expanding ring as a high-strain-rate test technique.* Review of Scientific Instruments, vol. 60, no. 3, pages 427–432, 1989. 28

[Grady 1980] D.E. Grady and M.E. Kipp. *Continuum modeling of explosive fracture in oil shale.* International Journal of Numerical and Analytical Methods in Geomechanics, vol. 17, pages 147–157, 1980. 26

[Grady 1982] D.E. Grady. *Local inertial effects in dynamic fragmentation.* Journal of Applied Physics, vol. 53, no. 1, pages 322–325, 1982. 18, 32, 87, 94, 103, 106, 121, 127, 131

[Grady 1983] D.E. Grady and D.A. Benson. *Fragmentation of metal rings by electromagnetic loading.* Experimental Mechanics, vol. 23, pages 393–400, 1983. 28, 115

[Grady 1985] D.E. Grady and M.E. Kipp. *Geometric statistics and dynamic fragmentation.* Journal of Applied Physics, vol. 58, no. 33, pages 1210–1222, 1985. 14, 105, 106, 107, 141

[Grady 1988] D.E. Grady. *The spall strength of condensed matter.* Journal of the Mechanics of Physics and Solids, vol. 36, no. 3, pages 353–384, 1988. 20, 94, 103, 131

[Grady 1990] D.E. Grady. *Particle-size statistics in dynamic fragmentation.* Journal of Applied Physics, vol. 68, no. 12, pages 6099–6105, 1990. 13, 141, 168

[Grady 1992] D.E. Grady and M.M. Hightower. Natural fragmentation of exploding cylinders. Shockwave and high strain rate phenomena in materials, 1992. 29

[Grady 1995] D.E. Grady and M.E. Kipp. *Experimental measurement of dynamic failure and fragmentation properties of metals.* International Journal of Solids and Structures, vol. 32, no. 17/18, pages 2779–2791, 1995. 15

[Grady 2001] D.E. Grady and N.A. Winfree. *Impact fragmentation of high-velocity impact projectiles on thin plates: a physical and statistical characterization of fragment debris.* International Journal of Impact Engineering, vol. 26, pages 249–262, 2001. 176, 177

[Grady 2003] D.E. Grady and M.L. Olsen. *A statistics and energy based theory of dynamic fragmentation.* International Journal of Impact Engineering, vol. 29, no. 1-10, pages 293–306, 2003. 27, 28, 115

[Grady 2006a] D.E. Grady. *Comparison of hypervelocity fragmentation and spall experiments with Tuller-Butcher spall and fragment size criteria.* International Journal of Impact Engineering, vol. 33, pages 305–315, 2006. 104

[Grady 2006b] D.E. Grady. *Fragmentation of Rings and Shells: The Legacy of N.F. Mott.* Springer, 2006. 14, 15, 17, 18, 21, 27, 106, 116

[Grady 2007] D.E. Grady. *Dynamic Fragmentation of Solids.* Rapport technique, 2007. 4, 13, 14, 23

[Grady 2008] D.E. Grady. *Fragment size distributions from the dynamic fragmentation of brittle solids.* International Journal of Impact Engineering, vol. 35, pages 1557–1562, 2008. 20, 104, 107

[Grady 2009] D.E. Grady. *Length scales and size distributions in dynamic fragmentation.* International Journal of Fracture, vol. 163, pages 85–99, 2009. 121, 127, 131, 132, 133, 134, 137

[Graham-Brady 2010] L.L. Graham-Brady. *Statistical characterization of mesoscale uniaxial compressive strength in brittle materials with randomly occurring flaws.* International Journal of Solids and Structures, vol. In press, corrected proof, 2010. 62

[Green 1968] S.J. Green and R.D. Perkins. *Uniaxial compression tests at varying strain rates on three geological materials.* Proceeding of 10th Symposium on Rock Mechanics, pages 35–54, 1968. 29

[Grégoire 2007] D. Grégoire, H. Maigre, J. Réthoré and A. Combescure. *Dynamic crack propagation under mixed-mode loading - Comparison between experiments and X-FEM simulations.* International Journal of Solids and Structures, vol. 44, pages 6517–6534, 2007. 31

[Griffith 1943] L. Griffith. *A Theory of the size distribution of particles in a communited system.* Canadian Journal of Research, vol. 21A, no. 6, pages 57–64, 1943. 24

[Grote 2001] D.L. Grote, S.W. Park and M. Zhou. *Dynamic behavior of concrete at high strain rates and pressures: I. experimental characterization.* International Journal of Impact Engineering, vol. 25, pages 869–886, 2001. 29

[Guduru 2002] P.R. Guduru and L.B. Freund. *The dynamics of multiple neck formation and fragmentation in high strain rate extension of ductile materials.* International Journal of Solids and Structures, vol. 39, no. 21-22, pages 5615–5632, 2002. 32

[Gudwska-Nowak 2009] E. Gudwska-Nowak, K. Psonka-Antonczyk, K. Weron, T. Elsasser and G. Taucher-Scholz. *Distribution of DNA fragment sizes after*

irradiation with irons. European Physical Journal, vol. 30, pages 317–324, 2009. 1

[Gumbel 1958] E.J. Gumbel. *Statistics of extremes.* Columbia University Press, New York, 1958. 63

[Gurney 1943] R.W. Gurney. *The initial velocity of fragments from bombs, shells and grenades.* Army Ballistic Research Laboratory Report BRL 405, 1943. 29

[Hassold 1989] G.N. Hassold and D.J. Srolovitz. *Brittle fracture in materials with random defects.* Physical Review B, vol. 39, no. 13, pages 9273–9281, 1989. 23

[Heilmann 1987] G. Heilmann, H. Hilsdorf and K. Finsterwalder. *Eine neue Halterung fur Zugversuche mit Beton-Probekorpern.* Material und Technik, vol. 15(4), pages 103–107, 1987. 44

[Herrmann 2006] H.J. Herrmann, F.K. Wittel and F. Kun. *Fragmentation.* Physica A, vol. 371, pages 59–66, 2006. 32

[Hidalgo 2007] C.R. Hidalgo and I. Pagonabarraga. *Fragmenting granular gases.* Letters Journal Exploring the Frontiers of Physics, vol. 77, no. 64001, 2007. 32

[Hild 2003] F. Hild, C. Denoual, P. Forquin and X. Brajer. *On the probabilistic-deterministic transition involved in a fragmentation process of brittle materials.* Computers and Structures, vol. 81, no. 12, pages 1241–1253, 2003. 26, 69, 84, 94, 104

[Hillerborg 1976] A. Hillerborg, M. Modeer and P.E. Petersson. *Analysis of crack formation and crack growth in concrete by means of fracture mechanics and finite elements.* Cement and Concrete Research, vol. 6, pages 773–782, 1976. 44

[Hoggat 1969] C.R. Hoggat and R.F. Recht. *Stress-strain data obtained at high strain rates using an expanding ring.* Experimental Mechanics, pages 441–448, 1969. 28

[Holian 1988] B.L. Holian and D.E. Grady. *Fragmentation by molecular dynamics: the microscopic "Bing Bang".* Physical Review Letters, vol. 60, no. 14, pages 1355–1358, 1988. 1

[Hopkinson 1914] B. Hopkinson. *A method of measuring the pressure produced in the detonation of high explosives or by the impact of bullet.* Philosophical transactions of the royal Society of London, Serie A, vol. 213, no. 437-4356, 1914. 28

[Housen 1999] K.R. Housen and K.A. Holsapple. *Scale effects in strength-dominated collisions of rocky asteroids.* Icarus, vol. 142, pages 21–33, 1999. 29

[Huang 2003] C. Huang and G. Subhash. *Influence of lateral confinement on dynamic damage evolution during uniaxial compressive response of brittle solids.* Journal of Mechanics of Physics and Solids, vol. 51, pages 1089–1106, 2003. 23

[Hughes 1966] B.P. Hughes and G.P. Chapman. *The complete strain-stress for concrete in direct tension.* Materials and Structures Journal Bulletin, vol. 30, pages 95–97, 1966. 44

[Hughes 2000] T. Hughes. The finite element method: Linear static and dynamic finite element analysis. Dover Publications, 2000. 37

[Ii 2005] S. Ii, C. Iwamoto, K. Matsuaga, T. Yamamoto and Y. Ikuhara. *TEMP in situ observation of fracture behavior in ceramic materials.* Applied Surface Science, vol. 241, pages 68–74, 2005. 55

[Ishi 1992] T. Ishi and M. Matsushita. *Fragmentation of long thin glass rods.* Journal of the Physical Society of Japan, vol. 61, no. 10, pages 3474–3477, 1992. 29

[Jayatilaka 1977] A.D.S. Jayatilaka and K. Trustrum. *Statistical approach to brittle-fracture.* Journal of Material Science, vol. 12, no. 7, pages 1426–1430, 1977. 62

[Jeulin 1993] D. Jeulin. *Random functions and fracture statistics models.* Geostatistics Troia'92, vol. 1, pages 225–236, 1993. 62

[Johansen 2000] A. Johansen and D. Sornette. *Critical ruptures.* The European Physical Journal B, vol. 18, pages 163–181, 2000. 12

[Johnson 2001] G.R. Johnson, R.A. Stryk, S.R. Beissel and T.J. Holmquist. *Conversion of finite-elements into meshless particles for penetration computations involving ceramic targets.* Proceedings of the 12th APS topical conference on shock compression of condensed matter, pages 1287–1290, 2001. 32

[Johnson 2003] G.R. Johnson and R.A. Stryk. *Conversion of 3D distorted elements into meshless particles during dynamic deformation.* International Journal of Impact Engineering, vol. 28, no. 9, pages 947–966, 2003. 32

[Johnson 2005] N.L. Johnson, S. Kotz and N. Balakrishnan. Univariate discrete distributions, third edition. John Wiley, New York, 2005. 113

[Kadono 2002] T. Kadono and M. Arakawa. *Crack propagation in thin glass plates caused by high velocity impact.* Physical Review E, vol. 65, no. 035107, 2002. 22

[Kanzaki 1997] S. Kanzaki, M.E. Brito, M.C. Valecillos, K. Hirao and M. Toriyama. *Microstructure designing of silicon nitride.* Journal of the European Ceramic Society, vol. 17, pages 1841–1847, 1997. 55

[Kiang 1966] T. Kiang. *Mass distribution of asteroids, stars and galaxies.* Zeitschrift fur Astrophysik, vol. 64, no. 426-432, 1966. 15, 29

[Klein 2001] P.A. Klein, J.W. Foulx, E.P. Chen, S.A. Wimmer and H.J. Gao. *Physics-based modeling of brittle fracture, cohesive formulations, and the application to meshfree methods.* Theoretical and Applied Fracture Mechanics, vol. 37, pages 99–166, 2001. 47

[Klopp 1985] R.W. Klopp, R.J. Clifton and T.G. Shawki. *Pressure-shear impact and the dynamic viscoplastic response of metals.* Mechanics of Materials, vol. 4, no. 3-4, pages 375 – 385, 1985. 29

[Kolmogorov 1941] A.N. Kolmogorov. *On the logarithmically normal distribution law of particle sizes at the subdivision.* Doklady Akademii Nauk, vol. 31, page 99, 1941. 22

[Kolsky 1949] H. Kolsky. *An investigation of the mechanical properties of materials at very high rates of loading.* Proceedings of the Physical Society of London B, vol. 62, pages 676–700, 1949. 28

[Kraft 2008a] R.H. Kraft and J.F. Molinari. *A statistical investigation of the defects of grain boundary properties on transgranular fracture.* Acta Materialia, vol. 56, pages 4739–4749, 2008. 27

[Kraft 2008b] R.H. Kraft, J.F. Molinari, K.T. Ramesh and D.H. Warner. *Computational micromechanics of dynamic compressive loading of a brittle polycrystalline material using a distribution of grain boundary properties.* Journal of the Mechanics and Physics of Solids, vol. 56, no. 8, pages 2618 – 2641, 2008. 27

[Krapivsky 2000] P.L. Krapivsky and S.N. Majumdar. *Traveling waves, front selection, and exact nontrivial exponents in random fragmentation problem.* Physical Review Letter, vol. 85, no. 26, pages 5492–5496, 2000. 22

[Kun 1996] F. Kun and H.J. Herrmann. *A study of fragmentation processes using discrete element method.* Computational Methods in Applied Mechanics and Engineering, vol. 138, pages 3–18, 1996. 32

[Kun 1999] F. Kun and H.J. Herrmann. *Transition from damage to fragmentation in collision of solids.* Physical Review E, vol. 59, no. 3, pages 2623–2632, 1999. 177

[Kun 2006] F. Kun, F.K. Wittel, H.J. Herrmann, B.H. Kröplin and K.J. Måløy. *Scaling Behavior of Fragment Shapes*. Physical Review Letters, vol. 96, no. 2, page 025504, 2006. 176

[Ladevèze 2000] P. Ladevèze, O. Allix, J.F. Deu and D. Lévêque. *A mesomodel for localisation and damage computation in laminates*. Computer Methods in Applied Mechanics and Engineering, vol. 183, no. 1-2, pages 105–122, 2000. 31

[Lamon 2007] J. Lamon. Mécanique de la rupture fragile et de l'endommagement, approches et probabilistes. Lavoisier, 2007. 55, 56, 62

[Lankford 1979] J. Lankford. *Uniaxial compressive damage in a α-SiC at low homologous temperatures*. Journal of the American Society of Ceramics, vol. 62, page 310, 1979. 23, 29

[Lankford 1981] J. Lankford. *Mechanisms responsible for strain rate dependent compressive strength in ceramic materials*. Journal of the American Ceramic Society, vol. 64, pages C33–C35, 1981. 23

[Lankford 1991] J. Lankford and R.C. Blanchard. *Fragmentation of brittle materials at high rates of loading*. Journal of Materials Science, vol. 26, pages 3067–3072, 1991. 23

[Leadbetter 1983] M.R. Leadbetter, G. Lindgren and H. Rootzen. Extremes and related properties of random sequences and processes. Springer-Verlag, 1983. 57, 63, 86

[Lee 1967] E.H. Lee. *The continuum mechanics aspect of material properties determination*. Energetics III, pages 85–122, 1967. 16

[Lemaitre 1985] J. Lemaitre. *A continuous damage mechanics model for ductile fracture*. Journal of Engineering Materials and Technology-Transations of the ASME, vol. 107, no. 1, pages 83–89, 1985. 31

[Lennon 2000] A.M. Lennon and K.T. Ramesh. *The thermoviscoplastic response of polycrystalline tungsten in compression*. Materials Science and Engineering A, vol. 276, no. 1-2, pages 9 – 21, 2000. 29

[Lesaint 1974] P. Lesaint and P.A. Raviart. *On a finite element method for solving neutron transport equation*. Mathematical Aspects of Finite Elements in Partial Differential Equations, de Boor, Academic Press: New York, 1974. 51

[Levy 2010] S. Levy and J.F. Molinari. *Dynamic fragmentation of ceramics, signature of defects and scaling of fragment sizes*. Journal of the Mechanics and Physics of Solids, vol. 58, no. 1, pages 12–26, 2010. 109, 110, 112, 127, 135, 138

[Libersky 1991] L.D. Libersky and A.G. Petschek. *Smoothed-particle hydrodynamics with strength of materials.* Proceedings of the Next Free-Lagrange Conference, pages 248–257, 1991. 32

[Lienau 1936] C.C. Lienau. *Random fracture for brittle solid.* Journal of the Franklin Institute, vol. 221, pages 485–494,674–686,769,787, 1936. 3, 11, 12, 141, 167

[Lienhard 1967] J.H. Lienhard and P.L. Meyer. *A physical basis for the generalized gamma distribution.* Quaterly of Applied Mathematics, vol. 25, no. 3, pages 330–334, 1967. 115

[Lindborg 1969] U. Lindborg. *A statistical model for the kinking of microcracks.* Acta Metallurgica, vol. 17, pages 521–526, 1969. 24

[Lindholm 1964] U.S. Lindholm. *Some experiments with the split Hopkinson pressure bar.* Journal of the Mechanics and Physics of Solids, vol. 12, pages 317–335, 1964. 29

[Lindholm 1968] U.S. Lindholm. *High strain-rate testing: Tension and compression.* Experimental Mechanics, vol. 8, no. 1, pages 1–9, 1968. 29

[Liu 1997] W.K. Liu, S.F. Li and T. Belytchko. *Moving least square reproducing kernel method. 1.: Methodology and convergence.* Computational Methods in Applied Mechanics and Engineering, vol. 143, no. 1-2, pages 113–154, 1997. 32

[Lucy 1977] L.B. Lucy. *Numerical approach for testing of fission hypothesis.* Astronomy Journal, vol. 82, no. 12, pages 1013–1024, 1977. 32

[Lundberg 1976] B. Lundberg. *A split Hopkinson bar study on energy absorption in dynamic rock fragmentation.* International Journal of Rock Mechanics and Mineral Science, vol. 13, pages 187–197, 1976. 29

[Magnier 1998] S.A. Magnier and F.V. Donzé. *Numerical simulations of impacts using a discrete element method.* International Journal for Numerical and Analytical Methods in Geomechanics, vol. 3, no. 3, pages 257–276, 1998. 32

[Maurel 2008] B. Maurel and A. Combescure. *A SPH shell formulation for plasticity and fracture analysis in explicit dynamics.* International Journal for Numerical Methods in Engineering, vol. 76, pages 949–971, 2008. 32

[Meibom 1996] A. Meibom and I. Balslev. *Composite power laws in shock fragmentation.* Physical Review Letters, vol. 76, no. 14, pages 2492–2494, 1996. 116, 157

[Mergheim 2004] J. Mergheim, E. Kuhl and P. Steinmann. *A hybrid discontinuous Galerkin/interface method for the computational modeling of failure.* Communications in Numerical Methods in Engineering, vol. 20, pages 511–519, 2004. 50

[Meulbroek 2008] J.P. Meulbroek, K.T. Ramesh, P.K. Swaminathan and A.M. Lennon. *CTH simulations of an expanding ring to study fragmentation.* International Journal of Impact Engineering, vol. 35, pages 1661–1664, 2008. 32

[Miller 1999] O. Miller, L.B. Freund and A. Needleman. *Modeling and simulation of dynamic fragmentation in brittle materials.* International Journal of Fracture, vol. 96, pages 101–125, 1999. 46

[Mock Jr. 1983] W. Mock Jr. and W.H. Holt. *Fragmentation behavior of armor iron and HF-1 steel explosive-filled cylinders.* Journal of Applied Physics, vol. 54, no. 5, pages 2344–2351, 1983. 28

[Moes 2002] N. Moes and T. Belytschko. *Extended finite element method for cohesive crack growth.* Engineering Fracture Mechanics, vol. 69(7), pages 813–833, 2002. 31

[Molinari 2007] J.F. Molinari, G. Gazonas, R. Ragupathy, A. Rusinek and F. Zhou. *The cohesive element approach to dynamic fragmentation: The question of energy convergence.* International Journal for Numerical Methods in Engineering, no. 69, pages 484–503, 2007. 128

[Momber 2000] A.W. Momber. *The fragmentation of standard concrete cylinders under compression: the role of secondary fracture debris.* Engineering Fracture Mechanics, vol. 67, pages 445–459, 2000. 23

[Mota 2003] A. Mota, W. Klug, M. Ortiz and A. Pandolfi. *Finite-element simulation of firearm injury to the human cranium.* Computational Mechanics, vol. 31, no. 1-2, pages 115–121, 2003. 30

[Mota 2008] A. Mota, J. Knap and M. Ortiz. *Fracture and fragmentation of simplicial finite element meshes using graphs.* International Journal for Numerical Methods in Engineering, vol. 73, pages 1575–1570, 2008. 30

[Mott 1943a] N.F. Mott. *Fragmentation of H.E. shells: A theoretical formula for the distribution of weights of fragments.* United Kingdom Ministry of Supply, vol. AC3642, 1943. 17

[Mott 1943b] N.F. Mott and E.H. Linfoot. *A theory of fragmentation.* United Kingdom Ministry of Supply AC3348, February 1943. 3, 12, 106, 167

[Mott 1947] N.F. Mott. *Fragmentation of shell cases.* Proceedings of the Royal Society of London Series A-Mathematical and Physical Sciences, vol. 189, no. 1018, pages 300–308, 1947. 3, 29, 106, 141, 167

[Moukarzel 2007] C. Moukarzel, S.F. Fernandez-Sabido and J.C. Ruiz-Suarez. *Phase transition in liquid drop fragmentation.* Physical Review E, vol. 75, no. 061127, 2007. 12

[Munjiza 2004] A. Munjiza. *The combined finite-discrete element method.* Wiley, 2004. 32

[Needleman 1990] A. Needleman. *An analysis of tensile decohesion along an interface.* Journal of the Mechanics and Physics of Solids, vol. 38, no. 3, pages 289–324, 1990. 46

[Nemat-Nasser 1994] S. Nemat-Nasser and H. Deng. *Strain-rate effect on brittle failure in compression.* Acta Metallurgica et Materialia, vol. 42, no. 3, pages 1013–1024, 1994. 27

[Nitsche 1971] J.A. Nitsche. *Uber ein Variationsprinzip zur Losung Dirichlet-Problemen bei Verwendung von Teilraumen, die keinen Randbedingungen uneworfen sind.* Abhandlungen aus dem Mathematischen Seminar der Universität Hamburg, vol. 36, pages 9–15, 1971. 51, 52, 53

[Noels 2006] L. Noels and R. Radovitzky. *A general discontinuous Galerkin method for finite hyperelasticity. Formulation and numerical applications.* International Journal for Numerical Methods in Engineering, vol. 68, pages 64–97, 2006. 51, 52

[Noels 2007] L. Noels and R. Radovitzky. *An explicit discontinuous Galerkin method for non-linear solid dynamics: Formulation, parallel implementation and scalability properties.* International Journal for Numerical Methods in Engineering, vol. 74, no. 9, pages 1393–1420, 2007. 51

[Oddershede 1993] L. Oddershede, P. Dimon and J. Bohr. *Self-organized criticality in fragmenting.* Physical Review Letters, vol. 71, no. 19, pages 3107–3110, 1993. 12, 26, 116, 157

[Oden 1998] J.T. Oden, I. Babuska and C.E. Baumann. *A discontinuous hp finite element method for diffusion problems.* Journal of Computational Physics, vol. 146, no. 2, pages 491 – 519, 1998. 51

[Ortiz 1999] M. Ortiz and A. Pandolfi. *Finite-deformation irreversible cohesive elements for three-dimensional crack-propagation analysis.* International Journal for Numerical Methods in Engineering, vol. 44, no. 9, pages 1267–1282, 1999. 30, 48, 168

[Paliwal 2006] B. Paliwal, K.T. Ramesh and J.W. McCauley. *Direct observation of the dynamic compressive failure of transparent polycrystalline ceramic (AlON).* Journal of the American Ceramic Society, vol. 89, pages 2128–2133, 2006. 23

[Paliwal 2008] B. Paliwal and K.T. Ramesh. *An interacting micro-crack damage model for failure of brittle materials under compression.* Journal of the Mechanics and Physics of Solids, vol. 56, no. 3, pages 896–923, 2008. 27

[Palmer 1973] A.C. Palmer and J.R. Rice. *The growth of slip surfaces in the progressive failure of over-consolidated clay*. Philosophical Transactions of the Royal Society of London, Serie A, vol. 332, pages 527–548, 1973. 46

[Pandolfi 1999] A. Pandolfi, P. Krysl and M. Ortiz. *Finite-element simulation of ring expansion and fragmentation. The capturing length and time scales through cohesive model of fracture*. International Journal of Fracture, vol. 95, no. 1-4, pages 279–297, 1999. 32

[Pandolfi 2002] A. Pandolfi and M. Ortiz. *An efficient adaptive procedure for three-dimensional fragmentation simulations*. Engineering with Computers, vol. 18, pages 148–159, 2002. 30, 48

[Peerlings 1996] R.H.J. Peerlings, R. De Borst, W.A.M. Brekelmans and J.H.P. De Vree. *Gradient-enhanced damage for quasi-brittle materials*. International Journal of Numerical Methods in Engineering, vol. 39, pages 3391–3403, 1996. 31

[Perfect 1997] E. Perfect. *Fractal models for the fragmentation of rocks and soils: a review*. Engineering Geology, vol. 48, pages 185–198, 1997. 12

[Pierce 1936] F.T. Pierce. *Tensile tests for cotton yarns, V:'the weakest link', theorems on the strength of long composite specimens*. Journal of Textile Institute, vol. 17, page T355, 1936. 56, 59

[Planas 1995] J. Planas, G.V. Guinea and M. Elices. *Ruptures modulus and fracture properties of concrete*. Fracture Mechanics of Concrete Structures, vol. 1, pages 95–110, 1995. 44

[Planas 2003] J. Planas, M. Elices, G.V. Guinea, F.J. Gomez, D.A. Cendon and Arbilla I. *Generalizations and specializations of cohesive crack models*. Engineering Fracture Mechanics, vol. 70, pages 1759–1776, 2003. 44

[Prabel 2007] B. Prabel, A. Combescure, A. Gravouil and S. Marie. *Level set X-FEM non matching meshes: Application to dynamic crack propagation in elastic-plastic media*. International Journal for Numerical Methods in Engineering, vol. 69, pages 1553–1569, 2007. 31

[Radovitzky 2010] R. Radovitzky, A. Seagraves, M. Tupek and L. Noels. *A scalable 3D fracture and fragmentation algorithm based on a hybrid, discontinuous Galerkin, cohesive element method*. Computer Methods in Applied Mechanics and Engineering, vol. In Press, Accepted Manuscript, pages –, 2010. 51

[Raghupathy 2006] R. Raghupathy, G.A. Gazonas, J.F. Molinari and F. Zhou. *Numerical convergence of the cohesive element approach in dynamic fragmentation simulations*. In Shock Compression of Condensed Matter, volume 845 of *American Institute of Physics Conference Series*, pages 654–657, 2006. 89

[Ramesh 2008] K.T. Ramesh. *Handbook of experimental mechanics. chapter 33: High rates and impact experiments.* Springer, 2008. 27

[Repetto 2000] E.A. Repetto, R. Radovitzky and M. Ortiz. *Finite-element simulation of dynamic fracture and fragmentation of glass rods.* Computational Methods in Applied Mechanics and Engineering, no. 1-2, pages 3–14, 2000. 30, 31

[Réthoré 2005] J. Réthoré, A. Gravouil and A. Combescure. *An energy-conserving scheme for dynamic crack growth using the eXtended finite element method.* International Journal for Numerical Methods in Engineering, vol. 63, pages 631–659, 2005. 31

[Rice 1980] J.R. Rice. *The mechanics of earthquake rupture.* Physics of the Earth's Interior, page 555, 1980. 46

[Ringler 2008] T. Ringler, L. Ju and M. Gunzburger. *A multiresolution method for climate system modeling: application of spherical centroidal Voronoi tessellations.* Ocean Dynamics, vol. 58, pages 475–498, 2008. 15

[Rosin 1933] P. Rosin and E. Rammler. *The laws governing the fineness of powdered coal.* Journal of the Institute of Fuel, vol. 7, pages 29–36, 1933. 3, 11, 34, 106, 167

[Rusinek 2007] A. Rusinek and R. Zaera. *Finite element simulation of steel ring fragmentation under radial expansion.* International Journal of Impact Engineering, vol. 34, no. 4, pages 799–822, 2007. 32

[Ryan 1998] E.V. Ryan. *Impact Fragmentation: From the Laboratory to Asteroids.* Icarus, vol. 133, pages 1–24, 1998. 29

[Schloegel] G. Schloegel K. Karypis and V. Kumar. *http://glaros.dtc.umn.edu/gkhome/metis/parmetis/overview.* -. 53

[Schuhmann 1941] E.V Schuhmann. *Principles of communition, size distribution and surface calculations.* AIME Technical Publication, vol. 1189, pages 1–11, 1941. 3, 12, 107

[Seagraves 2009] A. Seagraves and R. Radovitzky. *Dynamic failure of materials and structures. chapter 12: Advances in cohesive zone modeling of dynamic fracture.* Springer, 2009. 47, 51

[Shenoy 2003] V.B. Shenoy and K.S. Kim. *Disorder effects in dynamic fragmentation of brittle materials.* Journal of the Mechanics and Physics of Solids, vol. 51, pages 2023–2035, 2003. 21, 32

[Shockey 1974] D.A. Shockey, D.R. Curran, L. Seaman and C.F. Petersen. *Fragmentation of rock under dynamic loads*. International Journal of Rock Mechanics and Geomechanics Abstracts, vol. 11, pages 303–317, 1974. 4, 28, 29

[Stauffer 1985] D. Stauffer. Introduction to percolation theory. Taylor and Francis Ltd, 1985. 107

[Subhash 2000] G. Subhash and G. Ravichandran. Split-hopkinson pressure bar testing of ceramics. Materials Park, OH: ASM International, 2000. 29

[Swegle 1995] J.W. Swegle, D.L. Hicks and S.W. Attaway. *Smoothed particle hydrodynamics stability analysis*. Journal of Computational Physics, vol. 116, no. 1, pages 123–134, 1995. 32

[Taylor 1963] G.I. Taylor. Scientific papers of G.I. Taylor, vol. III, no. 44, 1963. 29

[Telle 1995] R. Telle, V. Carle, F. Predel, U. Schafer, U. Taffner and G. Petzow. *Ceramography of high performance ceramics part IX: pores and chips*. Praktische Metallographie, vol. 32, no. 5, pages 440–466, 1995. 55

[Thornhill 2001] T.F. Thornhill, W.D. Reinhard, L.C. Chhabildas, D.E. Grady and L.T. Wilson. *Cylinder fragmentation using gas gun technique*. Shock Compression of Condensed Matter, pages 515–518, 2001. 28

[Tuler 1984] F.R. Tuler and B.M. Butcher. *A criterion for the time dependence of dynamic fracture*. International Journal of Fracture, vol. 26, pages 322–328, 1984. 104

[Turcotte 1986a] D.L. Turcotte. *A fractal model for crustal deformation*. Tectonophysics, vol. 132, pages 261–269, 1986. 12

[Turcotte 1986b] D.L. Turcotte. *Fractals and Fragmentation*. Journal of Geophysical Research, vol. 91, no. B2, pages 1921–1926, 1986. 12, 22, 107, 168

[Weibull 1939] W. Weibull. *A statistical Theory of Strength of Materials*. Proceedings of the Ingeniors Vetenskapsakad, page 151, 1939. 3, 11, 23, 57, 63, 109, 123

[Wells 2004] G.N. Wells, K. Garikipati and L. Molari. *A discontinuous Galerkin formulation for strain-gradient dependent damage model*. Computer Methods in Applied Mechanics and Engineering, vol. 193, pages 3633–3645, 2004. 51

[Winter 1979] R.E. Winter. *Measurement of fracture strain at high strain rates*. Institute of Physics of London, vol. 47, pages 81–89, 1979. 28, 29

[Wittel 2003] F.K. Wittel, F. Kun, B.D. Kröplin and H.J. Herrmann. *A study of transverse ply cracking using discrete element method*. Computational Materials Science, vol. 28, pages 608–619, 2003. 32

[Wittel 2005] F.K. Wittel, F. Kun, H.J. Herrmann and B.H. Kröplin. *Breakup of shells under explosion and impact.* Physical Review E, vol. 71, no. 1, page 016108, 2005. 29, 107

[Wittel 2006] F.K. Wittel, F. Kun, B.D. Kröplin and H.J. Herrmann. *Study on the fragmentation of shells.* International Journal of Fracture, vol. 140, pages 243–254, 2006. 116

[Wittel 2008] F.K. Wittel, H.A. Carmona, F. Kun and H.J. Herrmann. *Mechanisms in impact fragmentation.* International Journal of Fracture, vol. 154, pages 105–117, 2008. 159

[Wolstenholme 1995] L.C. Wolstenholme. *A nonparametric test of the weakest-link Principle.* Technometrics, vol. 37, pages 169–175, 1995. 56, 59

[Xu 1994] X. Xu and A. Needleman. *Numerical simulations of fast crack growth in brittle solids.* Journal of Mechanics Physics of Solids, vol. 42, pages 1397–1434, 1994. 30, 46

[Zhang 1996] Y.G. Zhang and J. Ballman. *An explicit finite-difference scheme procedure for contact-impact analysis of crack edges.* Archive of Applied Mechanics, vol. 66, no. 7, pages 493–502, 1996. 30

[Zhang 1999] L. Zhang, X. Jin and H. He. *Prediction of fragment number and size distribution in dynamic fracture.* Journal of Physics, vol. 32, pages 612–615, 1999. 115

[Zhang 2006] H. Zhang and K. Ravi-Chandar. *On the dynamics of necking and fragmentation-I.Real-time and post-mortem observations in Al 6061-O.* International Journal of Fracture, vol. 142, pages 183–217, 2006. 28

[Zhang 2007] H. Zhang and K. Ravi-Chandar. *Dynamic fragmentation of ductile materials.* Journal of Physics D, vol. 45, page 214010, 2007. 28

[Zhao 2006a] J. Zhao, J.G. Cai, X.B. Zhao and H.B. Li. *Experimental study of ultrasonic wave attenuation across parallel fractures.* Geomechanics and Geoengineering: an International Journal, vol. 1, no. 2, pages 97–103, 2006. 68

[Zhao 2006b] J. Zhao, X.B. Zhao and J.G. Cai. *A further study on P-wave attenuation across parallel fractures with linear deformational behaviour.* Journal of Rock Mechanics and Mining Science, vol. 43, pages 776–788, 2006. 68

[Zhou 2004] F. Zhou, J.F. Molinari and Y. Li. *Three-dimensional numerical simulations of dynamic fracture in silicon carbide reinforced aluminum.* Engineering Fracture Mechanics, vol. 7, pages 1357–1378, 2004. 188

[Zhou 2005a] F. Zhou, J.F. Molinari and K.T. Ramesh. *A cohesive model based fragmentation analysis: effects of strain rate and initial defects distribution.* International Journal of Solids and Structures, vol. 42, pages 5181–5207, 2005. 123

[Zhou 2005b] F. Zhou, J.F. Molinari and T. Shioya. *A rate-dependent cohesive model for simulating dynamic crack propagation in brittle materials.* Engineering Fracture Mechanics, vol. 72, no. 9, pages 1383 – 1410, 2005. 30

[Zhou 2006a] F. Zhou, J.F. Molinari and K.T. Ramesh. *Analysis of the brittle fragmentation of an expanding ring.* Computational Materials Science, vol. 37(1-2), pages 74–85, 2006. 21, 32, 73, 84

[Zhou 2006b] F. Zhou, J.F. Molinari and K.T. Ramesh. *Characteristic fragment size distributions in dynamic fragmentation.* Applied Physics letters, vol. 88, no. 26, 2006. 32, 33, 106, 116

[Zhou 2006c] F. Zhou, J.F. Molinari and K.T. Ramesh. *Effects of material properties on the fragmentation of brittle materials.* International Journal of Fracture, vol. 139, no. 2, pages 169–196, 2006. 32, 87, 88, 135, 172

[Zienkiewicz 2003] O.C. Zienkiewicz, R.L. Taylor, S.J. Sherwin and J. Peiró. *On discontinuous Galerkin methods.* International Journal for Numerical Methods in Engineering, vol. 58, pages 119–1148, 2003. 51

[Zienkiewicz 2005a] O.C. Zienkiewicz and R.L. Taylor. The finite element method: For solid and structural mechanics. Elsevier, 6th édition, 2005. 37

[Zienkiewicz 2005b] O.C. Zienkiewicz and R.L. Taylor. The finite element method: Its basis and fundamentals. Elsevier, 6th édition, 2005. 37

[Ziff 1985] R.M. Ziff and E.D. McGrady. *The kinetics of cluster fragmentation and polymerization.* Journal of Physics A, vol. 18, no. 15, pages 3027–3037, 1985. 22

[Zukas 2004] J.A. Zukas. Introduction to hydrocodes. Elseivier, 2004. 30

Sarah Levy

1 rue du clos de l'ancyse, 30200, Bagnols-sur-Cèze, France
+33682001211 / +41762150759
sarah.levy@epfl.ch

EDUCATION

École Polytechnique Fédérale de Lausanne (EPFL), Switzerland　　　　September 2007 - Present
PhD Thesis

Laboratory: Laboratoire de Simulation Mécanique des Solides (LSMS)

Supervisor: Professor J.F. Molinari

Doctoral school of mechanics: courses include high performance computing, computational solid mechanics, space science, spacecraft design and system engineering, tutoring skills.

École Normale Supérieure de Cachan (ENS), Cachan, France　　　　September 2003 – September 2007
Agrégation & Master

4th year:　Master of Advanced Techniques for computational solid mechanics, passed with honors.

3th year:　Class preparing for the agrégation of mechanics.
The agrégation is a French national competitive examination dedicated to hire teaching staff of universities and classes préparatoires. Passed the agrégation examination in mechanics, third place.

1st and 2nd years:　Bachelor of Mechanics passed with honors.
The education includes courses on fundamental science (mathematics, continuum mechanics, and fluid mechanics) and engineering science (material science, mechanical design, conception, sizing, and specification).

RESEARCH AND TEACHING EXPERIENCE

Research :
- École Polytechnique Fédérale de Lausanne, Switzerland　　　　　　　September 2007 - Present
    "Exploring the physics behind dynamic fragmentation through parallel computing"

- The Johns Hopkins University (JHU), Baltimore, USA　　　　　　　April 2007 – June 2007
    "Stochastic modeling of the microstructure and simulation of one-dimensional fragmentation"

- Universidad de Concepción, Concepción, Chile　　　　　　　April 2006 – June 2006
    "Biomechanical modeling of the arm motion, and prosthesis design for disabled children"

Teaching assistant:
École Polytechnique Fédérale de Lausanne, Switzerland　　　　　　　September 2007 - Present
- Continuum mechanics: one semester, bachelor degree, Prof. J.F. Molinari
- Finite Elements Method: two semesters, bachelor degree, Prof. J.F. Molinari
- Selected chapters (wave mechanics, plasticity, and fracture mechanics): two semesters, master, Prof. J.F. Molinari
- Basics of continuum mechanics : four-day class, bachelor

JOURNAL PAPERS

1) S. Levy, J.F. Molinari, "Dynamic fragmentation of ceramics, signature of defects, and scaling of fragment sizes". Journal of the Mechanics and Physics of Solids, Vol 58(1), pages 12-26, 2010.

2) S. Levy, J.F. Molinari, A. Davison. "Fragmentation of a ring: predictable fragment size distribution". Submitted in Physical Reviews E.

3) S. Levy, J.F. Molinari, R. Radovitzky. "Dynamic fragmentation of a brittle plate under biaxial loading: strength or toughness controlled". To be submitted in the International Journal of Fracture.

4) S. Levy, J.F. Molinari, R. Radovitzky. "Fragment mass statistics: influence of the dimensionality". In preparation.

5) S. Levy, J.F. Molinari, R. Radovitzky. "Fragmentation mechanisms in three dimensions through fragment shape analysis". In preparation.

6) S. Levy, J.F. Molinari, R. Radovitzky. "Effects of secondary waves in fragmentation". In preparation.

CONFERENCE PAPERS

1) S. Levy, J.F. Molinari, "Statistical fragmentation of heterogeneous ceramics", 8th World Congress on Computational Mechanics (WCCM8), 5th European Congress on Computational Methods in Applied Sciences and Engineering (ECCOMAS 2008), 2008, Venice, Italy (2 pages).

2) S. Levy, A. Seagraves, J.F. Molinari, R. Radovitzky, "Discontinuous Galerkin method applied to fragmentation of heterogeneous materials", 9th Colloque en calcul des structures, 2009, Giens, France (6 pages).

3) S. Levy, J.F. Molinari, "Describing the dynamic response of a ceramic: The search for universality in fragment statistics", 12th International Conference on Fracture (ICF), 2009, Ottawa, Canada (9 pages).

4) S. Levy, A. Seagraves, J.F. Molinari, R. Radovitzky, "Parallel simulations of the fragmentation of heterogeneous structures", IV European Conference in Computational Mechanics (ECCM), 2010, Paris, France (2 pages).

PRESENTATIONS

1) S. Levy, J.F. Molinari, "Statistical fragmentation of heterogeneous ceramics", 8th World Congress on Computational Mechanics (WCCM8), 5th European Congress on Computational Methods in Applied Sciences and Engineering (ECCOMAS 2008), Venice, Italy, June 30-July 5, 2008.

2) S. Levy, A. Seagraves, J.F. Molinari, R. Radovitzky, "Discontinuous Galerkin method applied to fragmentation of heterogeneous materials", 9th Colloque en calcul des structures, Giens, France, May 25-29, 2009.

3) S. Levy, J.F. Molinari, "Describing the dynamic response of a ceramic: The search for universality in fragment statistics", 12th International Conference on Fracture (ICF), Ottawa, Canada, July 12-19, 2009.

4) S. Levy, A. Seagraves, J.F. Molinari, R. Radovitzky, "The discontinuous Galerkin method, a tool for parallel simulations in the context of dynamic fragmentation", Scientific Event on High Accuracy Numerical Methods and their application to Complex Physics Problems, Toulouse, France, December 7-8, 2009.

5) S. Levy, A. Seagraves, J.F. Molinari, R. Radovitzky, "Parallel simulations of the fragmentation of heterogeneous structures", IV European Conference in Computational Mechanics (ECCM), Paris, France, May 16-21, 2010.

POSTERS

1) ENAC's Day in Lausanne, Switzerland: "Understanding fragmentation: how numerical tools will help to improve the behavior of materials and structures subjected to blast loading", 2010.

2) Swiss Numerical Colloquium in Bale, Switzerland: "Simulating the fragmentation of large heterogeneous structures with the Discontinuous Galerkin method", 2009.

3) EPFL's Science Day in Lausanne, Switzerland: "Fragmentation simulations: a tool to understand how heterogeneous structures fragment under dynamic loadings". Best poster award for the doctoral school of mechanics, 2008.

COMPUTER SKILLS

Operating system: Linux, Windows
Programming languages: C++, C, Fortran, MPI, OpenMPI
Simulation softwares: CATIA, Solidworks, Matlab

LANGAGES

French: Mother tongue
English: Fluent (writing and speaking)
Spanish: Intermediate (writing and speaking)

OTHER ACTIVITIES

Conference organization: Active committee member of the EDCM 2010 (EPFL Doctoral Conference in Mechanics), for its first edition.
Student board: Culture and sport at ENS (Ecole Normale Supérieure de Cachan).
First aid: Red Cross in France, Samaritains at EPFL.